

Important Notice

This copy may be used only for the purposes of research and private study, and any use of the copy for a purpose other than research or private study may require the authorization of the copyright owner of the work in question. Responsibility regarding questions of copyright that may arise in the use of this copy is assumed by the recipient.

UNIVERSITY OF CALGARY

Full-wave Seismic Analysis: Source Comparisons, Land Streamer Tests, and Converted-
wave Processing

by

Gabriela M. Suarez Barbero

A THESIS

SUBMITTED TO THE FACULTY OF GRADUATE STUDIES
IN PARTIAL FULFILMENT OF THE REQUIREMENTS FOR THE
DEGREE OF MASTER OF SCIENCE

DEPARTMENT OF GEOSCIENCE

CALGARY, ALBERTA

NOVEMBER 2008

© Gabriela M Suarez Barbero 2008

UNIVERSITY OF CALGARY
FACULTY OF GRADUATE STUDIES

The undersigned certify that they have read, and recommend to the Faculty of Graduate Studies for acceptance, a thesis entitled "Full-wave Seismic Analysis: Source Comparisons, Land Streamer Tests, and Converted-wave Processing" submitted by Gabriela M Suarez in partial fulfilment of the requirements of the degree of Master of Science.

*Supervisor, Dr. R. R. Stewart
Department of Geoscience*

*Dr. G. F. Margrave
Department of Geoscience*

*Dr. M. Wieser
Department of Physics and Astronomy*

Date

Abstract

Two full-wave multicomponent seismic analyses are undertaken in this thesis. The first case assesses two land streamer surveys conducted by the CREWES project in the foothills of the Canadian Rocky Mountains. The first land streamer survey initially generated promising data with prominent reflections at around 50-60 ms and 300 ms. A second survey consisted of a comparison between land streamer and planted geophone data. Comparison of raw shots, amplitude spectra and stacking sections showed that the vertical channel data quality was similar for both datasets, while the planted geophone provided the highest quality radial channel data. In a 3D seismic survey acquired in this same area, seismic processing techniques for acquisition footprint removal constituted a way of improving the seismic images quality that are necessary for imaging near-surface structures and stratigraphy. The 2D and 3D seismic data correlated quite well and provided very promising pictures of the near surface.

The second analysis considered three 3-C 2D seismic lines acquired with different seismic sources (dynamite, heavy vibrator, and light vibrator) in the Spring Coulee area in southern Alberta. The objective was to compare sources for full-wave imaging. We found that the explosive source provided deeper penetration, higher frequency content and better resolution, but was highly variable from source to source location. The heavy vibroseis data appears to be more consistent, with similar characteristics to the dynamite especially in the shallow parts of the sections. The lighter vibrator data proved to be an efficient source for acquiring good quality P-wave data to 1000 ms, but not for converted wave data.

Acknowledgements

Two years have accumulated an enormous list of people that I would like to thank. Maybe the most important people have been the ones who have given me emotional support: thanks to my dear partner Gerardo, who patiently waited for me for two years and has given me all the TLC that I have needed; to my dear friend Diane who have been there every time I have had a meltdown, thanks for every smile, for every word of strength and for the moments of joy that together we have shared. To my family, for always being there for me.

I would also like to thank Kevin Hall, Joe Wong, Malcolm Beltran, Eric Gallant, David Henley, Rolf Maier, Peter Manning, Joanna Cooper, Alejandro Alcudia and the students of geophysic's summer school 2007 for their help during the acquisition of the land streamer experiments. Dr. Gary Margrave provided invaluable theoretical and practical input, and helpful suggestions, for which I am grateful. I am also grateful to WesternGeco and the sponsors of CREWES for their financial and technical support in this research. I also thank my supervisor Dr. Robert Stewart, for the guidance, direction and input he provided throughout the duration of this thesis.

Dedication

For my spouse and family: Gerardo, Mama, Papa, Florangel and Tommy. Without their love and support, I could never even started and completed one of my dreams come true.

I love you all !!!!

Table of Contents

Approval Page.....	ii
Abstract.....	iii
Acknowledgements.....	iv
Dedication.....	v
Table of Contents.....	vi
List of Tables.....	ix
List of Figures and Illustrations.....	x
List of Symbols, Abbreviations and Nomenclature.....	xix
CHAPTER ONE: INTRODUCTION.....	1
1.1 Introduction to the thesis.....	2
1.2 Software used.....	3
CHAPTER TWO: A FIELD COMPARISON OF 3-C LAND STREAMER VERSUS PLANTED GEOPHONE DATA.....	5
2.1 Location of the area of study.....	6
2.2 Description of the land streamer system.....	7
2.3 Test 1: 2007 Field School.....	9
2.4 Seismic processing and analysis of the data of Test 1.....	11
2.4.1 Comparison of P and P-S stacked sections.....	15
2.4.2 Refraction Analysis.....	16
2.4.3 Test 2: Comparison of 3-C land streamer versus planted geophone data, acquired in March 2008, over a grass-covered hill.....	17
2.5 Seismic Processing of the Test 2 data.....	19
2.5.1 Vertical Channel.....	21
2.5.2 Horizontal Channel.....	33
2.6 Analysis of the Test 2 data.....	36
2.6.1 Comparison of shot gathers and stacked sections.....	36
2.6.1.1 Raw shot gathers:.....	36
2.6.1.2 Unmigrated stacked sections:.....	37
2.6.2 Spectral analysis.....	39
2.6.2.1 F-x analysis of the raw shot gathers.....	39
2.6.2.2 F-x analysis of the unmigrated stacked sections.....	43
2.6.3 Frequency analysis of the receiver gathers.....	47
2.7 Conclusions.....	49
2.7.1 Conclusions for Land streamer Test 1.....	49
2.7.2 Conclusion for land streamer Test 2.....	49
CHAPTER THREE: USING F-K-K FILTERING METHODS TO SUPPRESS ACQUISITION FOOTPRINTS IN THE PRIDDIS 3D STACKED DATASET	51
3.1 Description of the seismic survey.....	52
3.2 Comparison of stacked sections from the 2D land streamer line, planted geophone line and 3D survey from the Priddis test site.....	54
3.3 F-K-K filtering as a method to improve the image on the Priddis 3D stacked volume.....	56

3.3.1 Quality measures to establish filtering parameters.....	56
3.3.2 Assessment of acquisition footprint pattern	58
3.3.2.1 Quality control stacks of selected in-lines, cross-lines and raw time slice sections before F-K-K filtering.....	58
3.3.2.2 F-K spectral analyses of selected in-line and cross-line stacks and raw time slice sections before F-K-K filtering.....	60
3.3.3 Filter modes	62
3.3.3.1 K-notch filtering	62
3.3.3.2 Coherency filtering	63
3.3.3.3 Post-stack trace interpolator.....	64
3.3.4 Parameterization of the filters	64
3.3.5 Filtering results.....	65
3.4 Seismic attributes from the 3D Priddis volume after footprint removal techniques	71
3.5 Conclusions.....	74
CHAPTER FOUR: SEISMIC SOURCE COMPARISON FOR COMPRESSIONAL AND CONVERTED-WAVE GENERATION AT SPRING COULEE, ALBERTA. Part I: Heavy vibroseis-dynamite	
4.1 Multicomponent surface-seismic acquisition	80
4.2 Vibroseis vs. Explosive sources.....	81
4.3 The Spring Coulee seismic experiment	85
4.3.1 Description of the survey.....	86
4.3.1.1 The ARAM Aries spread	87
4.3.1.2 Coincident source points of the ARAM Aries spread for the three source types.....	87
4.4 Conditioning of the data for the source comparison analysis	90
4.4.1 Vertical Channel.....	90
4.4.2 Horizontal Channel.....	96
4.5 Comparison and analysis of the source test datasets	100
4.5.1 . Part 1: Heavy vibroseis-dynamite comparison.....	102
4.5.1.1 Raw data: Characteristics of different types of signal and noise	102
4.5.1.2 Unmigrated stacked sections:	107
4.5.1.3 Seismic signal band estimation using f-x spectra	112
4.5.1.4 Frequency bandwidth estimation using filter panels	120
4.5.1.5 Signal and noise estimation	122
4.5.1.6 Quantified attribute measurements for the source comparison	124
4.6 Conclusions.....	136
CHAPTER FIVE: SEISMIC SOURCE COMPARISON FOR COMPRESSIONAL AND CONVERTED-WAVE GENERATION AT SPRING COULEE, ALBERTA. Part II: Heavy vibroseis-dynamite-envirovibe	
5.1 Raw data: Characteristics of different types of signal and noise	140
5.2 Unmigrated stacked sections	144
5.3 Seismic signal band estimation using f-x spectra	149
5.3.1 F-x analysis of the raw shot gathers	149
5.3.2 F-x analysis of the unmigrated stacked sections	152

5.4 Frequency bandwidth estimation using filter panels	155
5.5 Conclusions.....	158
CHAPTER SIX: CONCLUSIONS AND FUTURE WORK	160
6.1 Thesis summary	160
6.2 Future work.....	163
REFERENCES	165
APPENDIX A : ANALYSIS OF THE WEST CASTLE SEISMIC SURVEYS	171
A.1 Introduction.....	171
A.1.1 Location of the Area of Study	172
A.1.2 Previous geophysical investigations of the study area	173
A.1.3 Structure and stratigraphy of the survey area	174
A.2 Part I: Near surface characterization using the high-resolution 3-C seismic survey	175
A.2.4 Acquisition parameters of the high-resolution 3-C survey.....	176
A.2.5 Near-surface velocity structure.....	178
A.2.6 Discussion and Limitations	182
A.3 Part II. 2D seismic data processing and modelling of the vertical component data.....	183
A.4 Conclusions.....	189

List of Tables

Table 2.1. Main processing steps for the land streamer and planted geophone vertical channel data.	22
Table 2.2. Main processing steps for the land streamer and planted geophone P-S data. .	33
Table 3.1. In-line (IL) and cross-line (XL) wavenumber coordinates.	61
Table 4.1. Main processing steps for the heavy vibroseis vertical channel data.	91
Table 4.2. Main processing steps for the heavy vibroseis radial channel data.	97
Table A.1. Resulting near surface model for Area 1.	182
Table A.2. Resulting near surface model for Area 3.	182
Table A.3. Resulting near surface model for Area 4.	182

List of Figures and Illustrations

Figure 2.1. Aerial photograph showing the location of the study area: The first test on dirt road (red line), the second test on grass covered hill (yellow line).....	7
Figure 2.2. Land streamer system components: (a) land streamer basic configuration used on the first test; (b) top and bottom geophone plate, (c) geophone unit with wings to stop overturning, and (d) woven belt.	8
Figure 2.3. Illustration of the land streamer configuration used on the first (top) and second (bottom) land streamer seismic experiment: a 20 m streamer with 3-C geophones separated 1 m, with a sledgehammer P-wave source located at 1 m off the cable (Test 1) and a vibroseis source (test 2).	10
Figure 2.4. Actual land streamer configuration used in the first Priddis experiment. Individuals shown were participating in the University of Calgary's 2007 Geophysics Field School.....	11
Figure 2.5. Hammer seismic source used on the first land streamer experiment.	11
Figure 2.6. Three-component shot gathers for two shots: vertical component (left), radial component (centre) and transverse component (right).	12
Figure 2.7. Three vertical component shot gathers: (a) raw, (b) band-pass filter and AGC applied, (c) with radial trace filters applied and (d) radial trace filters plus Gabor deconvolution applied.	13
Figure 2.8. Radial component shot gathers with radial filters applied (left) and radial filters + Gabor deconvolution applied (right).	13
Figure 2.9. Amplitude spectrum for FFID 1798 for (a) the vertical component, and (b) for the radial component.	14
Figure 2.10. Stacked sections for the vertical component (left) and for the transverse component (right).....	16
Figure 2.11. Comparison of the VSP corridor stack (from Miong, 2008) with the first 100 ms of vertical component stacked section from the land streamer.	16
Figure 2.12. Comparison of P stacked section (left) with P-S stacked section (right).	16
Figure 2.13. Results of the refraction modeling for the land streamer Test 1.	17

Figure 2.14. Land streamer experiment site: (a) the vibroseis source next to the land streamer and conventional line; in (b) we can see the distance between the planted geophone and land streamer lines; in (c) is shown the 4-m distance between the source line and the receiver lines and in (d) and (e) are shown a receiver streamer configuration and the land streamer towing device, respectively.	19
Figure 2.15. Fold of coverage for the Priddis land streamer Test 2.....	20
Figure 2.16. Raw shot gathers from (a) the conventional line, and (b) the land streamer system. Vertical channel (left), radial channel (centre) and transverse channel (right).....	21
Figure 2.17. Description of the flow used for the FXCNS plus AAA techniques.....	25
Figure 2.18. Common source gathers for source position 18 of 40 in the planted geophone line (top) and land streamer line (bottom): (a) raw data; (b) after deconvolution; (c) deconvolution plus first and second pass of noise attenuation; and (d) final gather after all passes of noise attenuation.....	28
Figure 2.19. Stacked section comparison for the conventional line vertical component after noise attenuation procedures: (a) Brute stack; (b) Surface consistent deconvolution stack; (c) after first pass of noise attenuation; and (d) after all passes of noise attenuation.....	29
Figure 2.20. Stacked section comparison for the land streamer line vertical component after noise attenuation procedures: (a) Brute stack; (b) Surface consistent deconvolution stack; (c) after first pass of noise attenuation; and (d) after all passes of noise attenuation.	30
Figure 2.21. Final stacked section with the best output from noise attenuation, final stacking velocities and mute for the conventional line (top) and for the land streamer line (bottom).....	32
Figure 2.22. Side by side comparison of two consecutive portions of the stacked sections for the conventional line (left) and for the land streamer line (right).	32
Figure 2.23. Common source gathers for the radial component of the planted geophone line (top) and land streamer line (bottom): (a) raw data; (b) after deconvolution; (c) deconvolution plus first and second pass of noise attenuation; and (d) final gather after all passes of noise attenuation.....	34
Figure 2.24. Interval gamma used for the CCP binning.	35
Figure 2.25. Final CCP stacked section with the best output from noise attenuation, final stacking velocities and mute for the conventional line (top) and for the land streamer line (bottom).....	36

Figure 2.26. Comparison of two raw shot gathers. In (a), half of a split-spread record from the vertical component conventional line. The same shotpoint from the vertical component land streamer is shown in (b) with the lateral coordinate reversed to highlight the comparison. The same comparison is done of the same record for the radial component of the conventional line (c) and of the land streamer line (d).	37
Figure 2.27. Comparison of stacked sections in the vertical channel for the conventional line data (top) and for the land streamer data (bottom). Same sections as Figure 2.21 but zooming on the first 0.5 seconds.	38
Figure 2.28. Comparison of stacked sections in the radial channel for the conventional line data (top) and for the land streamer data (bottom). Same sections as Figure 2.25 but zooming on the first 0.6 seconds..	39
Figure 2.29. Average Fourier amplitude spectrum of a raw shot gather for the vertical channel (left) and radial channel (right) of the conventional (CL) and land streamer line (LS), with windows corresponding to (a) signal only area, (b) first break area, and (c) groundroll/noise area.....	42
Figure 2.30. F-x spectral analysis for the final unmigrated, unfiltered P-wave stack for conventional line and land streamer data computed over the time zone 70-300 ms. The f-x amplitude spectrum for the conventional line is shown in (a); (b) shows a similar spectrum for the land streamer data. The land streamer data show reduced signal power above 80 Hz. In (c) and (d) the f-x phase spectra are shown corresponding to (a) and (b), respectively. The conventional line data show very low phase coherence from 100 to 180 Hz and very weak coherence from 180 to 240 Hz. The land streamer data show good phase coherence from 50 to 80 Hz and very little at higher frequencies.	45
Figure 2.31. F-x spectral analysis for the final unmigrated, unfiltered PS-wave stack for conventional line and land streamer data computed over the time zone 60-500 ms. The f-x amplitude spectrum for the conventional line is shown in (a); (b) shows a similar spectrum for the land streamer data. The land streamer data show reduced signal power above 100 Hz. In (c) and (d) the f-x phase spectra are shown corresponding to (a) and (b), respectively. The conventional line data show very low phase coherence from 100 to 180 Hz and very weak coherence from 180 to 300 Hz. The land streamer data show good phase coherence from 50 to 100 Hz and very weak from 200 to 240 Hz.	46
Figure 2.32. Frequency analysis of the common receiver gathers for both lines. (a) and (b) show the contour plots for the vertical channel conventional line and land streamer, respectively. (c) and (d) show the same analysis but for the radial channels of the conventional line and land streamer data, respectively.	48
Figure 3.1. Post-survey shot and receiver locations extracted from the dataset headers..	53
Figure 3.2. CMP fold for the survey (from Lawton et al., 2008).....	53

Figure 3.3. Identification of some of the common reflectors for the land streamer, 3D and zero-offset VSP: (a) 3D crossline stacked section for the eastern edge, (b) 3D crossline stacked section western edge of the land streamer section and (c) for the VSP, 3D and land streamer.	55
Figure 3.4. Comparison of stacked sections from (a) the 2D land streamer line, (b) 2D planted-geophone line and (c) coincident 3D cross-line.....	55
Figure 3.5. Quality control in-line stacked sections prior to F-K-K filtering.	58
Figure 3.6. Quality control cross-line stacked sections prior to F-K-K filtering.....	59
Figure 3.7. Timeslices prior to F-K-K filtering.	59
Figure 3.8. F-K spectrum of a selected inline stacked section.....	60
Figure 3.9.(a) Time slices and their (b) F-K spectra prior to filtering.	62
Figure 3.10. Difference between the input and filtered cross-line stacked sections using the four different filters.	66
Figure 3.11. Difference between the input and filtered in-line stacked sections using the four different filters.	66
Figure 3.12. F-K spectra of selected cross-line stacked sections before and after the final chosen filtering.	68
Figure 3.13. First 200 ms of the filtered cross-line (left) and in-line (right) stacked sections, before and after using the four different filters.	69
Figure 3.14. Comparison of time slices 50, 80, and 90 ms before and after the four different filters tested on the Priddis dataset (F-K-K filtering: K-notch options 1 and 2, coherency filter and post-stack trace interpolation).	70
Figure 3.15. Seismic attributes extracted from the Priddis 3D stacked seismic volume. The attributes were extracted from time slice 160 ms with no horizon flattening....	73
Figure 3.16. Seismic attributes extracted from the Priddis 3D stacked seismic volume. The attributes were extracted from time slice 79 ms, with flattening of a horizon picked at approximately 100 ms.	73
Figure 4.1. Aerial photograph showing the location of the study area. Photograph from Google Earth.	86
Figure 4.2. Schematic diagram of the Spring Coulee experiment. Details of the ARAM layout are shown as well.	89
Figure 4.3. Shot locations of dynamite, mini-vibe and heavy-vibe sources.....	89

Figure 4.4. Fold coverage for the Spring Coulee full-length heavy vibroseis line (multicolour line) and for the segment of the line with coincident source locations (red line).	90
Figure 4.5. Common source gathers for the P-wave full-length heavy vibroseis line: (a) raw data, (b) pre-deconvolution noise attenuation, (c) after deconvolution, and (d) final gather after all passes of noise attenuation.....	92
Figure 4.6. Final CMP for (a) the vertical-component and (b) the radial-component of the full-length heavy vibroseis line.....	95
Figure 4.7. Final vertical-component stacked section with the best output from noise attenuation, final stacking velocities and mute for the full length heavy vibroseis line.....	96
Figure 4.8. Common source gathers for the radial-component full-length heavy vibroseis line: (a) raw data, (b) pre-deconvolution noise attenuation, (c) after deconvolution, and (d) final gather after all passes of noise attenuation.....	98
Figure 4.9. Common receiver stacked section before and after receiver statics. The red rectangles show areas where reflector continuity has improved due to the receiver statics.....	99
Figure 4.10. Final radial-component stacked section with the best output from noise attenuation, final stacking velocities and mute for the full length heavy vibroseis line.....	100
Figure 4.11. Comparisons of a portion of the vertical-component sections for the heavy vibroseis, dynamite and mini vibroseis sources before and after phase matching. All the datasets were matched to the heavy vibroseis data.	102
Figure 4.12. Comparison of two raw shot gathers. In (a), half of a split spread record from the vertical-component dynamite line. The same shotpoint from the vertical-component heavy vibroseis line is shown on (b) with the lateral coordinate reversed to ease the comparison. The same comparison is shown for the same record for the radial-component of the dynamite on (c) and of the heavy vibroseis line on (d)......	103
Figure 4.13. Three vertical-component raw shots are compared along the line. In (a), a shot from the beginning, middle and end of the heavy vibroseis line are shown. In (b), the same shot locations but for the dynamite line.....	105
Figure 4.14. Amplitude spectra for a window located on first breaks for shot locations 1266, 1365 and 1419 for (a) the heavy vibroseis and (b) the dynamite dataset. These three shots are the same shots shown in Figure 4.14.....	106

Figure 4.15. Three radial-component raw shots are compared along the line. In (a), shots from the beginning, middle and end of the heavy vibroseis line are shown. In (b), the same shot locations but for the dynamite line are shown.	107
Figure 4.16. Comparison of the vertical-component heavy vibroseis (top) and dynamite (bottom) stacked sections. The sections were generated with coincident data, with phase and amplitude matching of the dynamite to the vibroseis, best mute and velocities.	108
Figure 4.17. Zoomed sections of the shallow portion (0-1.2 s) of the final vertical-component stacked sections for the heavy vibroseis (left) and dynamite (right)....	109
Figure 4.18. Side-by-side comparison of different portions along the vertical-component stacked sections for the dynamite and heavy vibroseis.....	109
Figure 4.19. Portion of the amplitude- and phase-matched, vertical-component, heavy vibroseis (top) and dynamite (bottom) stacked section, zoomed in the zone of interest (500-1500 ms).	110
Figure 4.20. Comparison of the radial-component heavy vibroseis (top) and dynamite (bottom) CCP stacked sections. The sections were generated with coincident data, with phase- and amplitude-matching of the dynamite to the vibroseis, best mute and velocities.	111
Figure 4.21. Side-by-side comparison of different portions along the radial-component stacked sections for the dynamite and heavy vibroseis.....	111
Figure 4.22. Portion of the amplitude- and phase-matched, radial-component, heavy vibroseis (top) and dynamite (bottom) stacked section, zoomed in the zone of interest (500-2500 ms).	112
Figure 4.23. Analysis windows used for the average Fourier spectra amplitude calculation for the heavy vibroseis-dynamite comparison. The three zones for the vertical-component raw shot record are shown in (a) and in (b) the three zones for the radial-component raw shot record.	113
Figure 4.24. Average Fourier amplitude spectrum of a raw shot gather for the vertical channel (left column) and radial channel (right column) of the heavy vibroseis and dynamite data, with windows corresponding to: (a) and (b) signal-only area; (c) and (d) first-break area (vertical-component)/refraction event (radial-component); and (e) and (f) noise area.	116
Figure 4.25. F-x spectral analysis for the final unmigrated, unfiltered P-wave stack to compare heavy vibroseis and dynamite data computed over the time zone 432-1467 ms. The f-x amplitude spectrum for the heavy vibroseis is shown in (a); (b) shows a similar spectrum for dynamite data. (c) and (d) show the f-x phase spectra corresponding to (a) and (b), respectively.	118

Figure 4.26. F-x spectral analysis for the final unmigrated, unfiltered PS-wave stack to compare heavy vibroseis and dynamite data computed over the time zone 700-2500 ms. The f-x amplitude spectrum for the heavy vibroseis is shown in (a); (b) shows a similar spectrum for dynamite data. (c) and (d) show the f-x phase spectra corresponding to (a) and (b), respectively.	119
Figure 4.27. Filter panels for the vertical-component of a raw common shot gather from (a) the heavy vibroseis and (b) dynamite data.....	121
Figure 4.28. Filter panels for the radial-component of a raw common shot gather from (a) the heavy vibroseis and (b) dynamite data.	123
Figure 4.29. Signal and noise estimation for: (a) the vertical and (b) radial-component heavy vibroseis and dynamite data. For the vertical-component the analysis was done over the time zone 432-1467 ms and for the radial-component over the time zone 650-2567 ms.	124
Figure 4.30. Deterministic trace attributes calculated for all CMP locations in the vertical-component stacked sections: (a) Resolving factor, (b) time length and temporal resolution, and (c) frequency length. For every plot there is a curve corresponding to the vibroseis (HV) and to the dynamite (Dyn) data.	132
Figure 4.31. Deterministic trace attributes calculated for all CMP locations in the vertical-component stacked sections: (a) first zero-crossing, (b) bandwidth attributes and (c) total effective bandwidth. For every plot there is a curve corresponding to the vibroseis (HV) and to the dynamite (Dyn) data.	133
Figure 4.32. Deterministic trace attributes calculated for all CCP locations in the radial-component stacked sections: (a) Resolving factor, (b) time length and temporal resolution, and (c) frequency length. For every plot there is a curve corresponding to the vibroseis (HV) and to the dynamite (Dyn) data.	134
Figure 4.33. Deterministic trace attributes calculated for all CCP locations in the radial-component stacked sections: (a) first zero-crossing, (b) bandwidth attributes and (c) total effective bandwidth. For every plot there is a curve corresponding to the vibroseis (HV) and to the dynamite (Dyn) data.	135
Figure 5.1. Three vertical-component raw shots are compared along the line. In (a), shots from the beginning, middle and end of the heavy vibroseis line are shown. In (b) and (c), the same shot locations but for the dynamite and mini vibroseis lines are shown, respectively.	141
Figure 5.2. Comparison of two vertical-component raw shot gathers. In (a), half of a split-spread record from the dynamite and heavy vibroseis lines with the lateral coordinates reversed to ease the comparison. The same comparison is shown in (b) but for the mini vibroseis and heavy vibroseis data. The final comparison between the mini vibroseis and the dynamite is shown in (c).	142

Figure 5.3. Three radial-component raw shots are compared along the line. In (a), shots from the beginning, middle and end of the heavy vibroseis line are shown. In (b) and (c), the same shot locations but for the dynamite and mini vibroseis lines are shown, respectively. 143

Figure 5.4. Comparison of two radial-component raw shot gathers. In (a), half of a split spread record from the dynamite line and heavy vibroseis line with the lateral coordinates reversed to ease the comparison. The same concept is shown in (b) but for the mini vibroseis and heavy vibroseis data. The final comparison between the mini vibroseis and the dynamite is shown in (c). 144

Figure 5.5. Portions of the amplitude- and phase-matched, vertical-component, (a) heavy vibroseis, (b) dynamite and (c) mini-vibroseis stacked section, zoomed in on the early times of the section (0-1000 ms). 145

Figure 5.6. Portion of the amplitude- and phase-matched, vertical-component, (a) heavy vibroseis, (b) dynamite and (c) mini-vibroseis stacked section, zoomed in on the zone of interest (500-1500 ms). 146

Figure 5.7. Portions of the amplitude- and phase-matched, radial-component, (a) heavy vibroseis, (b) dynamite, and (c) mini-vibroseis stacked sections, zoomed in on the early times (0-1900 ms). 148

Figure 5.8. Analysis windows used for calculating the average Fourier spectra amplitudes for heavy vibroseis-dynamite-mini vibroseis data comparison. The three zones for the vertical-component raw shot record are shown in (a) and the three zones for the radial-component raw shot record in (b). 149

Figure 5.9. Average Fourier amplitude spectrum of a raw shot gather for the vertical channel ((a), (c) and (d)) and radial channel ((b),(d) and (f)) of the heavy vibroseis, dynamite data, and mini vibroseis, with windows corresponding to: (a) and (b) signal only area, (c) and (d) first break area and (e) and (f) groundroll/noise area. 151

Figure 5.10. F-x spectral analysis for the final unmigrated, unfiltered P-wave stack for heavy vibroseis, dynamite and IVI-mini vibroseis data comparison computed over the time zone 432-1467 ms. The f-x amplitude spectrum for the heavy vibroseis is shown in (a); (c) and (e) shows similar spectra for the dynamite and mini vibroseis data, respectively. In (b), (d) and (f) are shown the f-x phase spectra corresponding to (a), (c) and (e), respectively. 153

Figure 5.11. F-x spectral analysis for the final unmigrated, unfiltered PS-wave stack for the heavy vibroseis, dynamite and IVI-mini vibroseis data comparison computed over the time zone 700-2500 ms. The f-x amplitude spectrum for the heavy vibroseis is shown in (a); (c) and (e) shows similar spectra for the dynamite and mini vibroseis data, respectively. In (b), (d) and (f) are shown the f-x phase spectra corresponding to (a), (c) and (e), respectively. 154

Figure 5.12. Filter panels for the vertical component of a raw common shot gather from (a) the heavy vibroseis, (b) dynamite data, and (c) mini vibroseis data.....	156
Figure 5.13. Filter panels for the radial-component of a raw common shot gather from (a) the heavy vibroseis, (b) dynamite data, and (c) mini vibroseis data.	157
Figure A.1. Map showing the location of the Castle Mountain Resort area, which is close to the area where the seismic surveys were done.	172
Figure A.2. Photograph, looking south, of the West Castle River area of southern Alberta with the seismic line (shot in August-September 2006) annotated (from Stewart et al., 2006).	172
Figure A.3. Geologic cross-section from the south-west to north-east across the Lewis and Gardner Thrusts in the West Castle area (from Norris, 1993).	173
Figure A.4. Three-component shot gather for Area 1: vertical component (left), transverse component (middle) and radial component (right).	177
Figure A.5. Three-component shot gather for Area 3: vertical component (left), transverse component (middle) and radial component (right).	178
Figure A.6. Three-component shot gather for Area 4: vertical component (left), transverse component (middle) and radial component (right).	178
Figure A.7. Example of hodograms for some receivers of areas 1, 3 and 4.	181
Figure A.8. Raw shots after geometry: (a) South of the line, (b) middle of the line shots, and (c) north of the source line.	184
Figure A.9. Brute stacked section.	184
Figure A.10. Stacked section before and after deconvolution : Stack section with 1 st pass of noise rejection (top), stack section with 1 st pass of noise rejection + surface consistent deconvolution (bottom).	186
Figure A.11. Stacked section before (top) and after (bottom) pre-stack migration.	188
Figure A.12. Comparison of geologic cross-section of the West Castle area (top; Norris, 1993) to migrated section from Hall et al. (2007). LT = Lewis Thrust, GT = Gardiner Thrust; CT = Coleman Thrust.	189

List of Symbols, Abbreviations and Nomenclature

(Page 1 of 2)

Symbol	Definition
AAA	Anomalous amplitude attenuation
ACP	Asymptotic conversion point
AGC	Automatic gain control
CCP	Common conversion point
CDP	Common depth point
CL	Conventional line
COCORP	Consortium for Continental Reflection Profiling
CREWES	Consortium for Research in Elastic Wave Exploration
DYN, Dyn	Dynamite
f_c	Central frequency
FFID	Field file identification
F-K	Frequency-wave number
F-K-K, F-Kx-Ky	Frequency- wave number in x axis-wave number in y axis
f_P	Peak frequency
F-X	Frequency-offset
FXCNS	f-x coherent noise attenuation filter
H_f	High-frequency bandwidth
HV	Heavy vibroseis
GLI	Generalized linear inversion
IL	In-line
L_f	Frequency length
Lt	Signal length or time length
LS	Land streamer
MEMS	Micro-Electro-Mechanical Systems
MV	IVI Envirovibe, mini vibroseis
N(f)	Noise amplitude spectrum
NMO	Normal moveout
P(f)	Power at the frequency f
P_{max}	Maximum power
P-wave	Primary wave
QC	Quality control
RMS	Root-mean square
SCAC	Surface-consistent amplitude compensation
SEG	Society of Exploration Geophysicists

List of Symbols, Abbreviations and Nomenclature

(Page 2 of 2)

Symbol	Definition
S/N	Signal-to-noise
SNR	Signal-to-noise ratio
S-wave	Shear-wave
t_0	Reference time
TWT, twt	Two-way time
T-X-Y	Time-space
VSP	Vertical seismic profiling
W(f)	Amplitude spectrum of a seismic wavelet
W(fp)	Peak amplitude of a seismic wavelet
w(t)	Seismic time wavelet
XL	Cross-line
3-C	Three component
2D	Two dimensional
3D	Three dimensional
4D	Four dimensional

Chapter One: INTRODUCTION

The seismic method is by far the most important exploration geophysical technique in the oil and gas industry in terms of expenditures and the number of geophysicists involved. Its predominance is due to high accuracy, high resolution, and deep penetration (Telford et al., 1990). Other applications include: groundwater searches, civil engineering, and some applications in mineral exploration.

The advances in seismic surveys over the last decades have changed the way oil and gas fields are developed and managed. From being a predominantly exploration focused tool, the seismic method has progressed to become one of the most cost effective methods for optimising field production. In many cases, seismic results have increased the life of ‘mature’ fields by several years (Jahn et al., 2003).

Some of these recent advances in seismic surveying have brought a renewed interest in converted-wave imaging, enhancing even more the reliability and precision of lithologic and reservoir prediction and the added value of the seismic method as an exploration and production tool.

However, there is still a long way to go to improve the quality of our seismic sections, especially on the data acquisition side. Important aspects in seismic acquisition such as: determining optimal recording environments, survey design expertise, source type, and technological advances in equipment, are going to determine the success of converted-wave exploration, and the possibility of obtaining more interpretable converted-wave images. Therefore, the objectives of this research are: to 1) present two topics in seismic data acquisition that explore new technologies such as the 3-C land streamer system, and 2) to make a comparison of sources for converted-wave generation.

If proven useful, the land streamer system could be applied not only to environmental and engineering applications but also to real oil exploration projects, reducing costs, crew requirements and acquisition time. This system will also offer the possibility of enhancing near-surface images. Analyzing seismic sources for converted-wave generation will assist in determining what seismic source is ideal for the generation of P-waves and converted waves (P-to-S) for our specific area of study. It could also provide some detailed information about the characteristics of these seismic sources. This information could also be used as a guideline for the selection of acquisition parameters in future acquisition. The following section provides an outline of this thesis.

1.1 Introduction to the thesis

Various 3D and 2D seismic survey datasets were acquired from two survey areas: Priddis and Spring Coulee, Alberta. In Chapter 2, a preliminary land streamer data and a side-by-side comparison between land streamer and planted geophone data, from a site near Priddis, Alberta are described. The preliminary 3-C land streamer dataset is processed and analyzed to test the capabilities of this acquisition technique and obtain some near-surface information from the top 50 m. Then the second land streamer experiment, which consisted of a side-by-side comparison of this system with a 3-C planted-geophone line, is presented. The identical seismic data processing sequence applied to both datasets is described. The datasets are compared and analyzed using the raw field data and fully processed datasets, to determine the strength and weaknesses of this experimental acquisition technique.

In Chapter 3, we tried to improve the image quality of the 3D seismic survey acquired near Priddis, Alberta. Acquisition footprint removal techniques are tested on this

post-stacking, migrated 3D volume. Seismic attributes, are extracted from the final “improved” volume as a quality control tool to see if the image is optimum for the mapping of shallow stratigraphy and structure (depths of up to 500 m). To corroborate if the shallow reflections of the land streamer stacked sections of Chapter 2 are real, a comparison of these two sections with the corresponding 3-D cross-line is presented.

In Chapter 4, three 2D 3-C lines acquired with different seismic sources (IVI-mini vibroseis, 52,000 lb vibroseis, and explosives) in the Spring Coulee, Alberta area are described. A qualitative and quantitative study of these three seismic sources is done to investigate and compare their characteristics at this particular site in Spring Coulee, Southern Alberta.

Chapter 5 summarizes conclusions derived from this research project. Future work to improve the acquisition, analysis and comparison of the land streamer and source comparison datasets are also suggested.

Results of the seismic data processing, near-surface modeling, a preliminary interpretation of a 2D seismic survey seismic line acquired near West Castle River, Alberta, are shown in Appendix A.

1.2 Software used

The following software packages were used for the processing and analysis of the datasets presented in this thesis:

- *Microsoft Word* and *Microsoft Powerpoint* to assemble the text and images of this thesis
- *Microsoft Excel* for displaying the wavelet analysis of the source comparison
- MATLAB for receiver coupling analysis

- CREWES MATLAB library for the f-x analysis
- ProMAX, Landmark software, for seismic data processing
- OMEGA, WesternGeco software, for seismic data processing and part of the amplitude and wavelet analysis of the datasets
- Hampson Russell (GLI3D) for near-surface modeling
- GOCAD for preliminary seismic interpretation and attributes creation.

Chapter Two: A FIELD COMPARISON OF 3-C LAND STREAMER VERSUS PLANTED GEOPHONE DATA

Over the past two decades, high-resolution seismic methods have become popular for resolving a wide variety of geological, engineering, and environmental problems (van ver Veen et al., 2001). Investigations such as these require the imaging of shallow targets (< 300 m) using densely spaced sources and receivers, which are usually distributed over short acquisition spreads. However, using the traditional technique of planting geophones in the ground and physically moving cables in a CDP roll-along is costly, labour-intensive and time-consuming, especially for shear-wave surveys with their requirement for smaller spatial sampling (Pugin et al., 2004). To address some of these issues, towed land-streamer systems have been in use since the 1970s.

A land streamer could be defined as an array of geophones designed to be towed along the ground without planting. This idea comes from the seismic marine industry, where large volumes of high-resolution data are recorded using marine streamers. However, the first tests on land were restricted to ice or snow (“the snow streamer”) both of which provide smooth sliding surfaces suitable for long streamer use and good geophone coupling (van ver Veen et al., 2001). The concept of a towed land cable was patented by Kruppenbach and Bedenbender (1975; *ibid*, 1976).

Acquisition with the towed land streamer is somewhat similar to that of the marine streamer, but initially the land streamer is kept at a fixed location, and the shot positions are moved from the back to the front of the array. Once the shot position reaches the front, it is generally kept at a fixed distance relative to the first receiver. Sources and receivers are shifted simultaneously after each shot. The streamer is moved

up one shot interval, the shot is initiated once the streamer has been stationary for a few seconds, and the process repeated (van ver Veen et al., 2001).

Numerous successful case studies of land streamer acquisition have been presented during the last three decades, helping to improve near-surface imaging (van der Veen et al., 1998; *ibid*, 1999; *ibid*, 2001; Pugin et al., 2004; Ivanov et al., 2006; Lorenzo et al., 2006; Inazaki, 2006; Speece et al., 2007). To further develop this technology, especially for converted-wave recording, the CREWES Project acquired a 3-C land-streamer system. The first experiment was conducted during the summer of 2007 in the Priddis area located southwest of Calgary, Alberta. The objectives of this first attempt were to image the upper 50 m of the subsurface, test the capabilities of this acquisition technique, and propose future improvements that need to be undertaken to achieve better quality seismic data (Suarez and Stewart, 2007). A second test was conducted in the same location during March 2008 but with the objective of doing a side-by-side comparison of a planted 3-C geophone line and a land streamer line. This chapter describes the analysis done in the first and second experiments and discusses the results of the comparison from both acquisition systems.

2.1 Location of the area of study

The survey area was located about 5 km from the town of Priddis in the foothills of the Canadian Rocky Mountains, southern Alberta (Figure 2.1). Our geophysical test site is also home to the University of Calgary's Rothney Astrophysical Observatory. This area has been a location for extensive shallow VSP experiments by the CREWES project (Wong et al., 2007) and a 3D seismic survey.

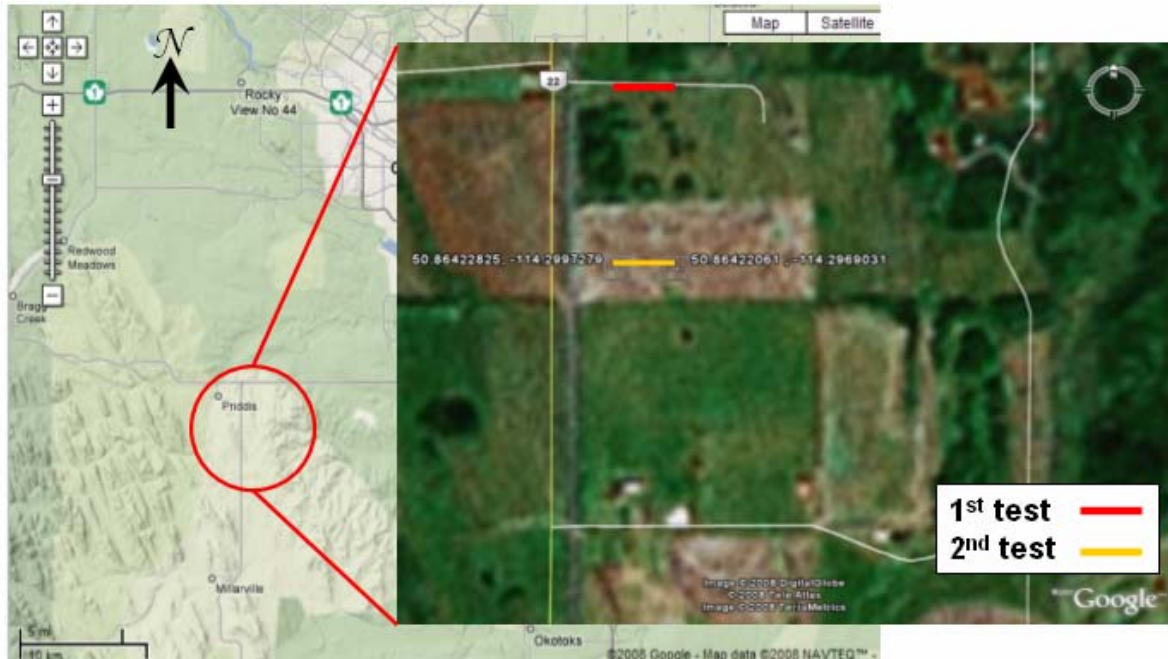


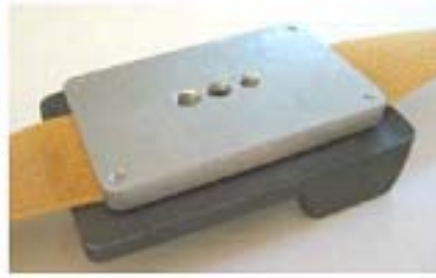
Figure 2.1. Aerial photograph showing the location of the study area: The first test on dirt road (red line), the second test on grass covered hill (yellow line). Photograph from Google Earth.

2.2 Description of the land streamer system

The basic land streamer system consists of a base plate, tow webbing, and top plate (Figure 2.2). It is designed to be used with existing geophones and cables. The top plate is drilled and tapped for any make of geophone but using a 3/8- inch screw we used our 3-C sensor geophones (Figure 2.2). The streamer's major characteristics are the non-stretch woven belts on which geophone units are mounted to form a multichannel geophone array. The coupling of geophones with the terrain is accomplished through the weight of the heavy metal baseplates (Inazaki, 2006).



(a)



(b)



(c)



(d)

Figure 2.2. Land streamer system components: (a) land streamer basic configuration used on the first test; (b) top and bottom geophone plate, (c) geophone unit with wings to stop overturning, and (d) woven belt. Photographs from R. Stewart and van ver Been et al., 2001.

2.3 Test 1: 2007 Field School

A short-spaced, short-length type land streamer configuration oriented nearly E-W (1 m; 60 channels, 20 m total) was used to acquire data on a dirt road (Figures 2.2, 2.3 and 2.4) at the Priddis test site. Our main focus was for depths shallower than 50 m. The total survey length was 210 m, with 10 m of streamer overlapping corresponding to every time that the source point was changed. A single shot point was recorded (off-end) for each streamer position at the same location to ensure better signal-to-noise ratio (Figure 2.3). In total, 38 shots were acquired, with 211 receiver stations and a total line length of 210 m.

The multicomponent land streamer survey employed a vertical-impact source and multicomponent geophones (Figure 2.3). The source was a 12 lb. sledgehammer with a handle trigger (Figure 2.2 and 2.5). The receivers were 10 Hz 3-C geophones that were being recorded at a 2 ms sampling rate by a Geometrics Geode recording system with 60 channels. The streamer was towed by a passenger van that was carrying the seismic recording system.

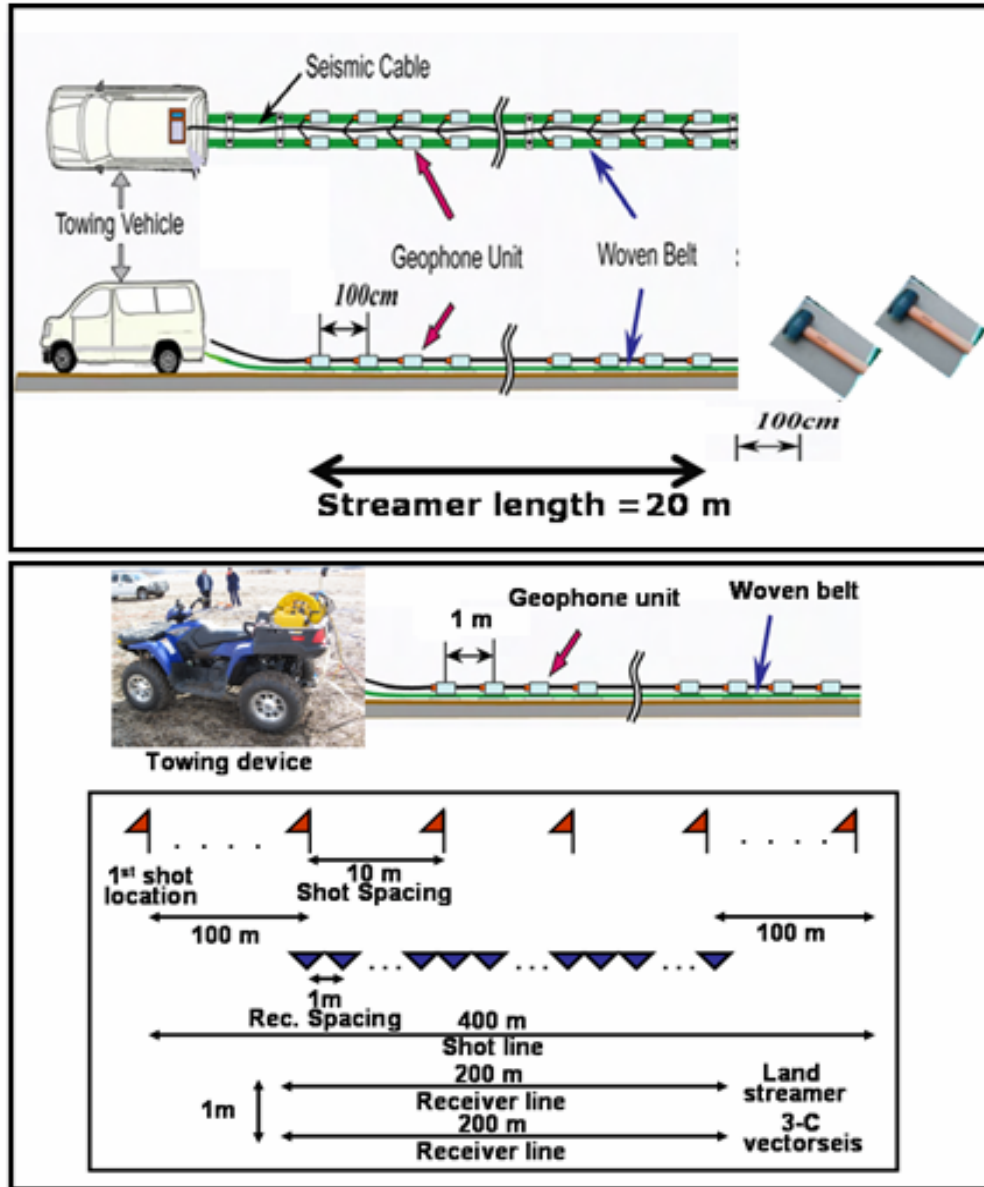


Figure 2.3. Illustration of the land streamer configuration used on the first (top) and second (bottom) land streamer seismic experiment: a 20 m streamer with 3-C geophones separated 1 m, with a sledgehammer P-wave source located at 1 m off the cable (Test 1) and a vibroseis source (test 2) (modified after Inazaki, 2006).



Figure 2.4. Actual land streamer configuration used in the first Priddis experiment. Individuals shown were participating in the University of Calgary's 2007 Geophysics Field School (photo from R. Stewart).



Figure 2.5. Hammer seismic source used on the first land streamer experiment.

2.4 Seismic processing and analysis of the data of Test 1

The processing was divided in three main stages. The first stage involved fixing field problems, such as shot resampling, setting a common trace length, and renumbering the channels. The second stage involved geometry building and vertical stacking of the multiple shots that were recorded for the same source point. The third stage involved noise attenuation, filtering and generating a common-shot stacking section of the data.

Examples of some of the raw shots showing the three components can be seen in Figure 2.6. Figures 2.7 and 2.8 show a comparison between the raw data and band-pass filter (10-50 Hz) and gain (AGC) data for the vertical and radial component. Looking at the raw data, we can notice a dominant coherent noise with a linear moveout of low seismic velocity between 100 m/s and 350 m/s, which correspond to the velocities of groundroll and air-wave. This strong noise trend suggests the application of surface-wave attenuation techniques such as F-K filters and radial filters. Another observation is that the vertical component data contains the best data, as expected.

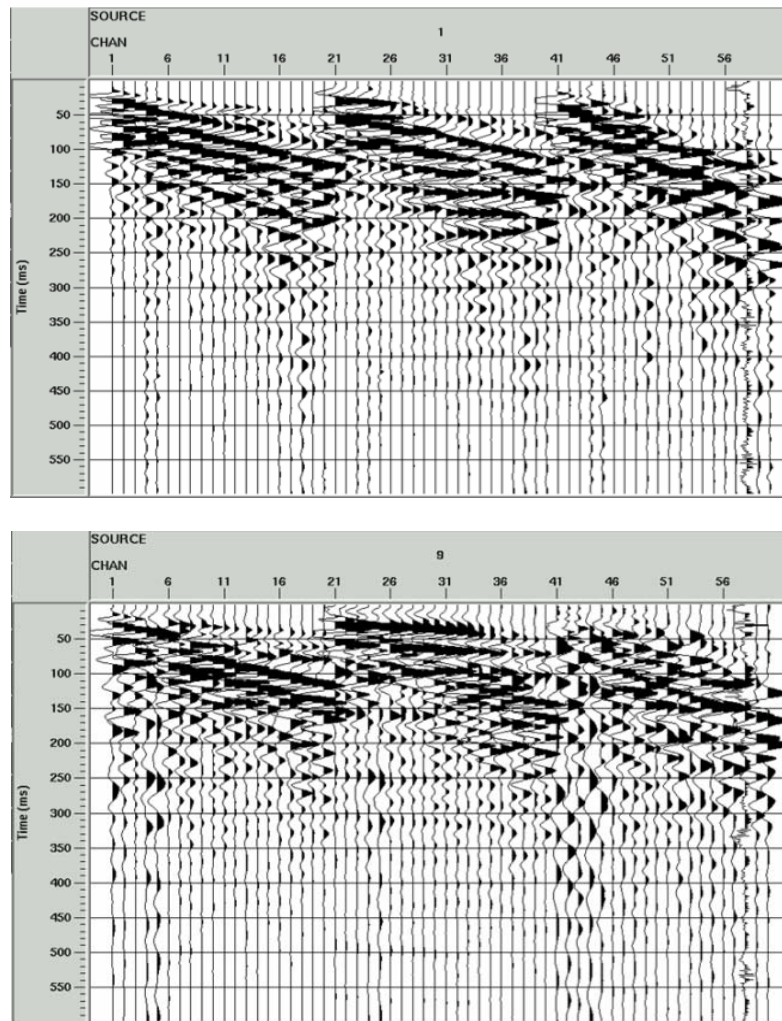


Figure 2.6. Three-component shot gathers for two shots: vertical component (left), radial component (centre) and transverse component (right).

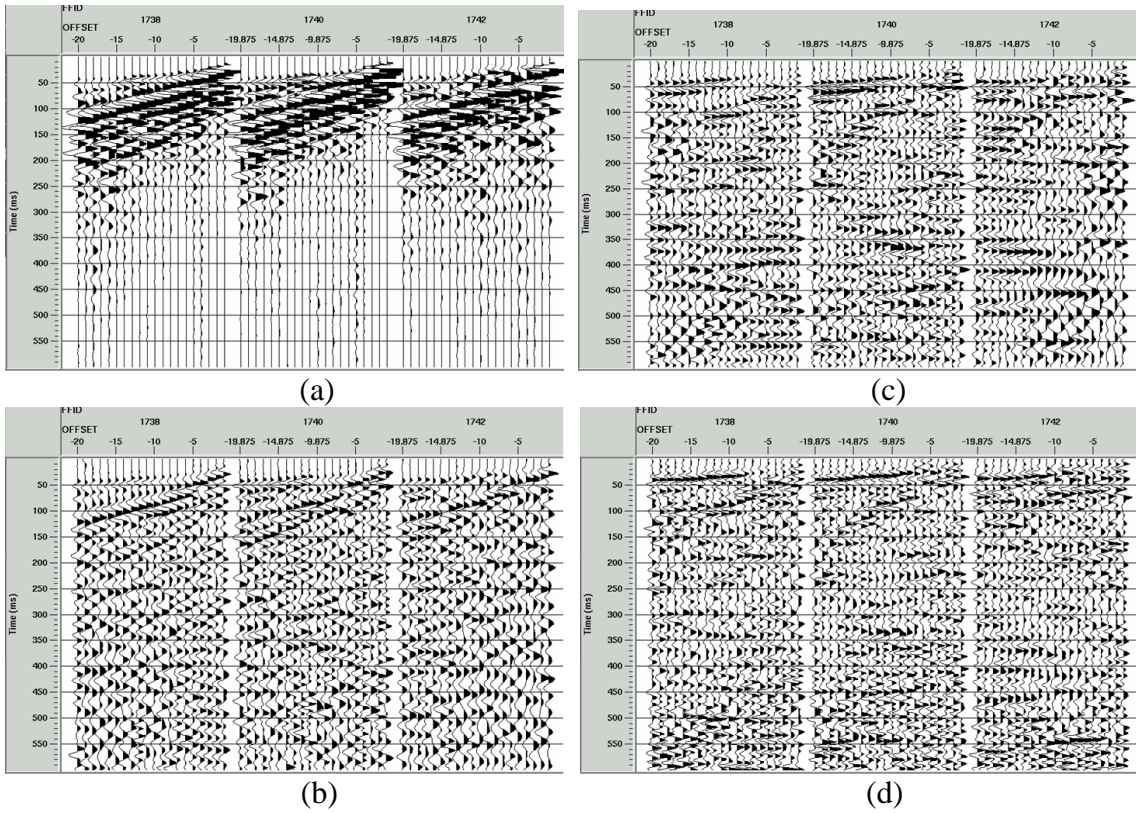


Figure 2.7. Three vertical component shot gathers: (a) raw, (b) band-pass filter and AGC applied, (c) with radial trace filters applied and (d) radial trace filters plus Gabor deconvolution applied.

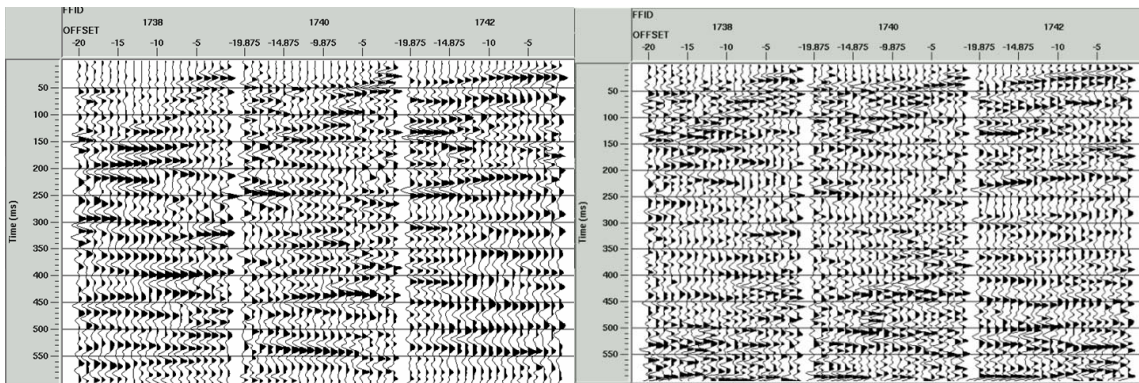


Figure 2.8. Radial component shot gathers with radial filters applied (left) and radial filters + Gabor deconvolution applied (right).

Amplitude spectra were derived for some of the shots to analyze the frequency content and assess the coupling quality. Figure 2.9 shows the amplitude spectrum for shot 1798. The response for the majority of the shots was similar to this example; with dominant frequencies on the low side around 30 Hz. Some of the possible causes for the low-frequency content of the data could be coupling problems, strength of the seismic source, or effects more associated with the lithology of the weathering layer of this area (mainly conglomerates and unconsolidated material) that might be absorbing the high frequencies generated by our seismic source.

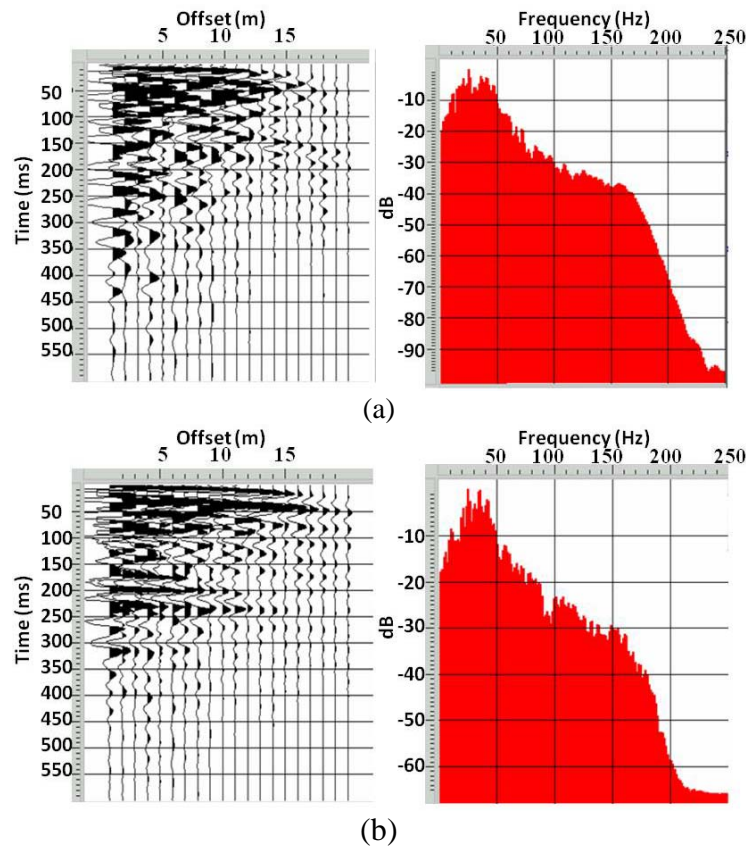


Figure 2.9. Amplitude spectrum for FFID 1798 for (a) the vertical component, and (b) for the radial component.

Radial filters with velocities on the range of 300 to 1000 m/s were applied to eliminate noise from the data in an attempt to identify seismic reflections. Prominent reflections around 30 ms and 300 ms were observed on the filtered dataset (Figures 2.7 and 2.8). However, there is still coherent noise in these shots that might appear as reflections. A conventionally acquired dataset for comparison would help us identify the near-surface seismic reflections of this area.

Some of these possible reflection events are better observed in the radial component shot (Figure 2.8) if we compare it with the vertical component, such as the event at 450 ms.

Constant velocity common source stacks were generated for this dataset. CDP stacks were not created because of the survey low fold. Figure 2.10 presents a portion of the stacked sections for the vertical component and the radial component with velocities that range between 200 m/s and 900 m/s. In the 700 m/s panel, a reflection at 30 ms could be observed and on some of the panels a weak event around 300 ms could be observed.

To corroborate that our only reflection around 30 ms is real, a zero-offset VSP corridor stack (Miong, 2008) acquired during summer 2007, was used (Figure 2.11). However, it is important to remember the difference in bandwidth between a VSP dataset and surface seismic, which in the case of this land streamer dataset is even more pronounced (30 Hz dominant frequency). Considering the limitations, the 30 ms reflection appears in both datasets, which suggests that it is real.

2.4.1 Comparison of P and P-S stacked sections

A way to find an approximate value for V_p/V_s is to identify a similar event in the P and P-S stacked sections and try to compress the images until we find a good match for these events (Figure 2.12). In the P-wave section the event at 30 ms was used, and in the

P-S section, the event at 70 ms. Compressing the P-S section we could suggest a V_p/V_s value around 3.7 for the location of this line. However, to get a more reliable result we will need P and P-S velocities from the surface seismic, VSP or well logs of the area. Some of this information will be obtained from the processing of the second land streamer test.

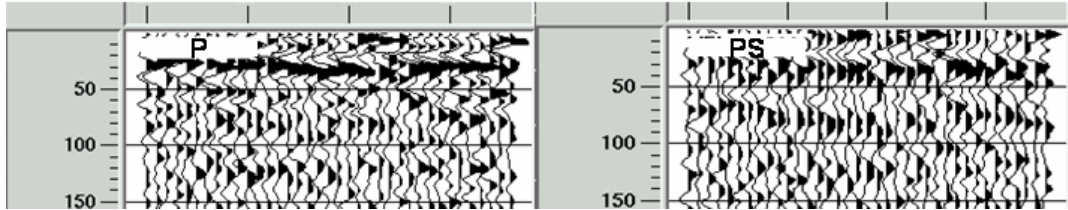


Figure 2.10. Stacked sections for the vertical component (left) and for the transverse component (right).

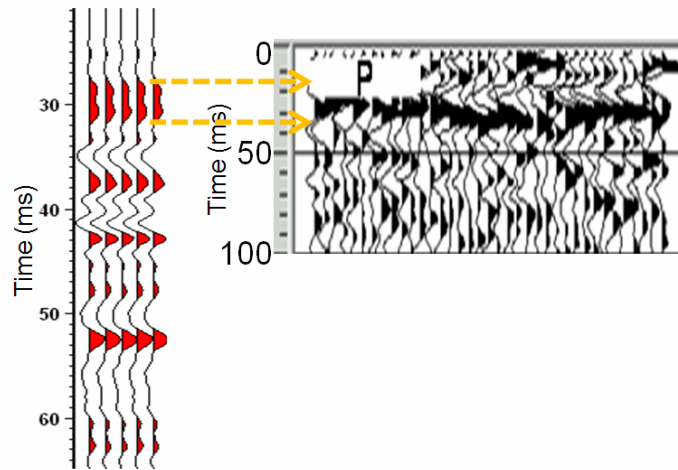


Figure 2.11. Comparison of the VSP corridor stack (from Miong, 2008) with the first 100 ms of vertical component stacked section from the land streamer.



Figure 2.12. Comparison of P stacked section (left) with P-S stacked section (right).

2.4.2 Refraction Analysis

As it is our intent to characterize the near-surface properties of this area, a refraction analysis of the 38 shots was undertaken with the vertical component data using

the first-break information. The 20 m offset range for this survey was a limitation, which is one of the reasons why we used the hand-picking method, rather than a more analytical method, such as trace correlation to extract the first arrivals. The next step in obtaining the near-surface model is to use the traveltimes observed from the P-wave refractions. The method used in our study is an inversion method called the Generalized Linear Inversion Method or GLI, which was implemented using the Hampson-Russell software package, GLI3D.

The resulting near-surface model is presented in Figure 2.13. This Figure shows two layers of thicknesses between 1 and 5 m and velocities of 330 and 920 m/s.

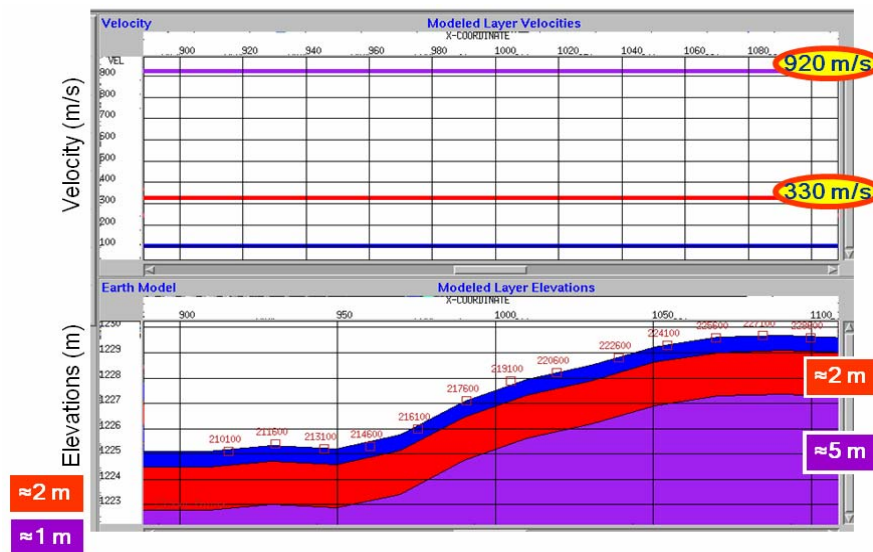


Figure 2.13. Results of the refraction modeling for the land streamer Test 1.

2.4.3 Test 2: Comparison of 3-C land streamer versus planted geophone data, acquired in March 2008, over a grass-covered hill.

A side-by-side multicomponent seismic line configuration oriented nearly E-W was used for the test (Figure 2.3 and 2.14). The test consisted of a 200-m planted-geophone seismic line, a 20-m land streamer system and a 400-m source line. For the 2D “conventional line” we used 200 3-C geophones at a spacing of 1 m. The same land streamer configuration used for Test 1 was kept (1 m; 60 channels, 20 m total) but this

time over a grass-covered surface, with a 10 times cable roll with no overlapping, to reach the 200 m length of the comparison line.

The multicomponent survey employed a Vibroseis source and multicomponent geophones (Figure 2.14). The source was an IVI Envirovibe (18,000 lb) with a 10- to 250-Hz sweep, an 11 seconds listening time, and a 4-times vertical stack. The receivers were 10-Hz 3-C geophones that recorded at a 1 ms sampling rate. The land streamer receivers were recorded by a Geometrics Geode recording system with 60 channels and the planted geophones or “conventional line” was recorded by an ARAM-ARIES recording system. The 400-m total line length was acquired in 10 parts, where every part corresponds to a different location of the 20-m length land streamer. For every streamer segment the 40 source locations spaced at 10 m were repeated, which means that the planted geophone line was recorded 10 times and the source line was fired 10 times. The first and last source points have a maximum offset of 300 m that correspond to the longest offset of the whole line. These two points were located 100 m off the receiver line. This maximum offset was reduced by 10 m with every location of the source until reaching the shortest offset of 200 m. This position corresponds to the location when the source is in the middle of the receiver line.

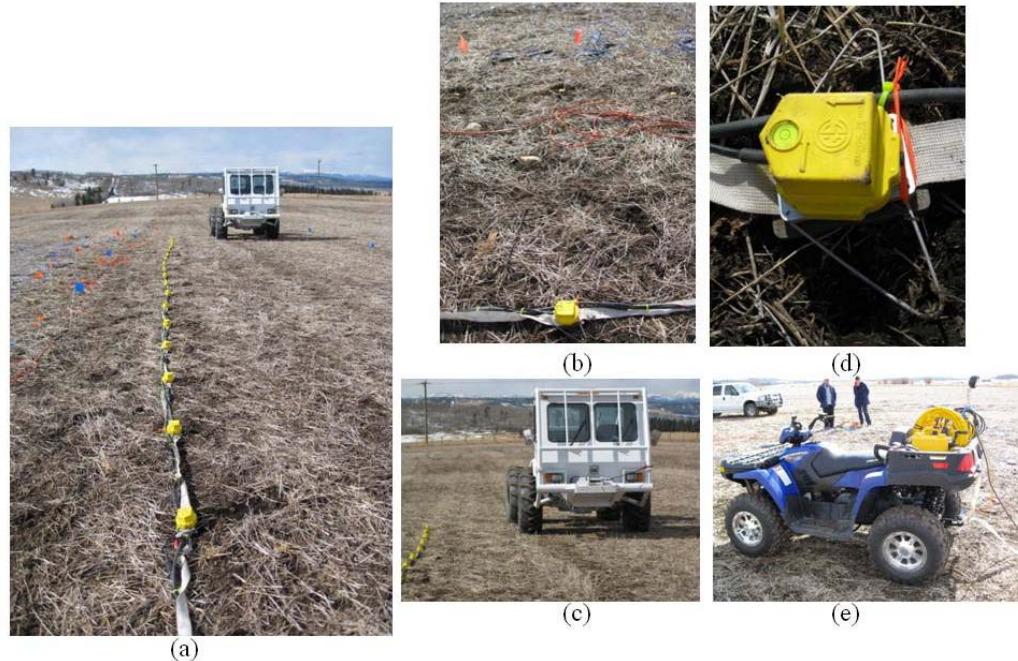


Figure 2.14. Land streamer experiment site: (a) the vibroseis source next to the land streamer and conventional line; in (b) we can see the distance between the planted geophone and land streamer lines; in (c) is shown the 4-m distance between the source line and the receiver lines and in (d) and (e) are shown a receiver streamer configuration and the land streamer towing device, respectively. Photos by G. Suárez.

In total, 40 shot locations were acquired, 200 receiver stations, 10 land streamer positions and a total line length of 400 m for the source line and 200 m for the receiver line (Figure 2.3).

2.5 Seismic processing of the Test 2 data

After acquisition, the coincident data sets were passed through the same processing sequence using identical processing parameters. The survey geometry resulted in a maximum fold of 19 for the vertical and for the radial channel sections (Figure 2.15).

The crucial step during the processing was the re-arrangement of the datasets to make them equivalent. Because the land streamer data was acquired using 10 runs of the same source line, the different segments have to be put together, numbered and sorted. Subsequently, a geometry assigned to it to construct a 200 m seismic line. For the

conventional line, the same process was undertaken because the same line was acquired 10 times. For every run, the equivalent traces to the land streamer were chosen, the same receiver locations were killed, and the same numbering, sorting and geometry were assigned.

Some of the re-arranged raw shot gathers for both systems (land streamer and planted geophone) can be seen on Figure 2.16. In the shots, we notice the strong noise trend that covers most of the gather, masking all the possible reflections. Correlation noise can be observed as well: this is caused by the proximity of the source to the line (4 m from the line). However, some reflections around 200 ms can be identified on the gathers that correspond to the source locations that were off the receiver line.

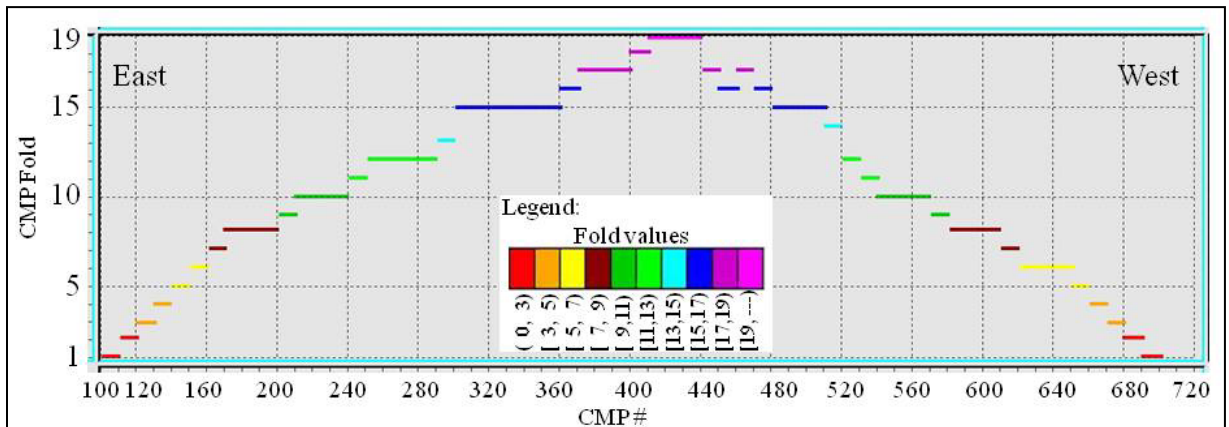
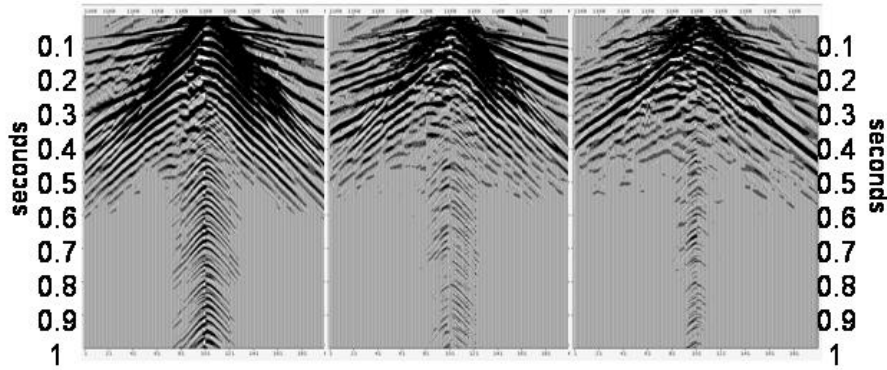
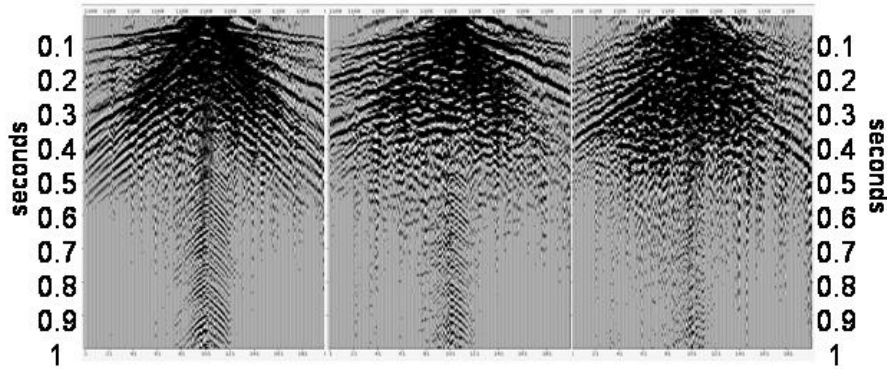


Figure 2.15. Fold of coverage for the Priddis land streamer Test 2.



(a)



(b)

Figure 2.16. Raw shot gathers from (a) the conventional line, and (b) the land streamer system. Vertical channel (left), radial channel (centre) and transverse channel (right).

2.5.1 Vertical Channel

Important processing steps are outlined in Table 2.1. The processing sequence used for this dataset emphasized noise rejection techniques. The necessity of focusing on noise rejection techniques can be seen on Figure 2.18(a), 2.19(a) and 2.20(a), where a raw shot gather and brute stacked sections show how the reflections are being masked by the strong noise trend.

The processing parameters were designed on the planted geophone dataset and identically applied on the land streamer datasets. A similar procedure was used for the velocities, statics and any other parameters that have not the same degree of confidence when they were calculated for the land streamer line.

1. Assign geometry
2. Trace editing : kill bad traces
3. True amplitude recovery: 10 db/sec gain
4. Surface-consistent deconvolution: spiking, 80 ms operator length, 2 windows
5. Signal enhancement (noise rejection): FXCNS + AAA
6. Velocity Analysis
7. Refraction and elevation statics: calculated using tomography and elevations
8. Sorting the data to common receiver domain
9. Signal enhancement (noise rejection): AAA
10. Sorting the data to common source domain
11. Signal enhancement (noise rejection): Even-odd AAA + FXCNS + trace mix
12. Signal enhancement (noise rejection): F-K filter + AAA
13. Signal enhancement (noise rejection): Cascade of F-K filters
14. Residual statics: calculated using Miser®
15. Velocity Analysis
16. Surface Consistent Amplitude Compensation (SCAC)
17. NMO correction
18. Automatic Gain Control: 150 ms
19. Bandpass filter: 8-48-90-96 Hz zero-phase filter
20. NMO correction
21. Top mute
22. CDP stack
23. Additional processes: random noise attenuation filter
24. Trace Balance

Table 2.1. Main processing steps for the land streamer and planted geophone vertical channel data.

Some parts of the statics solution for these lines were not important factors to be corrected because of small changes in elevation (1 or 2 m) and the gentle topography along the line. However, refraction and reflection statics solutions were calculated. As was previously pointed out, high amplitude, low-velocity surface wave noise dominates the near offsets while back-scattered surface waves and correlation noise degrade reflections. The noise is stronger for the planted geophone gathers than for the streamer ones. The datasets were processed as thoroughly as possible to attenuate the noise, enhance coherency, resolve the statics problems and determine velocity models for stacking.

A refraction solution was derived using a tomographic inversion of first-break traveltimes, removing the static inconsistencies observed and helping to enhance some of the reflections. We also applied residual statics later in the processing flow allowing a maximum shift of 36 ms. However, the improvement caused by the refraction statics could not be evaluated until stacking velocities were picked and some of the noise was rejected, allowing us to see some of the reflections of the area. To address the problem of noise, several passes of signal enhancement techniques were applied at different stages and different domains during the processing (Table 2.1). The first pass was done prior to deconvolution, but comparing the noise rejection followed by deconvolution results and the deconvolution-only results we saw no benefit on filtering data pre-deconvolution. Deconvolution acted as a good filter for some of the surface wave noise, improving the general look of the data, revealing some of the reflections. The deconvolution approach used was a surface-consistent spiking deconvolution with an operator length of 80 ms and one window. The results of the deconvolution in one of the shot gathers and in the stacked sections for both systems can be seen on Figures 2.18(b), 2.19(b) and 2.20(b).

The first signal enhancement pass applied to the data followed deconvolution. This first pass targeted surface wave noise, coherent and random, as well as some linear noise such as airblast. The noise attenuation techniques were applied in the shot domain and included an f-x coherent noise attenuation filter (FXCNS) and a band-limited f-x random noise attenuation filter (AAA or Anomalous Amplitude Attenuation).

The first technique (FXCNS) is designed to attenuate shot-generated coherent noise. It uses a frequency-space domain fan filter (Hildebrand, 1982) and a least-squares optimization scheme (Seeman and Horowicz, 1983), the noise is locally estimated at each

receiver for a specified range of apparent velocities and then subtracted from the data. The estimation procedure uses a trace's nearest neighbours, within an azimuth bin or 2-D line, to determine the content of coherent noise for a specified range of apparent velocities. The least-squares estimate is performed independently for each frequency over a specified portion of the bandwidth (Gaiser, 1995).

The second technique is called Anomalous Amplitude Attenuation (AAA). It uses the random occurrence and limited bandwidth of noise to separate it and remove it from the seismic signal. Pre-stack seismic data is transformed to the frequency domain in which a spatial median filter is applied. Any frequency bands that deviate from the median amplitude by a specified threshold are either zeroed or replaced with frequency bands from neighbouring traces. AAA is most effective when the input data sort-order is such that the noise is random in that domain.

A description of the flow used for the FXCNS plus AAA techniques is presented in Figure 2.17. A temporal automatic gain control (AGC) of 300 ms was applied to the data since it helps during the noise attenuation process, this gain was removed after filtering when we divide the seismic filtered data by the AGC operators that were output in the right branch of the flow. The FXCNS is parameterized defining the low and high pass velocities and frequencies, low and high stop velocities and frequencies. A 400-800 m/s pass for velocities, 100-1000 m/s stop for velocities, 3-90 Hz pass band and 1-100 Hz cut frequencies were used as our optimal parameters for the FXCNS. Difference plots as well as comparisons before and after were done to quality control and make sure reflections were not being attenuated. The AAA was calculated and applied for a frequency band from 0-500 Hz, the reason for this range is because as a first application

of this process we have as a target the high amplitude spikes that mask most of the surrounding noise and make it difficult for other techniques to differentiate between signal and noise.

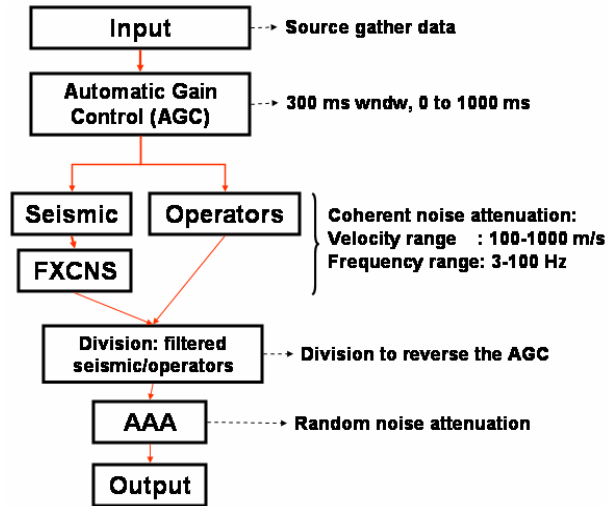


Figure 2.17. Description of the flow used for the FXCNS plus AAA techniques.

Velocity analysis on these datasets was not an easy task even after filtering. There did not seem to be many coherent events and some of these were masked by the remnants of the surface wave and airblast. In total, three velocity analyses were done for this data, after deconvolution and second noise attenuation passes.

A second pass for signal enhancement was applied in the common receiver domain: this domain was used because the noise appears weaker and more random. To attenuate some of the noise in the receiver domain, five consecutive passes of the band-limited f-x random noise attenuation filter (AAA) were used. The filters were designed to work in 25-Hz frequency bands (0-25 Hz, 20-45 Hz, 40-65 Hz) with overlaps of 5 Hz so we could control the strength of the threshold values at various times. The results of this pass showed how, in the common receiver gathers, part of the correlation noise could be attenuated, which was difficult to achieve in the common source and common midpoint domains. In the common source and common midpoint gathers, the correlation noise is

strong and consistent along all the traces, making attenuation difficult using most of the noise attenuation techniques. Examples of shot gathers and stacked sections before and after the application of the second pass are shown in Figures 2.18(d), 2.19(d) and 2.20(d). In the shot gather, Figure 2.18(d), we see how most of the low-frequency and correlation noise has been removed. This is more evident in the stacked sections where the noise shows a linear pattern for the deconvolution-only stacked section, but which, after the application of the first and second noise attenuation passes has been greatly removed, making most of the reflections on the section more evident.

A third and final signal enhancement pass was applied in the common source domain. This pass was divided in three parts. The first part is called even-odd AAA + FXCNS + trace mix; it uses the same processes previously described but applied to odd and even traces separately. The idea is that by having null traces between one trace and the next, the noise rejection modules could better differentiate noise from signal; this process has previously demonstrated success on common source gathers in land datasets contaminated with coherent noise. The flow has two branches: one corresponding to the even traces (right one) and one to the odd traces (left one). The input is passed through an amplitude diagnostic (trace attribute extract) that allow us to evaluate if there are amplitude outliers in the data that could reduce the effectiveness of our noise rejection modules. The peak amplitude values are calculated in 3 windows of 333 ms each. In the cases where high-amplitude values exist, it is applied to reject up to two percent of the data containing the outliers. The next step is to alternately nullify the odd and even traces for each set to be processed separately. Each branch contains eight passes of AAA, one pass of FXCNS and trace mix. The AAA modules were designed to work from 0-125 Hz

in 25 Hz frequency bands (0-25 Hz, 20-45 Hz, 40-65 Hz, 60-85 Hz, 80-105 Hz, 100-125 Hz) with an overlap of 5 Hz, and the other two modules from 125-500 Hz and 0-125 Hz. The FXCNS was applied in the same manner as in the first pass, using an AGC of 300 ms and then removing it from the data, dividing the filtered seismic data by the gain operators. Pass velocities of 300-2500 m/s, 250-2750 m/s stop velocities, 3-30 Hz pass frequencies and 1-35 Hz cut frequencies were used as our optimal parameters for attenuating part of the groundroll and some other coherent noise existent in the data. The trace mix is a way of creating a noise model of the airblast and the correlation noise that will be subtracted from the seismic data. To create the model, linear moveouts of 350 m/s to target the airblast, and 76 m/s to target part of the correlation noise, are applied to the shot gathers. The noise model is built mixing 12 traces to, then removing the linear moveout previously applied. The even-odd AAA + FXCNS + trace mix flow is finalized by combining even and odd traces to organize the data as in the original common source gather. With this process, part of the random noise, targeted by the AAA modules, as well as some of the airblast and correlation noise, has been removed. But noise is still very dominant in the gather, suggesting that different techniques should be applied to address coherent noise.

The second stage of the second signal enhancement pass includes an F-K polygonal filter and AAA modules. The F-K filter was designed to work on high frequency noise (180-500 Hz), most of it being part of the airblast. Once again the AAA modules were designed to work from 0-125 Hz in 25 Hz frequency bands (0-25 Hz, 20-45 Hz, 40-65 Hz, 60-85 Hz, 80-105 Hz, 100-125 Hz) with an overlap of 5 Hz, and the other two modules designed to work from 0-500 Hz and 125-500 Hz.

The third stage is aimed at attenuating the remaining coherent noise. A cascade of F-K filters (polygonal and fan-dip filters) was used to gradually work with the noise. The gradual application of this filter allowed us to identify new zones that needed attention but were previously overlooked due to the dominant noise that was attenuated in the previous F-K filter module. The results of this third stage can be seen on Figure 2.18(d), 2.19(d) and 2.20(d). Here we can see that some of the reflections previously obscured by the noise on the near offsets are revealed (Figure 2.18d); also the “cross-hatch” pattern created by the correlation noise looks smoother: this last observation is more noticeable in the stacked sections (Figures 2.19d and 2.20d). The stacked sections look “cleaner” and some of the events more continuous.

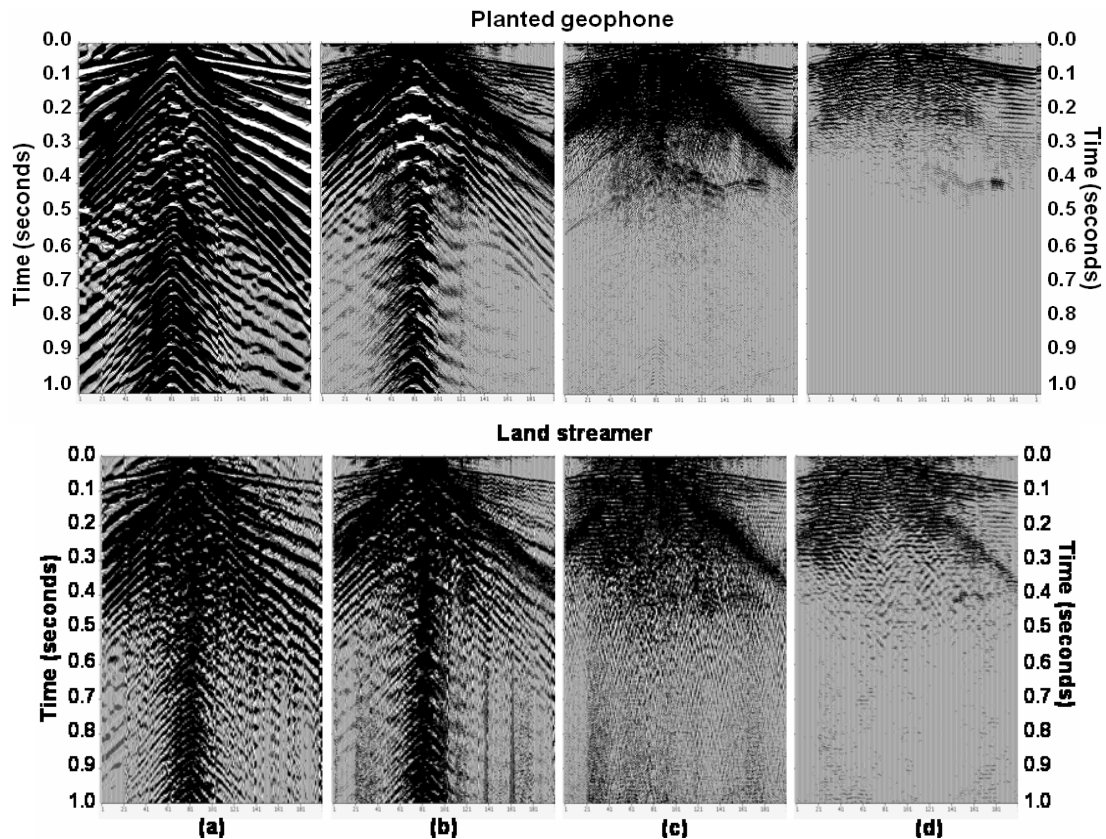


Figure 2.18. Common source gathers for source position 18 of 40 in the planted geophone line (top) and land streamer line (bottom): (a) raw data; (b) after deconvolution; (c) deconvolution plus first and second pass of noise attenuation; and (d) final gather after all passes of noise attenuation.

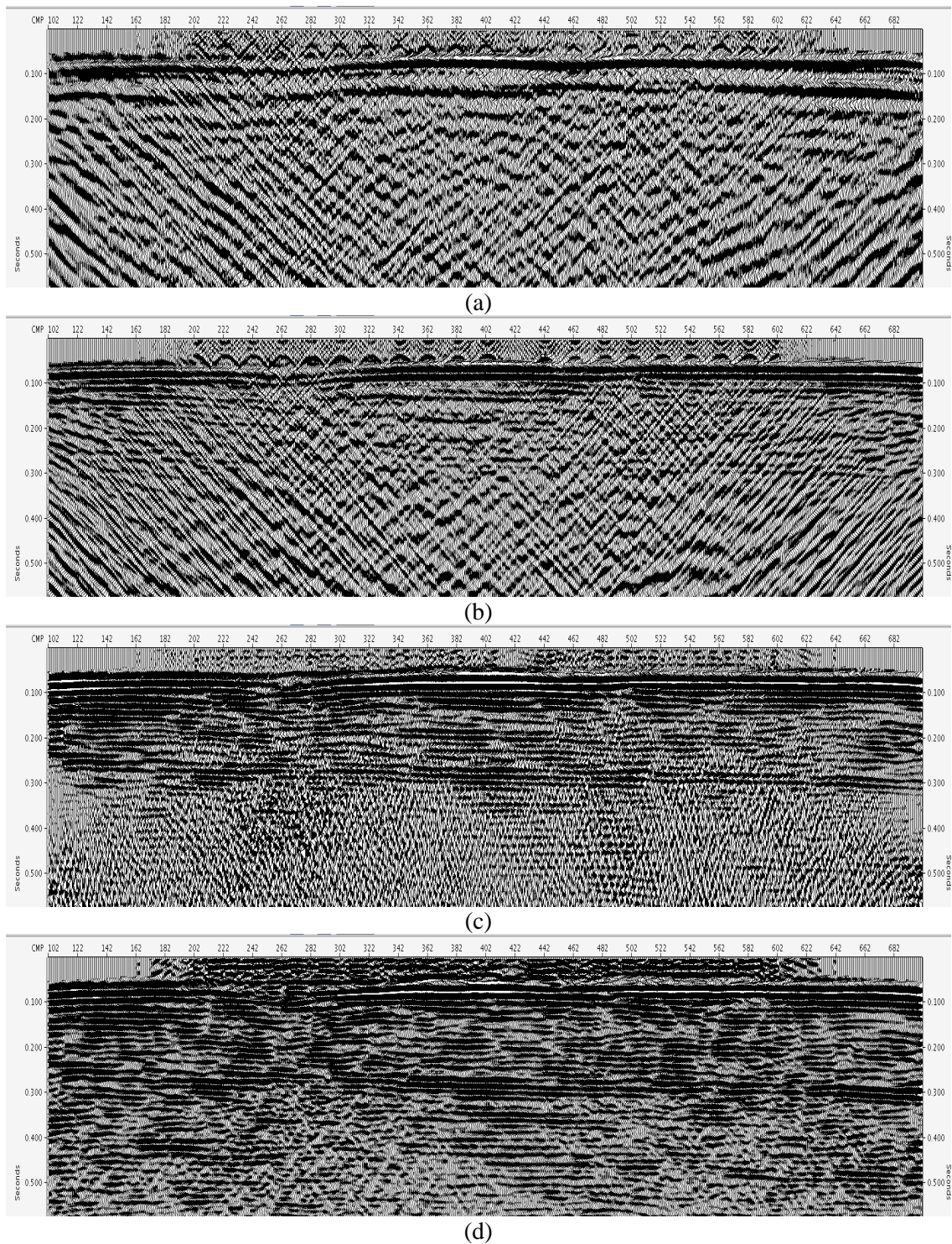


Figure 2.19. Stacked section comparison for the conventional line vertical component after noise attenuation procedures: (a) Brute stack; (b) Surface consistent deconvolution stack; (c) after first pass of noise attenuation; and (d) after all passes of noise attenuation.

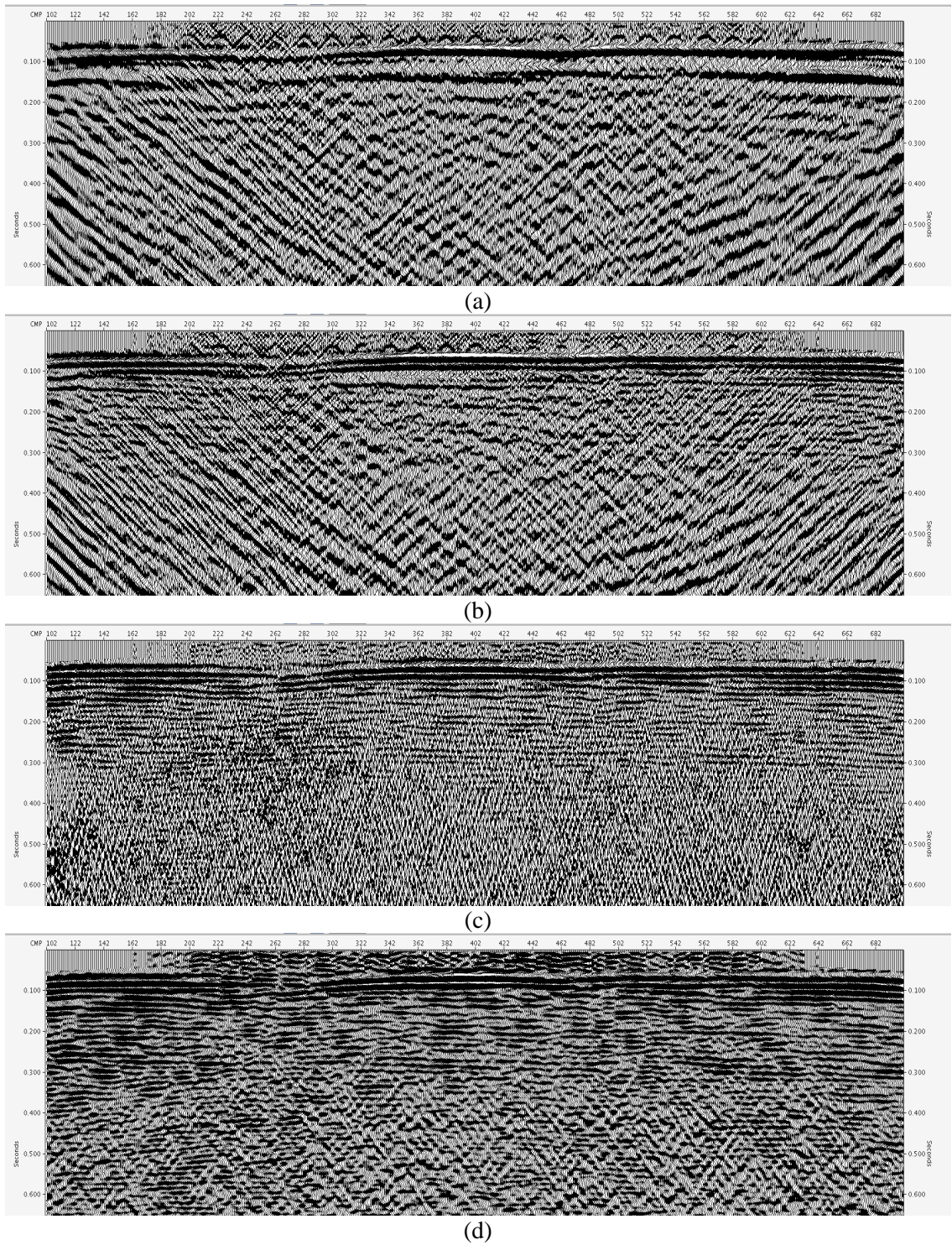


Figure 2.20. Stacked section comparison for the land streamer line vertical component after noise attenuation procedures: (a) Brute stack; (b) Surface consistent deconvolution stack; (c) after first pass of noise attenuation; and (d) after all passes of noise attenuation.

Up to this point, only an exponential gain amplitude compensation method has been applied to the data, and even with this kind of gain the data look unbalanced as a consequence of the poor performance of the exponential gain due to the low signal-to-noise ratio. All the stacked sections generated, from the brute stack to the deconvolution stacked section, have had a 150 ms pre-stacking automatic gain control window as an alternative to the unbalanced amplitude and the high level of noise. To try to balance the amplitudes, a surface-consistent amplitude compensation (SCAC) was calculated and applied to the data; using this method we were compensating for shot, detector and offset amplitude variations that are caused by acquisition effects and are not a consequence of the subsurface geology.

Figure 2.21 shows the final stacked sections generated with best velocities, final mutes, statics applied, and final noise attenuation datasets for both lines, and a side-by-side comparison of both sections is shown in Figure 2.22. The same processing sequence and parameters were used for both lines for comparison on a one to one basis. The analysis done on this datasets to determine how similar they are is presented on the next section.

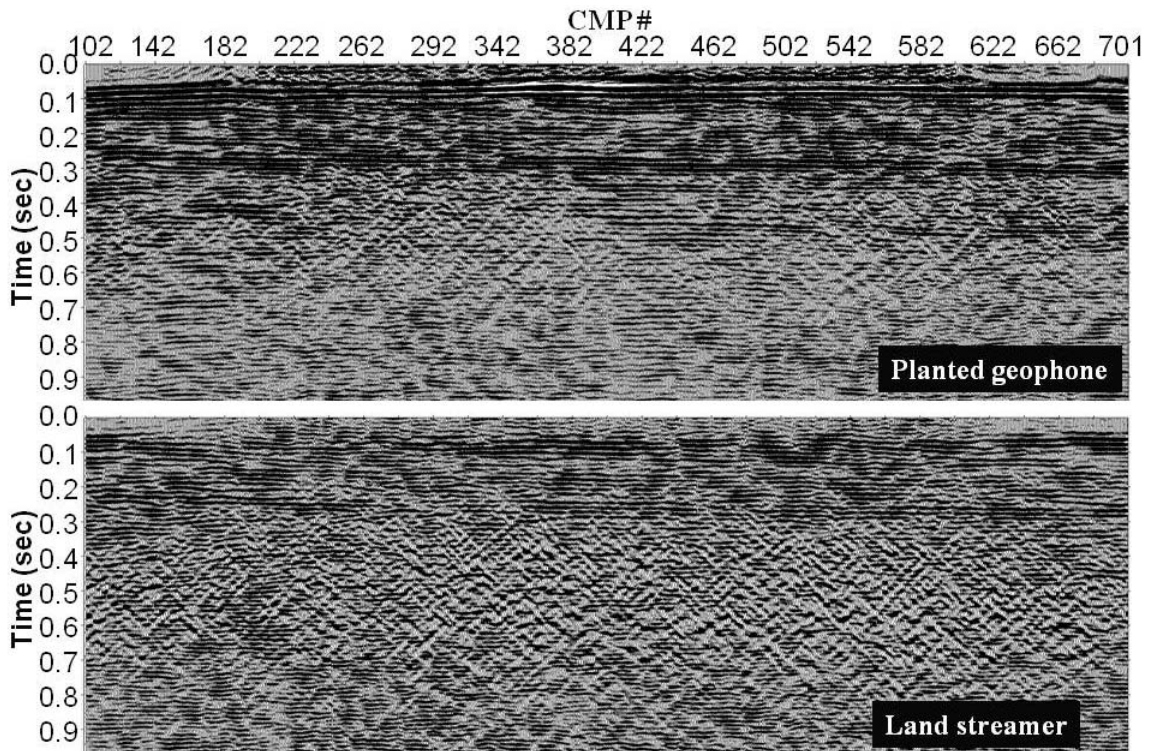


Figure 2.21. Final stacked section with the best output from noise attenuation, final stacking velocities and mute for the conventional line (top) and for the land streamer line (bottom).

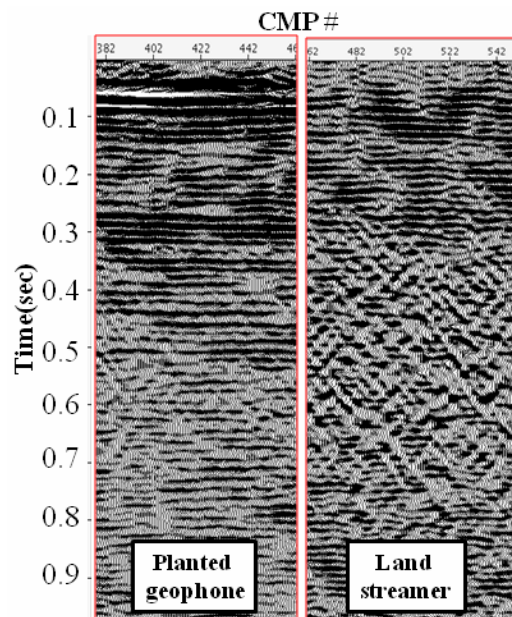


Figure 2.22. Side by side comparison of two consecutive portions of the stacked sections for the conventional line (left) and for the land streamer line (right).

2.5.2 Horizontal Channel

In general, the P-S data from both datasets had lower signal-to-noise ratios, reduced bandwidth and larger receiver statics compared to the compressional data. The P-S datasets were affected by additional problems of polarity reversals and mode leakage. Because of these and other factors, the horizontal channel data required several additional processing steps that were not required for the vertical channel data. Important processing steps for the horizontal channel are listed in Table 2.2. As can be noticed most of the same processes applied for the P-wave were applied for the converted-wave, with almost the same parameters.

1. Assign geometry
2. Bin data by CCP: asymptotic binning ($V_p/V_s=2$) and time-variant CCP binning (using picked V_p and V_{ps} velocities)
3. Trace editing : kill bad traces and flip polarity of negative offsets
4. True amplitude recovery: 10 db/sec gain
5. Surface-consistent deconvolution: spiking, 80 ms operator length, 2 windows
6. Signal enhancement: FXCNS + AAA
7. Velocity Analysis
8. Refraction and elevation statics: calculated using tomography and elevations
9. Receiver statics
10. Sorting the data to common receiver domain
11. Signal enhancement (noise rejection): Even-odd AAA + FXCNS + trace mix
12. Signal enhancement (noise rejection): F-K filter + AAA
13. Signal enhancement (noise rejection): Cascade of F-K filters
14. Residual statics: calculated using Miser®
15. Velocity Analysis
16. Surface Consistent Amplitude Compensation (SCAC)
17. NMO correction
18. Automatic Gain Control: 150 ms
19. Bandpass filter: 6-48-60-96 Hz zero-phase filter
20. NMO correction
21. Top mute
22. ACP stack
23. Additional processes: random noise attenuation filter

Table 2.2. Main processing steps for the land streamer and planted geophone P-S data.

Figure 2.23 shows an example of one of the common source gathers for both lines and its evolution as it was passing through the different processing steps. After all the noise attenuation steps, the shot gather shows some reflections for both lines with most of the correlation noise and groundroll having been removed (Figure 2.23(d)).

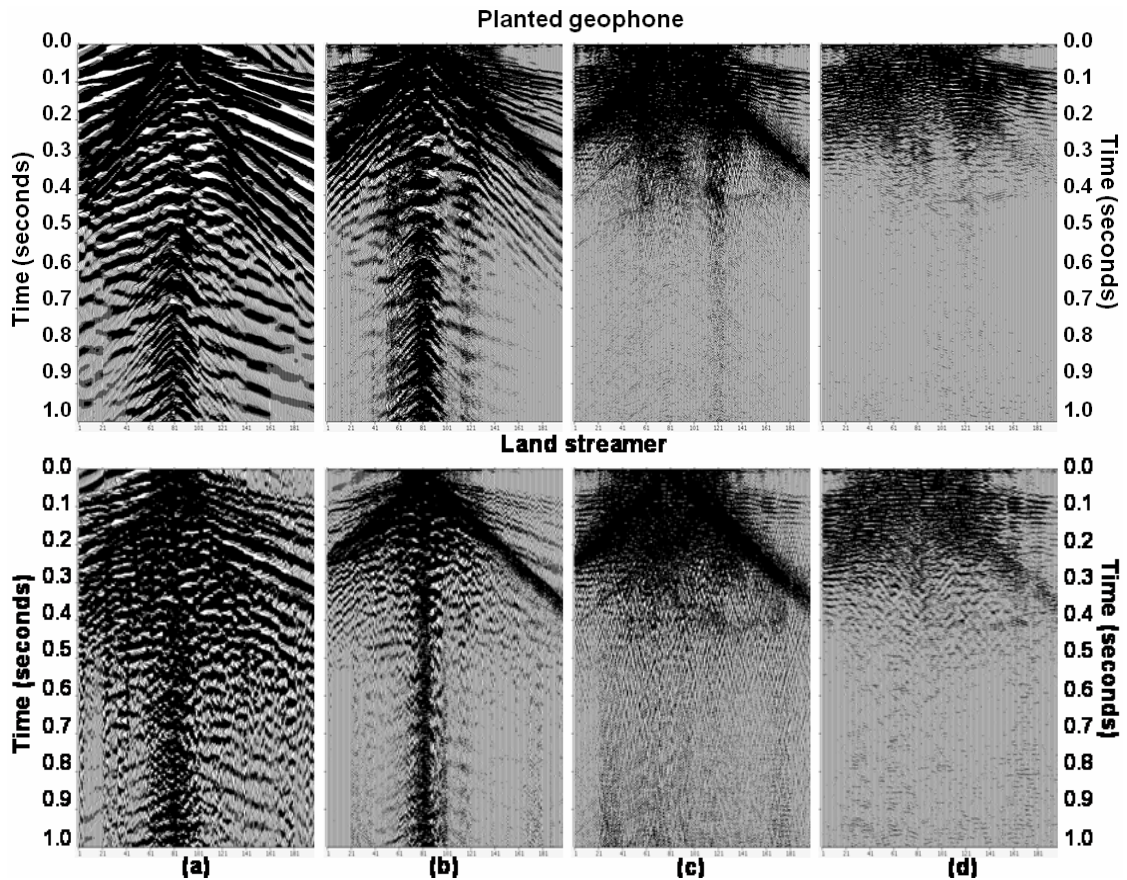


Figure 2.23. Common source gathers for the radial component of the planted geophone line (top) and land streamer line (bottom): (a) raw data; (b) after deconvolution; (c) deconvolution plus first and second pass of noise attenuation; and (d) final gather after all passes of noise attenuation.

Two trace-binning strategies for the radial-channel data were tested. The first one corresponds to an asymptotic binning and the second one to a time-variant binning. The land streamer and conventional line datasets were binned to a 0.5 m ACP spacing, assuming a V_p/V_s of 2.2 for the asymptotic binning option. The time-variant values of V_p/V_s used for the binning can be seen on Figure 2.24.

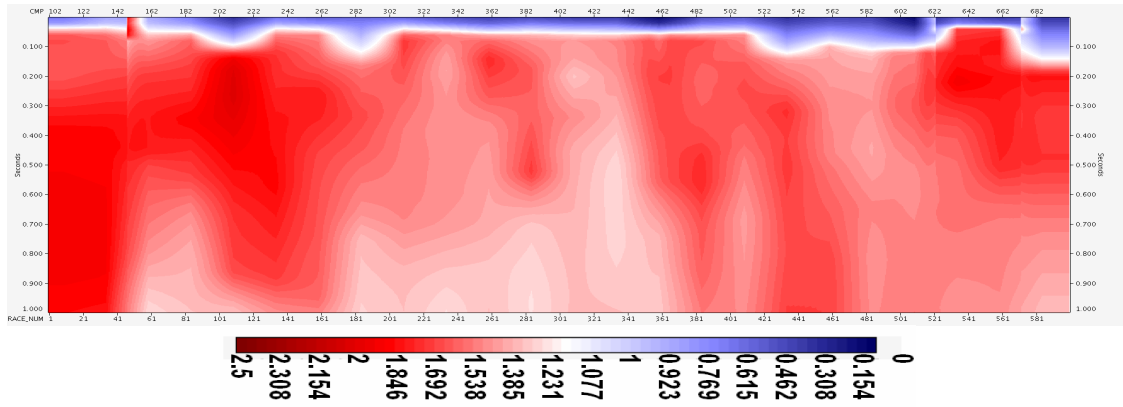


Figure 2.24. Interval gamma used for the CCP binning.

The final converted-wave stacked sections, generated with best velocities, final mutes, statics applied and final noise attenuation datasets for both lines, are shown in Figure 2.25. The same processing sequence and parameters were used for both lines as with the vertical component, to be able to compare them on a one to one basis. The analysis done on these datasets to determine their similarity is presented on the next section.

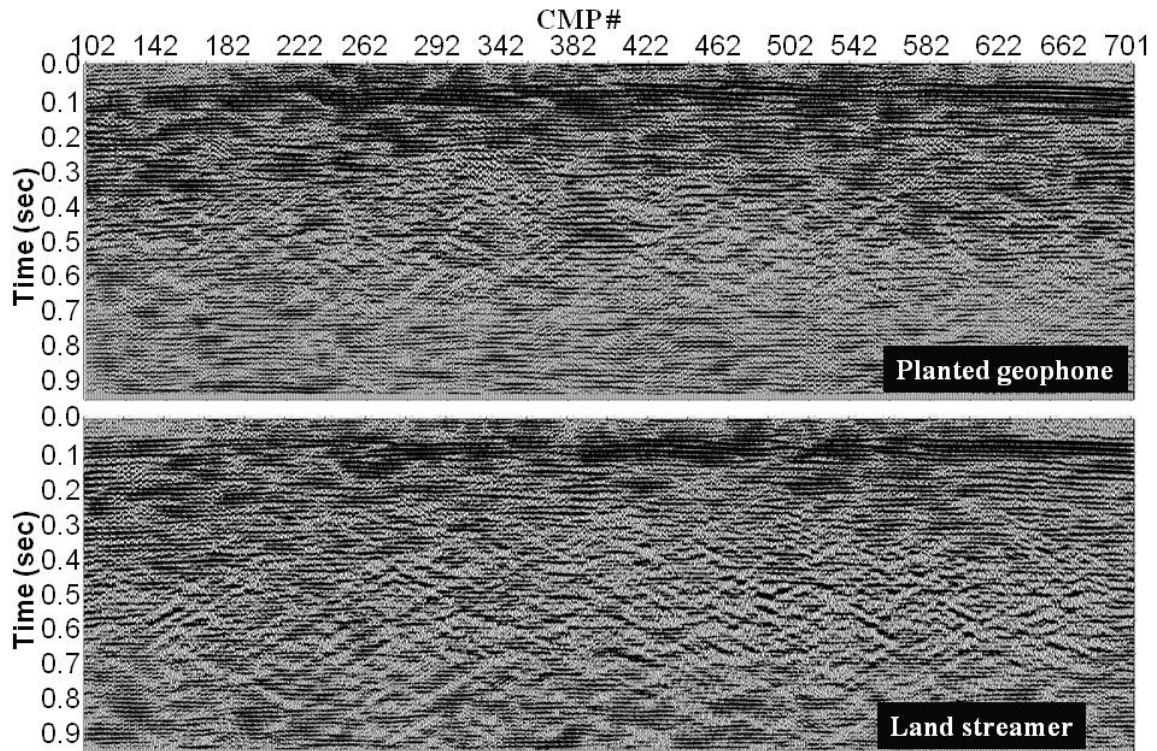


Figure 2.25. Final CCP stacked section with the best output from noise attenuation, final stacking velocities and mute for the conventional line (top) and for the land streamer line (bottom).

2.6 Analysis of the Test 2 data

2.6.1 Comparison of shot gathers and stacked sections

In Figure 2.16, the responses of the various geophones to the vertical, radial and transverse channels for a raw shot gather are compared.

2.6.1.1 Raw shot gathers:

Vertical channel: Unprocessed source gathers recorded with the streamer and conventional lines are similar (Figure 2.26a and 2.26b). The signal-to-ambient noise level is higher for the planted geophone line. On the raw shots for both datasets it is difficult to observe reflections as a consequence of the prominent coherent noise along the line, but differences are observed in the signal characteristics of the airwaves. They are strongest

in the conventional data and weakest in the streamer data, probably because the latter suppress slightly the higher frequency signals (van ver Veen et al., 2001).

Radial channel: The unprocessed source gathers in the land streamer look noisier and the events do not look very coherent compared to the conventional dataset (Figure 2.26c and 2.26d). The quality of the first breaks is poor for the land streamer. In general the source gather of the planted geophones shows much better signal, more coherency and less random noise.

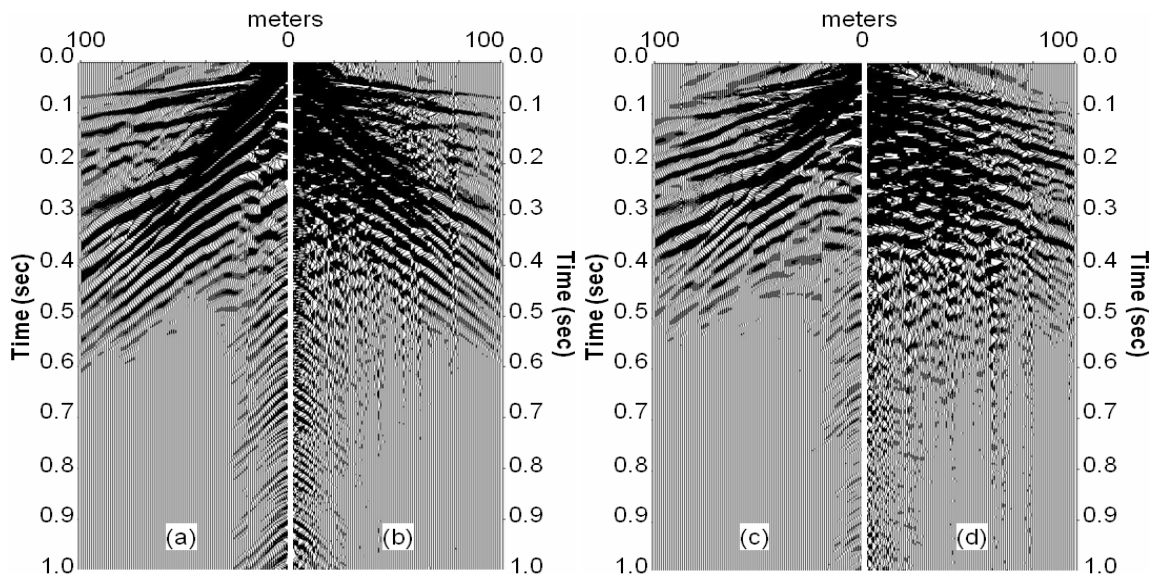


Figure 2.26. Comparison of two raw shot gathers. In (a), half of a split-spread record from the vertical component conventional line. The same shotpoint from the vertical component land streamer is shown in (b) with the lateral coordinate reversed to highlight the comparison. The same comparison is done of the same record for the radial component of the conventional line (c) and of the land streamer line (d).

2.6.1.2 Unmigrated stacked sections:

Vertical channel: The few reflections existent in this area are reasonably well imaged on both stacked sections (Figure 2.27); however, the land streamer section looks more contaminated with noise. There is a considerable difference in amplitude between the sections but the same events between 75 and 300 ms can be observed. Some of these

events that look like reflections were corroborated by comparison with the coincident inline of the 3D volume acquired in this site during 2007 (see chapter III, section 3.2).

Radial channel: In the stacked sections of the radial channel, the main reflections are present but they are not continuous throughout the line for the land streamer dataset (Figure 2.28). There are considerable differences in amplitude, events and signal-to-noise ratios for these two sections, where the quality of the streamer dataset is of much lower quality than for the vertical channel case, especially after 1.5 seconds where most of the reflectors that can be observed in the conventional lines cannot be observed on the land streamer. In both sections there is still present a strong linear noise that could not be eliminated from the data during the processing, this noise trend is more prominent in the streamer data.

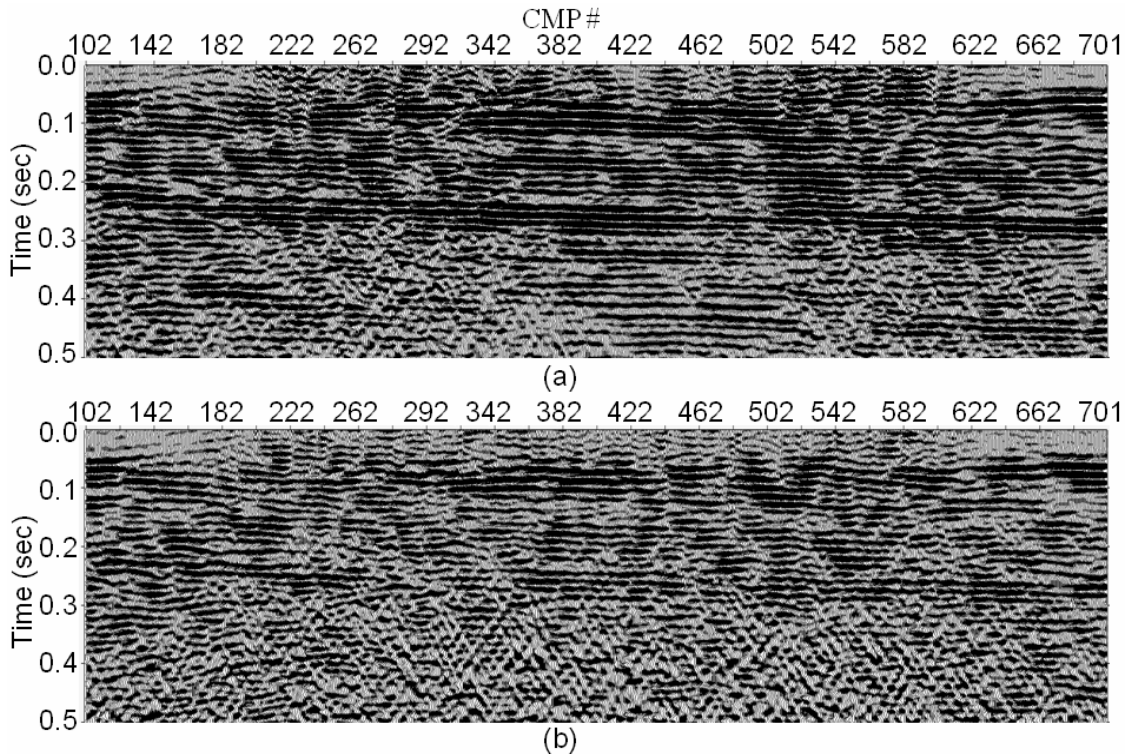


Figure 2.27. Comparison of stacked sections in the vertical channel for the conventional line data (top) and for the land streamer data (bottom). Same sections as Figure 2.21 but zooming on the first 0.5 seconds.

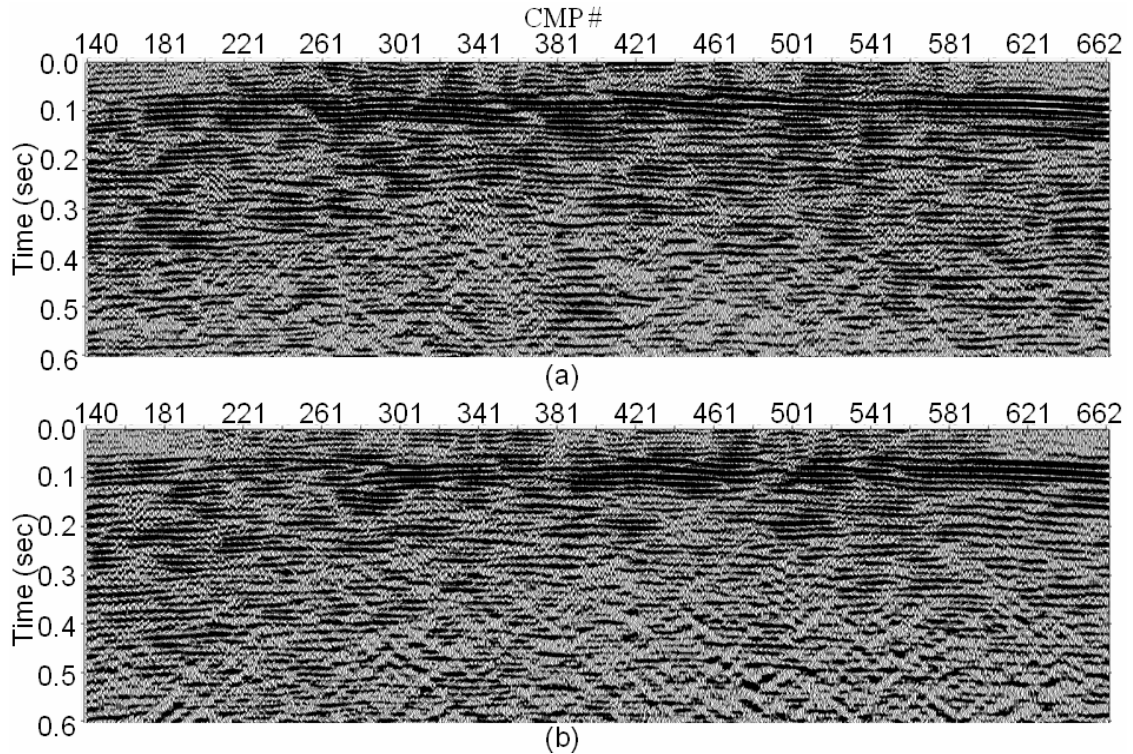


Figure 2.28. Comparison of stacked sections in the radial channel for the conventional line data (top) and for the land streamer data (bottom). Same sections as Figure 2.25 but zooming on the first 0.6 seconds.

2.6.2 Spectral analysis

2.6.2.1 F-x analysis of the raw shot gathers

Vertical channel: An average Fourier amplitude spectrum was calculated on a raw shot gather for a window corresponding to what were hoped to be subsurface reflections (Figure 2.29a). With this analysis, we see how the source gathers recorded with both systems are very similar: peaks and troughs match reasonably well up to 110 Hz; after 110 Hz the conventional line spectrum decays faster than the amplitudes for the land streamer line. Both curves are identical up to 50 Hz, after which the land streamer show greater power. It is important to mention that this comparison is not as diagnostic as with stacked data.

Using the same amplitude spectrum plot in Figure 2.29(a) and based on the potential band estimation method presented in Margrave (1999), we try to identify a “corner frequency” where the signal spectrum drops below the background noise level. This observation can be corroborated by the f-x analysis of the unmigrated stacked sections. The corner frequency for these datasets is not as evident as in the examples presented in Margrave (1999); however, the spectrum shows a trough in both datasets, at 160 Hz for the conventional line and at 180 Hz for the land streamer, which might be the corner frequency; after this trough the decay rate becomes similar for the remaining frequencies up to 250 Hz (maximum sweep frequency).

The same analysis was done in windows that cover a portion of the first breaks and the groundroll (Figure 2.29b and 2.29c). These last analyses were done to see if both systems could record the same seismic events (signal and noise) with the same characteristics. For the first-break window (Figure 2.29b), both spectra are smooth and with similar shapes, with the difference that the refractions show slightly greater energy for the land streamer. If we go back to the raw shot gathers (Figure 2.26a and 2.26b) we can notice how the first breaks for the land streamer present a better character than for the conventional line, being not so contaminated by the source generated noise in the near offsets.

For the window located in the noise area the results are very similar (Figure 2.29c), presenting in the land streamer curve more discontinuities than the one for the conventional line after the first 80 Hz. In the range 0 to 80 Hz, the curves are almost identical for both of them. For both datasets the Rayleigh waves exhibit a dominant

frequency near 50 Hz, which is very high for waves that usually have a much lower dominant frequency of around 8 Hz.

Radial channel: The same Fourier analyses were done in the radial channel, for signal, first arrivals, and groundroll windows (Figure 2.29). Surprisingly, in the signal-only window (Figure 2.29a) peaks and troughs match reasonably well up to 140 Hz, after which the land streamer shows slightly greater power.

For the radial channel we tried to use the “corner frequency” concept to identify the potential frequency band, but unfortunately in this case it is very hard to identify this frequency where the signal spectrum drops below the noise level. F-X analysis of the unmigrated stacked sections will be used to determine the bandwidth for the radial channel.

The result of the analysis on the first-breaks window shows that both spectra have similar shapes (Figure 2.29b). However, the curve corresponding to the conventional line shows more discontinuities along the frequency range. If we go back to the raw shot gathers (Figure 2.26c and 2.26d), we can notice how the first breaks for the land streamer present a better character than for the conventional line, not being so contaminated by the source-generated noise in the near offsets.

For the window located in the noise area, the Rayleigh waves exhibit a dominant frequency of 30 Hz. From the raw gathers (Figure 2.29c), we saw how the noise was stronger on the land streamer than in the conventional line, this is corroborated in this spectrum where the amplitudes of the Rayleigh waves are higher for the land streamer.

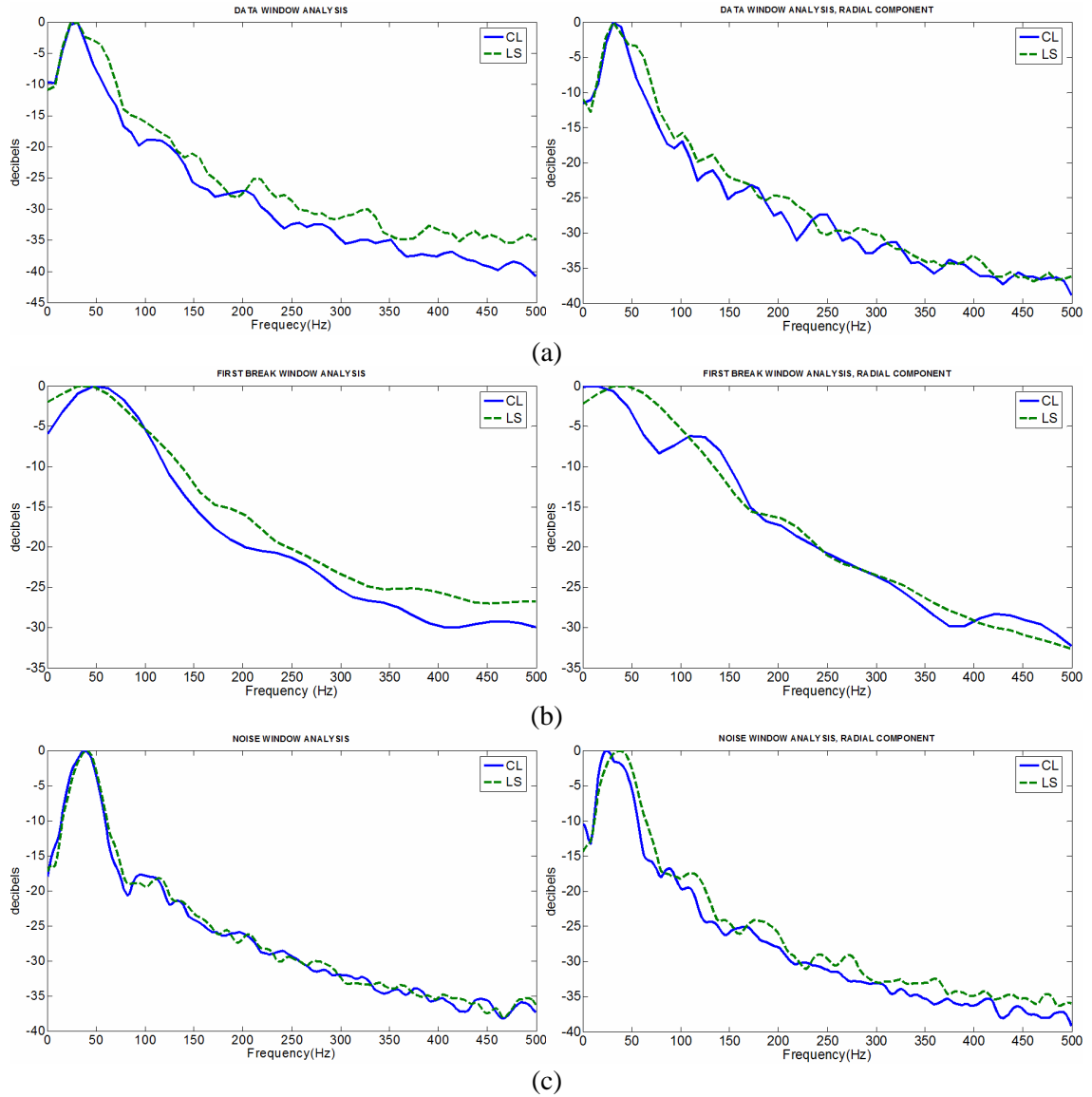


Figure 2.29. Average Fourier amplitude spectrum of a raw shot gather for the vertical channel (left) and radial channel (right) of the conventional (CL) and land streamer line (LS), with windows corresponding to (a) signal only area, (b) first break area, and (c) groundroll/noise area.

2.6.2.2 F-x analysis of the unmigrated stacked sections

Vertical channel: An f-x analysis of both unmigrated, unfiltered stacks is shown in Figure 2.30 to estimate the realized signal band. The realized signal band method computes the f-x Fourier spectra of unmigrated stacked sections, and plots the amplitude and phase spectra separately. The frequencies where signal is dominant are recognized by laterally-coherent spectral events while spectral power is indicated by strong (dark) regions on the amplitude spectrum (Margrave, 1999; Hamarbitan and Margrave, 2001).

The f-x amplitude spectra for both datasets (Figure 2.30a and 2.30b) shows a drop in spectral power above 160 Hz. The conventional line spectrum shows a drop above 110 Hz for CMP's 100 to 200 and 600 to 700 that corresponds with the edges of the line.

The phase coherence of the two datasets is contrasted in Figure 2.30(c) and (d). For both datasets there is a sudden reduction in phase coherence at about 110 Hz coincident with the drop in spectral power in Figure 2.30(a) and (b). However, for the conventional line data, subtle phase coherence persists up to 140 Hz, indicating low signal levels. In contrast, the land streamer data show good phase coherence to about 90 Hz but very little at higher frequencies. These observations may be interpreted as indicating similar signal levels in the two datasets below 90 Hz. In the 90-140 Hz band, the strength of the conventional line is greater than that of the land streamer data. On the other hand, from 180 to 240 Hz, the land streamer data show evidence of weak signal towards the edges of the line, whereas the conventional line dataset shows coherent, weak signal along all the line.

Radial channel: The f-x amplitude spectra for both datasets for the radial channel are contrasted in Figure 2.31. Surprisingly, the phase and spectral power spectrum for the radial channel are very similar to the vertical channel (Figure 2.30) — they show a drop

in spectral power above 160 Hz. The conventional line spectrum does not show the drop in spectral power in the 100 to 200 CMP range at the ends of the line. The spectral power looks slightly weaker for the radial channel than for the vertical.

The land streamer spectrum is very similar to the conventional line, but it looks noisier for the very low and high frequencies.

The phase coherence of the two datasets is contrasted in Figure 2.31(c) and (d). For both datasets there is a sudden reduction in phase coherence at about 110 Hz coincident with the drop in spectral power in Figure 2.31(a) and (b). This observation coincides with the vertical channel, but in the 40-110 Hz band of the radial channel the events look weaker. Above 110 Hz, there are no strong events with good coherency. From 180 to 240 Hz, both datasets show evidence of weak signal.

The phase coherence plots are very similar for both lines; maybe a subtle difference is in the low frequencies where the conventional line appears to have a higher content of low frequencies.

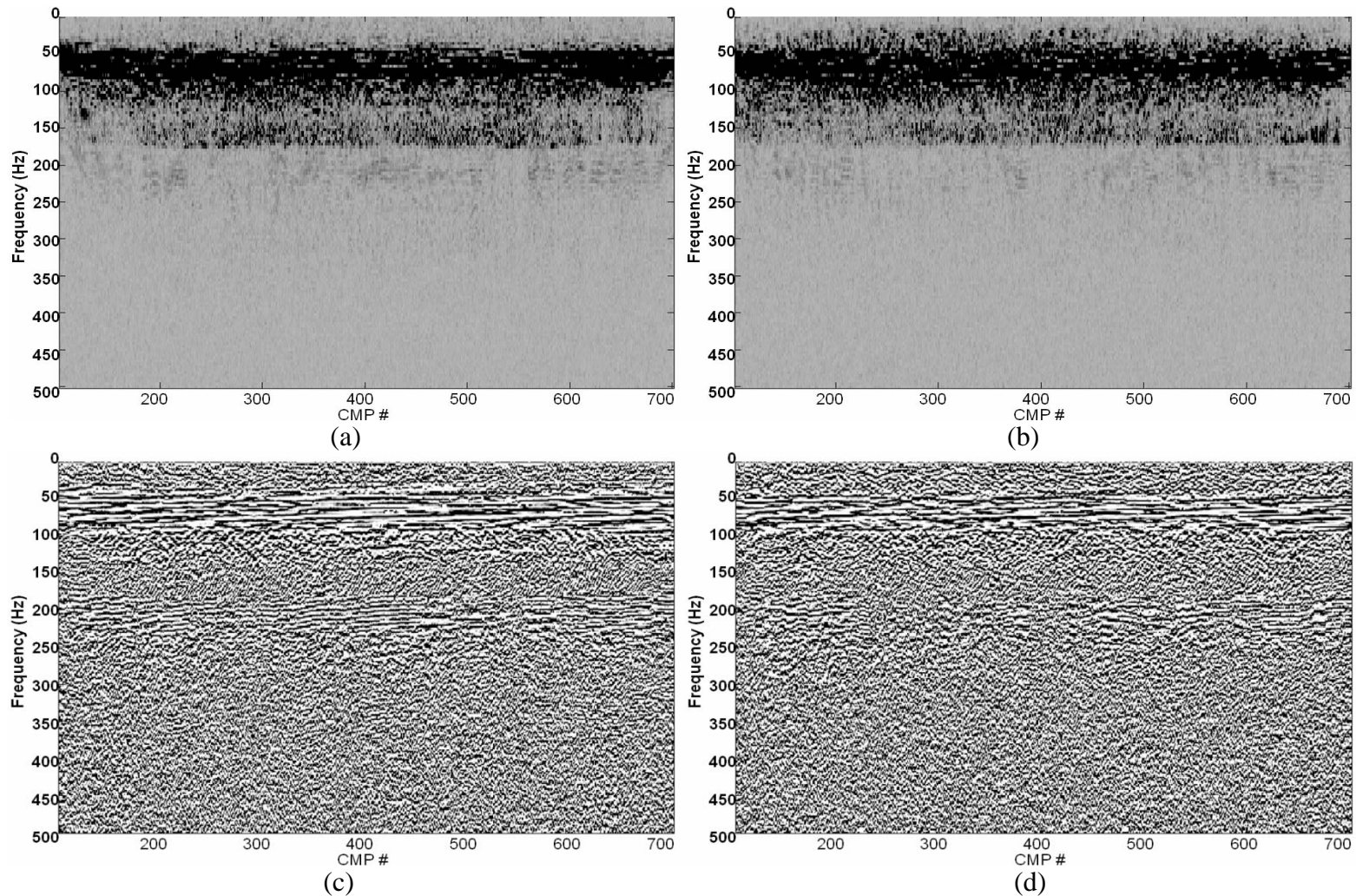


Figure 2.30. F-x spectral analysis for the final unmigrated, unfiltered P-wave stack for conventional line and land streamer data computed over the time zone 70-300 ms. The f-x amplitude spectrum for the conventional line is shown in (a); (b) shows a similar spectrum for the land streamer data. The land streamer data show reduced signal power above 80 Hz. In (c) and (d) the f-x phase spectra are shown corresponding to (a) and (b), respectively. The conventional line data show very low phase coherence from 100 to 180 Hz and very weak coherence from 180 to 240 Hz. The land streamer data show good phase coherence from 50 to 80 Hz and very little at higher frequencies.

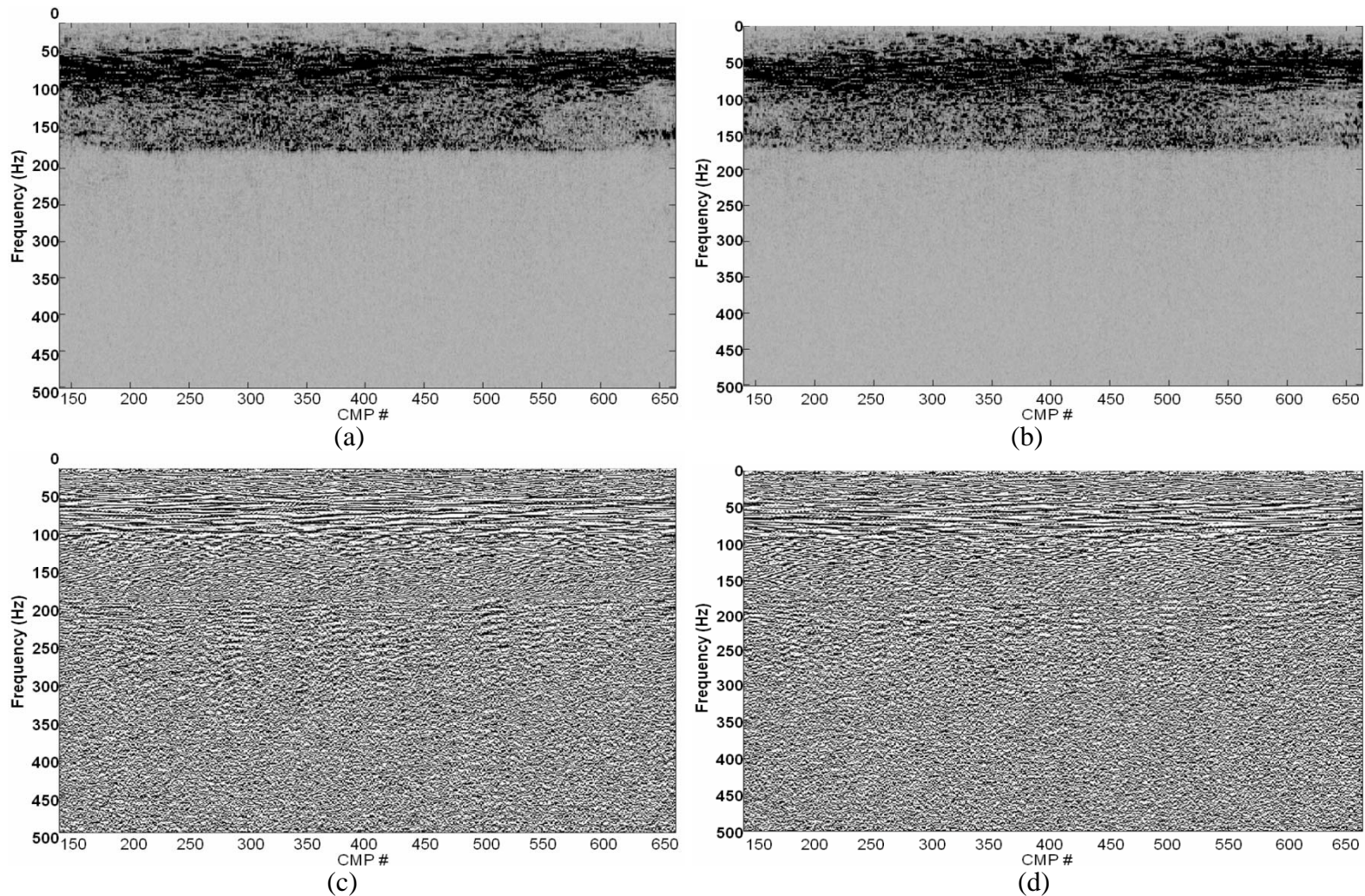


Figure 2.31. F-x spectral analysis for the final unmigrated, unfiltered PS-wave stack for conventional line and land streamer data computed over the time zone 60-500 ms. The f-x amplitude spectrum for the conventional line is shown in (a); (b) shows a similar spectrum for the land streamer data. The land streamer data show reduced signal power above 100 Hz. In (c) and (d) the f-x phase spectra are shown corresponding to (a) and (b), respectively. The conventional line data show very low phase coherence from 100 to 180 Hz and very weak coherence from 180 to 300 Hz. The land streamer data show good phase coherence from 50 to 100 Hz and very weak from 200 to 240 Hz.

2.6.3 Frequency analysis of the receiver gathers

Signal bandwidth may depend on receiver location (i.e. its location along the receiver line) and receiver depth. However, geophone coupling and the quality of the geophone planting might be controlling factors in the variation of the signal bandwidth as well. Variations in bandwidth across the receiver line are considered to indicate variations in geophone coupling (Cieslewicz and Lawton, 1998).

The relationship between frequency content, receiver location and geophone coupling can be depicted by plotting the spectra data in three dimensions with contour plotting. For every receiver gather of every dataset, a separate frequency spectrum was calculated in the appropriate time window, creating a matrix that represents location along the receiver line: the rows represent frequencies from zero Hz to Nyquist frequency; and each individual cell contains decibels below maximum amplitude of the frequency spectra.

Vertical channel: Figure 2.32(a) and (b) shows the frequency contour plots of the vertical channel for the conventional line and land streamer data. Between geophones of the two acquisition systems, the frequency spectra display a reasonable correlation between frequencies in the range 40-80 Hz. For low frequencies, amplitude attenuation is less for the land streamer dataset than for the conventional line. For high frequencies, attenuation is higher for the streamer than for the planted dataset.

In the data, 70 Hz contamination can be seen: this should be consistent between all the receiver stations, but in the plot the consistency is better for the land streamer than for the other dataset where it is only noticed at some segments of the line. This evidence is another indication of better receiver coupling for the land streamer in this frequency range.

Radial channel: Figure 2.32(c) and (d) show contoured plots of the difference in frequency spectra of converted-wave reflections for both datasets as recorded on the radial channel. For the radial channel there is a poor correlation between the frequency spectra of both datasets. The planted geophones do not have as great a variation in bandwidth across the receiver line as the land streamer phones. These observations indicate that for the converted-wave data the geophone coupling was better along the planted geophone line.

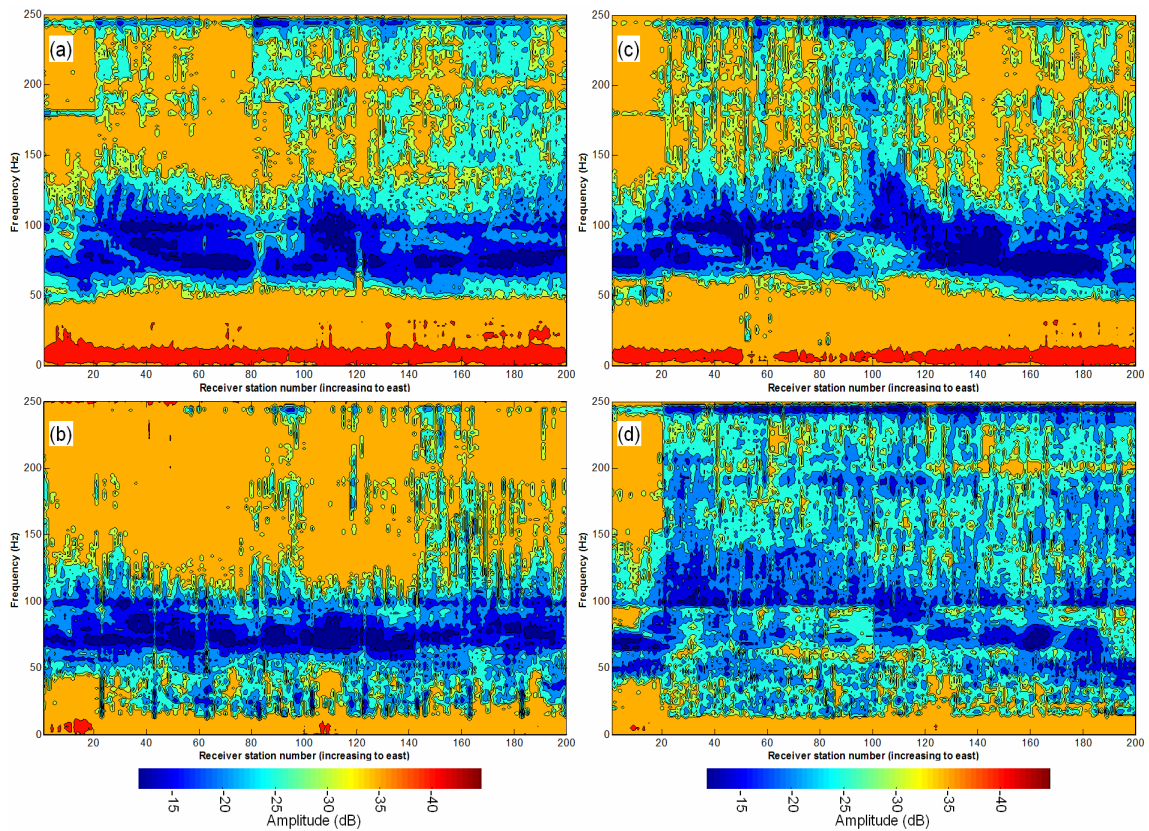


Figure 2.32. Frequency analysis of the common receiver gathers for both lines. (a) and (b) show the contour plots for the vertical channel conventional line and land streamer, respectively. (c) and (d) show the same analysis but for the radial channels of the conventional line and land streamer data, respectively.

2.7 Conclusions

2.7.1 Conclusions for Land streamer Test 1

This dataset constituted the first experiment conducted by the CREWES Project using a land streamer system. Seismic reflections of the first 50 m of the weathering layer were observed even with the limitation of the acquisition configuration used for the Priddis area. The low-frequency content of the data might suggest coupling problems or near-surface absorption of the high frequencies, as a result of the unconsolidated material characteristic of this area. However; to corroborate these theories requires further experimentation.

This first attempt demonstrated the versatility of this system and a reduction in time and labour by almost thirty percent for land seismic acquisition operations. Future improvements will involve a larger streamer with more channels and variable receiver spacings (smaller for near offsets and larger for long offsets), shots at every receiver location for every fix streamer location, and greater overlapping of the cable.

2.7.2 Conclusion for land streamer Test 2

A comparison between a 3-C land streamer and a 3-C planted-geophone line was undertaken. The analysis indicates that for the vertical component the datasets show similar events and characteristics.

The land streamer system recorded high-resolution seismic data on a grass-covered hill. Its geophone-to-ground coupling was good and very closely matched with the planted geophone line for the vertical channel but not for the radial and transverse channels.

Employing a vibratory source improved the acquisition speed and offered the possibility of generating repeatable signals, which were necessary to complete our experiment.

The raw shot gathers for the vertical channel were alike, showing the same characteristics for noise, first breaks and reflections. For the radial and transverse channels the results suggested that even when the main reflections are shown, they are not very similar to the data from the planted geophones.

After identical processing, the processed stacked sections showed the existence of seismic reflections in the area and corroborated the same results as the raw shot gathers for the vertical and radial channels. An f-x spectral analysis of the stacked sections revealed that for the vertical channel both datasets signal levels are similar below 90 Hz, with a drop in spectral power above 160 Hz and a reduction in phase coherence at 110 Hz. The planted geophone dataset shows low signal levels up to 140 Hz. In the radial channel the observations about the phase and spectral power are very similar to the vertical channel. The land streamer spectra are similar to the conventional line, but with higher noise levels for the very low and high frequencies.

These results confirm the benefits and versatility of this system compared with conventional methods of seismic data acquisition. As well as demonstrating how good quality data can be generated in different environments, the land streamer system shows potential for reducing acquisition time and labour for land seismic operations, and as an important tool in oil and gas exploration, mining, engineering, environmental, and archaeological applications.

Chapter Three: USING F-K-K FILTERING METHODS TO SUPPRESS ACQUISITION FOOTPRINTS IN THE PRIDDIS 3D STACKED DATASET

As part of the University of Calgary geophysics 2007 summer school, different types of data have been acquired, such as 2D and 3D shallow surface seismic reflection surveys, VSP and well-logs. Integrated analysis of this dataset has been presented by Miong et al., (2008) and Suarez et al., (2008), with the objectives of characterizing the geological and hydrological nature of the Priddis site. The Priddis site is located in the Canadian Foothills, where the largest single source of groundwater supply is the Paskapoo Formation (Grasby, 2006). The previously mentioned studies proposed the use of 3D surface seismic for groundwater detection; however, a high quality seismic image is needed to map such shallow and potentially thin and discontinuous targets at 50-100 ms.

Typically, 3D seismic surveys are used to map deeper targets than those studied at the Priddis site, but Lawton et al., (2008) illustrated the efficacy of the technique for characterizing targets shallower than 500 m (110-500 m range). Following this initiative of using a 3D seismic survey to identify shallow reflection events, we tried to improve the image and continuity of the shallow events using seismic data processing techniques in the post-stack migrated dataset. Using this improved image some seismic attributes are extracted from the 3D volume. As guidance for identifying the targets, the well log interpretation and correlation with the seismic as proposed by Miong et al., (2008) is employed.

When evaluating the acquisition parameters and the 3D post-stack migrated dataset, a strong linear pattern was observed. It was most noticeable in the time slices of the 3D cube and in the first 150 ms of the in-line/cross-line stacked sections. This linear

pattern could be a consequence of the sparse source and receiver line spacing used during the acquisition, resulting in dipping noise such as ground roll that is being insufficiently sampled for standard coherent noise suppression techniques to tackle. This linear pattern makes any kind of interpretation difficult on shallow parts of the sections and the time slices. It also influences the degree of confidence in seismic analysis, such as seismic attributes, that identifies and interprets results using time slices.

Using post-stack migrated data limits our ability to eliminate the ‘acquisition footprint’. One of the reasons is because the migration “smears” the aliased energy, which is very difficult to eliminate once it has spread out from its original fixed position prior to migration. However, our intent is to make the footprint problem less noticeable, albeit with the knowledge that, because we are working on a post-stack migrated dataset, it is going to be very difficult to completely remove it. Two techniques for post-stack footprint removal are tested in this chapter: F-K-K filtering methods and post-stack trace interpolation.

3.1 Description of the seismic survey

The 3D seismic survey employed an orthogonal geometry, with receiver and source lines 50 m apart oriented north-south and east-west, respectively. Shot and receivers were spaced 10 m apart along their respective lines (Lawton et al, 2008).

The equipment used was similar to the conventional line equipment. It consisted of a 600-channel ARAM Aries recording system and a 17,400 lb Envirovibe built by IVI. Geophones used were single vertical-component marsh phones containing SM-24 10 Hz elements (Lawton et al, 2008).

The final survey geometry is illustrated in Figure 3.1, and the final CDP fold of the survey is shown in Figure 3.2, with a maximum fold of 43.

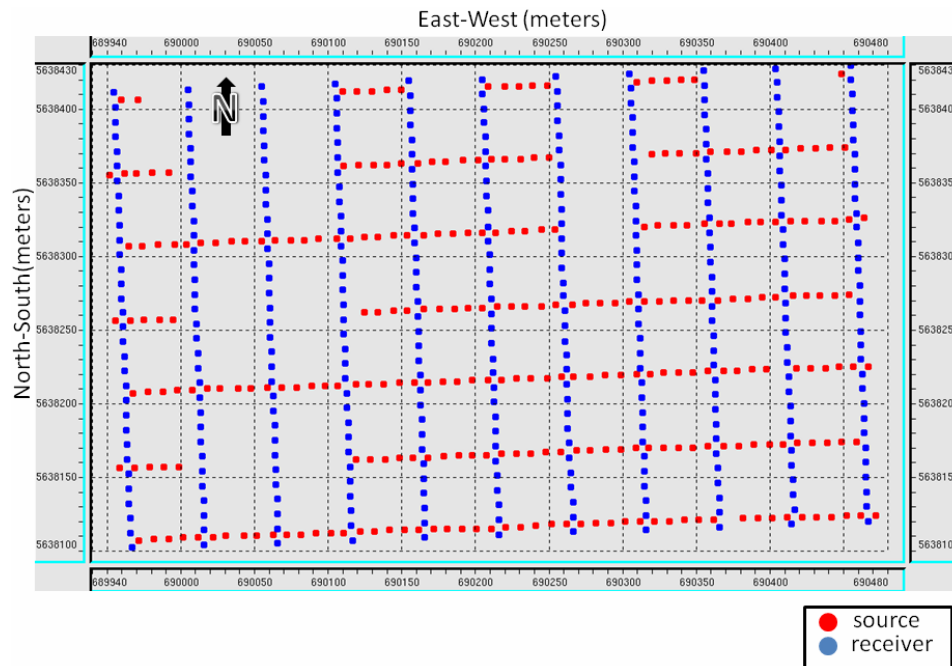


Figure 3.1. Post-survey shot and receiver locations extracted from the dataset headers.

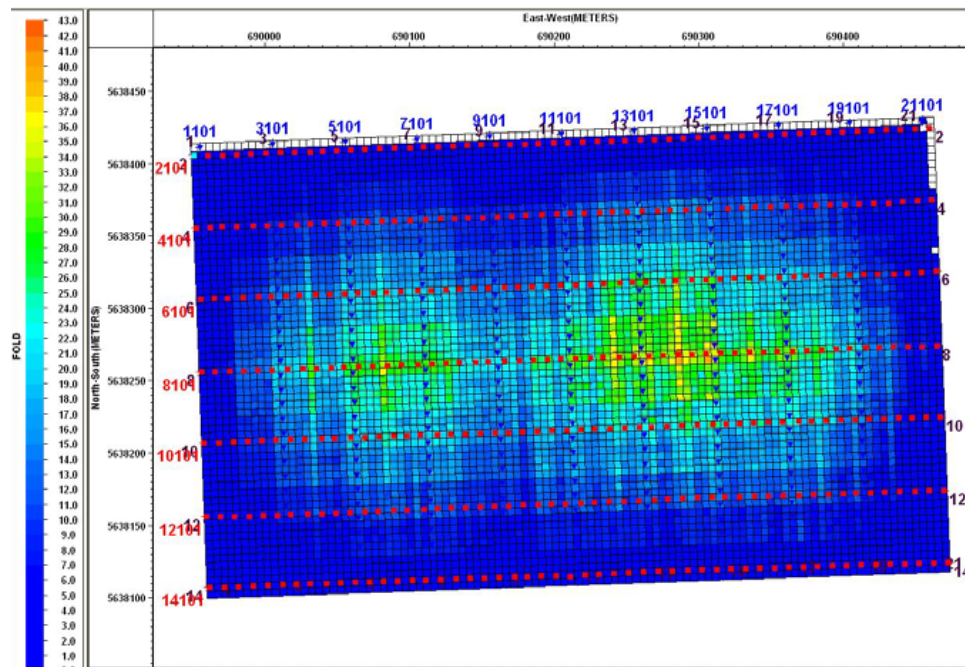


Figure 3.2. CMP fold for the survey (from Lawton et al., 2008).

3.2 Comparison of stacked sections from the 2D land streamer line, planted geophone line, VSP and 3D survey from the Priddis test site

In chapter 2, it was shown how the few reflections existing in the Priddis test site are well imaged on both the stacked sections of the land streamer Test 2 (Figure 3.3a and 3.3b). The same events between 75 and 300 ms can be observed. To corroborate if these shallow reflections are real, a comparison of these two sections with the corresponding 3D cross-line (Figure 3.3 and 3.4) and a zero-offset VSP (Figure 3.3c) was undertaken. The most obvious observation is that the 3D cross-line section provides better imaging below 300 ms, but it cannot resolve the shallower reflectors that are present in the land streamer experiment datasets. From the correlation of the first 300 ms from both edges of the lines presented on Figure 3.3, we can see how the strongest reflectors of the 3D section at 50, 80 and 260 ms (red, blue and light green arrows) are present in all three sections. Some of the weakest reflections in the 3D section at 100, 115, 130 and 200 ms (dark green, yellow, purple and magenta arrows) are correlated in the other two sections, where they look stronger.

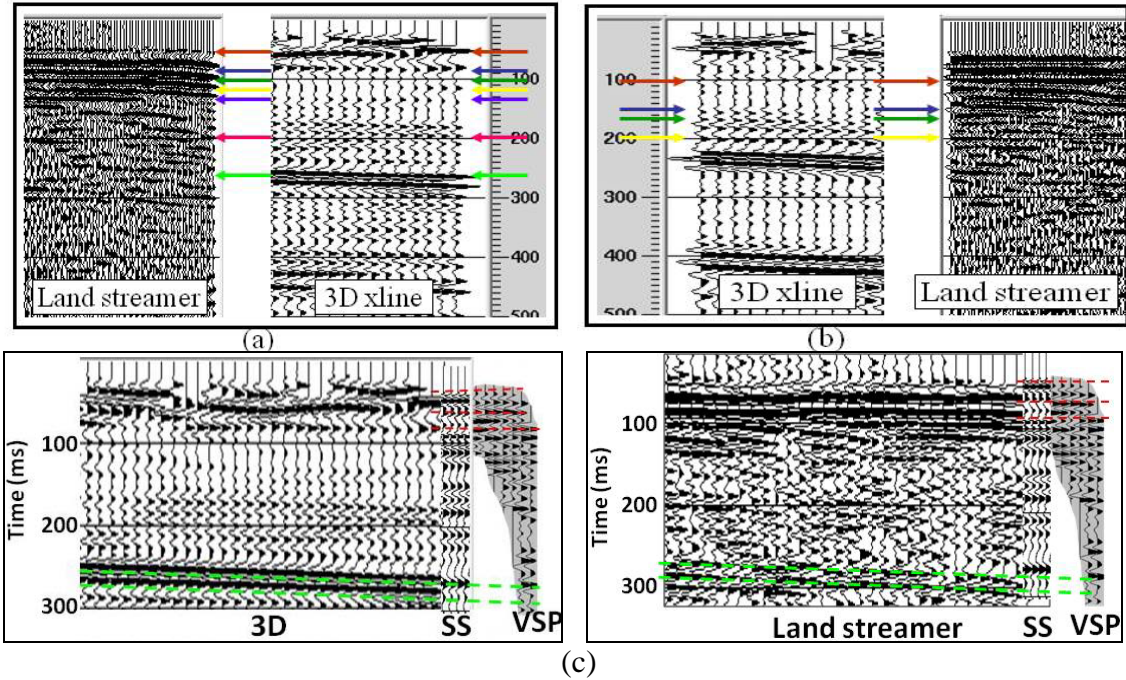


Figure 3.3. Identification of some of the common reflectors for the land streamer, 3D and zero-offset VSP: (a) 3D crossline stacked section for the eastern edge, (b) 3D crossline stacked section western edge of the land streamer section and (c) for the VSP, 3D and land streamer.

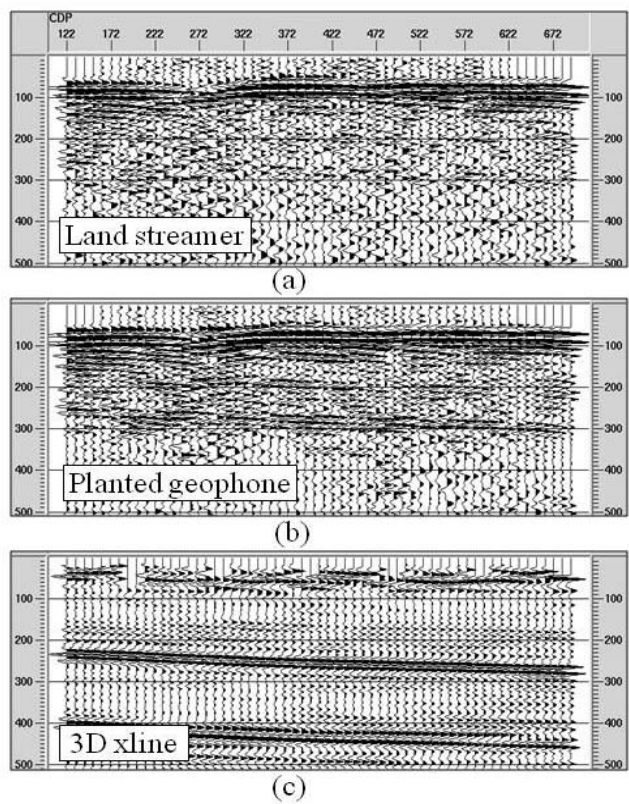


Figure 3.4. Comparison of stacked sections from (a) the 2D land streamer line, (b) 2D planted-geophone line and (c) coincident 3D cross-line.

3.3 F-K-K filtering as a method to improve the image on the Priddis 3D stacked volume

An ‘acquisition footprint’ is an undesired amplitude effect which can affect both land and marine 3D data. The footprint is characterised by ‘striping’ patterns seen on shallow time-slices, and as persistent dipping noise on stack sections. There are various causes for this such as changes in source or receiver characteristics, or the presence of steeply dipping noise or multiples. Regardless of the instigating factor, the end effect arises through a common mechanism – spatial aliasing.

Coarse spatial sampling (i.e. large source/receiver line spacing) during land acquisition can result in dipping noise insufficiently sampled to be suppressed by standard noise reduction methods. Advanced F-Kx-Ky filtering (otherwise referred to as F-K-K) provides a means of removing the aliased energy from 3D stack volumes. This creates a more desirable product, and reduces the likelihood that multichannel processes (such as migration) will make the problem worse.

3.3.1 Quality measures to establish filtering parameters

It is vital that thorough quality control be carried out in order to establish appropriate F-K-K filtering parameters. The following quality control (QC) products are examined:

- Quality control stacks of selected in-lines and cross-lines before F-K-K filtering, after F-K-K filtering, and difference sections

These plots are used as visual indicators to display the effectiveness of the filter, and to confirm that only noise has been removed. In particular, the difference plots (input minus filtered) should ideally only contain the dipping linear noise, and perhaps some

random scatter noise. Comparison of the input displays against the difference sections should indicate if primary signal is being eroded.

- Raw time slice sections before F-K-K filtering, raw time slice sections after F-K-K filtering, and difference time slice sections

These seismic plots provide similar information to the in-line/cross-line stacks. Time slices provide a ‘bigger picture’ of the data volume at a particular horizon, as opposed to the discrete sampling of selected lines, and it is sometimes easier to see if important structures are being compromised.

- F-K spectral analyses of selected in-lines and cross-lines before and after F-K-K filtering

Comparison of F-K spectral analyses before and after filtering is another method of quality controlling the filter application. It is much easier to identify the separate components of primary signal and unwanted noise in F-K space. The F-K spectral plot can be used to assist in identifying which portions of energy we want to remove, and establish if the filter has been successful.

- F-K Spectral analyses of raw time slices (particularly shallow times) pre- and post-F-K-K filtering

F-K spectral analyses of shallow time slices are extremely useful in confirming whether or not the interference is strictly geometry related. If it is, the noise pattern will appear as a regular grid of energy locations in F-K space (with the primary signal located at the origin of both axes).

F-K analysis after filtering is important in establishing if any undesired energy persists, and if so what may be done to improve the filter (e.g. change in edit location control, size of edit spots for notch filtering).

3.3.2 *Assessment of acquisition footprint pattern*

Quality control displays were generated to identify the footprint pattern. These displays include in-line and cross-line stacked sections, time slices and F-K spectra of selected stacked and time slice sections.

3.3.2.1 Quality control stacks of selected in-lines, cross-lines and raw time slice sections before F-K-K filtering

Figures 3.5, 3.6 and 3.7 show selected cross-line and in-line stacks and raw time slices of the 3D migrated volume. Six cross-line stacked sections oriented north-south and three in-line stacked sections oriented east-west show that in the first 150 ms of data there is a loss of continuity in the reflectors, and a “cross-hatch” pattern (dipping noise) that makes these very shallow reflectors difficult to interpret. This effect is clearer and stronger in the in-line sections and, if we correlate this with the time slices of Figure 3.7, shows a preferential alignment of the events in the north-south direction.

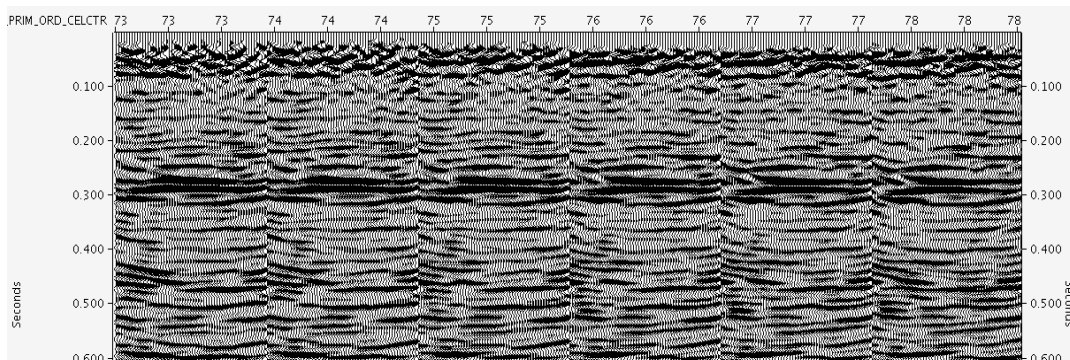


Figure 3.5. Quality control in-line stacked sections prior to F-K-K filtering.

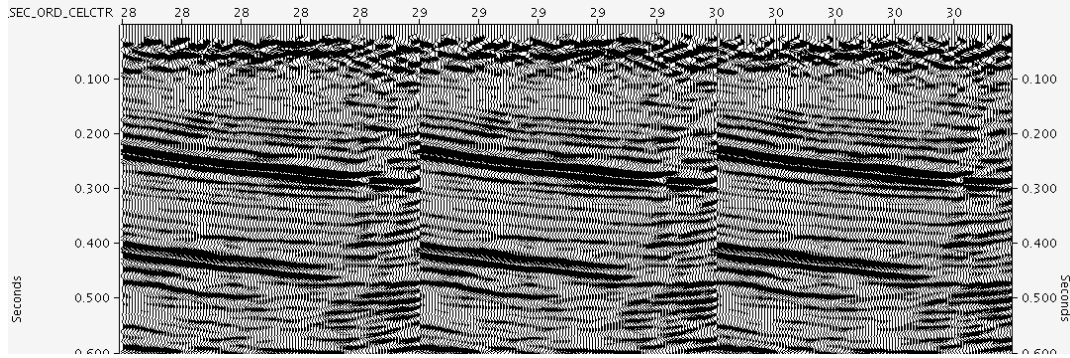


Figure 3.6. Quality control cross-line stacked sections prior to F-K-K filtering.

The characteristic pattern that can be identified in the presence of a geometry footprint is not as clear as it usually is in other cases. What can be identified is a sort of striping pattern on the time slices (Figure 3.7) that appears in approximately the first 150 ms.

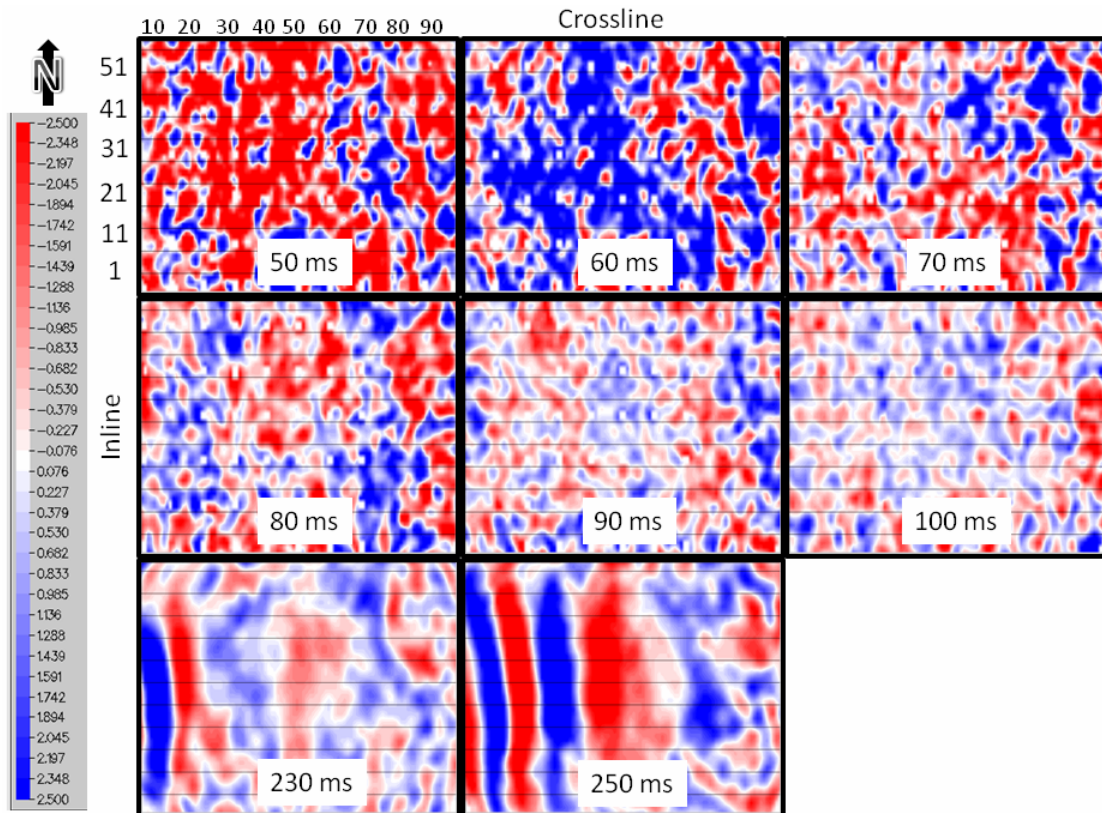


Figure 3.7. Timeslices prior to F-K-K filtering.

3.3.2.2 F-K spectral analyses of selected in-line and cross-line stacks and raw time slice sections before F-K-K filtering

F-K spectral analyses of selected in-lines, cross-lines, and time slices yield further information regarding the characteristics of the footprint pattern. The F-K spectrum of one of the in-line (Figure 3.8) shows the primary energy at wavenumber zero. However, there are additional, weaker energy maxima that, before migration, would be at regular intervals along the wavenumber axes but, because they were “smeared” by the migration, do not appear so regular. These maxima are the aliased groundroll that appears as dipping noise/amplitude striping on the first 150 ms of the seismic.

The regular intervals of the weaker energy could be set as every 20 cycles/km, according to the F-K spectrum on the in-line stacked section. This number will be corroborated when we calculate the locations of the aliased energy using the acquisition geometry parameters.

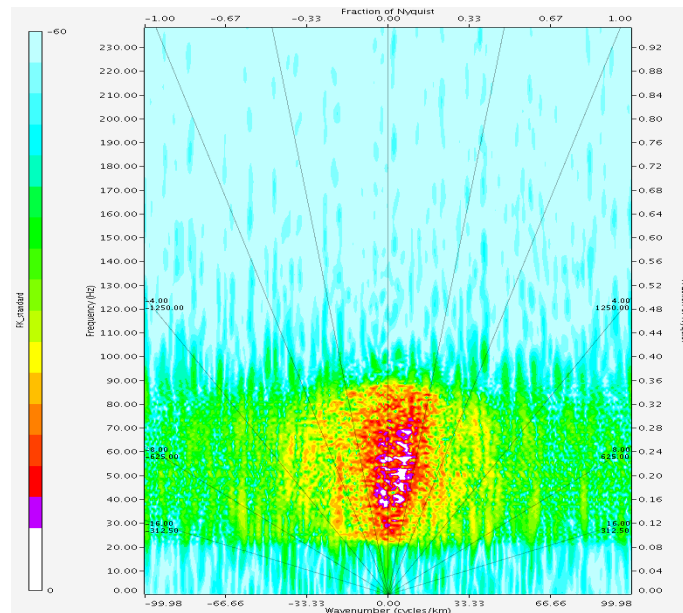


Figure 3.8. F-K spectrum of a selected inline stacked section.

Given details of the recording parameters for this dataset, it is possible to calculate the locations of the aliased energy, calculating the number of IL and XL per km with the receiver and source line spacing. The data were recorded in a ‘swath with orthogonal source line’ configuration, using a source line spacing of 50 m, a receiver line spacing of 50 m, and bin size of 5 m. The following table lists the predicted locations of aliased energy in terms of wavenumber cycles per km:

IL Wavenumber	XL Wavenumber
100	100
80	80
60	60
40	40
20	20
-20	-20
-40	-40
-60	-60
-80	-80
-100	-100

Table 3.1. In-line (IL) and cross-line (XL) wavenumber coordinates.

These locations are more easily described by their periodicity in terms of CMP bins. In that case, the aliased maxima are predicted to occur every **10 CMPs** in-line, and every **10 CMPs** cross-line.

The following image (Figure 3.9) shows the F-K spectra of time slices from 50 to 78 ms. The primary energy is shown at the origin (0,0), surrounded by a grid of aliased energy points. Although this display does not permit accurate determination of the energy point locations, it is very useful as a qualitative quality control tool.

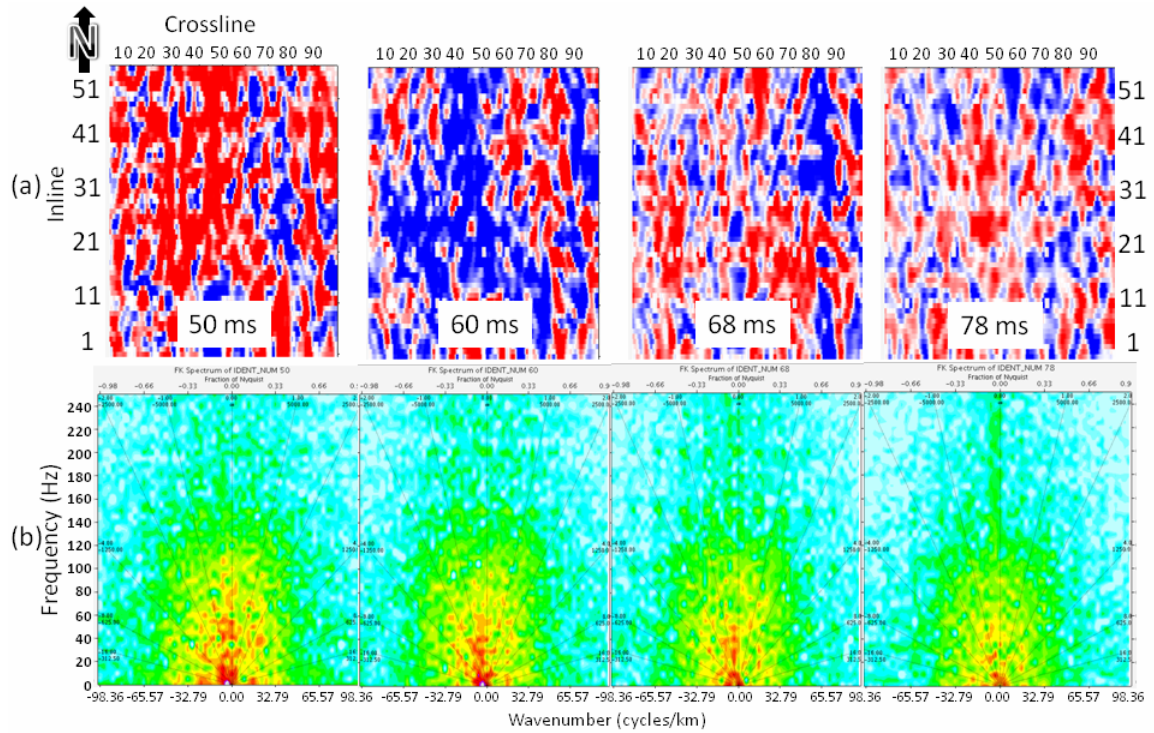


Figure 3.9.(a) Time slices and their (b) F-K spectra prior to filtering.

3.3.3 Filter modes

Having established that a prominent footprint pattern exists, and that there is justification for attempting to remove it, an F-K-K filter and trace interpolation methods can be designed to attenuate the unwanted energy.

F-K-K filtering can be applied in two ways: as a K-notch filter or as a coherency filter. Both methods are effective, and can be used in tandem.

3.3.3.1 K-notch filtering

In principle, 3D K-notch filtering works in a similar way to 2D K-notch filtering when applied to 3D stack data. The important difference is that the filter is applied to both in-line and cross-line directions without re-sorting the data. 3D seismic data is Fourier-transformed from the T-X-Y (time-space) domain to the F-Kx-Ky (frequency-

wavenumber) domain. Within separate frequency slices in Kx-Ky space, the designated areas of unwanted energy are zeroed.

The K-notch filtering can be designed in three different ways: auto-detecting Kx-Ky spots; generating Kx-Ky spots using the orthogonal geometry, and user-defining Kx-Ky spots. In our test only the results of the first two methods are shown because they produced the best results without attenuating signal from the stacked sections.

Option 1: Auto Detect Kx-Ky Spots to Notch Filter

- When this parameter set is active, the program automatically detects the locations for K-notching.

Option 2: Orthogonal Geometry to Generate Kx-Ky Spots to Notch Filter

- This parameter set allows the user to define the K notches in terms of inline and cross-line periodicity, and is mutually exclusive to the '*Auto Detect Kx-Ky Spots to Notch Filter*' parameter set.
- For the Priddis dataset, using the periodicity of the K notches calculated in section 3.3.2.2 with the acquisition parameters, it was user-specified at 10 CMPs in-line, 10 CMPs cross-line.

3.3.3.2 Coherency filtering

In addition to notch filtering, there is another F-K-K technique available for removing aliased energy from 3D stack volumes. Coherency filtering works by considering the aliased energy to be random noise. By transforming incoherent events from T-X-Y into an amplitude plateau in the F-Kx-Ky domain, the zeroing of samples lower in amplitude than this plateau produces an enhancement in coherent events when inverse transformed back to the T-X-Y domain.

3.3.3.3 Post-stack trace interpolator

The post-stack trace interpolator spatially interpolates traces from a dataset to yield constant trace spacing within a 3D grid or along a 2D profile. This is obtained through the summation of adjacent traces that have been time-variantly shifted to line up at the angles of maximum coherency. The interpolation is accomplished by a weighted average of input trace amplitudes along the dip directions associated locally with the most coherent energy.

For this method, the option for filling of input mute holes was used. For this option, the program calculates an expected start time for the middle trace, based on a linear interpolation of the start times from the surrounding traces. The mute hole is filled using a portion of the interpolated trace up to the expected start time.

For the interpolation of the Priddis dataset, a bin cell size one half that the regular cell size (5 m) was used. The interpolation was applied on the best output dataset from the F-K-K filtering.

3.3.4 *Parameterization of the filters*

The ‘*Time Window Length*’ and ‘*Time Overlap*’ parameters are the most important parameters. They control the length of the filter window(s) in time, and the overlap between windows. In general, the shorter the windows, the stronger the filter effect. Time windows of 200, 500 and 1000 ms were tested. The 1000 ms window with an overlap of 50 % was selected because it was the weaker filter that produced the best results.

3.3.5 Filtering results

After applying the various filtering options for the F-K-K technique with a 1000 ms window, and applying the post-stack trace interpolator on the 3D stacked volume, we can compare and evaluate the results to select the image.

Once again we will examine the same quality control displays used in section 3.3.2, but with a careful examination of the difference plots before and after filtering on the in-line/cross-line stacked sections. This will indicate whether the primary signal is being eliminated.

Figures 3.10 and 3.11 show the difference plots between the input and filtered data for the same stacked sections of section 3.3.2.1. In these plots, we noticed that the coherency filter is attenuating a lot of signal from the sections: for this reason it is the first to be discarded. The K-notch auto detect filter has no affect on any signal but only deals with the pattern from the edges and doesn't help much on the rest of the section or the shallow part. The K-notch orthogonal option produced the best results, removing part of the linear noise that shows in the difference sections as linear dipping noise to the right and to the left. On top of the K-notch orthogonal, a trace interpolation every 2.5 m was done; as we can see after the F-K-K filtering there still remains footprint noise that is being super-sampled by the interpolation process trying to improve the spatial aliasing. The difference plot of the trace interpolation is also seen on Figures 3.10 and 3.11; the plots show more removal of the linear dipping noise.

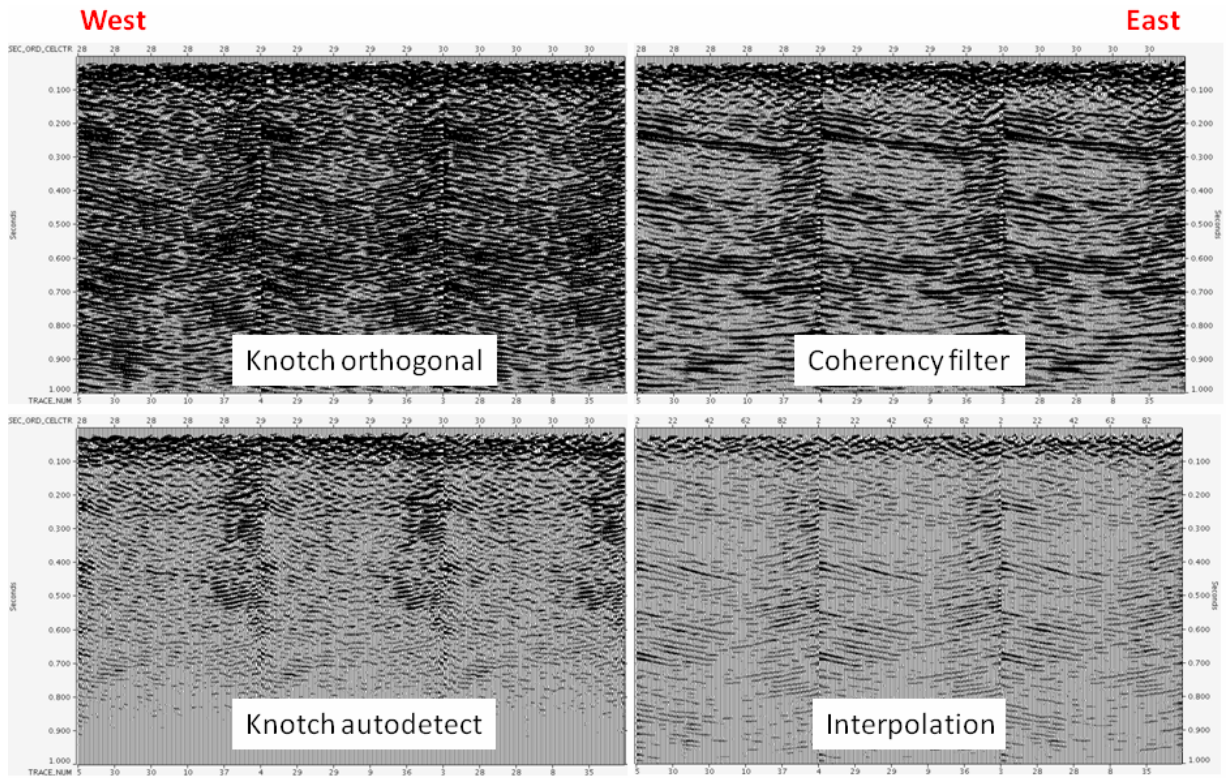


Figure 3.10. Difference between the input and filtered cross-line stacked sections using the four different filters.

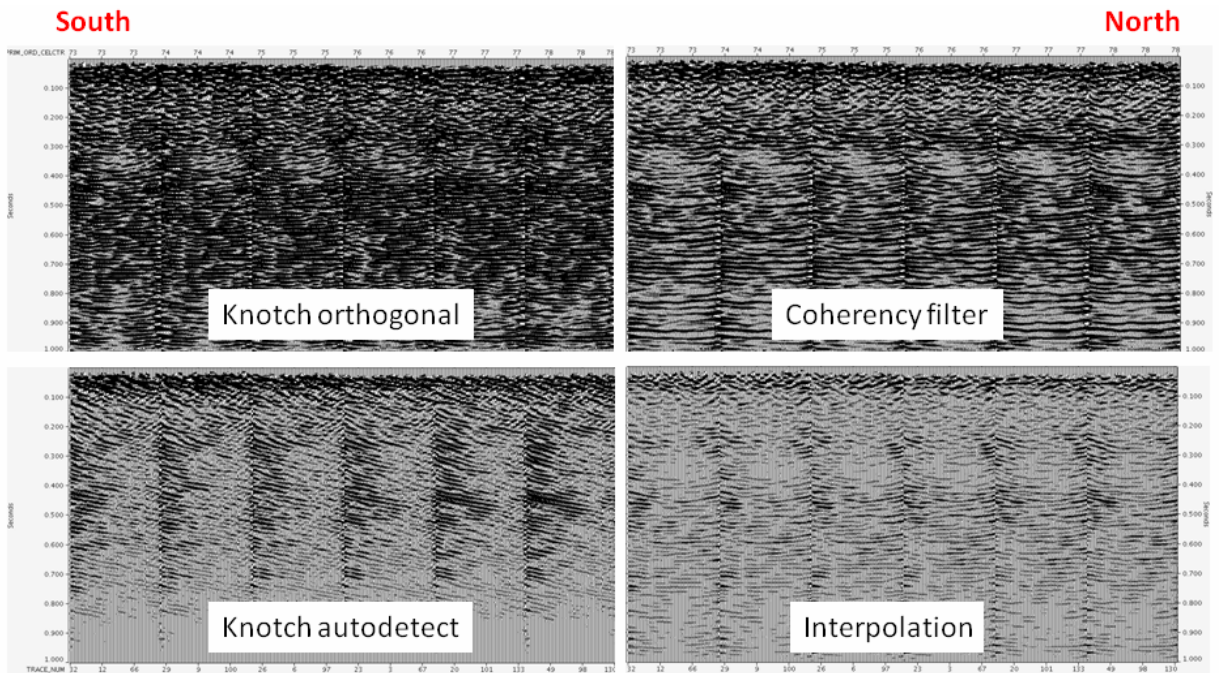


Figure 3.11. Difference between the input and filtered in-line stacked sections using the four different filters.

Figure 3.13 shows the comparison before and after filtering for the same cross-lines and in-lines in section 3.3.2.1. In this figure, only the first 150 ms of the dataset (the area of interest) are shown. The coherency filter improves this shallow part but its effect is too strong at later times, harming the reflections. The K-notch auto-detect option doesn't greatly improve our area of interest: compared with the original dataset, it doesn't seem to make any difference. As in the difference plots, the K-notch orthogonal option and the post-stack interpolator give the best results. The continuity of the reflectors at around 50 and 80 ms is greatly improved, to the point that a "channel-like" shape of the reflectors around 80-90 ms can be observed in the in-line sections. However, if we take a close look at the most shallow reflector on cross-line number thirty, the continuity is better with the trace interpolator. This last observation is local to some lines of the whole volume, but overall these two last methods produce similar results but with amplitude differences.

The amplitude differences are better seen on the time slices displays. Figure 3.14 shows a comparison of time slices at 50, 80 and 90 ms before and after applying different filtering options. The original or raw time slices show no distinguishable features such as channels; they show a pattern more oriented north-south (in-line) which is mainly caused by the acquisition footprint. The coherency filter and the K-notch auto-detect options maintain the north-south pattern, but make it smoother. However, there are still no recognizable events after its application. The K-notch orthogonal option and the trace interpolator make the footprint effect smoother, eliminating the north-south striping from the time slices.

Figure 3.12 shows the F-K spectrum before and after applying a 3D K-notch filter (K-notch orthogonal), which produced the best results among all the options tested. As was pointed out on Figures 3.8 and 3.9, the primary energy is located at the origin but with the application of the filter most of the energy spread out along the wavenumber axis has been removed and now the regular noise pattern is more evident at approximately every 20 wavenumber per cycle.

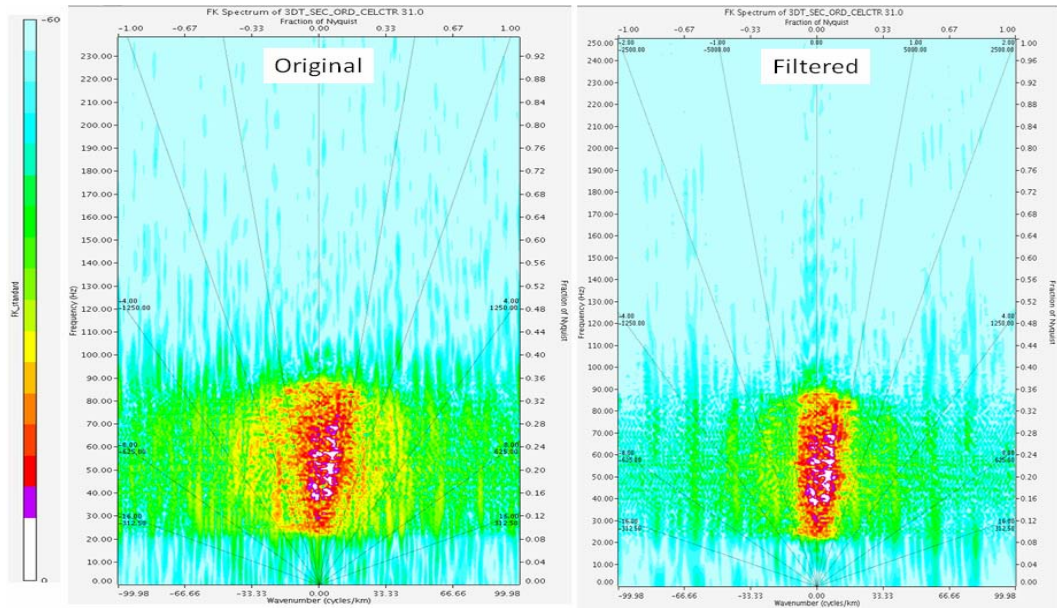


Figure 3.12. F-K spectra of selected cross-line stacked sections before and after the final chosen filtering.

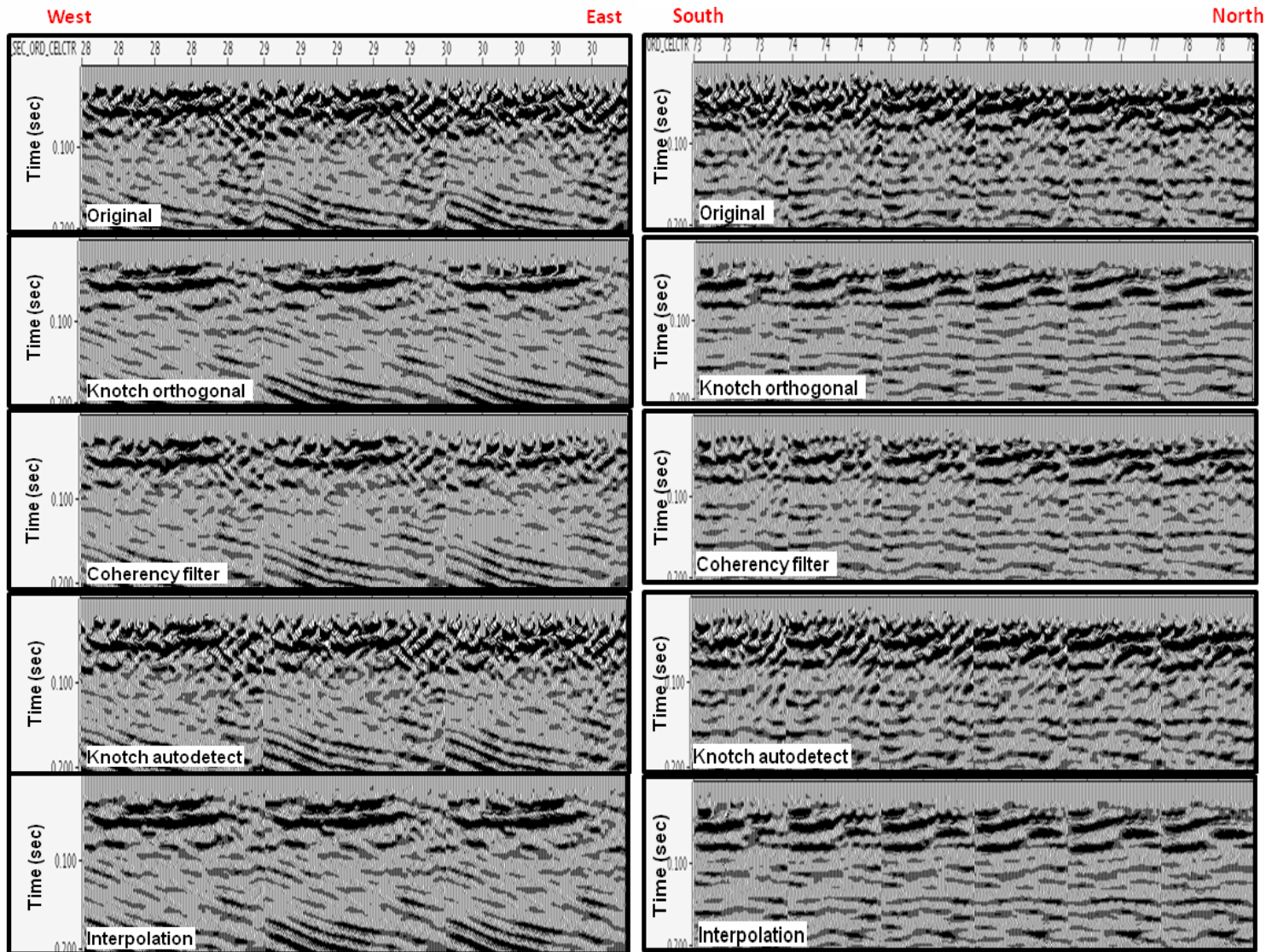


Figure 3.13. First 200 ms of the filtered cross-line (left) and in-line (right) stacked sections, before and after using the four different filters.

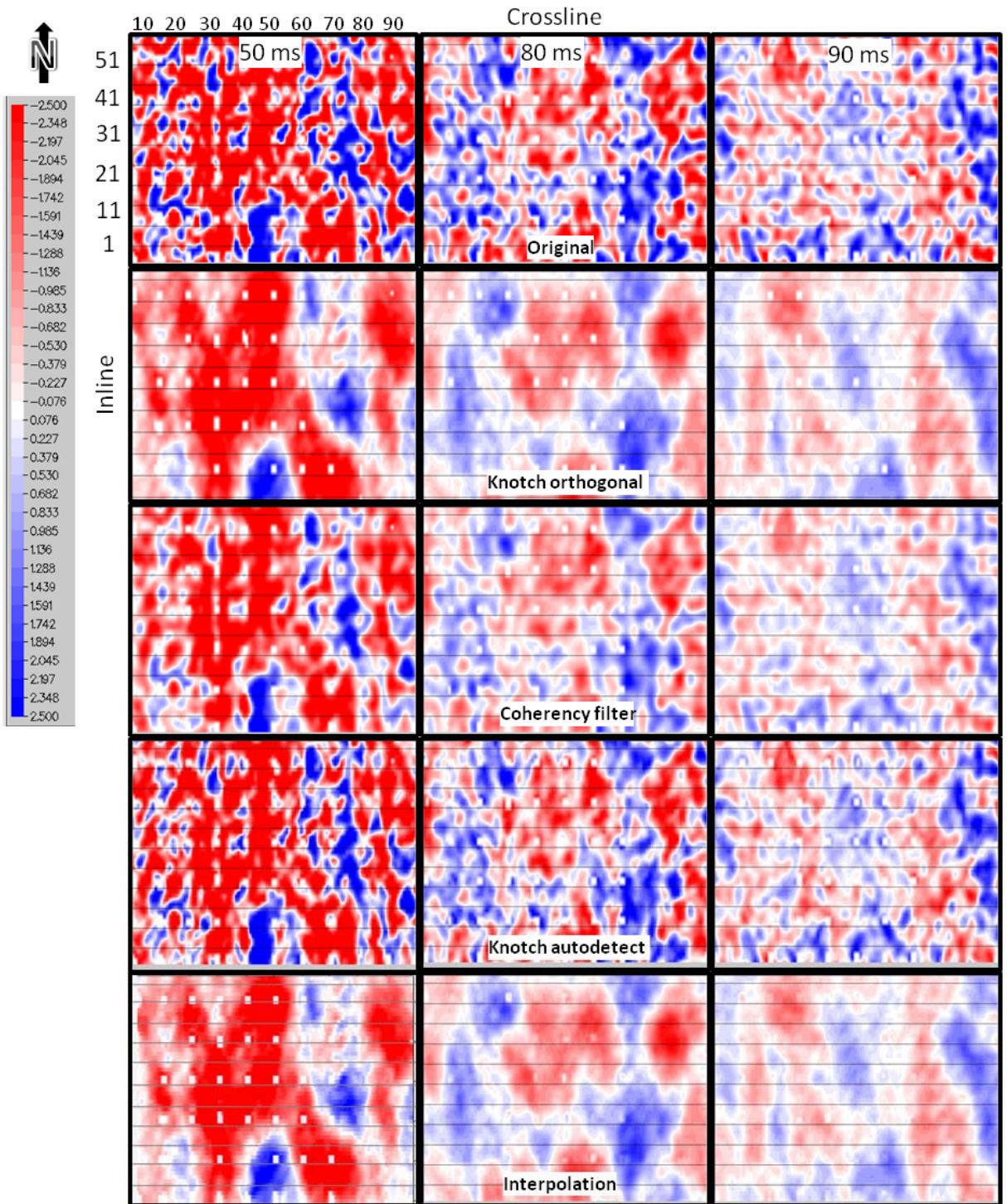


Figure 3.14. Comparison of time slices 50, 80, and 90 ms before and after the four different filters tested on the Priddis dataset (F-K-K filtering: K-notch options 1 and 2, coherency filter and post-stack trace interpolation).

3.4 Seismic attributes from the 3D Priddis volume after footprint removal techniques

The main objective of the footprint removal process was to improve the image of the 3D volume to make it more interpretable. Extracting seismic attributes from the time slices (beyond seismic amplitudes) constitutes a good quality tool to assess whether the image is optimum for observing features that might be revealed with different attributes.

At the Priddis site, time slice images are very useful for seismic interpretation. In this area, the main objectives are to create an image of the near-surface and, in particular, map the shallow stratigraphy and structure (to depths of up to 500m), especially channel systems. Here, we are trying to use seismic methods to characterize the groundwater saturated zones of the Paskapoo formation, which contains complicated sand channel systems.

Figures 3.15 and 3.16 show attributes extracted from the results of the K-notch orthogonal filtered Priddis volume. The attributes in Figure 3.15 correspond to a time slice located at 160 ms with no horizon flattening, and those in Figure 3.16 correspond to a time slice located at 72 ms from a horizon that was flattened at 150 ms.

In the correlation between synthetic seismograms and well-logs created by Miong (2008), the sandstones are represented by positive amplitudes (peaks) and the shales by negative amplitudes (troughs). This information is helpful for correlating the lithological information with the values from the attributes of Figures 3.15 and 3.16. In the amplitude displays for each time slice, there are some positive amplitude bodies that might correspond with observations from the correlations, where the sandstones have positive amplitudes and the shales negatives. In the 160-ms time slice, the continuity attribute shows the amplitude continuity of the reflections; this display shows in more detail some

of the features observed in the amplitude display. The positive values (light blue to pink) in this display correspond with the positive values for the amplitudes (gray to yellow). The second derivative is generally very useful for identifying discontinuities and its positive/negative values should correlate with the positive/negatives for the amplitude. For this time slice, the negative red values match with the green negative values from the continuity and the dark grey negative values from the amplitudes.

For the 79 ms time slice, there is a similar correlation between the three displays, where the positive and negative values for the amplitudes, envelope, and phase correlate.

Some of the events in these attributes show different features such as channel-like events. Without detailed knowledge of the geology and stratigraphy we cannot make definitive interpretations; however, the improved data quality now reveals some fascinating features.

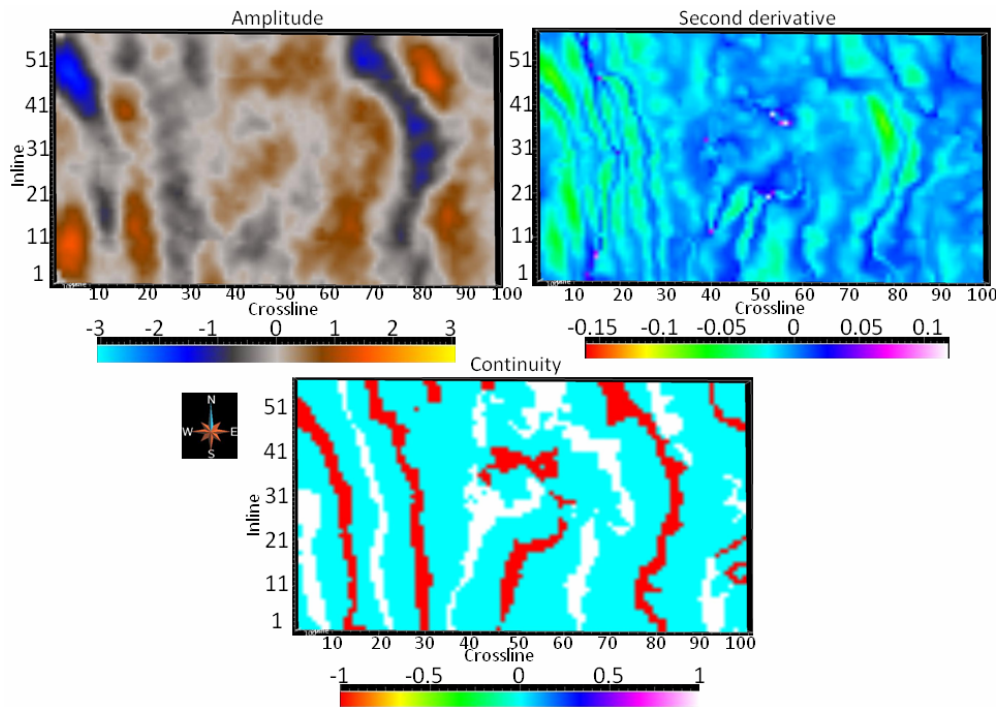


Figure 3.15. Seismic attributes extracted from the Priddis 3D stacked seismic volume. The attributes were extracted from time slice 160 ms with no horizon flattening.

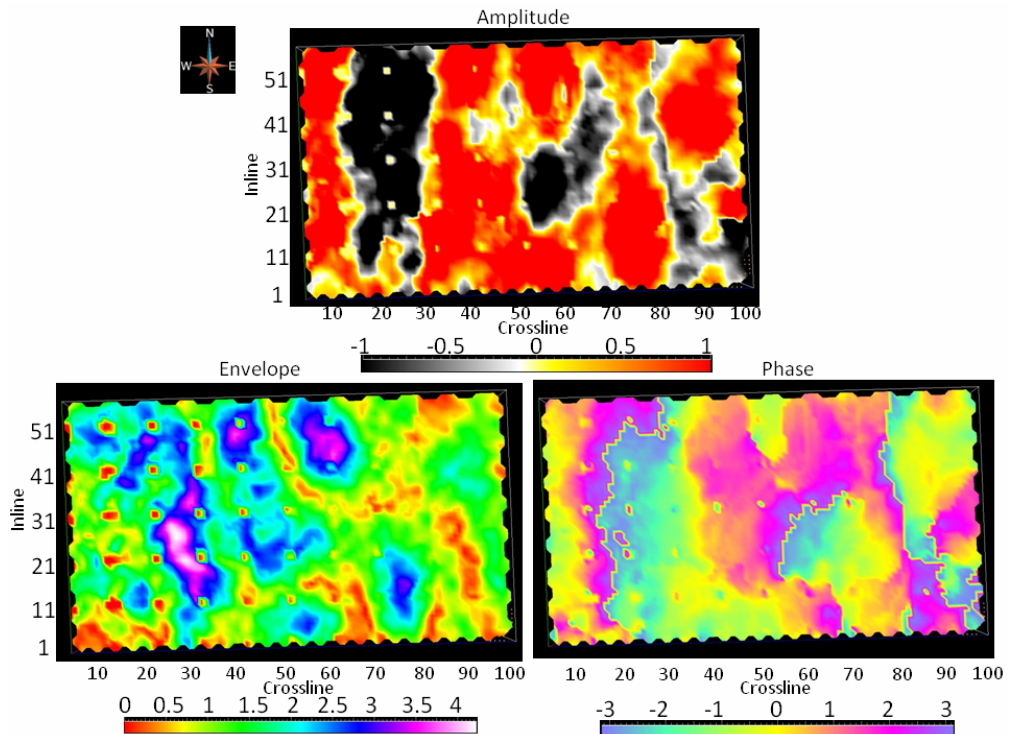


Figure 3.16. Seismic attributes extracted from the Priddis 3D stacked seismic volume. The attributes were extracted from time slice 79 ms, with flattening of a horizon picked at approximately 100 ms.

3.5 Conclusions

We tried to improve the image and continuity of the shallow events using different seismic data processing techniques for post-stack footprint removal in the 3D migrated volume from Priddis, Alberta.

A comparison of stacked sections from the land streamer, planted geophones and the coincident cross-line section from the 3D was done. The stronger reflection events between 75 and 300 ms can be observed in all the sections. However, the 2D lines from the land streamer Test 2 have better resolution and higher frequency content in the first 300 ms of data. However, the 3D cross-line section has better imaging below 300 ms.

An assessment of the acquisition footprint pattern pre- and post-application of the filtering is necessary to identify the characteristics of the footprint pattern and evaluate the results of the filter applied.

A strong linear pattern was more noticeable in the time slices of the cube and in the first 150 ms of the stacked sections. This pattern is likely to be a consequence of the sparse line spacing used during the acquisition.

For the 3D Priddis volume, the footprint pattern is not as evident as in other cases; it is identified as a sort of striping pattern that appears in the first 150 ms of data.

The F-K spectra show regular intervals of weaker energy every 20 cycles/km, this value was corroborated calculating the locations of the aliased energy using the survey recording parameters.

A K-notch with a 1000 ms window and a post-stack interpolator were tested for F-K-K filtering. Of the K-notching methods, the K-notch orthogonal option produced the best results, removing part of the linear noise from the sections. A post-stack trace

interpolator on top of the K-notch filter further improved the continuity of some shallow reflectors at 50 and 80 ms.

The F-K spectra post-filtering shows less energy spread out. However, because of the “smearing” effect of the migration, it is very difficult to remove all the aliased energy without harming the signal.

Using the improved image after filtering, seismic attributes were extracted from the 3D cube. These attributes were used as a quality control tool to assess whether the image was optimal for observing stratigraphic and structural features of interest. Using only the images derived from these attributes, we observed some fascinating features that could be subjects for study in future exploration projects in this specific location.

**Chapter Four: SEISMIC SOURCE COMPARISON FOR COMPRESSSIONAL
AND CONVERTED-WAVE GENERATION AT SPRING COULEE, ALBERTA
Part I: Heavy vibroseis-dynamite.**

In seismic reflection surveys, good quality data is more likely assured by choosing optimum acquisition parameters with respect to the target zone (Scheffers et al., 1997). One of the key parameters is the selection of the appropriate seismic source and its characteristics. This selection should be based upon several criteria which are related to the type of the problem under consideration. Some of the important criteria to consider are the source energy content, which should be large enough so that adequate information is recorded from the desired maximum depth of the survey; and the produced reflection pulse, which should have high and broad frequency content to obtain the required resolution for the exploration of the particular problem. Other selection criteria are related to the signal-to-noise ratio, convenience, safety requirements, and repeatability. Finally, all previous criteria are judged with respect to the total cost of the project and the most appropriate source for the project budget would be selected (Karastathis et al., 1995).

A number of comprehensive source tests have been carried out (Davis and Lawton, 1985; Pullan and MacAulay, 1987; Miller et al., 1986, 1992; Parker et al., 1993; Tilander and Lattimore, 1994; Karastathis et al., 1995; Steer et al., 1996; Scheffers et al., 1997; Bühnenmann and Holliger, 1998; Staples et al., 1999; Bremner et al., 2002; Quigley, 2004; Calvert et al., 2005). These efforts have been mostly geared toward shallow seismic reflection, refraction seismic applications and deep seismic reflection profiling. The most detailed seismic comparison studies have been done by the source comparison

subcommittee of the Engineering and Groundwater Committee of the SEG, a group of shallow-seismic P-wave source owners, the Geological Survey of Canada, and the Kansas Geological Survey. These studies were undertaken at three test sites (New Jersey in 1985; California in 1988, and Houston in 1991), testing between 12 and 26 different sources to try to address some of the questions related with energy, frequency content, signal-to-noise ratio, source wavelet, portability, cost, site preparation requirements, repeatability, environmental damage and constraints, and safety requirements (Miller et al., 1994). The results from these experiments allowed them to conclude that subsurface explosive sources seem to possess the highest dominant frequency, broadest bandwidth, and recorded amplitudes and, therefore, have the greatest resolution potential at these sites.

Other seismic source comparisons, but with deeper objectives that should be mentioned, are the deep reflection surveys in the Williston Basin of Montana and North Dakota. These surveys were carried out by the Consortium for Continental Reflection Profiling (COCORP), with the objective of testing hybrid source imaging of the continental lithosphere. Vibroseis and explosive sources were tested. Traditionally, the vibroseis technique was employed as the primary source in land-based deep profiling; this choice was influenced by the logistical flexibility, uniformity and ease-of-permitting of vibroseis sources. However, after looking at the successful cases where explosive sources were used for crustal reflection programs (Damotte and Bois, 1990; Pfiffner et al., 1988; Finlayson et al., 1990), COCORP decided to try a joint explosive/vibroseis experiment (Steer et al., 1996). The COCORP experiment showed how explosive generated energy decays at ambient noise levels for longer times and depths (35-60 s,

105-180 km) than the vibroseis generated energy (7-9 s, 20-30 km). However, the explosive source energy proved highly variable, with source-to-source ground coupling being a major limiting factor in shot efficacy. The influence of explosive charge size was also tested, concluding that a well placed moderate sized dynamite charge (30 Kg) proved to be as efficient as larger charges (90 kg).

Other source comparisons studies with different geophysical applications include the search for high-frequency sources that will facilitate tomographic studies of potential radioactive waste disposal sites (Bühnemann and Holliger, 1998), and 2D high-resolution surveys (Scheffers et al., 1997). In the first experiment, seven different seismic sources were tested, including minivibrators and explosives; of the seismic sources tested, small explosive charges had the most favourable S/N and favourable characteristics. In the second experiment, explosive sources were tested once again but the novelty is the use ofIVI-mini vibrators, which constituted the first time that this kind of device was used on a large scale in Europe in the high resolution frequency range (Scheffers et al., 1997). This second experiment concluded that for shallow targets (100-400 m) both the vibroseis and the dynamite source give good results; however, dynamite gives a higher penetration than vibroseis data leading to a better imaging of the deeper subsurface (depths greater than 500 m).

Source comparisons between different types of sources (e.g. airgun and dynamite, vibroseis and dynamite), have also looked for improvements in the parameters used (e.g. depth of source, sweep length), chemical composition and equipment design, among others. Seismic explosives have had an extensive testing history; key parameters tested are charge size and depth (Davis and Lawton, 1985; Amano et al., 1994). Innovations

such as the metalized explosives (e.g. family of explosives in which oxidizable metals are added to the explosive mixture) have been introduced in the last six years (Bremner et al., 2002; Quigley and Thompson, 2004).

For vibroseis methods, the attenuation of harmonics through shooting methodology (Bargain, 2006), bandwidth improvement and better source coupling using 80,000 lb vibrators (van Baaren, 2001), and the design of a high-frequency controller to improve the high-frequency performance of the vibrators (Wei, 2007), are some of the most recent accomplishments in the past several years.

Technological advances have improved the performance of the different source types; however, the previous studies have showed clear differences in the source performance due to site condition. The performance of a particular source has proven, in practice, to vary between study areas (Miller et al. 1986; Miller et al. 1992; Pullan and MacAllay 1987; Bühnemann and Holliger, 1998).

From this premise, we want to find the best source under specific conditions and locations. It is therefore useful to conduct a quantitative comparative study of various sources in a particular environment to study in detail the characteristics of each one (Karastathis et al, 1995).

Following the initiatives of previous experiments, the CREWES Project acquired three 2D 3-C lines with different seismic sources (IVI-mini vibroseis, 52,000 lb vibroseis and explosives), receivers and recording systems in January, 2008. One of the main objectives was to investigate the characteristics of three seismic sources at Spring Coulee, Southern Alberta. This chapter describes the analyses done on these three seismic lines

acquired with different sources and discusses the results of the comparison between all of them.

4.1 Multicomponent surface-seismic acquisition

Complementary to P-wave exploration, information extracted from shear waves can enhance the reliability and precision of lithologic and reservoir prediction. However, S-wave sources have been expensive, scarce, and not easily applicable to some environments while S-S seismic sections are often noisy and can have limited resolution, (Stewart et al., 2002).

Converted-wave surveys are the solution when exploration problems demand shear wave solutions (Thomsen, 2001). They are relatively inexpensive, compared to pure shear surveys, and an alternative and effective way to obtain S-wave information. However, in the industry there is still the perception that embarking on multicomponent surveys is a risky and expensive endeavour. Although geology has often played a role, suboptimal equipment, acquisition design and processing have also contributed to this perception.

The advent of 3-component MEMS-based land acquisition systems has led to renewed interest in converted-wave imaging (Calvert et al., 2005). However, there is still a long way to go to improve the quality of our P-S sections, especially on the acquisition side. This is where the determination of optimal recording environments, survey design expertise, source type and associated parameters, and technological advances in equipment, are going to determine the success of converted-wave exploration and the possibility of obtaining more interpretable converted-waves images.

The study of seismic sources for converted-wave generation has not been the subject of much experimentation. Some case studies have highlighted the importance of

low frequencies to obtain good bandwidth in any PS-wave image, even for P-wave objectives with the widening use of acoustic impedance inversions (Calvert et al., 2005). For this reason, more research is necessary to determine which vibrator sweep parameters will provide the best P-S data, how much time should be spent in the low-frequency portion of the sweep, and if cost is not a constraint, which is the ideal dynamite charge, depth size and type to be used. As part of the Spring Coulee experiment, converted-wave data was recorded with the purpose of doing one of the first source comparisons for this type of data, characterizing them and finding the best one for this specific site

4.2 Vibroseis vs. Explosive sources

Dynamite and vibroseis sources are the most widely used onshore seismic sources. The selection of one source in preference to the other is based on multiple parameters that can be categorized as technical (e.g. source charge, frequency content, repeatability) or operational (e.g. environmental damage, safety requirements, portability and costs).

One important factor to consider during the selection is that individual seismic source signals should have a high degree of predictability and repeatability to allow accurate assessment of the charge size and/or vertical stacking requirements (Bühnemann and Holliger, 1998). An analysis of the consistency of the seismic data, in both signal and noise content, generated across multiple shot points can provide insight as to how the field data will interact with later data processing work. Improved shot-to-shot consistency of the generated source wavelet in terms of amplitude and character can benefit data processing especially with the treatment of common-receiver or cross-spread gathers. There is also potential benefit to 4D methods (Quigley and Thompson, 2004). Another important factor is frequency content; successful reservoir delineation depends on spatial

and temporal resolution, and these two parameters are enhanced by high frequencies (Wei, 2007). Low frequencies should also be considered, because they are very important for converted-wave generation (Calvert et al., 2005).

Dynamite sources sometimes yield better signal-to-noise ratio (SNR), deeper penetration and broader frequency content than vibroseis. An advantage of vibroseis sources is that they can cross lines in urban zones and they may be allowed where dynamite is not permitted (Tilander and Lattimore, 1994; Scheffers et al., 1997). Dynamite acquisition requires a larger field crew than vibroseis due to the need for shot-hole drilling, and explosive handling crew on site prior to recording. This is compensated by dynamite's higher and more stable production rate-about 1.5 times faster than vibroseis due to shorter registration times, i.e., no sweep).

For shallow targets (100-400 m) both vibroseis and dynamite sources often give good results. However, dynamite can often provides deeper penetration (around 500 m deeper) than vibroseis data leading to a better imaging of the deeper subsurface (Scheffers et al., 1997).

The choice of vibroseis technique is largely influenced by logistical flexibility, uniformity, easier permit restrictions and safety considerations (Brown, 1986). Vibroseis shows lower overall amplitudes and corresponding shallow decay to ambient noise levels or background (Steer et al, 1996).

The most effective vibroseis acquisition method for preserving data quality is dictated by two key parameters: source signature repeatability and magnitude of the generated harmonics. For a given source effort, the relative importance of these two parameters, along with the effectiveness of the processing methods used to compensate

for the lack of source repeatability and/or energetic harmonics, determine the most suitable method (Bagaini, 2006). Vibrators must be capable of generating the required frequencies with sufficient fundamental force to retain reflection signal above noise at the objective target depths. However, because of the limitations existing in mechanical and hydraulic components, a vibrator can only maintain sufficient force amplitude in a certain frequency range, generally from 10 Hz to 80 Hz (Wei, 2007).

The signal-to-noise ratio and bandwidth of explosive-sourced seismic data are the direct result of the properties of the explosives used and the near-surface conditions. It has been reported that the amplitude and signature of seismic waves generated with the dynamite are affected not only by the charge size but also by the depth of the energy source (e.g., Winkel, 1989). Multivariant testing has confirmed that the efficacy of seismic explosives can be improved in many environments. Analysis of these datasets suggests that there are specific explosive characteristics that can, if properly combined, change the amount of signal energy produce by a given charge. This reinforces the contention that the design of the explosive utilized is critical to the ultimate quality of seismic data (Bremner et al, 2002).

For explosive sources, results have shown that an inadequate charge results in poor deep data, whereas too large a charge results in a lower signal-to-noise ratio and degradation of shallow events (Davis and Lawton, 1985).

Data acquired with downhole explosive sources at sites with a shallow water table and fine-grained sediments are most likely to possess the highest frequencies and broadest bandwidth (Miller et al., 1994).

If test shots are analyzed, an improved bandwidth and S/N could be achieved with a dynamite source but sometimes the possible improvement in P-wave image quality is not considered sufficient to merit the increased survey cost. For converted-wave generation low frequencies are very important, so explosive sources are ideal, but if there is a constraint for cost or regulatory reasons, vibrators could be used if sufficient time is spent in the low-frequency portion of the sweep (Calvert et al., 2005)

Deep reflection seismic studies of the lower crust revealed that, on a shot-to-shot basis, more energy from the explosive sources penetrates through the shallow sediments to the lower crust (35–60 s two-way traveltime, 105–180 km depth) than from the vibroseis source. This is equally true for smaller (9.5 kg) and relatively large (90 kg) explosive charges (Steer et al., 1996; Bühnemann and Holliger, 1998). Based on visual inspections made at the shot-gather level to determine signal strength, shot-to-shot variation, frequency content, and any variations in noise; the explosive data appear generally superior to vibroseis data, this is because the vibroseis method was developed as a “low impact” source that takes advantage of common depth point (CDP) redundancy to achieve useful S/N levels at depth (Schrodt, 1987; Brocher and Hart, 1991). Comparison of stacked seismic sections from both sources has indicated that the vibroseis is superior, particularly in the shallower portions of the section (7-9 s two-way traveltime, 20-30 km depth). The higher redundancy and more uniform source-to-ground coupling of vibroseis sources facilitated static corrections and subsequent stacking enhancement. The inferior quality of the dynamite sections could be the consequence of characteristic source-to-source variability and source-to-ground coupling (Yilmaz, 1987). We know that vibroseis data is bandwidth-limited by the correlation process. However,

previous studies have shown that observations for shot gathers and stacked sections do not change if the explosive data is band-pass filtered to match the vibroseis bandwidth (Steer et al, 1996).

In an area of rough surface topography and outcropping high-velocity carbonates a high-fold vibroseis acquisition method demonstrated clear advantages in terms of signal quality and reduced cost over conventional, lower-fold dynamite acquisition. A comparison of shot gathers from the two acquisition methods showed that the vibroseis technique resulted in an increase in relative amplitude of reflection energy versus groundroll and linear noise trains. This increase may be due to improved source coupling, noise cancellation due to multiple sweeps, source moveup, and the statistical advantages of cross-correlation. For this case study (Tilander and Lattimore, 1994), the cost per kilometre of the high fold vibroseis program was nearly half that for conventional dynamite (\$23,000/km for the vibroseis vs. \$38,000/km for the dynamite).

4.3 The Spring Coulee seismic experiment

As part of the research campaign undertaken by the CREWES Project during 2008, a 3-C 2D seismic survey was acquired on two sections of land where the mineral rights are owned by the University of Calgary (Ostridge and Stewart, 2008). The sections are located in Southern Alberta (14 and 23-004-23W4; Figure 4.1).

This seismic experiment was a joint effort between ARAM, CGGVeritas, The CREWES Project, and the University of Calgary. The objectives of the test included seismic receiver and source comparison, as well as an exploration project motivated by the hydrocarbon production potential of the area.

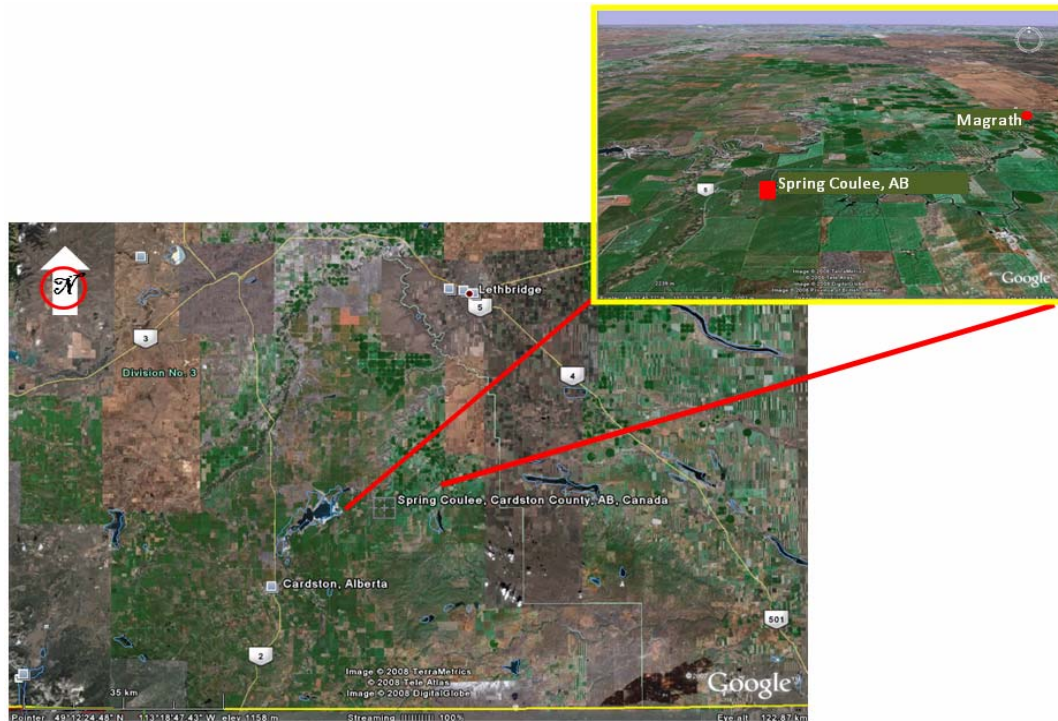


Figure 4.1. Aerial photograph showing the location of the study area. Photograph from Google Earth.

4.3.1 Description of the survey

The Spring Coulee datasets were recorded in a 3D manner due to the simultaneous recording of the multiple shot and receiver lines (Figure 4.2). Two different recording systems, three types of receivers, and three types of sources were employed on the survey. Geophone data was recorded using an ARAM Aries system and the accelerometers on a Sercel 428XL system. Both receivers and recording systems acquired data produced by dynamite, heavy vibroseis and an IVI-minivibroseis as seismic sources.

The geophone sensors were SM7 10 Hz 3C and SM24 10 Hz 3C elements, and the accelerometers were DSU3 MEMS. The sources were 52 dynamite shot points (2 kg at 15 m depth), 657 vibrated points with two 48,000-lb vibroseis units and 134 vibrated points with one IVI Envirovibe (18,000 lb).

4.3.1.1 The ARAM Aries spread

The data used in the source comparison was that recorded with the ARAM Aries system and SM7 10 Hz 3C geophones. A detailed description of the spread is presented below.

The Aries spread consisted of five lines, two of them receiver lines referred to as lines 1 and 3, and three source lines referred to as lines 2, 4 and 6 (Figure 4.2). Line 1 has 652 receiver points, using SM7 10Hz 3C elements in an ARAM-manufactured case. Line 3 has 40 receiver points spaced every 10 m, with SM24 10Hz 3C elements located in the middle of the line (168 to 208). For the source lines, line 2 corresponds to the 62 vibrated points of the IVI Envirovibe (18,000lb) with a 4-times vertical stack sweeping a 10 to 200 Hz sweep with an 11 s listening time. This source was used to test the line and provide shallow data. Line 4 corresponds to the 196 vibrated points from the two 48,000-lb vibroseis units with a 4-times vertical stack sweeping 4 to 130 Hz with a 12 s listening time. The last source line, line 6, is comprised of 54 dynamite points at depths of 15 m, located right in the middle of the receiver lines.

The receivers were located every 10 m and the sources every 30 m, and the lines were separated approximately one metre.

4.3.1.2 Coincident source points of the ARAM Aries spread for the three source types

All three lines yielded only 54 coincident source locations (Figure 4.3). These points were located approximately in the centre of the full length six-kilometre line. The comparison datasets were divided into two groups, the division based on the number of traces per shot and dead traces. Because the mini-vibroseis (IVI Envirovibe) was recorded while the receiver line was still being laid out as a test line, not all the 652 receivers were in place, leaving dead or very noisy traces. Only 470 traces were kept and

for some shot gathers a quarter of the total traces were dead or had to be killed because of unplanted receivers.

The first group consists of the comparison of the heavy vibroseis versus dynamite sources with a maximum of 652 traces and good quality data. The second group will be presented on Chapter 5, and consists of the heavy vibroseis, dynamite, and mini vibroseis sources with a maximum of 470 traces, and with the same dead traces to make an exact comparison of the datasets. The data of the mini vibroseis does not have the same quality as the other two sources but can still be used for comparison in the shallow region of the data.

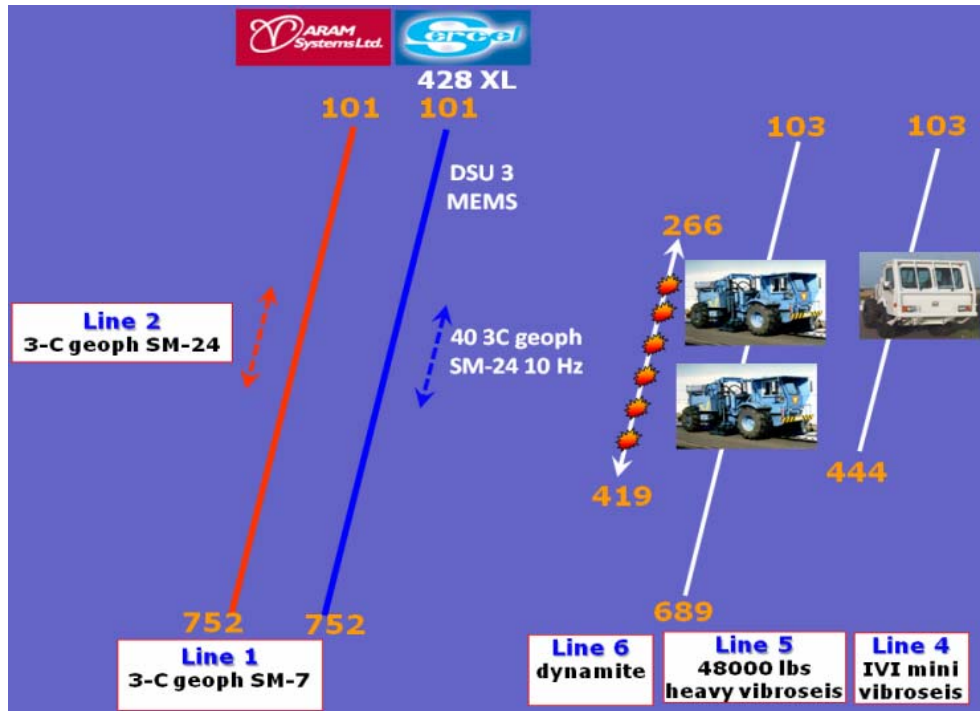


Figure 4.2. Schematic diagram of the Spring Coulee experiment. Details of the ARAM layout are shown as well.

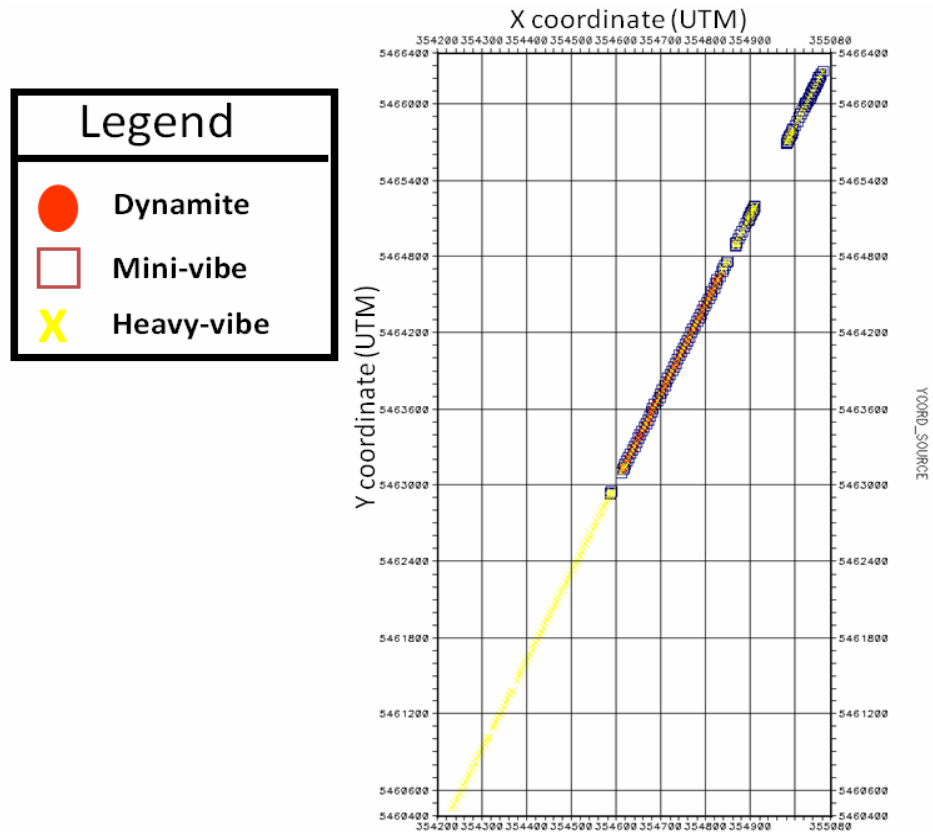


Figure 4.3. Shot locations of dynamite, mini-vibe ad heavy-vibe sources.

4.4 Conditioning of the data for the source comparison analysis

After acquisition, the coincident source points were passed through the same processing sequence using identical processing parameters in most cases. The survey geometry resulted in a maximum fold of 200 for the six-kilometre heavy vibroseis line and a maximum of 50 for the coincident sources lines (Figure 4.4).

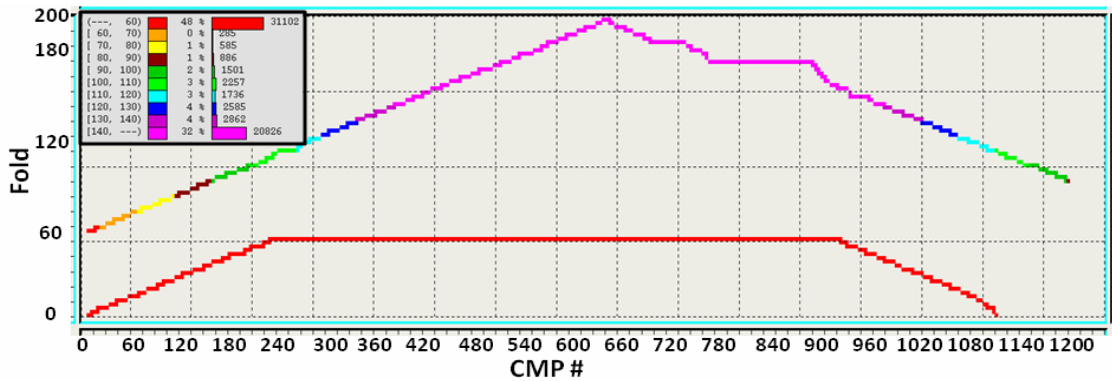


Figure 4.4. Fold coverage for the Spring Coulee full-length heavy vibroseis line (multicolour line) and for the segment of the line with coincident source locations (red line).

The processing parameters were designed for the full-length heavy vibroseis line and tested on the shorter lines used for the source comparison. In general, the quality of the data was very good: clear reflections can be observed in the raw data up to 2.2 s and stronger surface-waves were observed for the dynamite dataset.

4.4.1 Vertical Channel

Important processing steps are outlined in Table 4.1. The processing sequence used for these datasets emphasizes noise rejection techniques and statics.

The processing parameters were designed on the heavy vibroseis dataset and almost identically applied on the source comparison datasets except for the source statics and the surface-consistent amplitude compensation (SCAC) that were calculated individually for every source type. The same applies to the velocities, receiver statics and

any other parameters used on the noise attenuation flows. As an extra step to allow a one-to-one comparison, the shorter lines for the source comparison were trace selected and edited to have common live and dead traces, and phase and amplitude matched to the heavy vibroseis dataset.

1. Assign geometry
2. Trace editing : kill bad and noisy traces
3. True amplitude recovery: time function gain ($t^{1.5}$)
4. Signal enhancement (noise rejection): FXCNS + AAA + least-squares filters
5. Surface-consistent deconvolution: 4 ms gap, 80 ms operator length, 2 windows
6. Sorting the data to common receiver domain
5. Signal enhancement (noise rejection): AAA
6. Velocity analysis
7. Refraction and elevation statics: calculated using EGRM and elevations
8. Residual statics: two passes (max shift 36 and 24 ms), calculated using Miser®
9. Velocity analysis
10. Sorting the data to common midpoint domain
11. Signal enhancement (noise rejection): RNA+AAA
12. Velocity analysis
13. Surface consistent amplitude compensation (SCAC)
14. Signal enhancement (noise rejection): AAA
15. Phase and amplitude matching: dynamite and Envirovibe to heavy vibroseis
16. NMO correction
17. Automatic gain control: 500 ms
18. Time-variant filter
19. NMO correction
20. Top mute
21. CDP stack
22. Additional processes: random noise attenuation filter

Table 4.1. Main processing steps for the heavy vibroseis vertical channel data.

The static solution for these lines was an important factor to be corrected because of the 70-metres change in elevation between the north and south sections of the line. The raw shots show high-amplitude, low-velocity surface-wave noise dominating the near offsets and random noise in the deeper parts (Figure 4.5a). The datasets were processed as accurately as possible to attenuate the noise, enhance coherency, resolve the statics problems and determine velocity models for stacking.

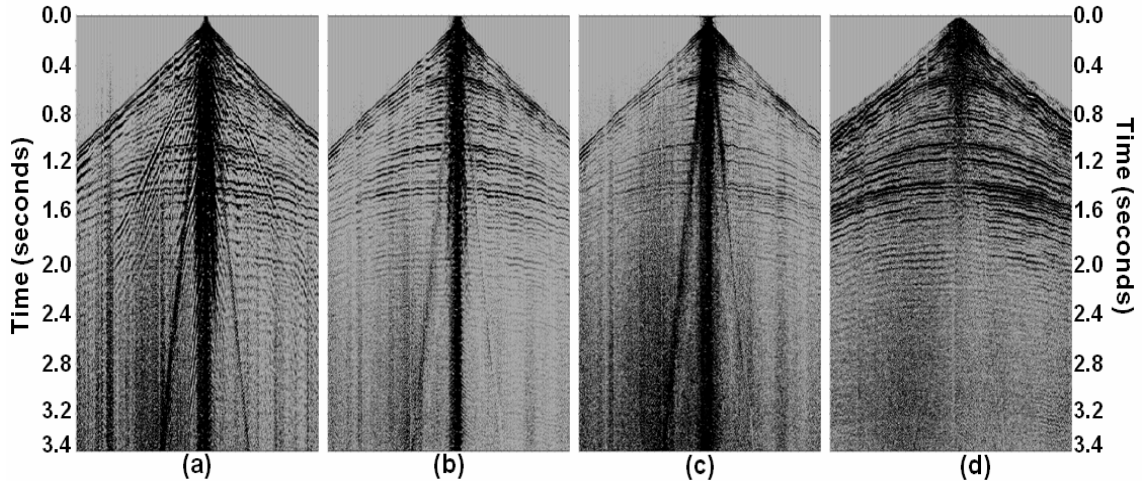


Figure 4.5. Common source gathers for the P-wave full-length heavy vibroseis line: (a) raw data, (b) pre-deconvolution noise attenuation, (c) after deconvolution, and (d) final gather after all passes of noise attenuation.

A refraction solution was derived using the extended generalized reciprocal method (EGRM) on the first-break traveltimes, removing the static inconsistencies observed and enhancing some of the reflections. We also applied two passes of residual statics later in the processing flow allowing a maximum shift of 36 and 24 ms. The improvement caused by the refraction and reflection statics was evaluated on the output of the first noise rejection flow, stacked with the first pass of velocities that were picked, allowing us to see more clearly the reflections of the area. To address the problem of noise several passes of signal enhancement techniques were applied at different stages and in different domains during the processing (Table 4.1). The first pass was done prior to deconvolution, targeting surface-wave noise, coherent and random, as well as some linear noise such as airblast. The noise attenuation techniques of the first pass were applied in the shot domain and included an f-x coherent noise attenuation filter (FXCNS) and a band-limited f-x random noise attenuation filter (AAA or anomalous amplitude attenuation). The noise was removed subtracting the noise model through least-squares adaptive filters, divisions and direct subtractions. Figure 4.5(b) shows a shot gather

before and after the first noise attenuation pass. The explanation of how this technique works and how it was designed and applied for our specific case study is given in the description of the P-wave processing flow in chapter 2. The optimal parameters for the low- and high-pass velocities and frequencies, low- and high-stop velocities, and frequencies on the FXCNS were 600-2500 m/s for the pass velocities, 475-2750 m/s stop velocities, 3-20 Hz pass frequencies and 1-25 Hz cut frequencies. The AAA was calculated and applied to a frequency band of 0-125 Hz, trying to remove the high-frequency random noise and amplitude spikes that make it difficult for other techniques to differentiate between signal and noise.

Deconvolution was the next step, acting as an effective filter for some of the remaining surface-wave noise and improving the resolution of the data. A surface-consistent gapped deconvolution was used with a gap length of 4 ms and an operator length of 80 ms, calculating the operators in two windows. The result of the deconvolution on one of the shot gathers can be seen on Figure 4.5(c).

Velocity analysis for these datasets was an easy task because of the good signal-to-noise ratio. In total, three velocity analyses were completed for this data: after deconvolution, statics, and a final noise attenuation pass. A second pass of signal enhancement, divided in two parts, was applied in the common receiver and common midpoint domains. The first part was done in the common receiver domain because this is where the noise looks more random and weaker. The noise model created with a random noise attenuation module was divided from the input dataset. For the second part, the data was sorted to common midpoint order. In this domain, ten consecutive passes of the band-limited f-x random noise attenuation filter (AAA) were used. The filters were

designed to work in 25-Hz frequency bands (e.g. 0-25 Hz, 20-45 Hz, 40-65 Hz) with an overlap of 5 Hz so we could control the strengths of the threshold values at different times.

Up to this point only an exponential gain amplitude compensation method has been applied to the data, and even with this kind of gain the results look unbalanced as a consequence of the coherent and random noise on the raw data. To try to balance the amplitudes, a surface-consistent amplitude compensation (SCAC) was calculated and applied to the data; by using this method, we were compensating for shot, detector and offset amplitude variations caused by acquisition effects and not a consequence of the subsurface geology. In applying the SCAC, we are trying to take all the datasets to the same RMS amplitude level, so they become comparable.

In the presence of some high amplitude spikes, SCAC adds some extra noise to the data, so a noise rejection technique to eliminate these new spikes is necessary. The third pass of signal enhancement was applied after SCAC in the CMP domain. Five consecutive passes of the band-limited f-x random noise attenuation filter (AAA) designed to work in the high frequencies (80 Hz to Nyquist) were applied to attenuate these high amplitude spikes.

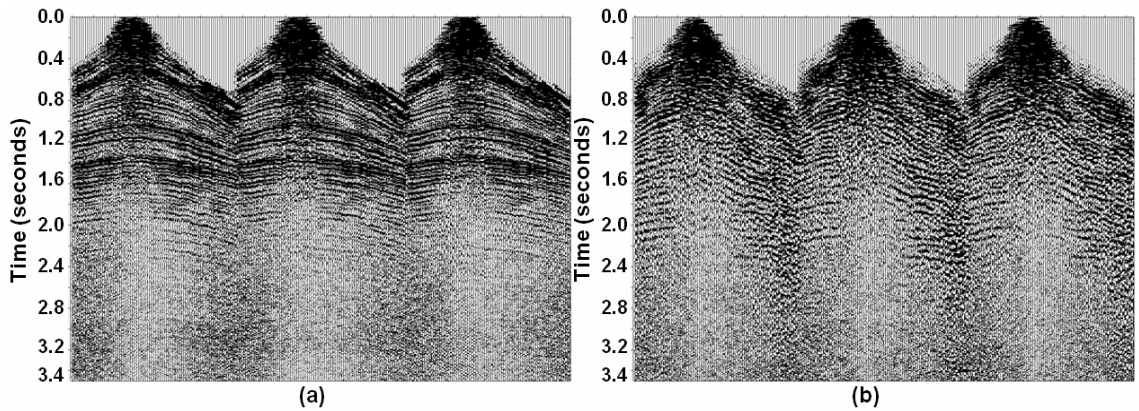


Figure 4.6. Final CMP for (a) the vertical-component and (b) the radial-component of the full-length heavy vibroseis line.

The results of the final noise attenuation pass can be seen in Figure 4.5(d). Here we notice how most of the low and high-frequency coherent noise has been eliminated, especially at times later than 1.6 s, which is the basement for this area. Processing for early times and near offsets, it was a compromise between keeping signal and removing noise, so care was taken to apply the same noise rejection techniques but not as aggressively as for longer offsets and later times. The dominant random noise at the deeper parts of the section was almost entirely removed. Most of the high-amplitude spikes and traces were balanced in relation to the surrounding traces. The amplitude balance revealed reflections that could not be previously seen at longer offsets and deeper times.

An example of some of the final CMP gathers is shown in Figure 4.6(a). The same observations made for the shot gather apply to these CMP gathers. Maybe the random noise still left is more evident in this domain as well as some of the remaining noise at the near offsets. Overall, the target zone (500-1500 ms) looks well balanced and shows strong reflections.

The final full-length heavy vibroseis line stacked section generated with best velocities, final mutes, statics applied and final noise attenuation is shown in Figure 4.7. The same processing sequence and parameters employed for the full-length heavy vibroseis line were used for the shorter source lines for comparison on a one-to-one basis. The comparative analysis on the datasets is presented in next section.

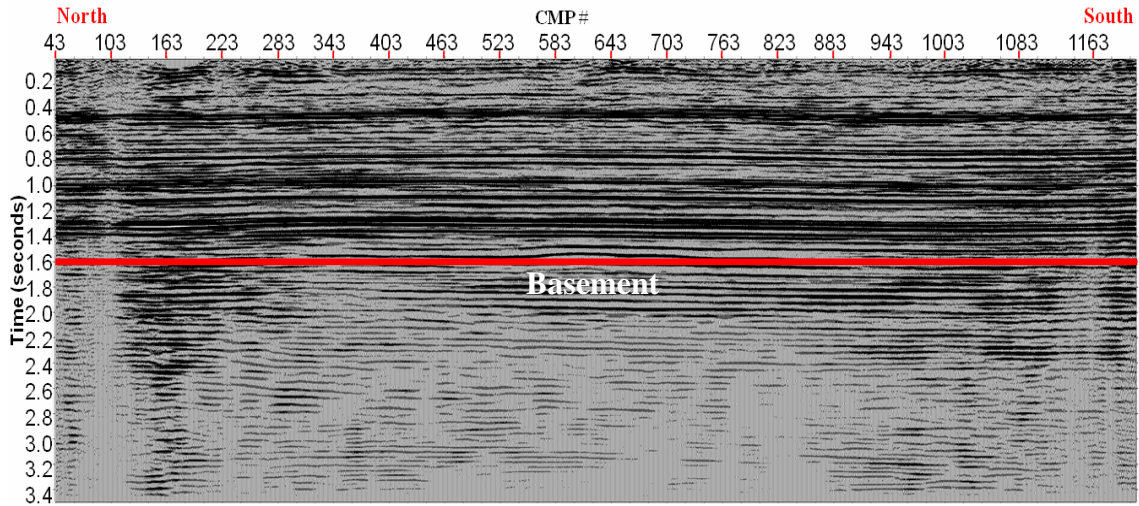


Figure 4.7. Final vertical-component stacked section with the best output from noise attenuation, final stacking velocities and mute for the full length heavy vibroseis line.

4.4.2 Horizontal Channel

The Spring Coulee P-S datasets were 6 seconds long for the heavy vibroseis and dynamite lines, and 3 seconds long for the mini vibroseis line. This last line was shorter because it was recorded as a test line. However, for shallow data analysis, it still could be used even for the comparison of P-wave sources for converted-wave generation.

The P-S datasets had lower signal-to-noise ratios, reduced bandwidth and larger receiver statics compared to the compressional data. Because of these and other factors, the horizontal channel data required several additional processing steps that were not required for the vertical channel data. Important processing steps for the horizontal

channel are listed in Table 4.2. As can be noticed most of the same processes applied for the P-wave were applied for the converted-wave with similar parameters.

1. Assign geometry
2. Trace editing : trace renumber, kill bad and noisy traces
3. True amplitude recovery: time function gain (t^1)
4. Signal enhancement (noise rejection): FXCNS + AAA + least square filters
5. Surface-consistent deconvolution: 4 ms gap, 80 ms operator length, 2 windows
6. Sorting the data to common receiver domain
5. Signal enhancement (noise rejection): AAA
10. Sorting the data to common midpoint domain
11. Signal enhancement (noise rejection): RNA+AAA
12. Velocity analysis
13.Surface-consistent amplitude compensation (SCAC)
14. Signal enhancement (noise rejection): AAA
7. Statics update: update headers with P-wave refraction source statics and residual statics
9. Receiver statics: calculated using Miser®
2. Bin data by CCP: time-variant CCP binning (Thomsen vels depths method)
10. Sorting the data to new “common midpoint” order
15. Phase and amplitude matching: dynamite and Envirovibe to heavy vibroseis
16. NMO correction
17. Automatic gain control: 500 ms
18. Time variant filter
19. NMO correction
20. Top mute
21. ACP stack
22. Additional processes: random noise attenuation filter

Table 4.2. Main processing steps for the heavy vibroseis radial channel data.

An example of one of the common source gathers and its evolution from raw to final result as it was passing through the different processing steps is shown in Figure 4.8. After all the noise attenuation steps (Figure 4.8d), the shot gathers reveal some reflections and most of the random and coherent noise has been removed from them.

An example of some of the final CMP gathers is shown on Figure 4.6(b). Comparing them with the vertical-component ones, we see that the data quality is not as good and is noisier-reflections could only be observed up to 2.5 s. This last observation is better seen on the final P-S stacked section shown in Figure 4.10 and later sections.

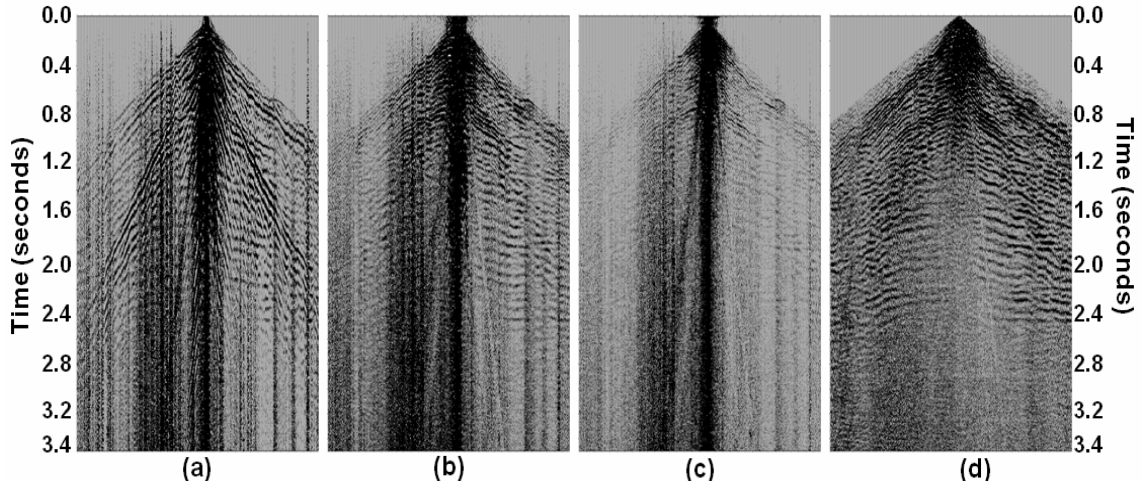


Figure 4.8. Common source gathers for the radial-component full-length heavy vibroseis line: (a) raw data, (b) pre-deconvolution noise attenuation, (c) after deconvolution, and (d) final gather after all passes of noise attenuation.

Receiver statics are of key importance in processing converted-wave data. Shear wave statics are almost always larger than compressional wave statics, sometimes by more than an order of magnitude (Lawton and Harrison, 1992). Receiver statics were resolved independently from shot statics using a separate method. Figure 4.9(a) shows common receiver stacked traces for the heavy vibroseis radial channel data. Each trace has a maximum fold of 196. Reflector continuity is not excellent due to receiver statics. Continuity improved after applying the MISER algorithm to resolve the receiver statics. This method tries to align all the reflections across a large time window and not only one event as in the hand statics method. This tool works by first stacking together a user-defined number of traces from the original receiver stack to create a model trace, then correlating the model trace against each trace in the section over a user-defined time window. The time of maximum correlation of each trace with the model trace was applied as a static correction. Figure 4.9(b) shows the receiver stacked traces after event alignment for reflections between 200 and 2400 ms. Reflected events exhibit improved continuity compared to the initial receiver statics stack (Figure 4.9a).

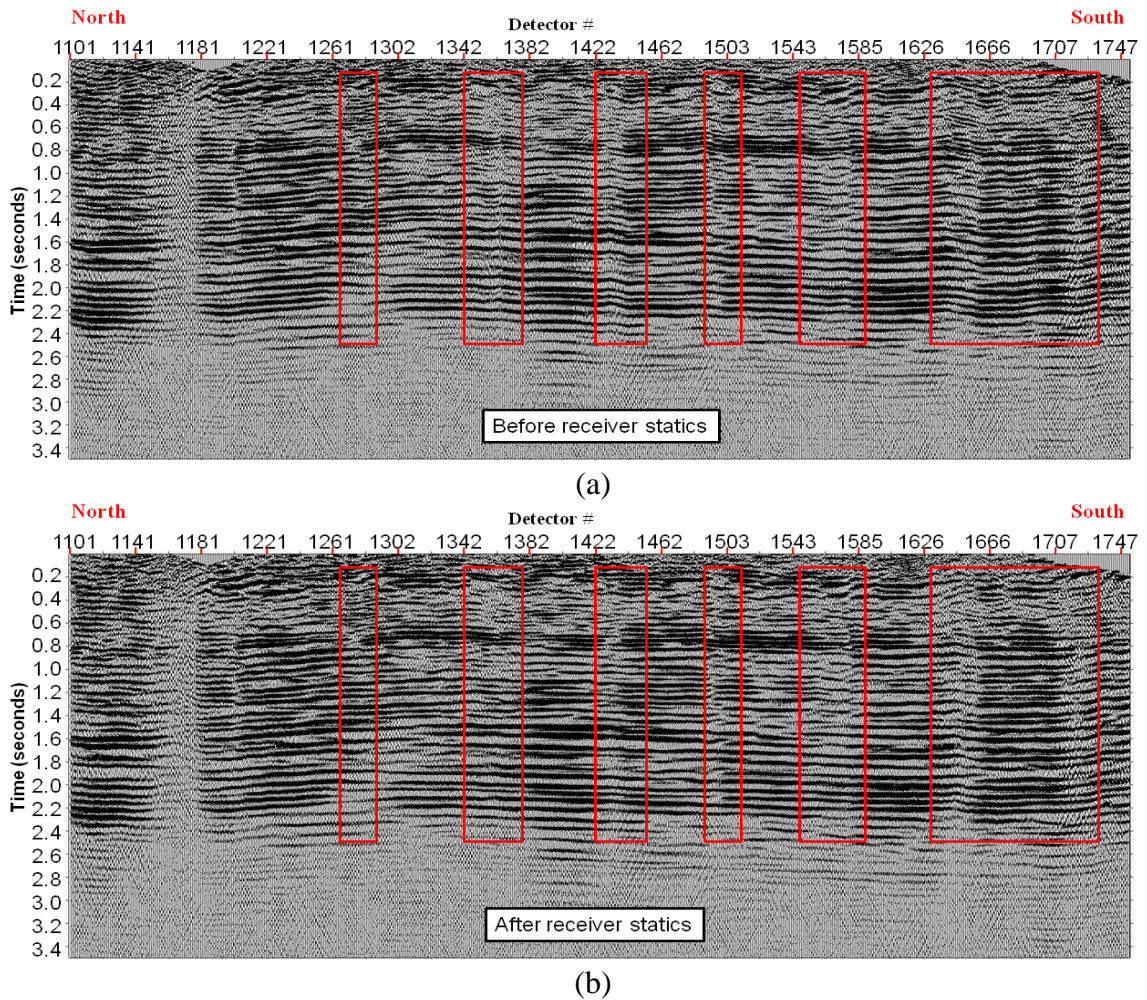


Figure 4.9. Common receiver stacked section before and after receiver statics. The red rectangles show areas where reflector continuity has improved due to the receiver statics.

The datasets were binned to a 5-m ACP spacing for the time-variant binning (Thomsen, 1999). Eta values were picked in an effort to include the effect of higher-order moveout on the velocities and improve the binning. However, for this dataset the eta values were relatively small (3-6 %) and did not cause any major improvement, so they were not used.

The final converted-wave stacked sections, generated with best velocities, final mutes, statics applied, and final noise attenuation datasets for both lines, are shown in Figure 4.10. As with the vertical-component, the same processing sequence and almost

all parameters were used for all datasets to be able to compare them on a one-to-one basis. The comparative analysis on the datasets is presented in next section.

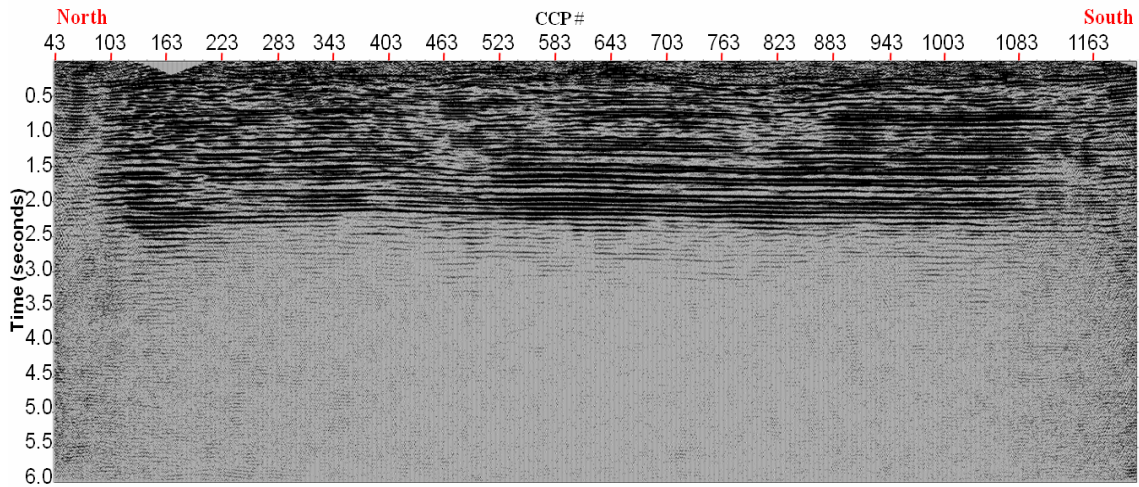


Figure 4.10. Final radial-component stacked section with the best output from noise attenuation, final stacking velocities and mute for the full length heavy vibroseis line.

4.5 Comparison and analysis of the source test datasets

The analysis of the 54 coincident locations for the three types of sources was divided in two parts, each of them corresponding to the two groups presented in the description of the coincident datasets.

An important aspect of a one-to-one comparison is the similarity between the datasets. By the term “similarity” we are referring to the same conditions. For our type of comparison, we are expecting datasets that were acquired at the same time, with the same geometry, fold, receiver and source spacing, and recorded with exactly the same recording system to exhibit as close to equivalent conditions as possible. Usually it is difficult to gather all these conditions at the same time, but the Spring Coulee experiment meets almost all of these conditions with only some modification needed to make these datasets optimal for comparison.

The only requirements left to meet for the comparison were related to seismic processing. Different seismic sources generate wavelets that differ in phases and amplitudes; some of these wavelets are not necessarily zero phase as it is expected by some processes such as deconvolution. Phase and amplitude matching statistical analysis take care of these differences. They are usually necessary while merging seismic surveys acquired in different environments, with different types of sources, receivers, and recording systems, or over different periods of time, such as 4D surveys. In our case, we want to correct for the differences attributed to the use of different sources.

All the datasets were matched to the heavy vibroseis data. The amplitude and phase matching methods were done separately. The survey amplitude matching consisted of an automated method to create a residual amplitude compensation function derived from the division of the RMS amplitude compensation function calculated within a discrete time window from each survey. The comparison survey is then multiplied by this residual function so the amplitudes are scaled to closely match the amplitudes of the target survey.

The phase match was designed as a “global matching operator” — this refers to the application of a single constant filter to every trace of the survey to better match datasets. The filter was derived statistically by comparing the datasets themselves. A cross-correlation between both datasets was calculated using a portion of the stacked sections over a window with good signal-to-noise ratio. A shaping filter was designed to match the zero-phase equivalent of the cross-correlation to the cross-correlation between both datasets. This filter was convolved with the dataset to match the target survey, correcting for the phase component.

A comparison of a small portion of the stacked sections before and after phase matching for the three types of sources is shown on Figure 4.11.

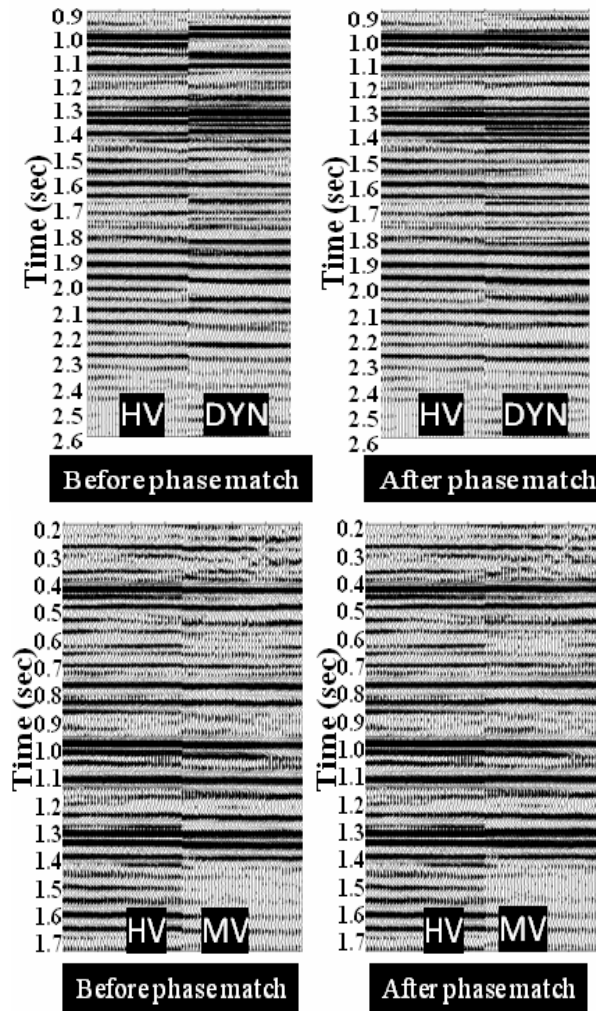


Figure 4.11. Comparisons of a portion of the vertical-component sections for the heavy vibroseis, dynamite and mini vibroseis sources before and after phase matching. All the datasets were matched to the heavy vibroseis data.

4.5.1 . Part 1: Heavy vibroseis-dynamite comparison

4.5.1.1 Raw data: Characteristics of different types of signal and noise

For a better understanding of the differences between the various sources, the most significant signal and noise waves shall be described as they were observed in the raw data. Consistency from shot to shot along the line is another characteristic that should be considered as it reflects how variable the source is and how dependent it is on the near

surface conditions. This is also an important point to take into account for future 4D methods and because it can benefit data processing especially with the treatment of common-receiver or cross-spread gathers.

Vertical channel: Qualitative analysis of the raw shots indicates an improved bandwidth and S/N with the dynamite source, but also shows an increase in the level of groundroll amplitude and in the low-frequency noise (Figure 4.12a and 4.12b). The vibroseis data shows less prominent groundroll and low-frequency noise but stronger airwave and high-frequency noise especially at short offsets and deeper times.

The vibroseis data yields better shallow data than the dynamite (from 0- 0.6 s). However, the dynamite signals appear to have much deeper energy penetration leading to a better imaging of the deeper subsurface. At first glance, it appears there may be more reflection energy from the dynamite shots.

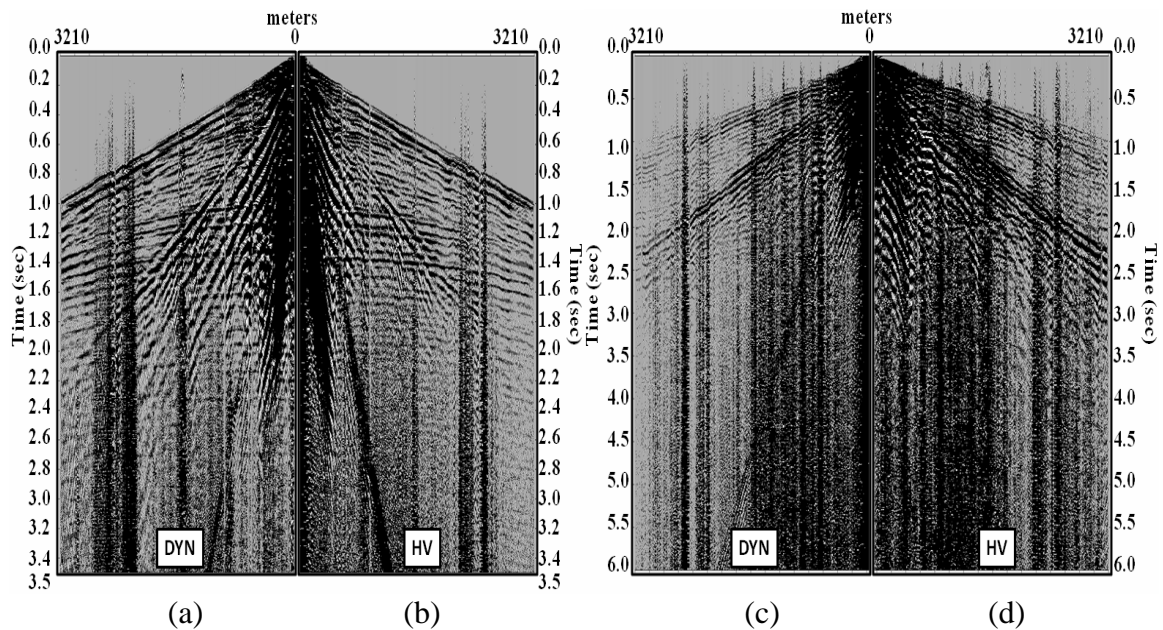


Figure 4.12. Comparison of two raw shot gathers. In (a), half of a split spread record from the vertical-component dynamite line. The same shotpoint from the vertical-component heavy vibroseis line is shown on (b) with the lateral coordinate reversed to ease the comparison. The same comparison is shown for the same record for the radial-component of the dynamite on (c) and of the heavy vibroseis line on (d).

Although deep reflections are dramatically clearer on certain explosive source records (e.g., Figure 4.13, shot 1266), the quality of such data varies considerably. These differences occur because shots could have been placed in different media (clay, sand, shale, or sandstone), into different hole sizes, and with varying amounts of water saturation. Shot-to-shot variability can be evaluated comparing shots from different locations along the line (Figure 4.13); another method is analyzing amplitude spectra from first breaks to see how their character varies (Figure 4.14). Figure 4.13 presents three shots located at both ends and at the centre of the coincident source locations. For the vibroseis, the records appear slightly consistent in terms of the data character and in the level and nature of the ground roll. The amplitude levels from shot to shot are more consistent for the vibroseis than for the dynamite data, where we see a big amplitude difference between the centre shot with respect to the other ones. The first dynamite shot appears to have more reflected energy, which is not the case for the vibroseis shots where the events appear consistently across all shots.

Amplitude spectra in a window located on the first breaks from all three shots of every source (Figure 4.14) indicates that there is some variability from shot to shot in the dynamite, however this is not what is expected when we have different near-surface media: there might be small changes in the conditions but it does not cause a substantial difference. The first breaks on the vibroseis present similar characteristics from shot to shot with small variations.

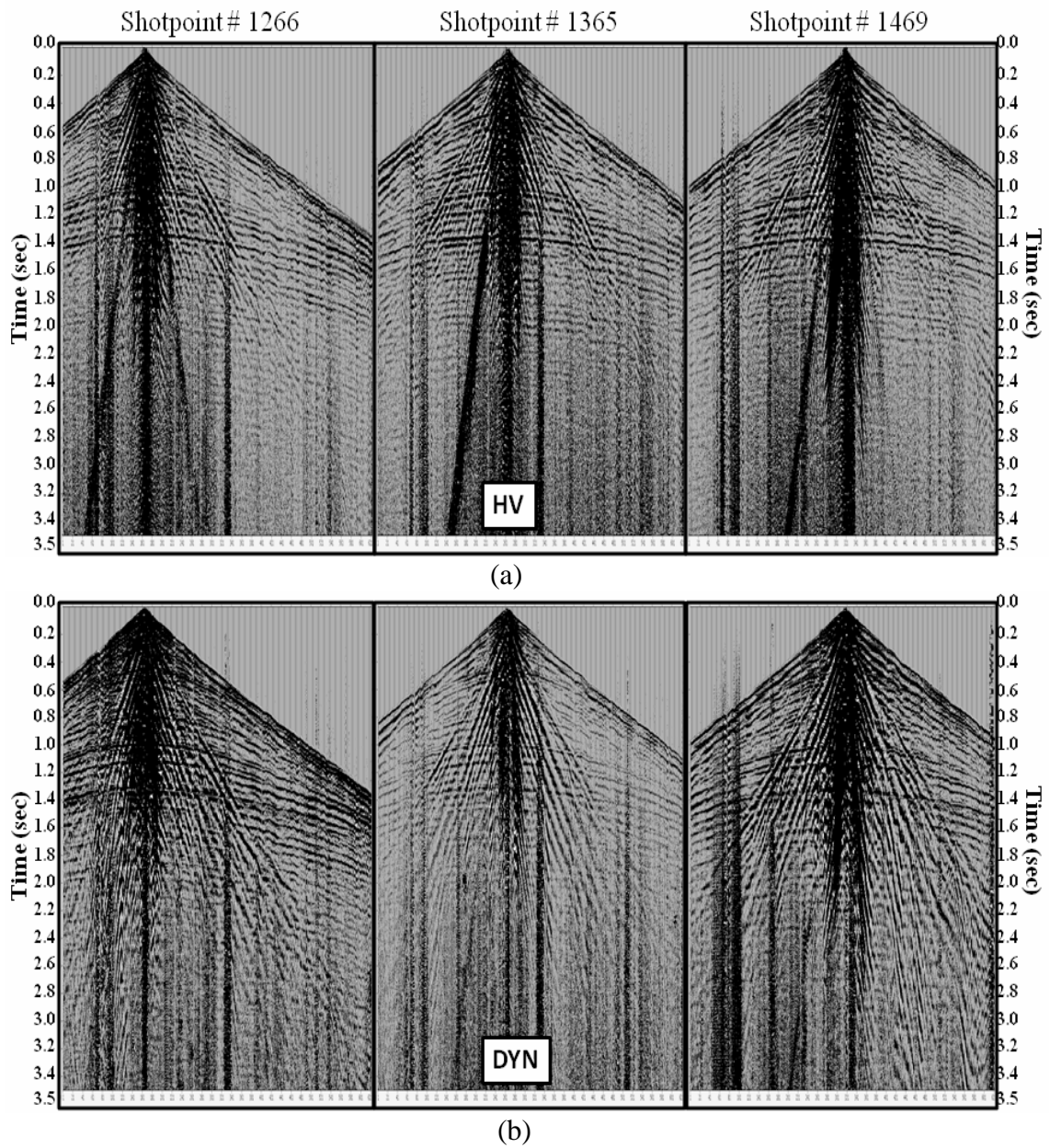


Figure 4.13. Three vertical-component raw shots are compared along the line. In (a), a shot from the beginning, middle and end of the heavy vibroseis line are shown. In (b), the same shot locations but for the dynamite line.

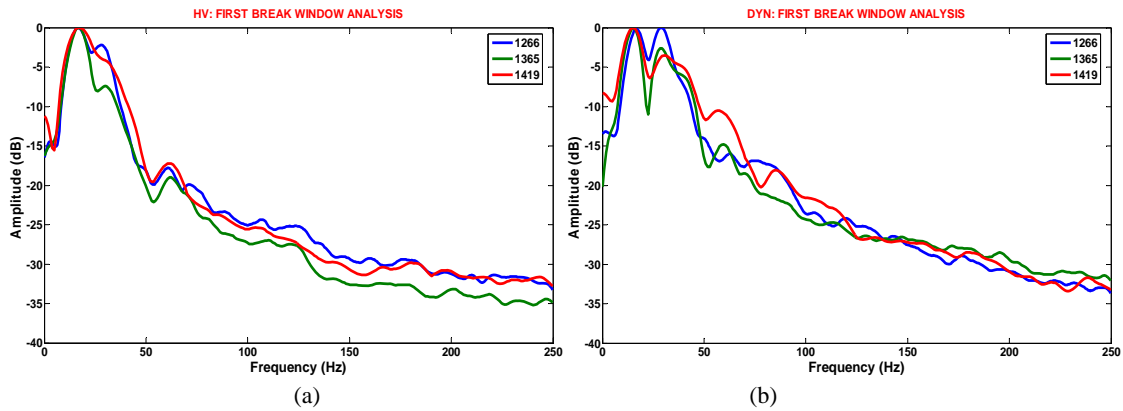


Figure 4.14. Amplitude spectra for a window located on first breaks for shot locations 1266, 1365 and 1419 for (a) the heavy vibroseis and (b) the dynamite dataset. These three shots are the same shots shown in Figure 4.14.

Radial channel: Compared to the vertical-component, the converted-wave data looks noisier, with less bandwidth and the reflection energy is not as strong or evident (Figures 4.12c and 4.12d). The overall noise content appears to be less in the dynamite than in the vibroseis data, where strong random noise masks most of the reflections. The near offsets are more contaminated with noise in the dynamite data and the amplitude level is lower. The frequency content looks higher in the dynamite data than in the vibroseis data.

The consistency from shot to shots looks similar for both datasets (Figure 4.15); there is not as much difference in amplitude levels between the dynamite shots as in the vertical-component.

Not many observations could be made regarding the energy penetration for the converted-waves because of the difference in amplitude and the noise that is masking most of the reflections. The apparent reflections go up to 2.5 s and they are more evident on the vibroseis data, but once again this observation could be driven by the amplitude differences.

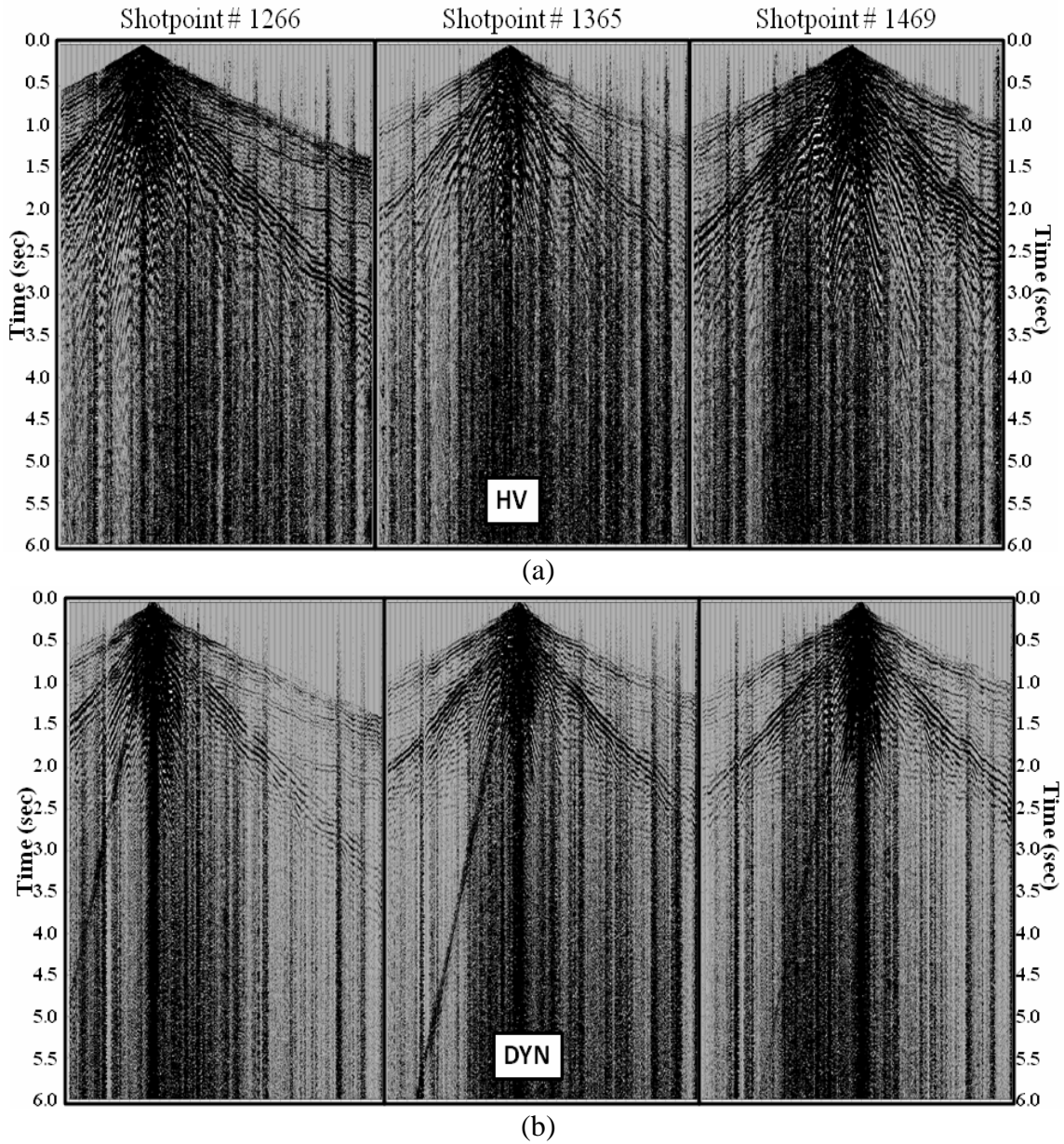


Figure 4.15. Three radial-component raw shots are compared along the line. In (a), shots from the beginning, middle and end of the heavy vibroseis line are shown. In (b), the same shot locations but for the dynamite line are shown.

4.5.1.2 Unmigrated stacked sections:

Vertical channel: The dynamite data appear generally superior to vibroseis data at the shot-gather level. This is perhaps to be expected, because the vibroseis method was developed as a “low impact” source that takes advantage of common depth point (CDP) redundancy to achieve useful S/N levels at depth (Schrodt, 1987). The comparison of the

stacked seismic sections indicates that the vibroseis is superior in the shallow section (0–0.6 s) (Figure 4.16 and 4.17) and the dynamite in the deeper section (0.6–2 s) (Figure 4.18 and 4.19). The higher redundancy and more uniform source-to-ground coupling of vibroseis sources facilitated static corrections and subsequent stacking enhancement (Schrodt, 1987).

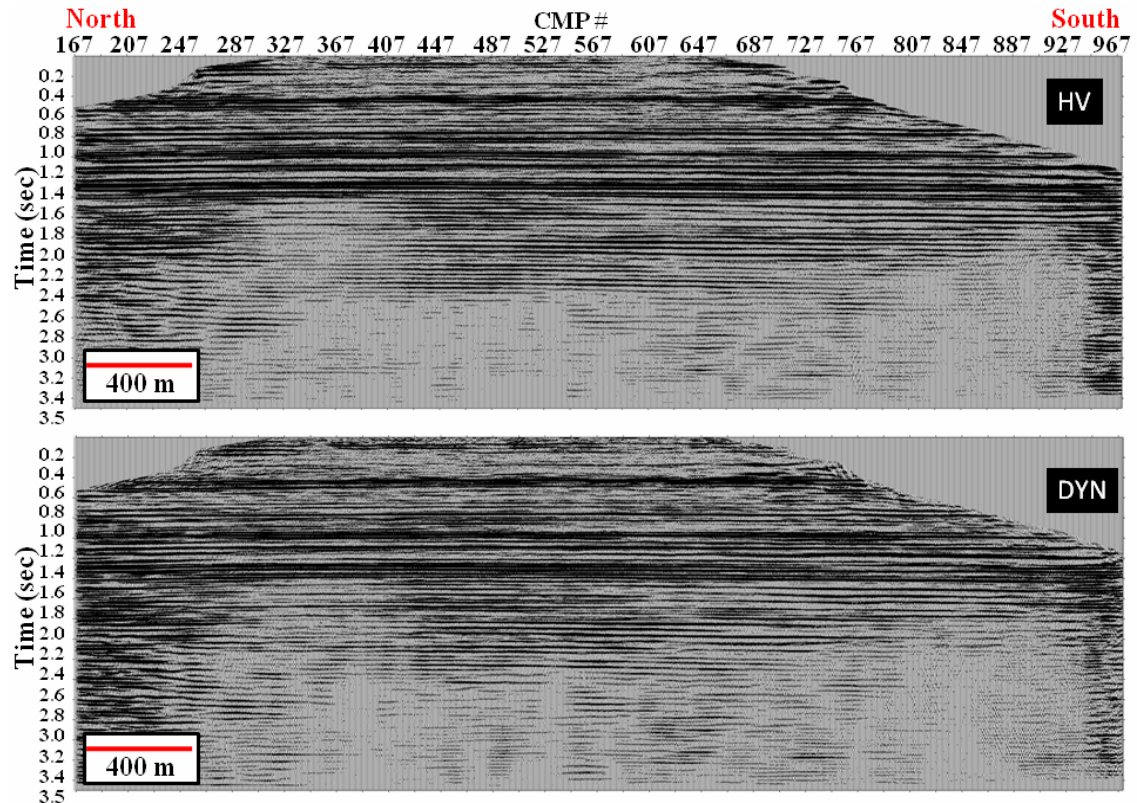


Figure 4.16. Comparison of the vertical-component heavy vibroseis (top) and dynamite (bottom) stacked sections. The sections were generated with coincident data, with phase and amplitude matching of the dynamite to the vibroseis, best mute and velocities.

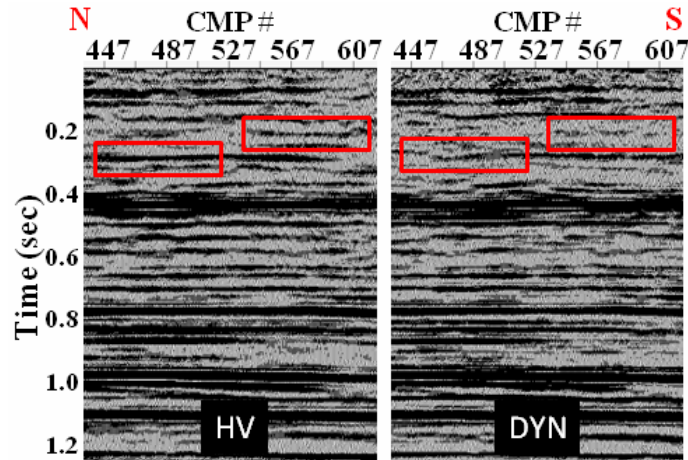


Figure 4.17. Zoomed sections of the shallow portion (0-1.2 s) of the final vertical-component stacked sections for the heavy vibroseis (left) and dynamite (right).

The target zone for this area is located between 0.5 and 1.5 s two way time, so as to focus the comparison in this portion of the section. A side-by-side zoomed section and full stacked sections are presented in Figures 4.18 and 4.19. Analysis of these zoomed sections indicated improved bandwidth and S/N could be achieved with a dynamite source, but the possible improvement in P-wave image quality might not be considered sufficient to select this as the source of preference: survey cost related factors would have to be evaluated to make this decision.

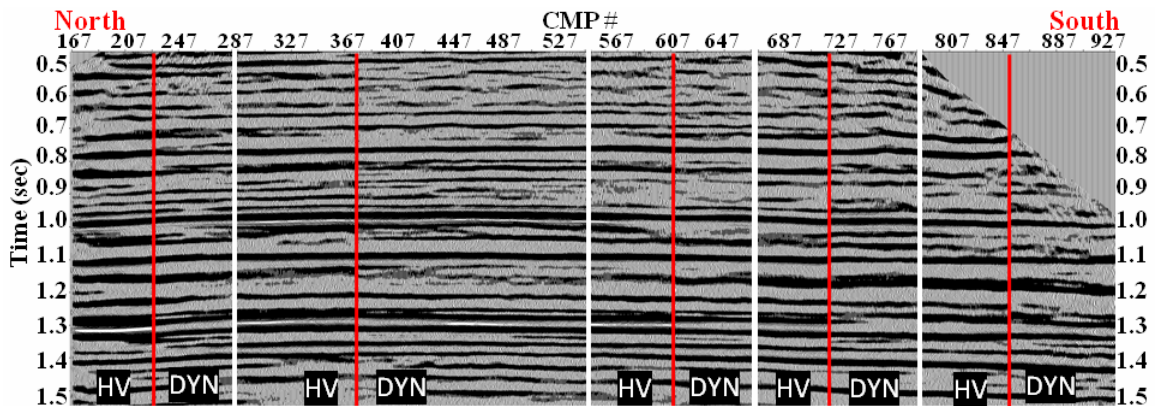


Figure 4.18. Side-by-side comparison of different portions along the vertical-component stacked sections for the dynamite and heavy vibroseis.

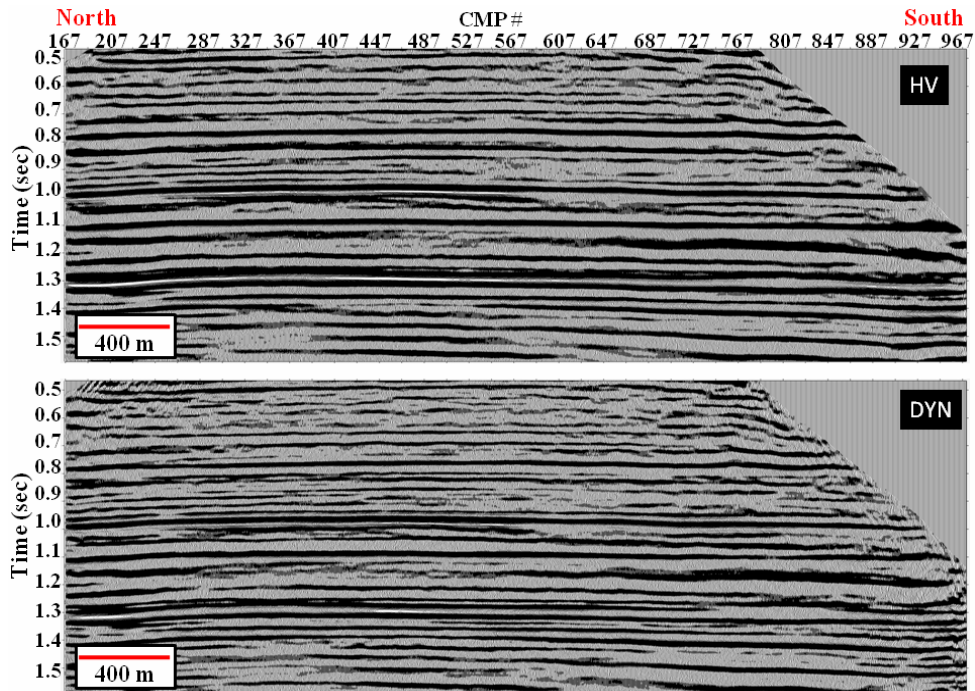


Figure 4.19. Portion of the amplitude- and phase-matched, vertical-component, heavy vibroseis (top) and dynamite (bottom) stacked section, zoomed in the zone of interest (500-1500 ms).

Radial channel: The same observations made for the vertical channel stacks applied to the radial channel stacks (Figure 4.20, 4.21 and 4.22). However, the difference on the shallow reflectors is not as noticeable as for the vertical; in the deeper parts the dynamite shows better resolution that might reflect higher frequency content.

Between CMP's 287 and 447 there is an area of lower amplitude in comparison with the rest of the section. This difference cannot be observed in the vertical channel and might be due to a higher attenuation of the converted-wave by scattering and absorption that did not allow us to obtain usable high frequencies. Another reason could be that the receiver statics were not completely resolved and needed more iterations. In this portion, the dynamite data appear to have more continuous reflectors between 1.5 and 1.9 s.

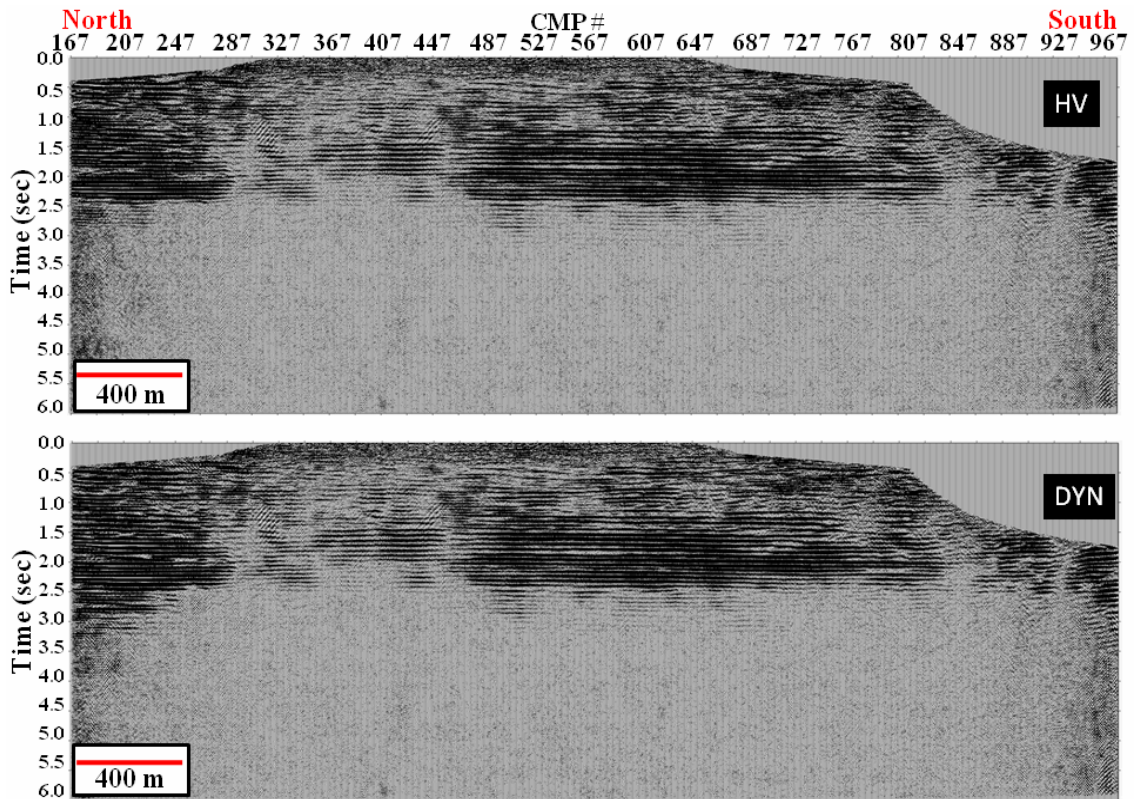


Figure 4.20. Comparison of the radial-component heavy vibroseis (top) and dynamite (bottom) CCP stacked sections. The sections were generated with coincident data, with phase- and amplitude-matching of the dynamite to the vibroseis, best mute and velocities.

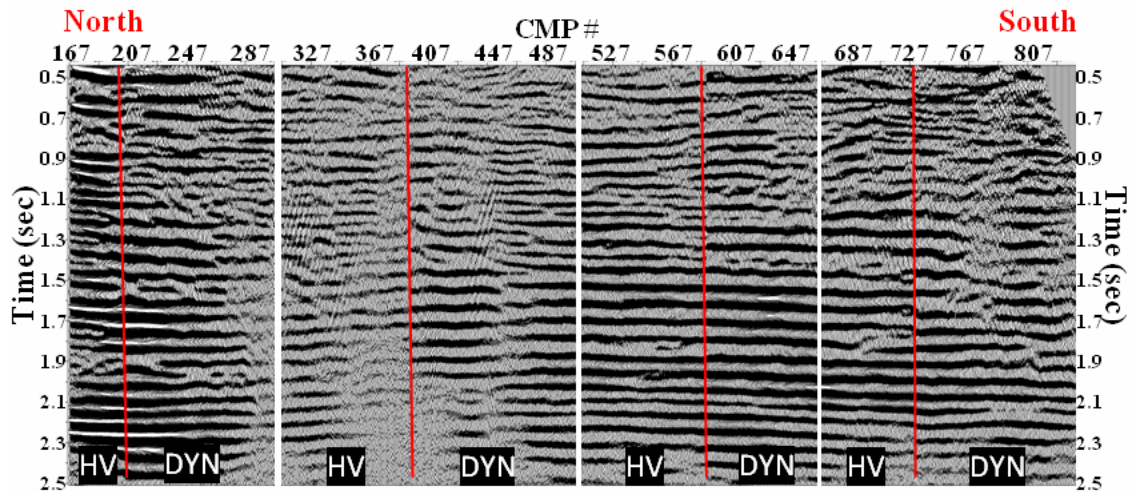


Figure 4.21. Side-by-side comparison of different portions along the radial-component stacked sections for the dynamite and heavy vibroseis.

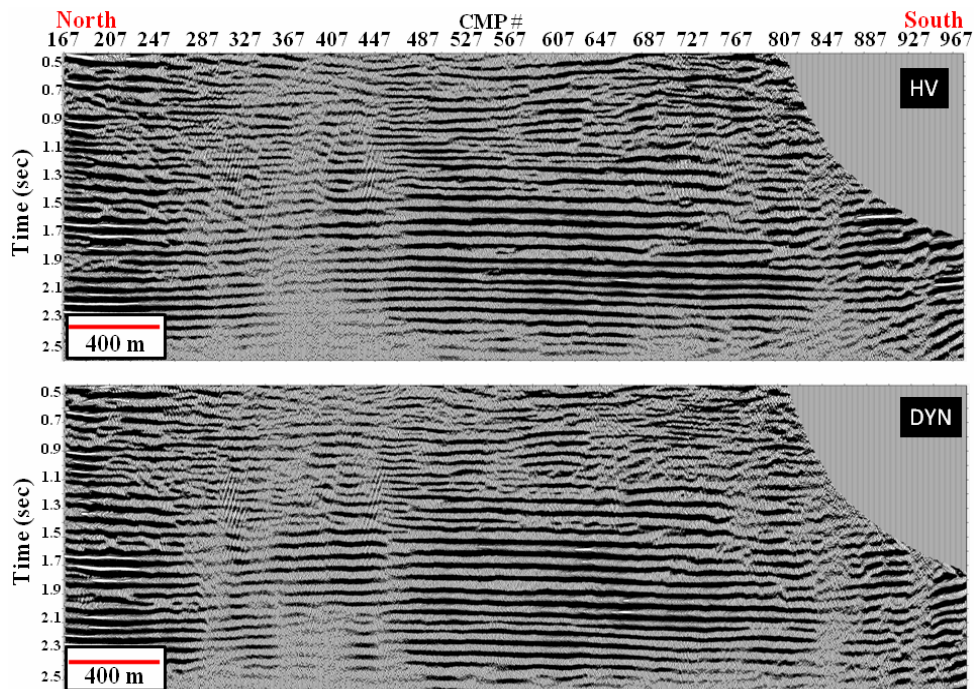


Figure 4.22. Portion of the amplitude- and phase-matched, radial-component, heavy vibroseis (top) and dynamite (bottom) stacked section, zoomed in the zone of interest (500-2500 ms).

4.5.1.3 Seismic signal band estimation using f-x spectra

An f-x analysis of raw shot gathers and unmigrated stacked sections was done on the different source datasets to estimate the potential signal band and the realized signal band, respectively. The potential signal band is the maximum possible signal band inherent that will be obtained with seismic processing techniques, but because the data has not been processed it is estimated in raw data. The realized signal band is the estimation done after processing the raw data; it can be used as a comparison method between different processing sequences or for acquisition parameter tests (Margrave, 1999).

The potential band estimation method is based on the “corner frequency” concept, which is the frequency where the signal spectrum will drop below the background noise

level and produce a “corner frequency” which is a measure of the potential signal band (Margrave, 1999).

The realized signal band method computes the f-x Fourier spectra of unmigrated stacked sections, and plots the amplitude and phase spectra separately. The frequencies where signal is dominant are recognized by laterally-coherent spectral events while spectral power is indicated by strong (dark) regions on the amplitude spectrum (Margrave, 1999; Hamarbitan and Margrave, 2001).

Figure 4.23 shows the windows selected to calculate the average amplitude spectra on areas corresponding to data, noise and first break for the vertical channel data; and the same events for the radial channel, except for the selection of a refraction event instead of the first breaks. The selection of these windows will allow us not only to estimate the potential bandwidth; it will allow us to determine if both sources could reproduce the same seismic events (signal and noise) with the same characteristics.

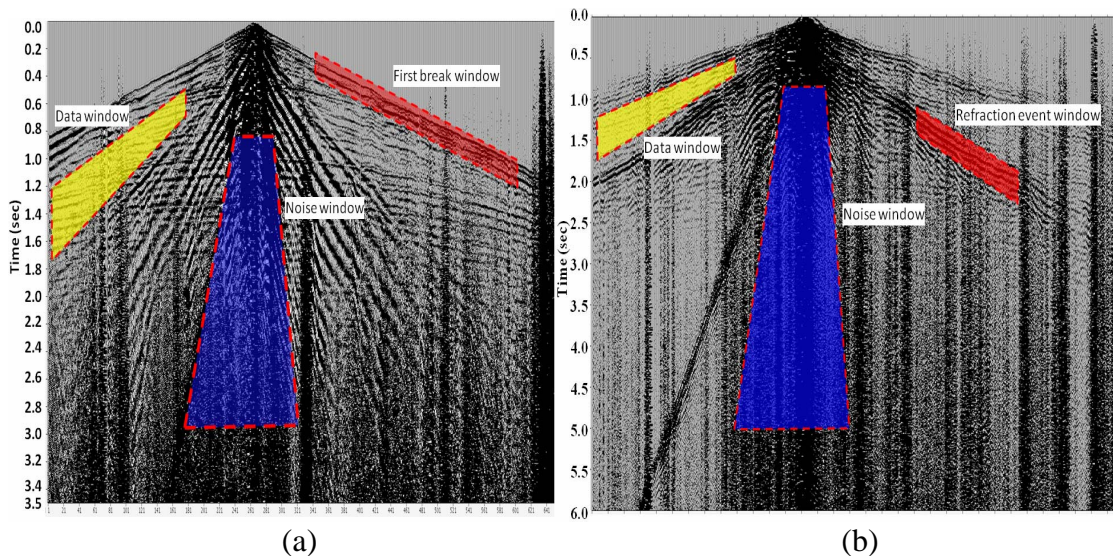


Figure 4.23. Analysis windows used for the average Fourier spectra amplitude calculation for the heavy vibroseis-dynamite comparison. The three zones for the vertical-component raw shot record are shown in (a) and in (b) the three zones for the radial-component raw shot record.

4.5.1.3.1 F-x analysis of the raw shot gathers

Vertical channel: An average Fourier amplitude spectrum was calculated on a raw shot gather for a window corresponding to what is hoped to be subsurface reflections (Figure 4.24a). From 0-10-Hz the dynamite shows slightly higher power; then, to about 40 Hz, the curves are similar, with a dominant frequency of 25 Hz. After 40 Hz, dynamite exhibits higher power up to 65 Hz; finally, the vibroseis amplitudes remain higher until reaching the maximum sweep frequency (130 Hz).

Using the same amplitude spectrum plot shown in Figure 4.24(a) and based on the potential band estimation method presented in Margrave (1999), we identified the “corner frequency” for both datasets, which seems to be located around 70-75 Hz. The corner frequency was approximately identified where the signal attenuated spectrum drops below the constant background noise level (Figure 4.24a).

The same analysis was done in windows that cover a portion of the first breaks and noise (Figure 4.24c and 4.24e). The first break window (Figure 4.24c) is intended to characterize refracted energy from shallow interfaces. The dynamite shows slightly more power between 0-5 Hz and in the 25-160 Hz range. In the 5-25 Hz band the curves are very close.

In the window located in the noise area (Figure 4.24e), the vibroseis shows a much stronger Rayleigh wave on the high-frequency side (25-250 Hz). From 0-25 Hz the curves are similar.

Radial channel: The same Fourier analyses were done in the radial channel, for signal, refracted wave, and noise windows (Figure 4.24b, 4.24d and 4.24f). In the data window (Figure 4.24b), the dynamite shows slightly higher amplitudes up to about 10

Hz, but from 10-25 Hz the curves are similar with a dominant frequency of 20 Hz; in the 30-40 Hz range the dynamite shows higher amplitudes. Above 40Hz, the amplitude levels of the vibroseis are 5 dB higher than the dynamite. For the radial channel datasets, the apparent corner frequency is around 40-45 Hz for the vibroseis and 50 Hz for the dynamite.

For the refracted arrival window, the event selected could be a P-S-P refraction that appears strongly in both datasets (Figure 4.24d). This event shows almost the same power for both sources to about 30 Hz. After 30 Hz, the vibroseis power is higher by 4 dB until it reaches the maximum sweep frequency.

In the noise window (Figure 4.24f), the dynamite shows slightly stronger Rayleigh waves up to 20 Hz, then the vibroseis yields much stronger waves with a dominant frequency of 15 Hz until it reaches the maximum sweep frequency.

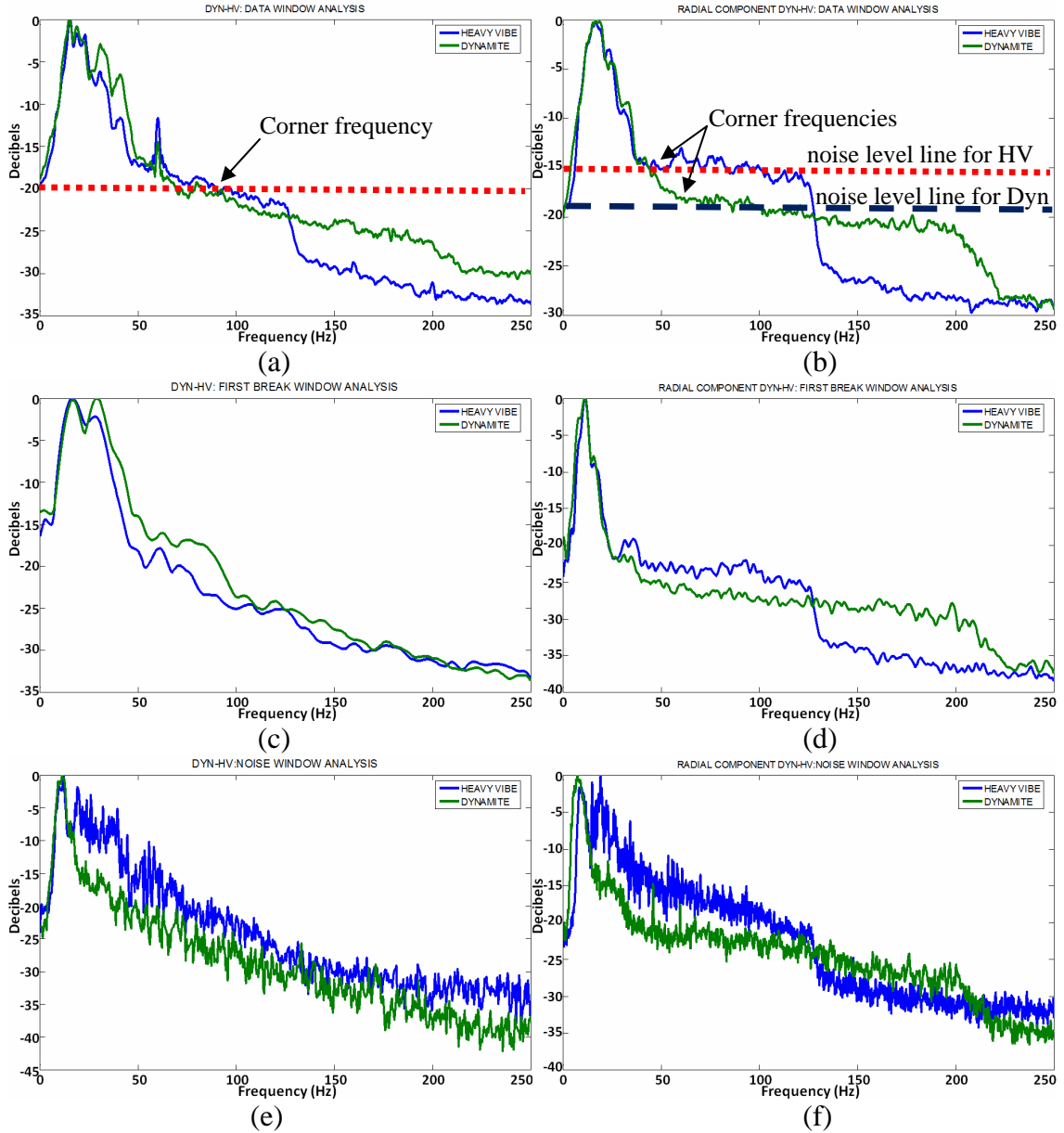


Figure 4.24. Average Fourier amplitude spectrum of a raw shot gather for the vertical channel (left column) and radial channel (right column) of the heavy vibroseis and dynamite data, with windows corresponding to: (a) and (b) signal-only area; (c) and (d) first-break area (vertical-component)/refraction event (radial-component); and (e) and (f) noise area.

4.5.1.3.2 F-x analysis of the unmigrated stacked sections

Vertical channel: An f-x analysis of both unmigrated, unfiltered stacks to estimate the realized signal band is shown in Figure 4.25.

The f-x amplitude spectrum for both datasets (Figure 4.25a and 4.25b) shows a drop in spectral power at 40-45 Hz. Above this frequency, the dynamite shows weaker amplitudes than for the range 15-40 Hz, but they are still stronger than the vibroseis up to 55 Hz.

The phase coherence of the two datasets is contrasted in Figure 4.25(c) and (d). For the vibroseis, there is a reduction in phase coherence at 40-45 Hz that is coincident with the drop in spectral power in Figure 4.25(a). However, subtle phase coherence persists up to at least 85 Hz. The dynamite reduces its phase coherence at about 55 Hz. These observations may be interpreted as indicating similar signal levels below 45 Hz. In the 45-60 Hz band, the signal strength of the dynamite is greater. On the other hand, from 60 to 90 Hz both datasets look weak but the vibroseis shows more coherency.

Radial channel: The same f-x analysis for both unmigrated, unfiltered CCP stacked sections is shown on Figure 4.26. The f-x amplitude spectra for both datasets (Figure 4.26a and 4.26b) are similar without major differences. They show a drop in spectral power at 20 Hz. After this frequency the data shows little signal.

There is a reduction in coherency for the two sections at about 25 Hz (Figure 4.26c and 4.26d). From 25 to 35 Hz there is evidence of weak signal but not very coherent. From 35 to 55 Hz the signal is coherent but weak.

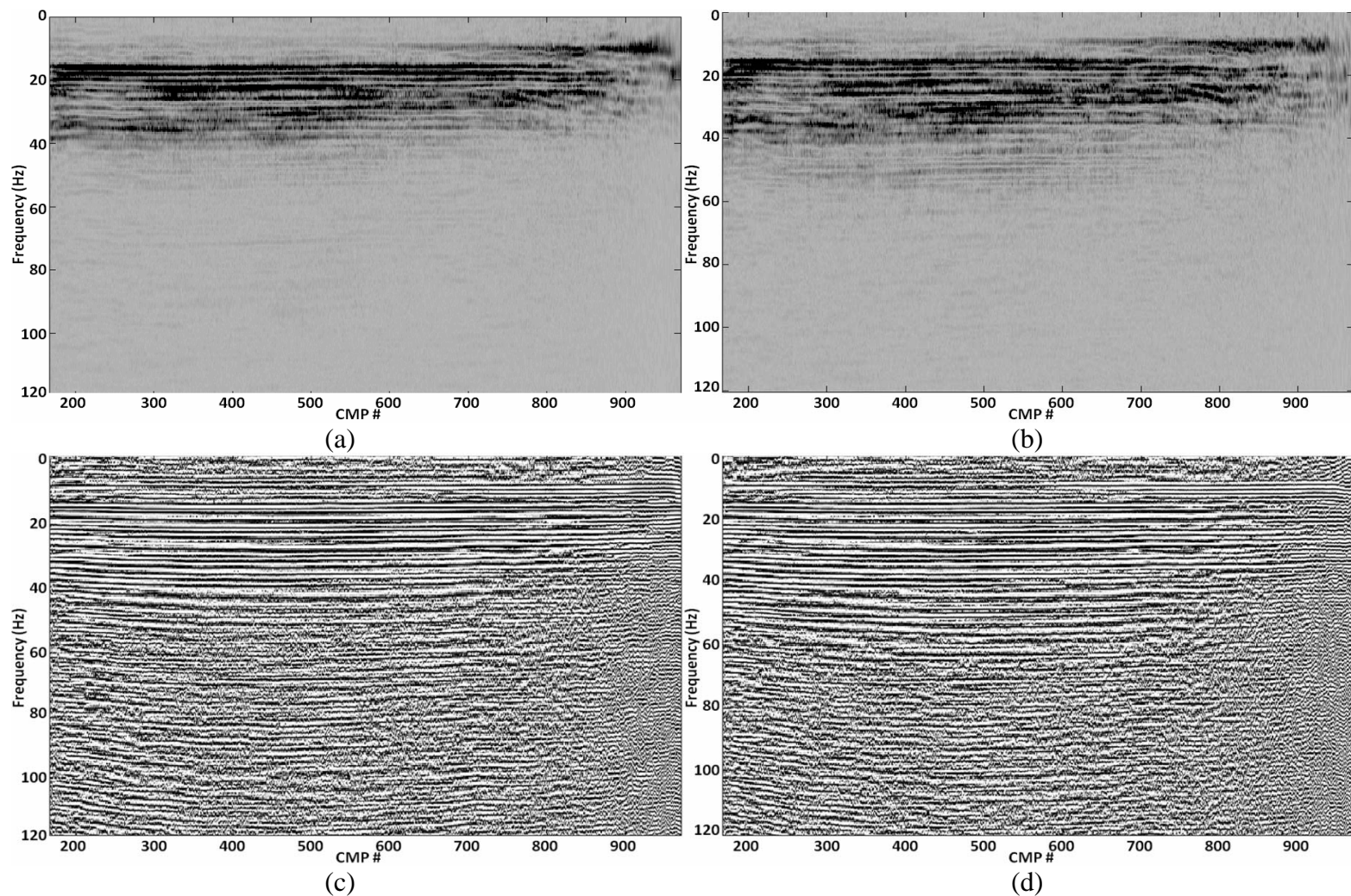


Figure 4.25. F-x spectral analysis for the final unmigrated, unfiltered P-wave stack to compare heavy vibroseis and dynamite data computed over the time zone 432-1467 ms. The f-x amplitude spectrum for the heavy vibroseis is shown in (a); (b) shows a similar spectrum for dynamite data. (c) and (d) show the f-x phase spectra corresponding to (a) and (b), respectively.

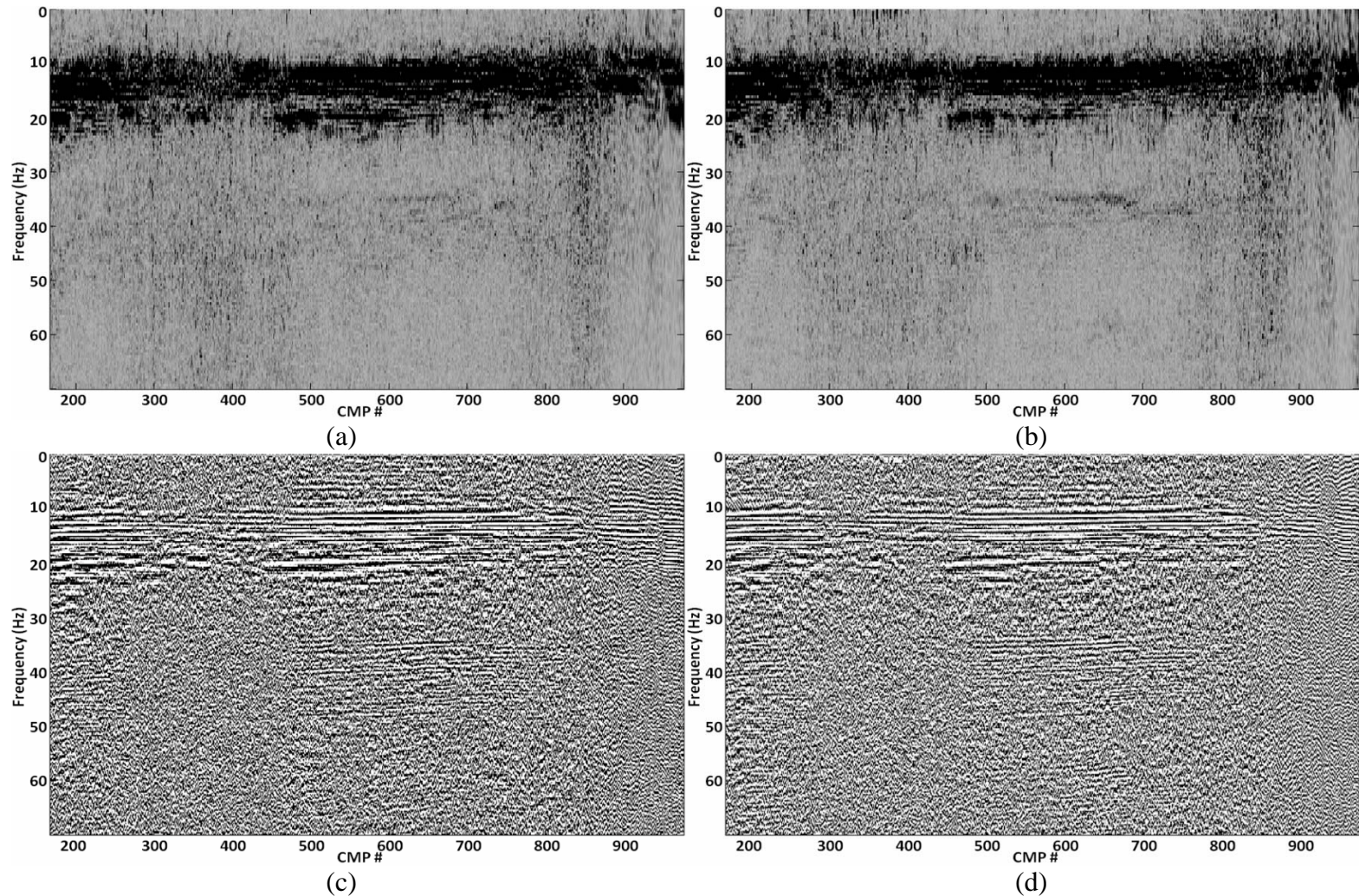


Figure 4.26. F-x spectral analysis for the final unmigrated, unfiltered PS-wave stack to compare heavy vibroseis and dynamite data computed over the time zone 700-2500 ms. The f-x amplitude spectrum for the heavy vibroseis is shown in (a); (b) shows a similar spectrum for dynamite data. (c) and (d) show the f-x phase spectra corresponding to (a) and (b), respectively.

4.5.1.4 Frequency bandwidth estimation using filter panels

A common method used in data processing for signal bandwidth determination is to build filter panels. Filter panels are displays showing data filtered by a sequence of narrow band-pass filters to see the effect of different passbands (Sheriff, 2002).

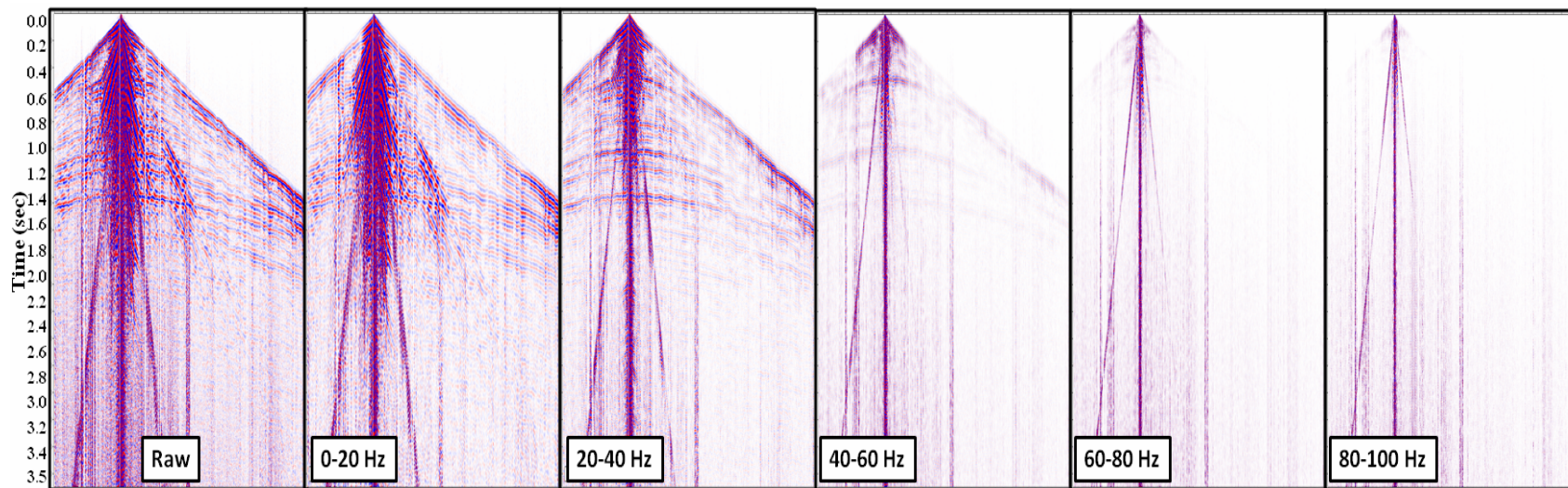
In Figures 4.27 and 4.28 are shown the filter panels created for the vertical and radial channel of a raw shot gather. In every case, two panel sets corresponding to the vibroseis and dynamite sources were created.

Vertical channel: In the heavy vibroseis panels, signal is present from top to bottom in the 0-20-, and 20-40-Hz bands (Figure 4.27a). Not much signal is noted below 1 s in the 40-60-Hz band. The 60-80-Hz band shows very weak signal to about to 0.4 s. Finally the 80-100-Hz band shows no signal, only noise.

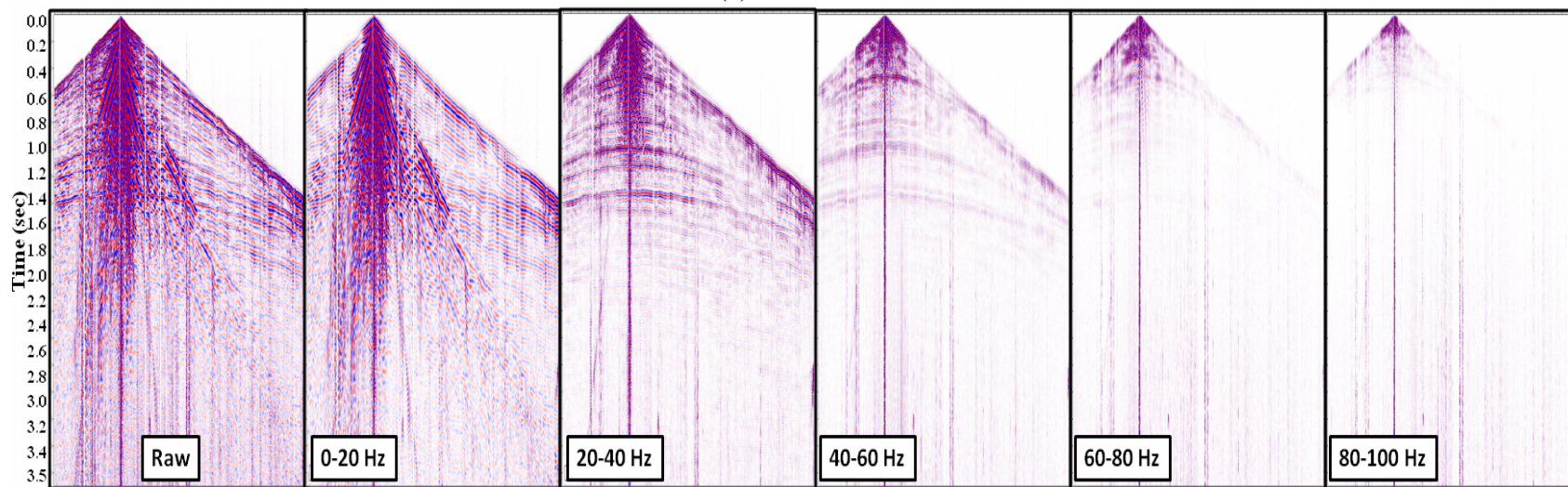
Similar observations are made for the 0-20-, 20-40-Hz bands on the dynamite panels (Figure 4.27b). In the 40-60-, and 60-80-Hz bands, the signal looks stronger than the vibroseis — the signal is observed to about 1.4 and 0.6 s, respectively.

The filter panels indicate that the signal band is confined to lower frequencies at late times and higher frequency bands of useful signal are confined to the shallow part of the section.

These results corroborate some of the observations from the average f-x Fourier spectrum of Figure 4.24(a). In that analysis, the corner frequencies indicate a potential bandwidth of about 70-75- Hz for the dynamite and the vibroseis. Using the filter panels we could say that the bandwidth of the dynamite is slightly higher (70-80 Hz) than the vibroseis (60-70 Hz).



(a)



(b)

Figure 4.27. Filter panels for the vertical-component of a raw common shot gather from (a) the heavy vibroseis and (b) dynamite data.

Radial channel: Analogous to the analysis of the vertical channels, signal is present from top to bottom in the 0-20-Hz band (Figure 4.28). The 20-40-Hz band shows very weak signal below 1.5 s. In the 40-60-, and 60-80-Hz bands the signal is confined to early times (0-0.5 s).

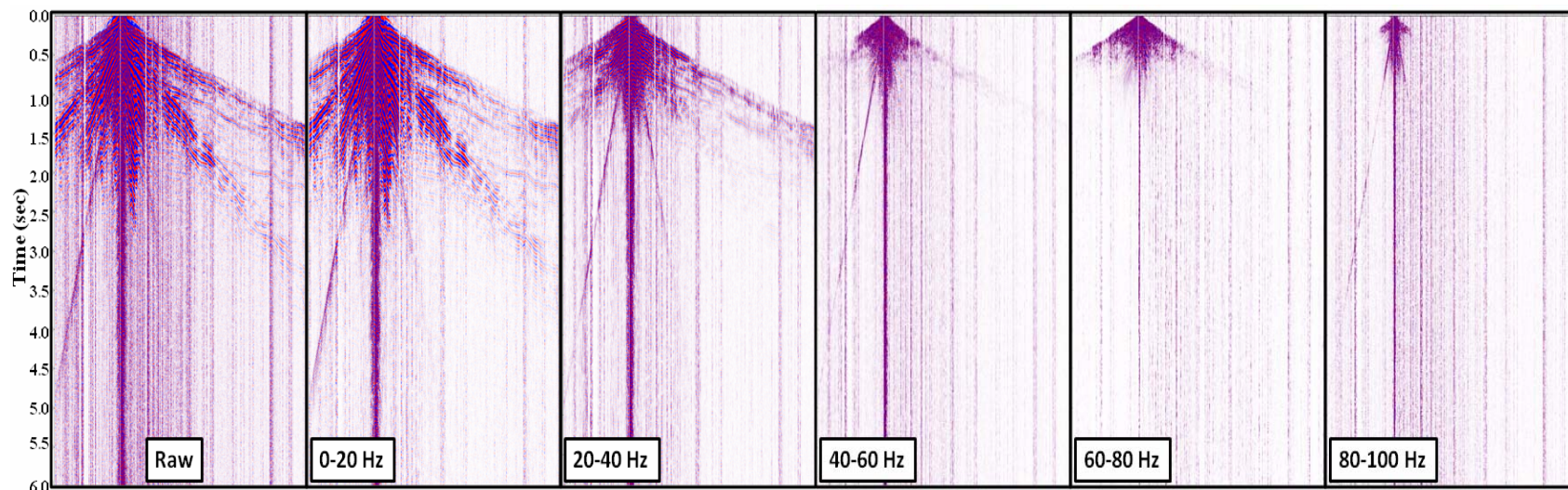
There is no apparent difference between dynamite and vibroseis. These results also corroborate the observations from the average f-x Fourier spectra analysis, where the bandwidth of both datasets was between 40-50 Hz.

4.5.1.5 Signal and noise estimation

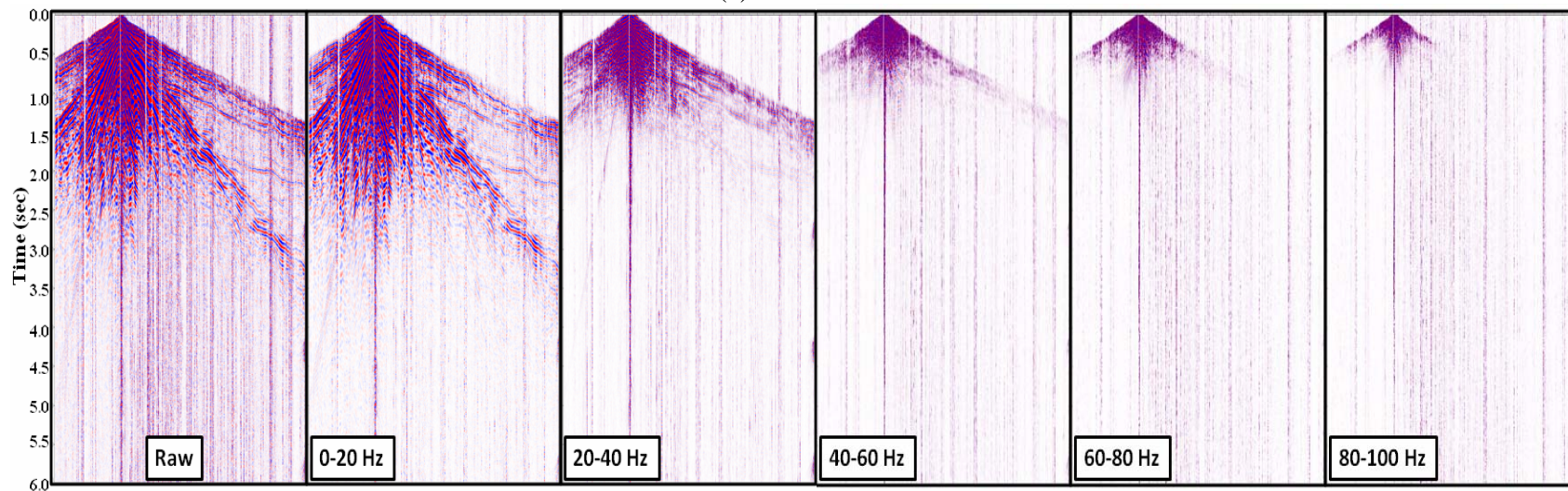
Signal and noise spectral analysis give an approximation of these two parameters. They are not particularly accurate but give an idea of the difference between coherent events and random events. Coherent events represent “signal” but sometimes the noise can be coherent and thus seen as “signal”, so care must be taken with this kind of analysis.

Signal and noise estimation was done for the comparison between heavy vibroseis and dynamite for the vertical and radial channels (Figure 4.29a and 4.29b). For the vertical channel, signal and noise levels are very similar, with the dynamite estimate being slightly higher for both from 50 Hz to about 200 Hz (Figure 4.29a). From 0 to 40 Hz the heavy vibroseis estimates are slightly higher for the “signal” and between 15 and 50 Hz for the noise.

For the radial channel the estimates are very similar as well (Figure 4.29b). For the “signal”, the dynamite estimates are slightly higher through the entire frequency range. Regarding the noise, it is difficult to distinguish between both curves.



(a)



(b)

Figure 4.28. Filter panels for the radial-component of a raw common shot gather from (a) the heavy vibroseis and (b) dynamite data.

The similarity of the estimates for both channels and types of sources gives an indication that in all stacked sections there is not much difference in the contents of coherence and random events between sources. This is not an indication of which one has better signal or more noise but gives us confidence that the datasets are very similar.

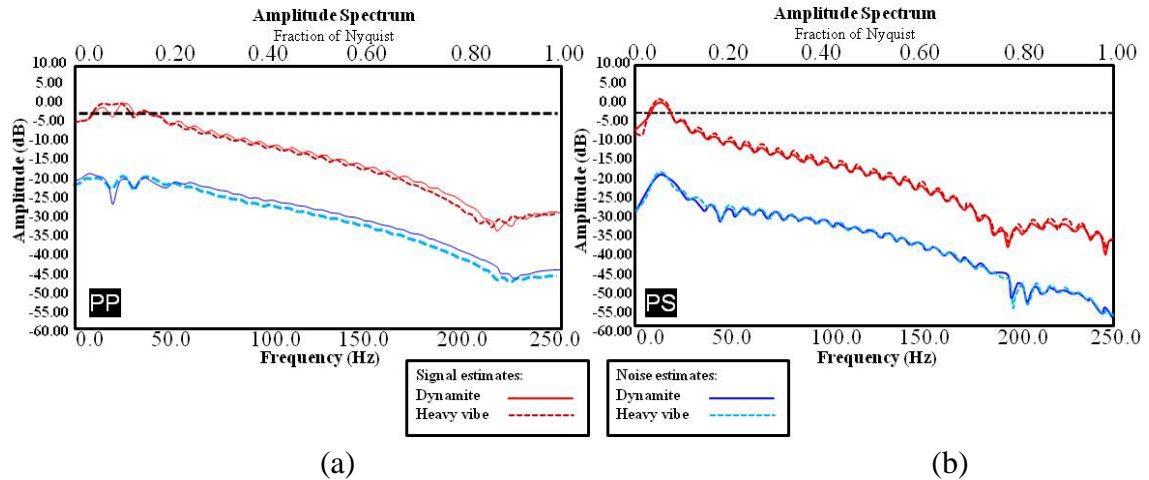


Figure 4.29. Signal and noise estimation for: (a) the vertical and (b) radial-component heavy vibroseis and dynamite data. For the vertical-component the analysis was done over the time zone 432-1467 ms and for the radial-component over the time zone 650-2567 ms.

4.5.1.6 Quantified attribute measurements for the source comparison

Seismic resolution is one of the most important parameters in seismic exploration. Defining resolving power or vertical resolution is a difficult task because it is not a quantity that depends on a single factor, but instead depends on the seismic system and on the type of distribution of the reflections. It has been proposed (Berkhout, 1984; Widess, 1982) that the resolving power of seismic data be defined by quantitative properties. These properties are calculated using the assumption that the distribution of reflections and of noise be treated as a random (Gaussian) distribution (Widess, 1982).

Resolution implies separating into constituent parts; for seismic this means separating constituent reflections. A reflection includes a time variable and a waveform variable, so any attributes that will help us characterize these variables will allow us to

determine distinctness and therefore resolution (the process of making constituent reflections distinct).

4.5.1.6.1 Attributes

In addition to all the analyses that have been done to compare both datasets, a deterministic method is used to obtain statistical information about the data quality. The statistical trace attributes have been determined in a selected time window of 500-2500 ms TWT over the whole stacked section to cover the most relevant targets.

This analysis is based on quantified attribute measurements on seismic data. The following statistical attributes were used for the deterministic analysis:

Category Resolution

Seismic resolution defines the amount of detail in terms of vertical and lateral changes in the subsurface can be derived from seismic data.

Vertical resolution determines the ability to distinguish between the properties of inhomogeneities which are vertically displaced from each other. By decreasing the duration of the seismic time wavelet (time length) the vertical resolution is improved. Vertical resolution is defined by absolute temporal bandwidth.

Lateral resolution determines the ability to distinguish inhomogeneities which are laterally displaced from each other. It is defined by absolute spatial bandwidth that is determined by the amount of high-frequency energy.

In practice, high spatial resolution only occurs if both the vertical and lateral resolution is large.

The attributes included in the category resolution are:

- Resolving factor

The resolving factor of seismic signals is the inverse of the product of time and frequency length. It is a dimensionless attribute.

- Time length (signal length in the time domain)

The time length of a wavelet could be quantified. This quantification is achieved by calculating its relative second-order moment. The smallest possible signal length is achieved by a finite frequency range zero-phase wavelet with a cosine-shaped amplitude (Berkhout, 1984).

For a seismic time wavelet $w(t)$, the relative second-order moment is introduced as a criterion for signal length or wavelet's time length L_t :

$$L_t^2 = \frac{\int (t - t_0)^2 w^2(t) dt}{\int w^2(t) dt}$$

where t_0 represents a reference time that is defined as:

$$t_0 = \frac{\int t w^2(t) dt}{\int w^2(t) dt}$$

- Frequency length (signal length in the frequency domain)

The frequency length (L_f) quantifies how the energy of the individual spectral components is distributed around the central frequency (f_c). For one spectral component at f_c , L_f is minimum (= zero).

The concept is analogous to the time length but replacing time functions with frequency functions, with the distribution of spectral components around a central frequency f_c .

For the one-sided amplitude spectrum of a seismic wavelet $W(f)$, the relative second-order moment is introduced as a criterion for signal length in the frequency domain L_f :

$$L_f^2 = \frac{\int_0^{\infty} (f - f_c)W(f)|^2 df}{\int_0^{\infty} |W(f)|^2 df},$$

where f_c represents the central frequency that is defined as:

$$f_c = \frac{\int_0^{\infty} f|w(f)|^2 df}{\int_0^{\infty} |w(f)|^2 df}.$$

We attempt to have short zero-phase wavelets (short time length), so that their amplitude spectra are broad and smooth. In terms of the frequency length, if this is increased the width of the main lobe of the zero-phase wavelet is decreased.

Some other attributes included in this category are temporal resolution and first zero-crossing, which are described in the following paragraphs.

- Temporal or vertical resolution
- First zero crossing:

The lag-time (in ms) of the first zero-crossing of the autocorrelation function.

Category Bandwidth

Frequency content is intimately tied to vertical and lateral resolution. Both low and high frequencies are needed to increase temporal resolution (Yilmaz, 2001). There is a close relationship between the amount of separation between reflectors and the desired bandwidth.

The attributes included in this category are:

- Mid-frequency:

The frequency (in Hz), which is the reference (or central) frequency of the amplitude spectrum.

- Peak-frequency:

The frequency (in Hz) for which the amplitude spectrum is maximum.

- High-frequency bandwidth:

The effective bandwidth (in Hz) from peak frequency to Nyquist frequency above a certain level specified where signal amplitude is above noise level. The actual attribute put out is the sum of peak frequency plus high-frequency effective bandwidth (effective high-corner frequency).

Given an input wavelet $w(t)$ whose amplitude spectrum is $W(f)$ and the peak amplitude is $w(fP)$, the high-frequency (H_f) bandwidth above a noise amplitude spectrum $N(f)$ is calculated as:

$$H_f = \frac{\sum_{fP}^{MAX} W^2(f)df}{W^2(fP)} - \frac{df}{2} \Leftrightarrow W(f) > N(f)$$

$$H_f = fP + H_f$$

- Low-frequency bandwidth:

The effective bandwidth (in Hz) from zero to peak frequency above a certain level specified where signal amplitude is above noise level. The actual attribute put out is the difference of peak frequency and low-frequency effective bandwidth (effective low-corner frequency).

With the same notation used for the high-frequency bandwidth, the low-frequency bandwidth is calculated as:

$$L_f = \frac{\sum_0^{fP} W^2(f)df}{W^2(fP)} + \frac{df}{2} \Leftrightarrow W(f) > N(f)$$

$$L_f = fP - L_f$$

- Total effective bandwidth:

The total effective bandwidth is the difference of the effective high and low corner frequencies. It is defined as the width of a boxcar with the same total power and the same peak power:

$$\int_0^{\infty} \frac{p(f)df}{P_{\max}}$$

where $p(f)$ is the power at the frequency f and p_{\max} is the maximum power.

4.5.1.6.2 Analysis of the deterministic trace attributes for the Spring Coulee source

comparison heavy vibroseis-dynamite:

Figures 4.30, 4.31, 4.32 and 4.33 present the attributes explained in previous pages. All these plots are similar with respect to the information they provide. They reflect vertical and lateral resolution, quantifying wavelet attributes.

Vertical channel: From these attributes, we are looking for the smallest signal length, a higher frequency length, smaller values for the first zero crossing, higher frequency content, and broader signal bandwidth. The wavelet that meets all these requirements holds better resolution.

The time length and temporal resolution graph (Figure 4.30b) indicates that the dynamite have smaller values than the vibroseis, with differences between 2 and 4 ms. The frequency length values (Figure 4.30c) for the dynamite in the 150 to 800 CMP range are higher, with average values of 10 Hz and 8 Hz for the vibroseis. The 800-950 CMP range shows anomalous values that might correspond to noise or low fold areas.

First zero-crossing values (Figure 4.31a) are smaller for the dynamite in the 150-550 CMP range, with average values of 8.5 ms and 9 ms for the vibroseis. After CMP 550 the values continue increasing. This indicates that there are some areas in the section that might have better imaging and resolution.

The bandwidth attributes (Figure 4.31b) corroborate some previous observations, such as the mid-frequency and peak frequency values. The dynamite shows slightly higher frequencies compared to vibroseis (about 5 Hz higher) but on the low-frequency side the curves are almost indistinguishable.

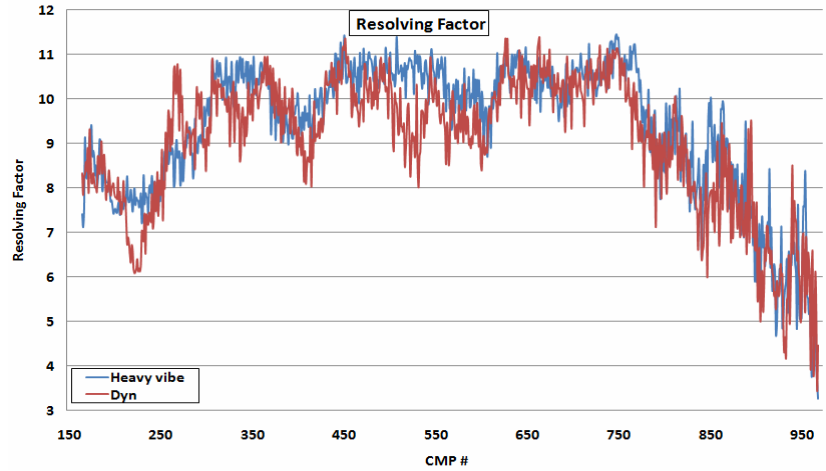
The total effective bandwidth (Figure 4.31c) is not a very indicative factor because it's not always easy to identify accurately the peak and low-frequency bandwidth for its determination. However, looking at the plot we could say that dynamite data have a higher effective bandwidth.

From these attributes we derive supporting evidence for what has been consistently observed from previous analyses: dynamite performs better than heavy vibroseis.

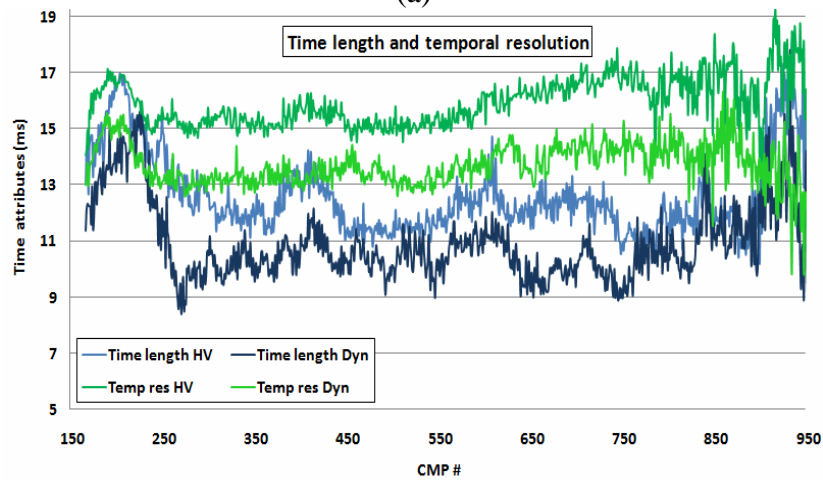
Radial channel: A general conclusion from all these attributes is that vibroseis and dynamite produce similar results (Figures 4.32 and 4.33). The differences are not very evident; perhaps in the frequency length plot the vibroseis data have a slightly higher value, but this observation is not constant throughout the CMP range.

If the values of the attributes for the radial channel are compared with those for the vertical channel, we see how the data is of less quality with less resolution and more contaminated with high-frequency noise. This is indicated by longer wavelets, with smaller frequency length and shorter bandwidth.

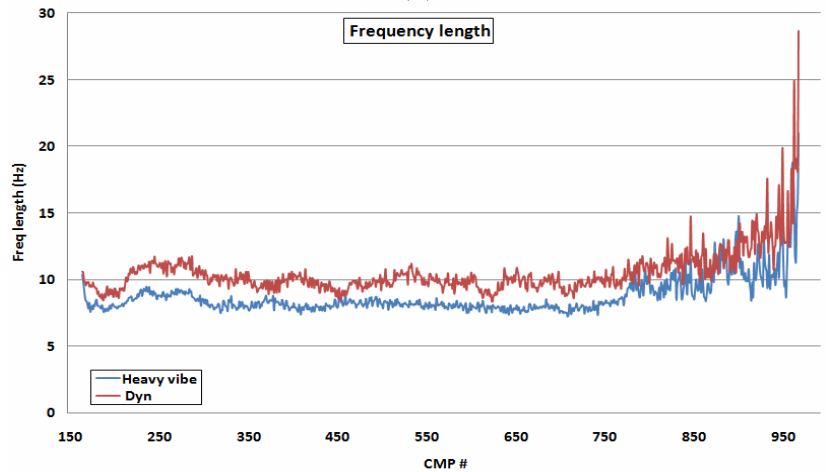
A positive observation from these analyses is that the apparent lower frequency content is much better for the radial channel, which is an important factor previously discussed for converted-waves. Another observation from these attributes is that the heavy vibroseis shows a slight advantage over the dynamite.



(a)

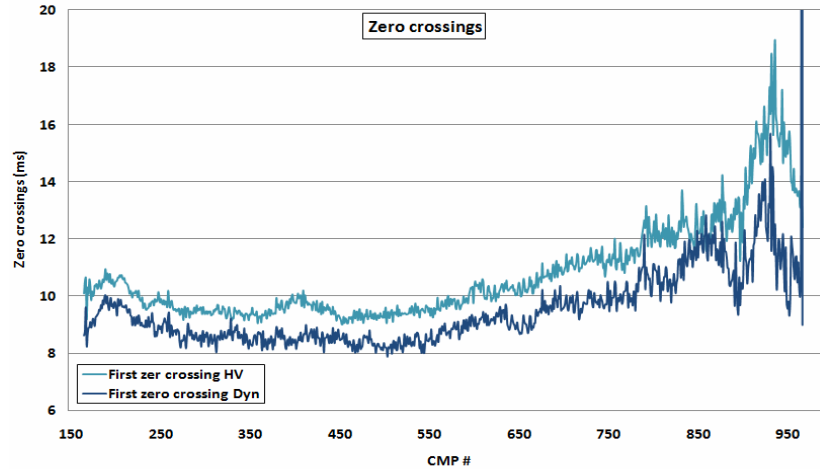


(b)

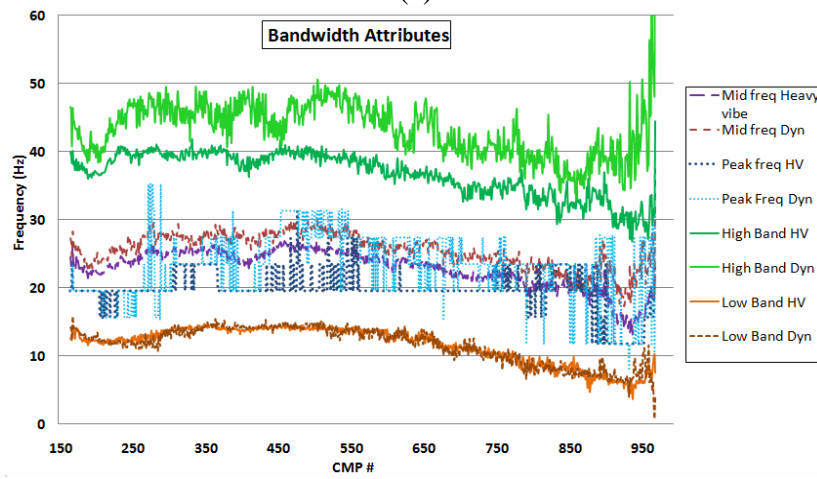


(c)

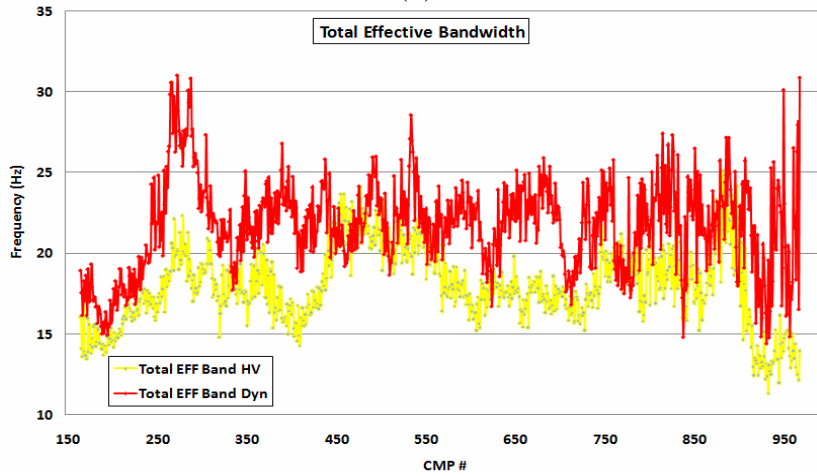
Figure 4.30. Deterministic trace attributes calculated for all CMP locations in the vertical-component stacked sections: (a) Resolving factor, (b) time length and temporal resolution, and (c) frequency length. For every plot there is a curve corresponding to the vibroseis (HV) and to the dynamite (Dyn) data.



(a)

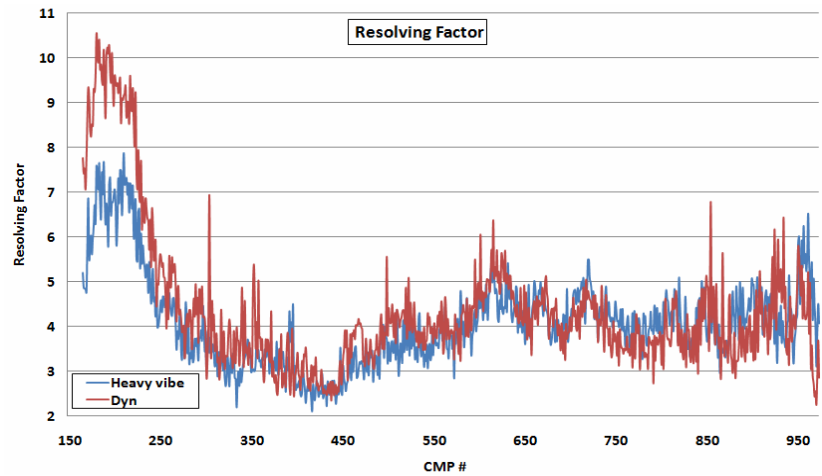


(b)

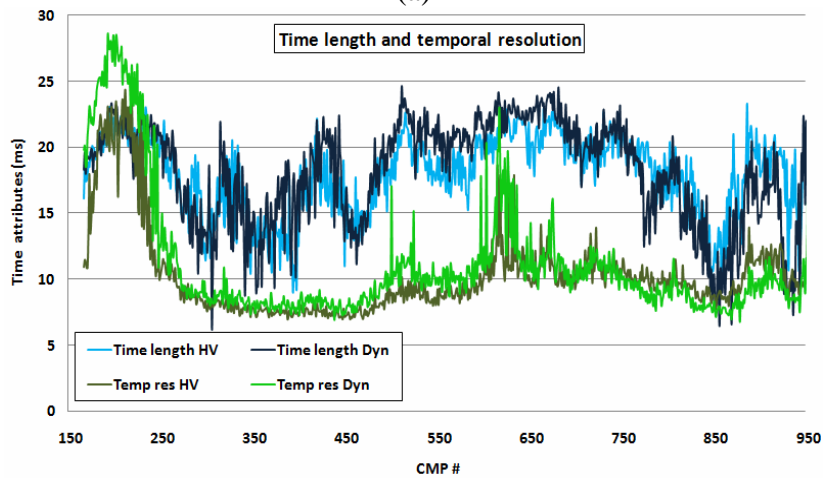


(c)

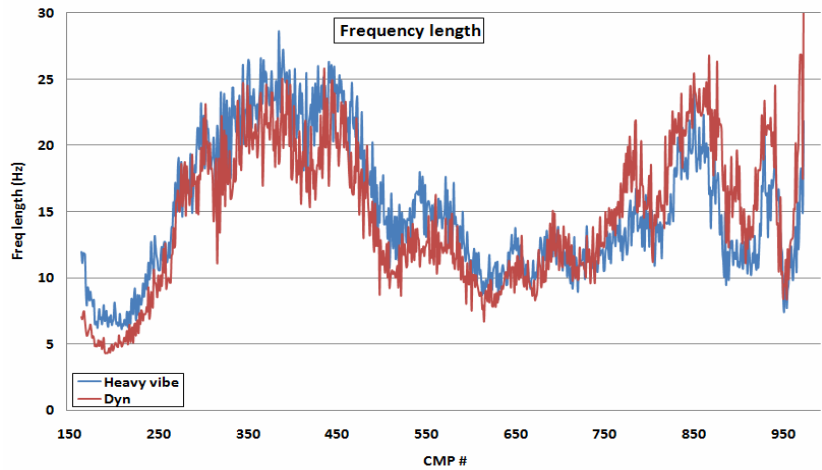
Figure 4.31. Deterministic trace attributes calculated for all CMP locations in the vertical-component stacked sections: (a) first zero-crossing, (b) bandwidth attributes and (c) total effective bandwidth. For every plot there is a curve corresponding to the vibroseis (HV) and to the dynamite (Dyn) data.



(a)

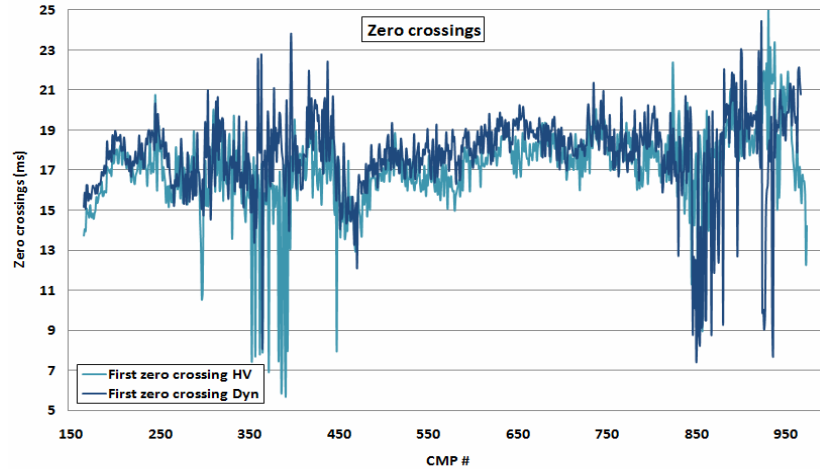


(b)

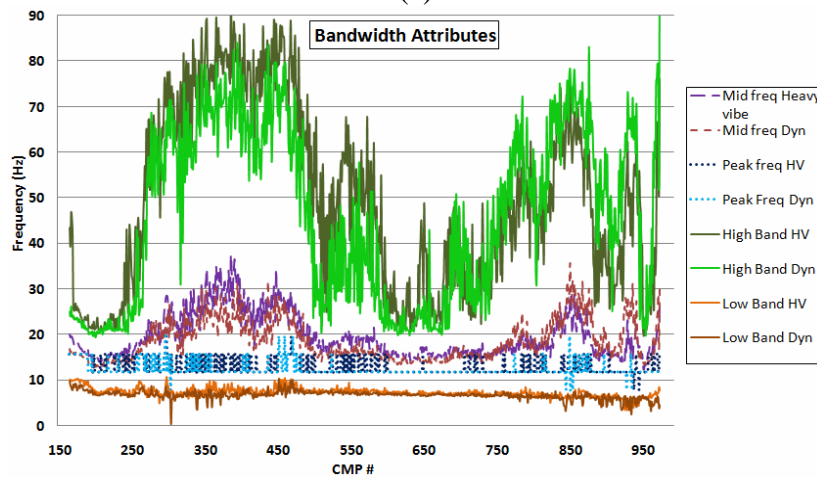


(c)

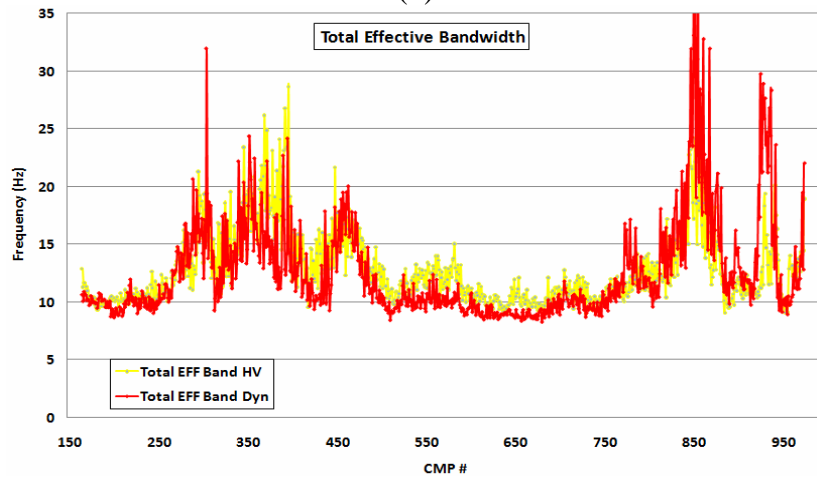
Figure 4.32. Deterministic trace attributes calculated for all CCP locations in the radial-component stacked sections: (a) Resolving factor, (b) time length and temporal resolution, and (c) frequency length. For every plot there is a curve corresponding to the vibroseis (HV) and to the dynamite (Dyn) data.



(a)



(b)



(c)

Figure 4.33. Deterministic trace attributes calculated for all CCP locations in the radial-component stacked sections: (a) first zero-crossing, (b) bandwidth attributes and (c) total effective bandwidth. For every plot there is a curve corresponding to the vibroseis (HV) and to the dynamite (Dyn) data.

4.6 Conclusions

Seismic data generated with three seismic sources was recorded under similar conditions for receivers, recording systems, and timing. An area, some of which contain University of Calgary mineral rights, located in the Spring Coulee area in Alberta, was used as the test site for this experiment. Additional datasets were acquired during this test with the objectives of comparing different types of receivers and recording systems.

Analyses of these seismic sources (heavy vibroseis, dynamite and mini vibroseis) were undertaken to conduct a comparative study in this particular environment in order to study in detail the characteristics of each one, and its capability for generating converted-waves. The qualitative analyses included visual inspections of raw shot gathers, fully processed unmigrated stacked sections and filter panels. The quantitative analyses included f-x analyses of raw shot gathers and unmigrated stacked sections, signal and noise estimation, and quantified attribute measurements to define which source performs better in terms of seismic resolution.

The comparison was divided in two parts, attending to the difference in data quality and record length. In the first part the heavy vibroseis and the explosive source were compared, while all three sources were compared in the second part.

Based on visual inspections made at the shot gather level to determine signal strength, shot-to-shot variation, frequency content, and any variations in noise; the explosive data appear slightly generally superior to vibroseis data. However, the quality of the dynamite records is variable, which could be a consequence of the different near-surface media where the shots are located. This last observation is not the case for the radial channel data, where the consistency from shot to shot looks similar.

The vertical and radial channel unmigrated stacked sections indicate an apparent improvement in resolution for the heavy vibroseis in the shallow portion of the section (0-0.5 s), and for the dynamite in the deeper part of the section (0.5-2 s). For the target zone (0.5-1.5 s), improved bandwidth and S/N was achieved with the dynamite source.

Average amplitude spectra were calculated for the raw shot gathers on three windows corresponding to data, noise and first breaks (for the vertical channel) and refraction event (for the radial channel). The data window seems to show slightly higher power for the dynamite in the very low and very high frequencies, while both sources (dynamite and heavy vibroseis) have a similar amplitude values in the 10-40 Hz range. In the radial channel, the amplitudes are very similar but in the 10-25 Hz range. For the noise window in the vertical and radial channels, the vibroseis shows much stronger Rayleigh waves for frequencies higher than 20-25 Hz. Similar power values for the first breaks (vertical channel) and refraction event (radial channel) are seen in the 5-25 Hz range.

An estimation of the signal bandwidth was achieved using the corner frequency concept on the average amplitude spectrum calculated on a data window for the raw shot gathers. Other methods used for this estimation included the realized signal band using f-x analysis of unmigrated stacked sections (amplitude spectrum and phase coherence), and filter panels of a raw shot gather. The results of this analysis indicated an apparent signal bandwidth of 70-75 Hz for the P-wave and 30-40 Hz for the converted wave. Similar signal levels for both sources are observed below 45 Hz for the vertical channel and below 20 Hz for the radial channel. However, the bandwidth of the dynamite is slightly higher for both components.

A signal and noise estimation analysis was done to determine similarity between both sources. The similarity of the estimates for both channels and type of sources indicated that there is not much difference in the contents of coherent and random events in the stacked sections of both sources.

To summarize, our source comparison results showed how the dataset quality of the dynamite and heavy vibroseis sources for P- and converted-wave generation are very similar; only small resolution improvements are achieved with the dynamite. Based on our observations, we could say that in terms of data quality any of the sources could be used; however, these criteria should be judged with respect to the total cost of the project and the most appropriate source for the project budget. In general terms, the source cost differs if 2D or 3D seismic projects are considered. For 2D projects the vibroseis source might be the most cost-effective option, considering the cost of shot-hole drilling and larger field crews required for dynamite, but dynamite is shot faster so less recording crew time is needed and the use of vibroseis might depend on topography, and how fast can trucks go around obstacles (e.g. river, valleys). However, for 3D projects the expense of dynamite for 2D projects is compensated by a higher and more stable production rate (about 1.5 times higher than with vibroseis due to shorter registration times).

Chapter Five: SEISMIC SOURCE COMPARISON FOR COMPRESSIONAL AND CONVERTED-WAVE GENERATION AT SPRING COULEE, ALBERTA.
Part II: Heavy vibroseis-dynamite-Envirovibe.

The objective of the second part of the source comparison is to show the benefits and limitations of the use of 18,000-lb vibroseis trucks (IVI-Envirovibe) for exploration projects that involve the use of converted-wave data. A very detailed comparison of the 48,000-lb vibroseis and explosive source was presented in Chapter 4, Part 1 of the analysis. In this chapter, we still compare these two datasets but focus more on the differences with the mini vibroseis data.

Beforehand, we know that the quality of the Envirovibe data is not the best because it was a test line objective during the acquisition; added to the fact that not all the receivers were planted. However, having this type of source recorded with the same system as the other two, and with enough data to establish a comparison, it was decided to present one of the few case studies where two commonly employed exploration sources are compared with a type of source used for shallow targets and environmental and engineering applications. Our analysis is going to be concentrated on the shallow section of the data and include some of the tools presented in the analysis of part one, such as f-x average Fourier analysis on raw and processed data and filter panels.

The maximum number of traces per shot is 470 traces, so the fold for this data is decreased. For the vertical and radial channels of the mini vibroseis only 3 s of data were recorded, so all the datasets were shortened to 3 s.

5.1 Raw data: Characteristics of different types of signal and noise

Vertical channel: A first observation about the Envirovibe data is the higher content of random noise and the weaker-looking reflections compared to the other two sources (Figure 5.1c). However, signal can be observed clearly up to 1.5 s as in the other two sources (Figure 5.1a and 5.1b). The characteristics of the coherent noise are very similar to the heavy vibroseis data, with less prominent groundroll and low-frequency noise but stronger airwaves and high-frequency noise especially at short offsets and deeper times.

The shot-to-shot variability of the mini vibroseis is evaluated comparing shots from different locations along the line. Figure 5.1 presents three shots located at both ends and the centre of the coincident source locations for the three sources. For both vibroseis record sets (Figure 5.1a and 5.1c), it appears to be more consistent in terms of the data character and in the level and nature of the ground roll. The amplitude levels from shot to shot are also more consistent than for the dynamite data.

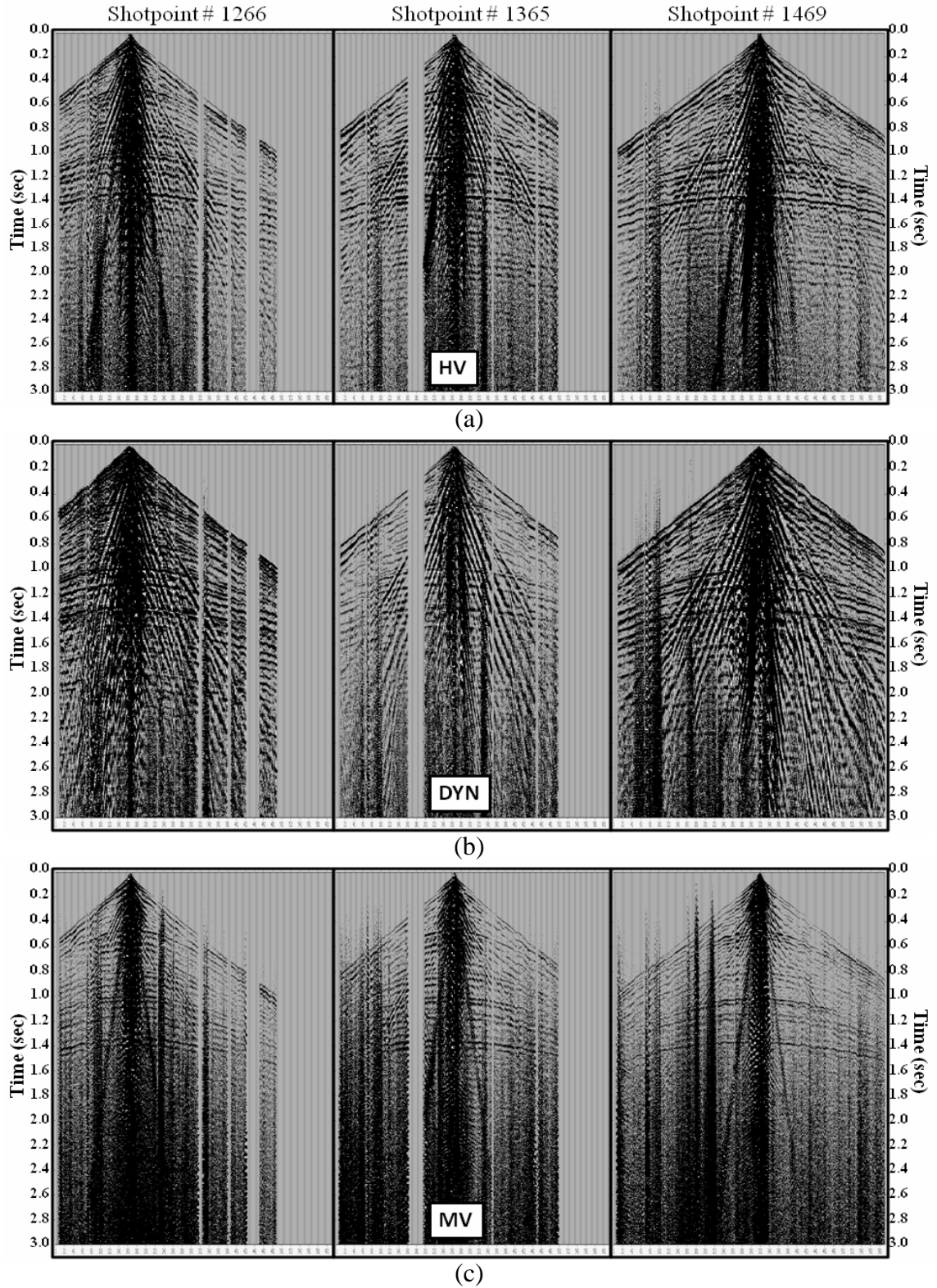


Figure 5.1. Three vertical-component raw shots are compared along the line. In (a), shots from the beginning, middle and end of the heavy vibroseis line are shown. In (b) and (c), the same shot locations but for the dynamite and mini vibroseis lines are shown, respectively.

Figure 5.2 presents a direct comparison of half of a split spread record for the three source types. In this figure the differences in signal to noise ratios and signal penetration between the mini vibroseis and the other two sources are more evident.

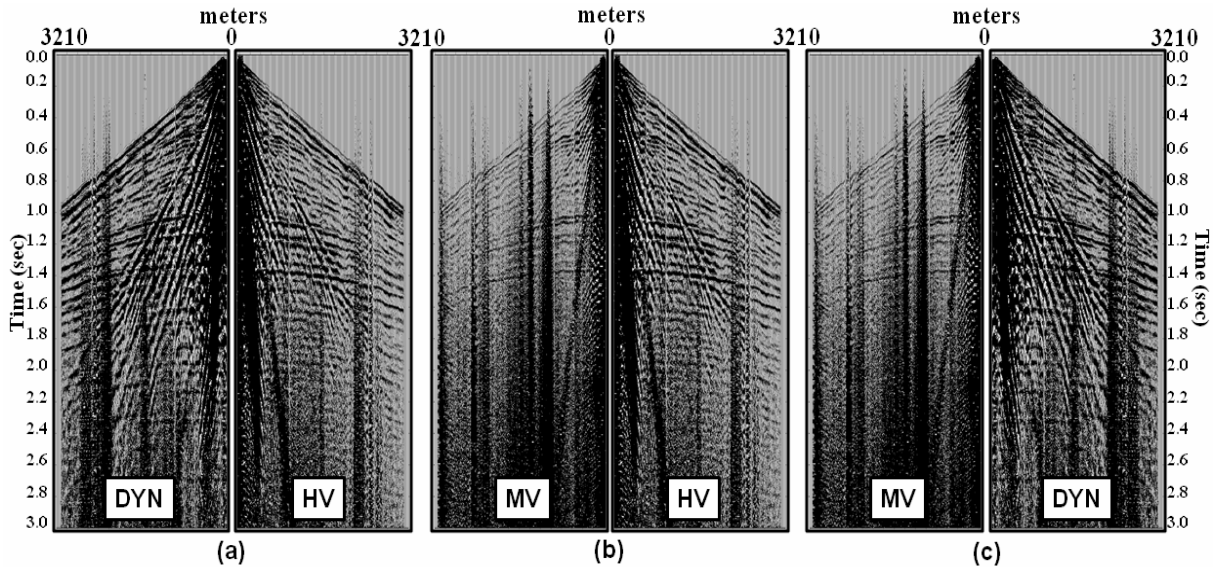


Figure 5.2. Comparison of two vertical-component raw shot gathers. In (a), half of a split-spread record from the dynamite and heavy vibroseis lines with the lateral coordinates reversed to ease the comparison. The same comparison is shown in (b) but for the mini vibroseis and heavy vibroseis data. The final comparison between the mini vibroseis and the dynamite is shown in (c).

Radial channel: In the radial channel, the differences with the mini vibroseis data are more dramatic (Figure 5.3). Not many reflections can be identified and the amplitude level shows a big difference with respect to the other two sources. Only weak data could be observed at the near offsets and early times (Figure 5.3c). The random noise level appears to be stronger than for the vertical channel. Despite the low signal to noise ratio of the Envirovibe data, there is consistency from shot to shot.

The familiar comparison of half a split spread shot is shown in Figure 5.4 for the radial channel. This figure shows in a more illustrative way the observations presented in the previous paragraph.

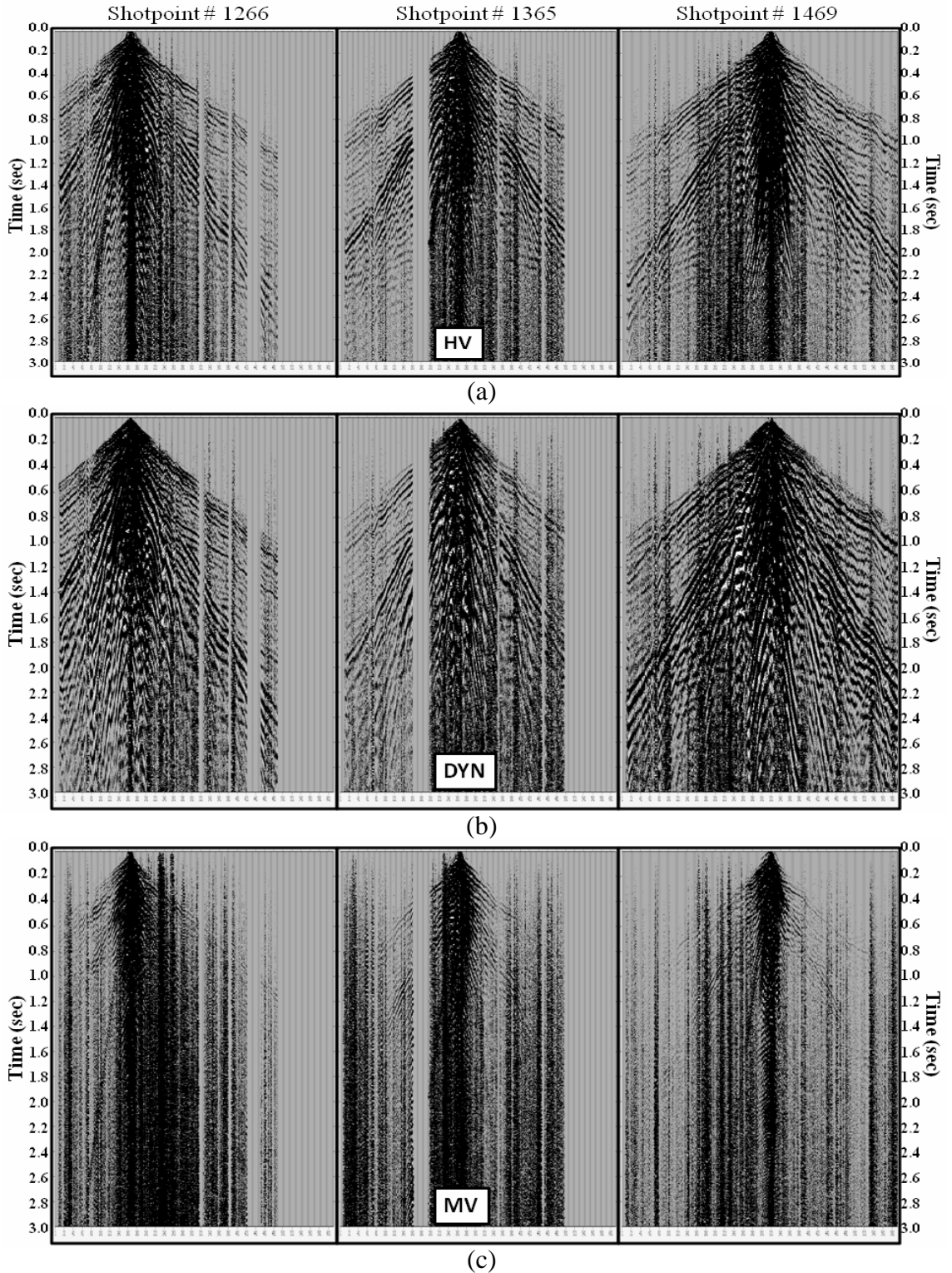


Figure 5.3. Three radial-component raw shots are compared along the line. In (a), shots from the beginning, middle and end of the heavy vibroseis line are shown. In (b) and (c), the same shot locations but for the dynamite and mini vibroseis lines are shown, respectively.

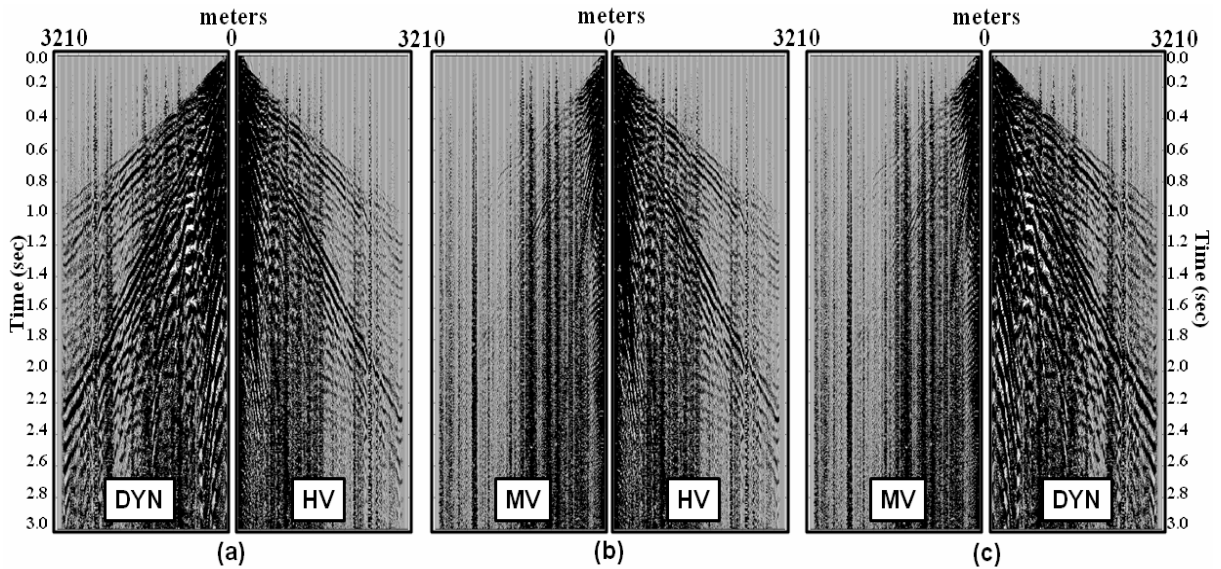


Figure 5.4. Comparison of two radial-component raw shot gathers. In (a), half of a split spread record from the dynamite line and heavy vibroseis line with the lateral coordinates reversed to ease the comparison. The same concept is shown in (b) but for the mini vibroseis and heavy vibroseis data. The final comparison between the mini vibroseis and the dynamite is shown in (c).

5.2 Unmigrated stacked sections:

Vertical channel: Two portions of the stacked sections are presented in Figures 5.5 and 5.6. Figure 5.5 shows the shallow portion from 0-1 s and Figure 5.6 shows the portion of the section corresponding to the target zone (0.5 to 1.5 s). In Figure 5.5, the events between 0-0.5 s look more continuous and stronger than those from the heavy vibroseis and dynamite data. The events between 0 and 0.5 s are similar for the heavy and mini vibroseis.

Between 0.6 and 0.8 s the heavy vibroseis events appear more continuous and resolved than those from the mini vibroseis, which in turn are better than the dynamite data. At later times (0.8-1 s), the dynamite shows better energy penetration with higher vertical resolution and more lateral continuity of the events. The mini vibroseis shows lower high amplitudes and fewer events at this deeper part of the section.

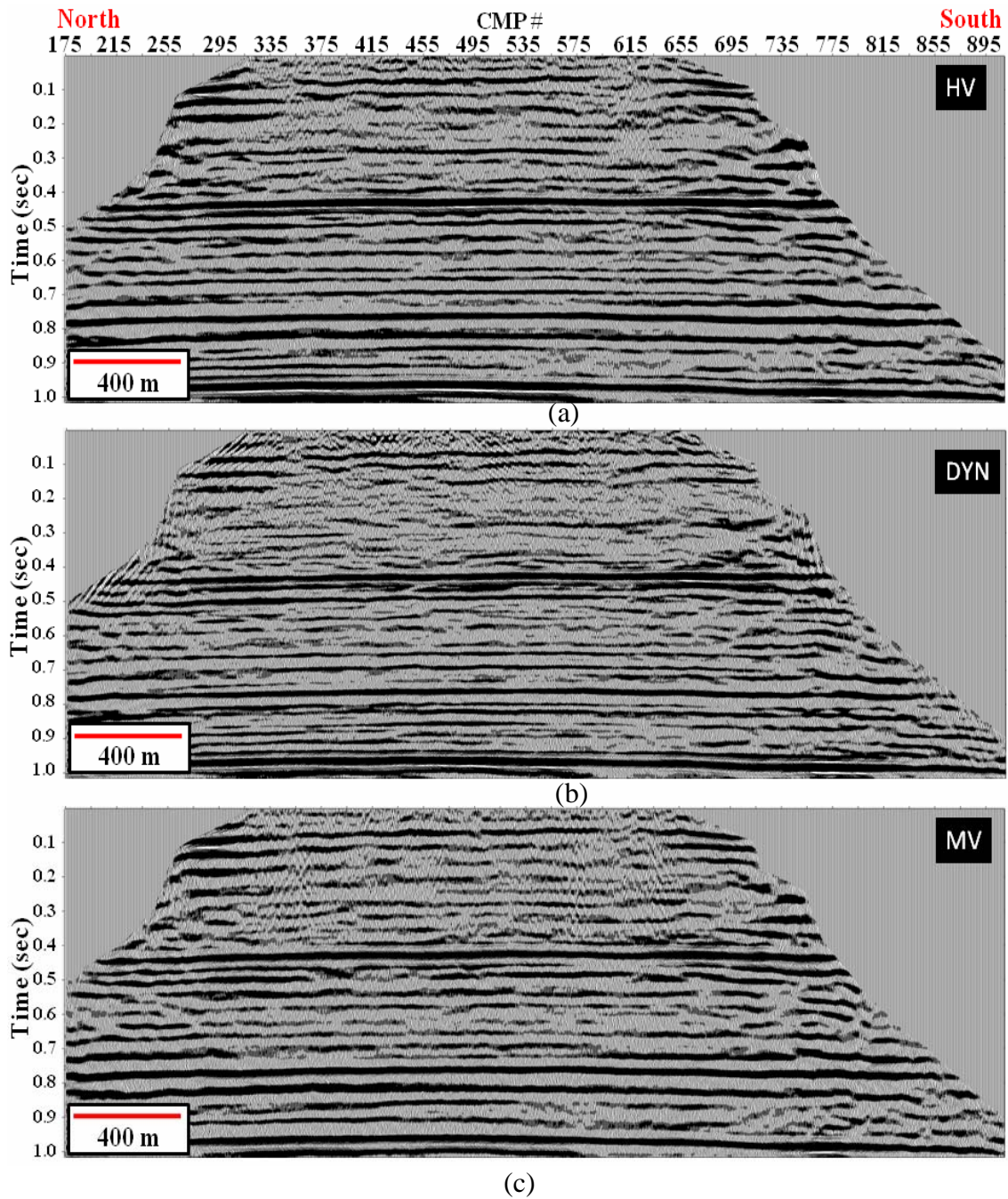


Figure 5.5. Portions of the amplitude- and phase-matched, vertical-component, (a) heavy vibroseis, (b) dynamite and (c) mini-vibroseis stacked section, zoomed in on the early times of the section (0-1000 ms).

In Figure 5.6, the mini vibroseis reveals all major reflections at less than 1 s, some of them with better continuity but lower frequency content than the same events in the

heavy vibroseis data. The dynamite maintains better resolution at times below 1 s, followed by the heavy vibroseis data, and with the mini vibroseis worst.

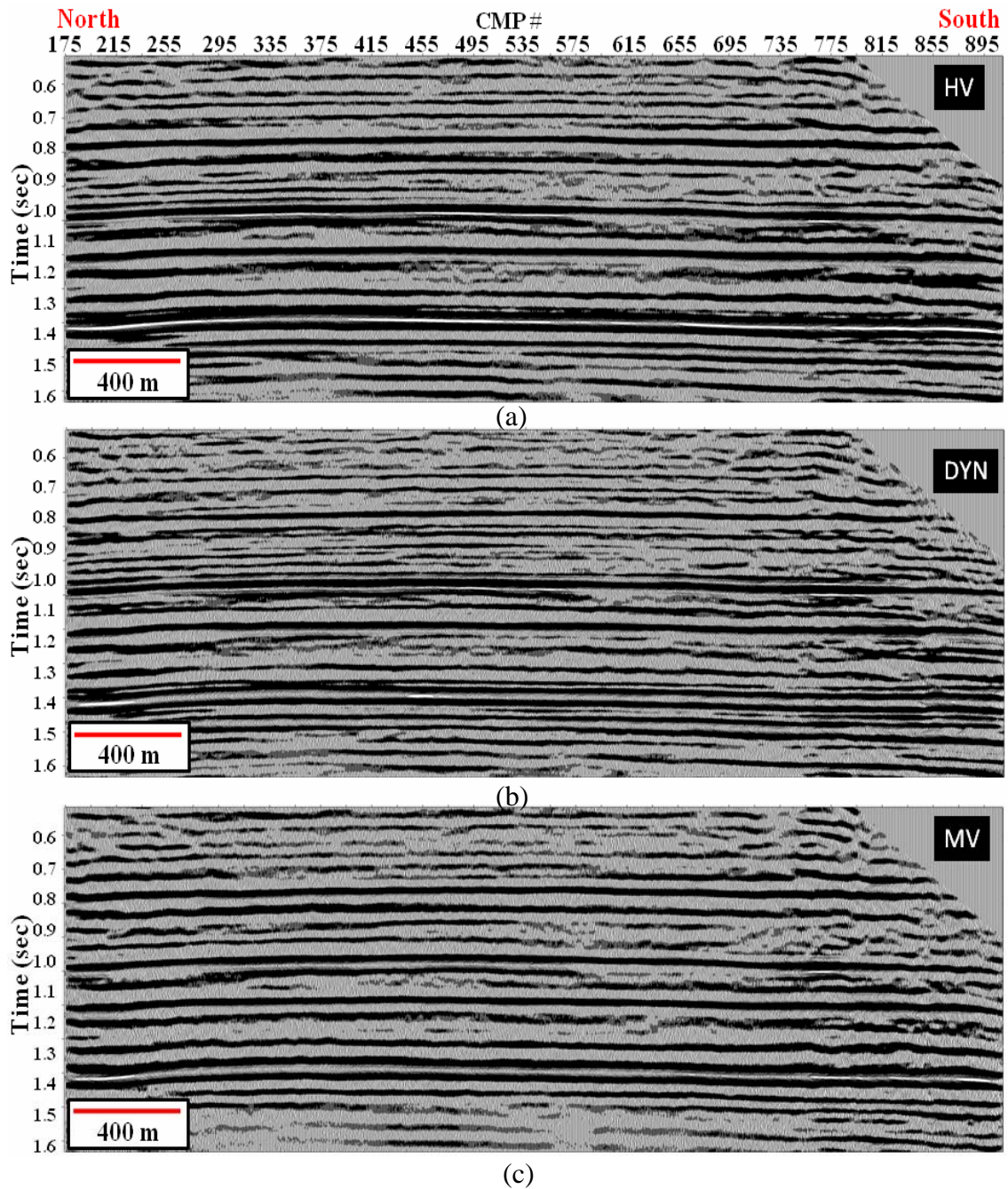


Figure 5.6. Portion of the amplitude- and phase-matched, vertical-component, (a) heavy vibroseis, (b) dynamite and (c) mini-vibroseis stacked section, zoomed in on the zone of interest (500-1500 ms).

Radial channel: For the radial channel, the mini vibroseis section is of much lower quality (Figure 5.7). No energy can be observed below 1s. The strongest reflectors are observed at the ends of the lines. There are not many continuous reflectors to be seen at the centre of the section.

Compared to the other two sources and based on the stacked section quality, we would not choose the mini vibroseis as an optimum source for converted-wave generation.

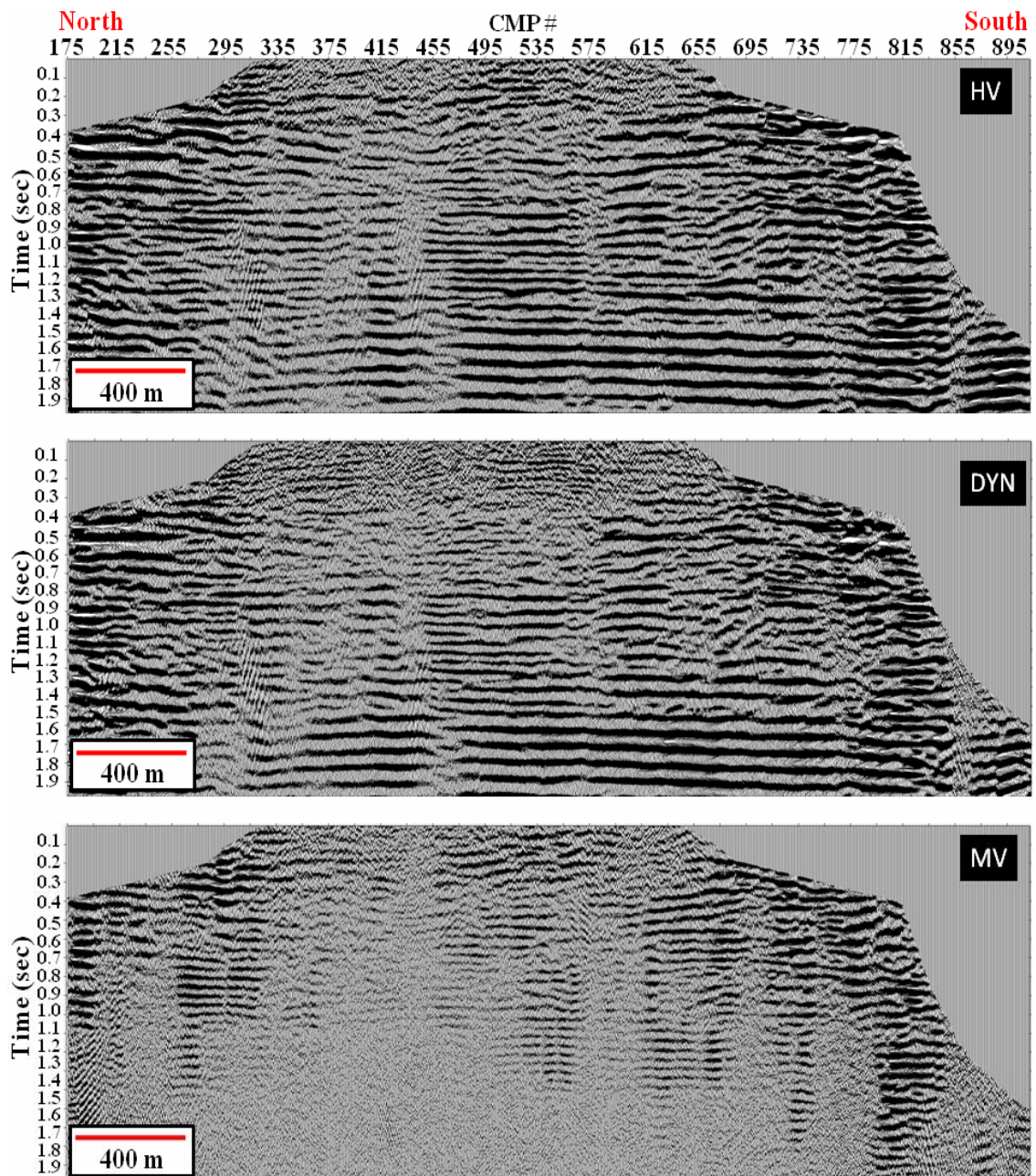


Figure 5.7. Portions of the amplitude- and phase-matched, radial-component, (a) heavy vibroseis, (b) dynamite, and (c) mini-vibroseis stacked sections, zoomed in on the early times (0-1900 ms).

5.3 Seismic signal band estimation using f-x spectra

Figure 5.8 shows the windows selected to calculate the average amplitude spectra on areas corresponding to vertical channel data, noise (groundroll or air wave), and first breaks, and the same events for the radial channel except for the selection of a refraction event instead of the first breaks. Selecting these windows allow us not only to estimate potential bandwidth; it also allows us to determine whether the mini vibroseis source can reproduce the same seismic events (signal and noise) with similar characteristics to the heavy vibroseis and dynamite.

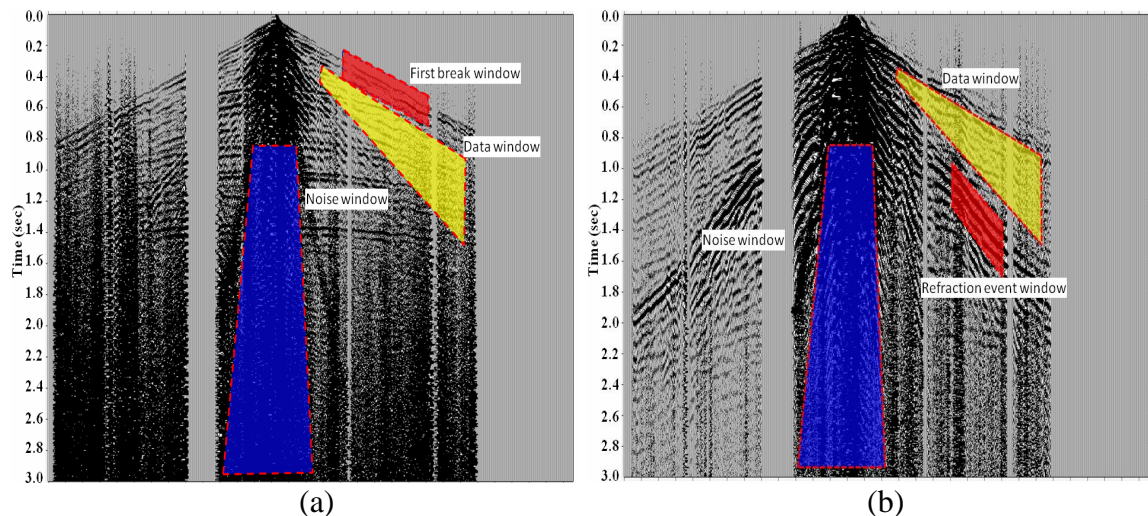


Figure 5.8. Analysis windows used for calculating the average Fourier spectra amplitudes for heavy vibroseis-dynamite-mini vibroseis data comparison. The three zones for the vertical-component raw shot record are shown in (a) and the three zones for the radial-component raw shot record in (b).

5.3.1 *F-x analysis of the raw shot gathers*

Vertical channel: An average Fourier amplitude spectrum was calculated on a raw shot gather for a window corresponding to what was hoped to be subsurface reflections (Figure 5.9a). The three curves have the same shape up to 50 Hz, but from 0 to 20 Hz the amplitudes are slightly lower for the mini vibroseis. After 50 Hz, the mini vibroseis curve shows greater amplitudes with differences of up to 15 dB. At 50 Hz it looks like the

corner frequency is reached by the Envirovibe. The big difference in the amplitudes after the Envirovibe reaches the corner frequency might indicate higher levels of background noise.

The same analysis was done in windows covering a portion of the first breaks and noise (Figure 5.9c and 5.9e). In the first window (Figure 5.9c), the behaviour of the curves for the three sources is similar between 20 and 50 Hz. At low frequencies, the amplitude levels are lower for the mini vibroseis data, but at frequencies greater than 50 Hz they are higher.

In the window located in the noise area (Figure 5.9e and f), the mini vibroseis shows a much stronger Rayleigh wave with higher frequencies for the vertical and radial channels. From 0 to 20 Hz, there is apparently no Rayleigh wave for the vertical channel; this is the case for the radial channel but between 0 and 30 Hz.

Radial channel: The same Fourier analyses were done in the radial channel, for signal, refracted wave, and noise windows (Figure 5.9). In the data window (Figure 5.9b), the same observations for the vertical channel applied to the radial channel, with the difference that after the corner frequency at 50 Hz the level of background noise appeared much greater than for the P-wave.

For the refracted arrival window the event selected could be a P-S-P refraction that appears strongly in both datasets. In this window, there is no similarity between the mini vibroseis, the heavy vibroseis and dynamite (Figure 5.9d). The amplitudes are much higher with almost constant amplitude values across the frequency range. A lack of low-frequency is observed for this refraction event in the mini vibroseis data.

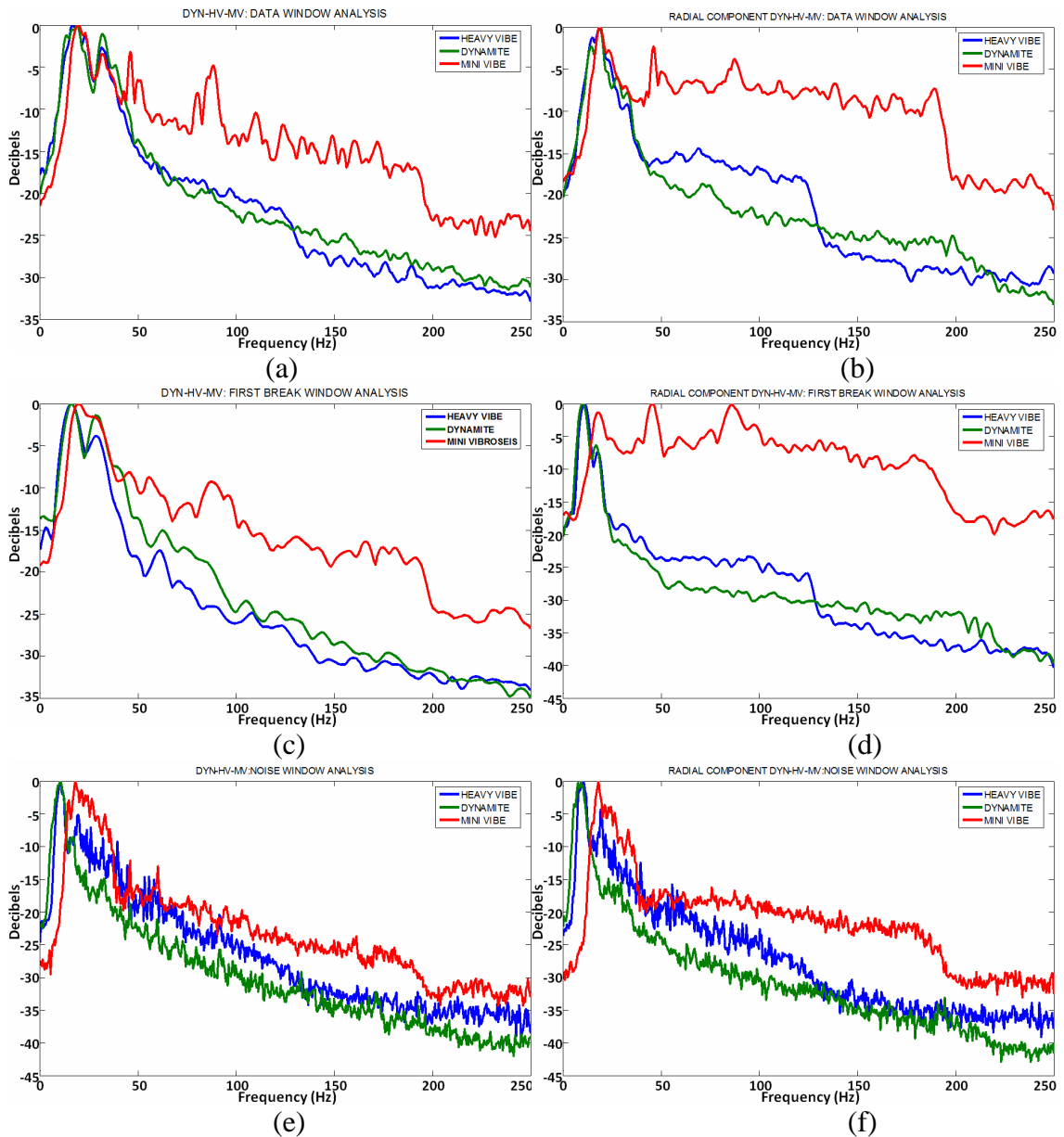


Figure 5.9. Average Fourier amplitude spectrum of a raw shot gather for the vertical channel ((a), (c) and (e)) and radial channel ((b),(d) and (f)) of the heavy vibroseis, dynamite data, and mini vibroseis, with windows corresponding to: (a) and (b) signal only area, (c) and (d) first break area and (e) and (f) groundroll/noise area.

5.3.2 *F-x analysis of the unmigrated stacked sections*

Vertical channel: An f-x analysis of both unmigrated, unfiltered stacks is shown in Figure 5.5 to estimate the realized signal band.

While in the dynamite and heavy vibroseis there is a drop in spectral power at 45-50 Hz (Figure 5.10a and 5.10c), for the mini vibroseis this happens at about 30-35 Hz (Figure 5.10e). Above this frequency there is no signal.

The lower frequencies show up at around 18 Hz, while for the other two sources the events start to be seen at 8-10 Hz.

Figures 5.10(b), (d) and (f) contrast the phase coherences of the three datasets. For the heavy vibroseis and dynamite, there is a reduction in phase coherence at around 60 Hz; for the mini vibroseis this reduction is seen at 40 Hz and is coincident with the drop in spectral power. However, subtle phase coherence persists up to at least 95 Hz for the heavy vibroseis and dynamite, and up to 70 Hz for the mini vibroseis.

These observations could be interpreted as a similar signal level below 40 Hz for the three sources.

Radial channel: The same f-x analysis for both unmigrated, unfiltered CCP stacked sections is shown on Figure 5.11. The f-x amplitude spectrum for the mini vibroseis shows little signal between 12 and 25 Hz (Figure 5.11e). For the other two sources, clear and strong signal is shown in this range (Figure 5.11a and 5.11c). One possible explanation is that this is caused by the lack of reflection continuity in the mini vibroseis data.

Figures 5.11(b), (d) and (f) contrast the phase coherence of the three datasets. The mini vibroseis data shows almost no coherent events, the only weak and coherent event is

seen for frequencies between 15-20 Hz and in the 500-800 CMP range; this same event is seen in the CMP range 200-500 but with less coherency (Figure 5.11f).

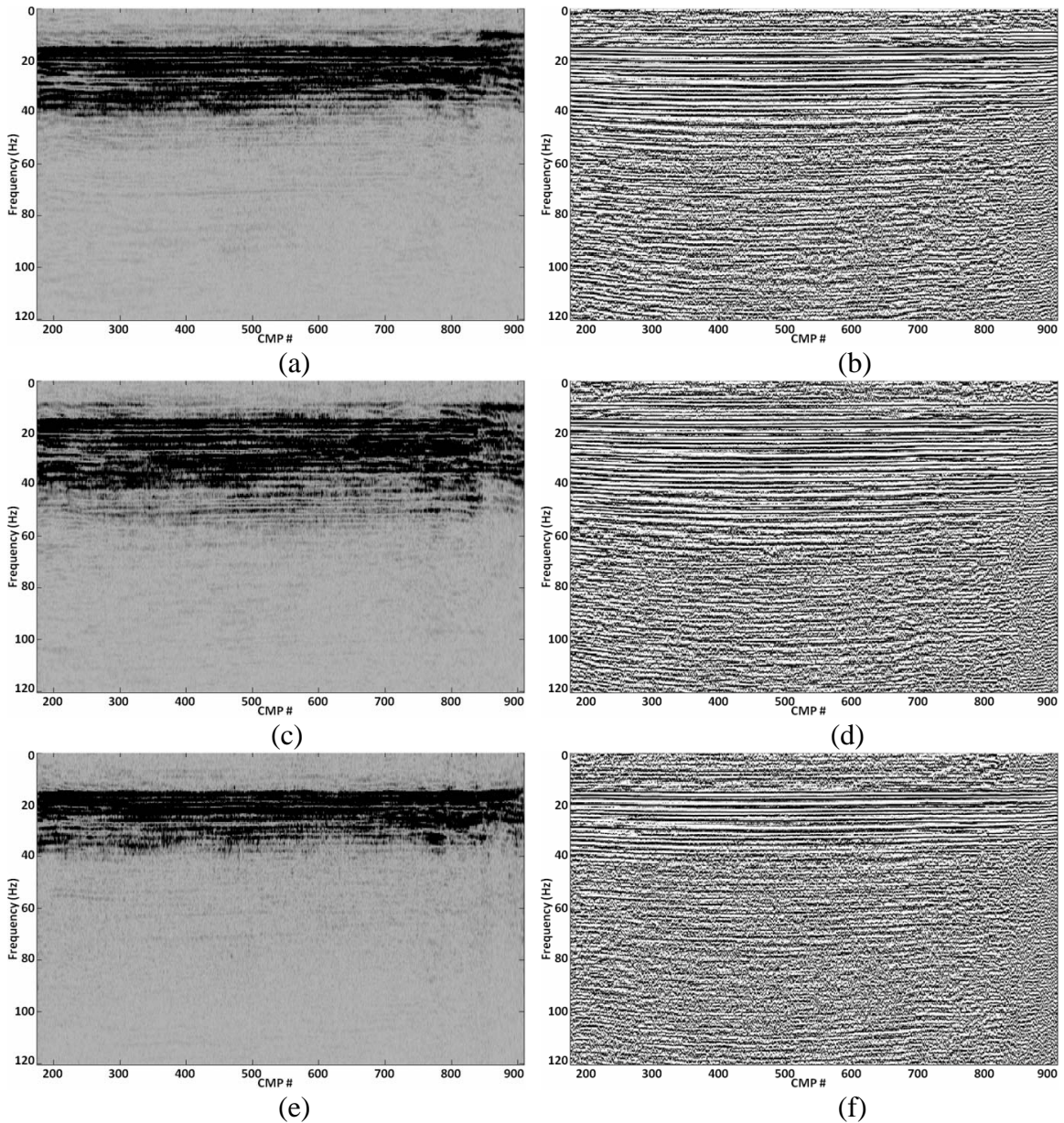


Figure 5.10. F-x spectral analysis for the final unmigrated, unfiltered P-wave stack for heavy vibroseis, dynamite and IVI-mini vibroseis data comparison computed over the time zone 432-1467 ms. The f-x amplitude spectrum for the heavy vibroseis is shown in (a); (c) and (e) shows similar spectra for the dynamite and mini vibroseis data, respectively. In (b), (d) and (f) are shown the f-x phase spectra corresponding to (a), (c) and (e), respectively.

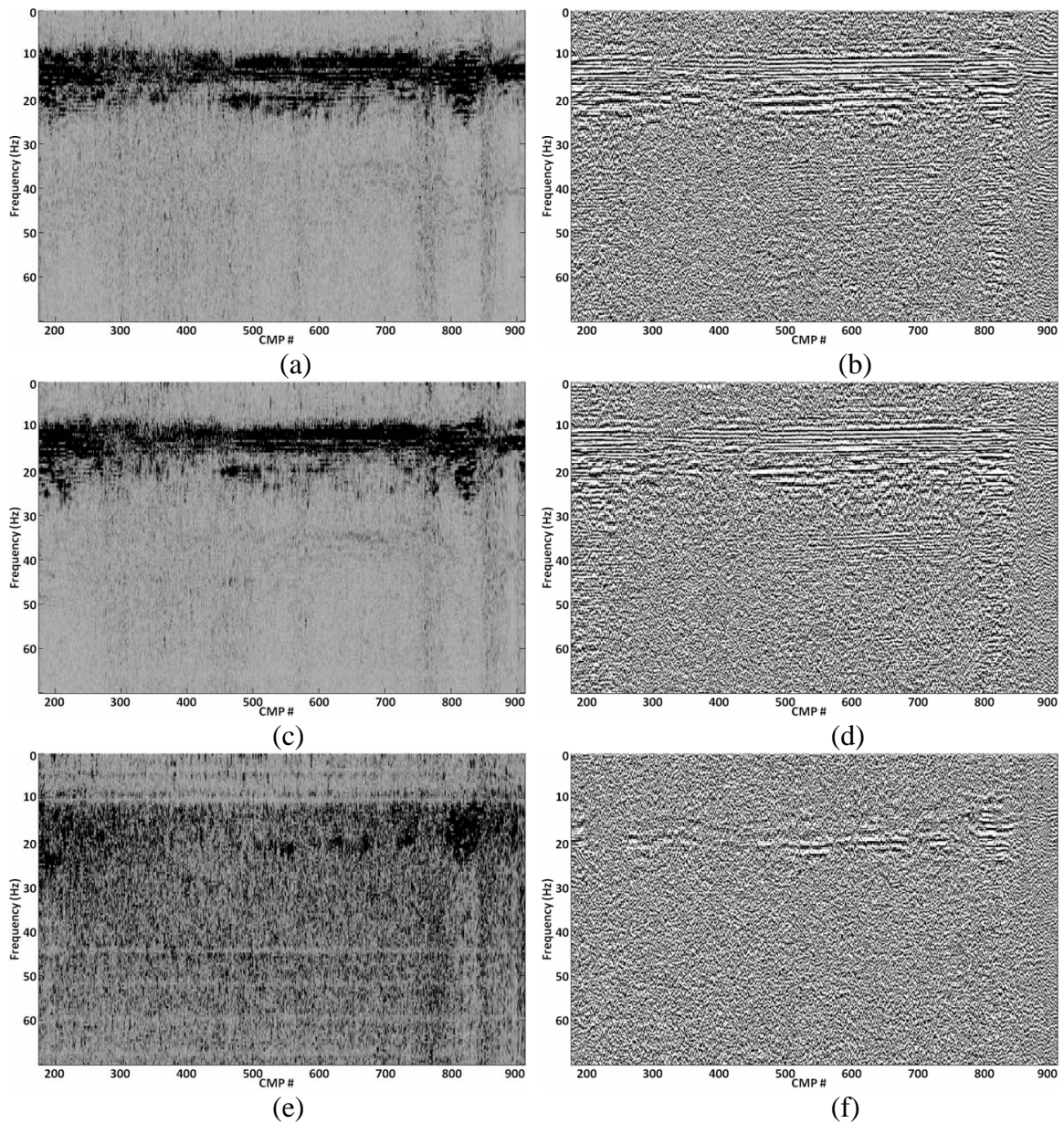


Figure 5.11. F-x spectral analysis for the final unmigrated, unfiltered PS-wave stack for the heavy vibroseis, dynamite and IVI-mini vibroseis data comparison computed over the time zone 700-2500 ms. The f-x amplitude spectrum for the heavy vibroseis is shown in (a); (c) and (e) shows similar spectra for the dynamite and mini vibroseis data, respectively. In (b), (d) and (f) are shown the f-x phase spectra corresponding to (a), (c) and (e), respectively.

5.4 Frequency bandwidth estimation using filter panels

The same filter panel ideas presented on Part 1 of the source comparison (chapter 4) are used in Part 2 as methods for signal bandwidth determination.

Figures 5.12 and 5.13 show the filter panels created for the vertical and radial channel of a raw shot gather. In each case three-panel sets corresponding to the heavy vibroseis, dynamite and mini vibroseis sources were created.

Vertical channel: Signal is present from top to bottom in the 20-40-Hz band for all three sources. In the mini vibroseis 0-20 Hz band there is some signal between 1 and 1.5 s but not above it (Figure 5.12c). In the 40-60-Hz band not much signal is noted below 0.5 s, with a weak event seen at 1 s. Finally the 60-80-, and 80-100-Hz bands show no signal, only noise.

The filter panels indicate that the signal band for the mini vibroseis is confined at medium frequencies (10-45 Hz). These results corroborate some of the previous observations from the f-x Fourier analysis, where the potential and realized bandwidths were around 40-50 Hz.

Radial channel: For the radial channel there is not a single panel where signal is present from top to bottom. In these panels there is not much evidence of the presence of signal. There is a big contrast between the noise and signal amplitudes that makes the signal difficult to be seen on these panels.

The 20-40-Hz band shows weak signal up to 1 s for the mini vibroseis (Figure 5.13c). Looking at the raw data, it is also difficult to see any signal above the noise.

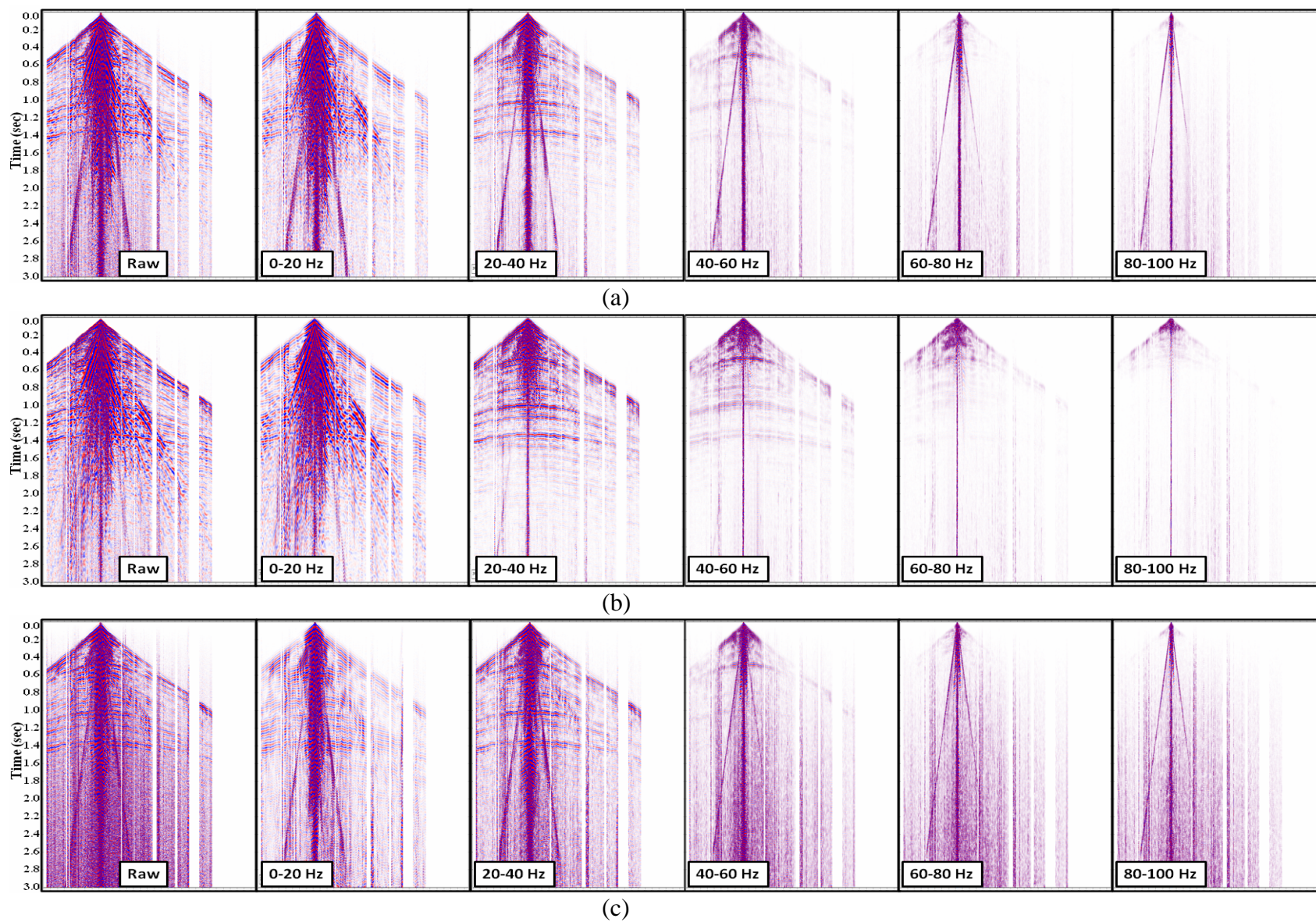


Figure 5.12. Filter panels for the vertical component of a raw common shot gather from (a) the heavy vibroseis, (b) dynamite data, and (c) mini vibroseis data.

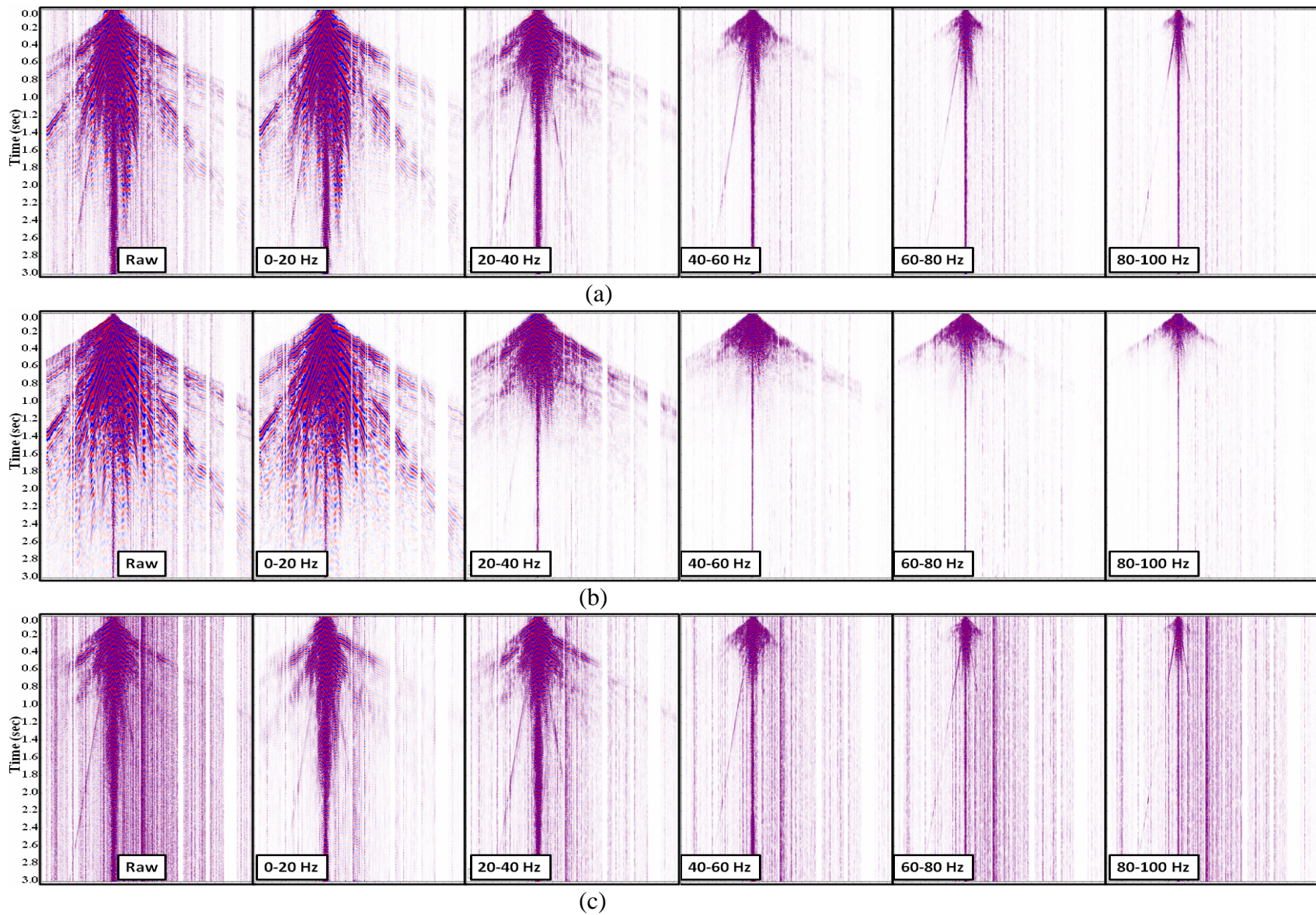


Figure 5.13. Filter panels for the radial-component of a raw common shot gather from (a) the heavy vibroseis, (b) dynamite data, and (c) mini vibroseis data.

5.5 Conclusions

Most of the analyses undertaken to compare the heavy vibrator and the dynamite were repeated to include the 3 s of data acquired with our mini vibroseis. The analyses were concentrated on the shallow section of the data. The vertical-component raw shot gathers showed data up to 1.5 s, and indicated a higher content of random noise and weaker looking reflections in comparison with the other two sources. The radial channel raw shot gather did not contain many reflectors, only weak data at early times and near offsets could be observed.

The mini vibroseis vertical-component unmigrated stacked sections corroborated some of the raw gather observations: data were confined to the first 1.5 s of data, with lower resolution. For the radial channel, the section is of much lower quality than the other two sources, with no energy below 1 s and discontinuous reflectors.

Once again, average amplitude spectra were calculated for the raw shot gathers on three windows for both components. In the vertical-component, the data window showed higher amplitudes for frequencies above 50 Hz that might indicate higher levels of noise; and lower power for frequencies between 0-20 Hz. The noise window indicated much stronger Rayleigh waves for the minivibe for frequencies higher than 20 Hz. In the radial channel, there were no similarities between the three sources for the refracted arrival window; for the data and noise windows, similar observations to the vertical-component applied.

For the signal bandwidth estimation of the mini vibroseis we used the same methods employed in the first comparison. The results of these analyses indicated an apparent signal bandwidth of 18 to 40 Hz for the P-wave and little signal for the range

12-25 Hz for the converted wave. For the P-wave, low frequencies are not observed, while for the converted waves there are not many coherent events.

The mini vibroseis proved to be a good source for generating near-surface P-wave data but not very efficient for converted-wave generation.

Chapter Six: CONCLUSIONS AND FUTURE WORK

6.1 Thesis summary

Seismic data acquisition is a topic under continuous evolution. Recent technological advances in the field have brought a renewed interest in converted-wave exploration. These advances include experimenting with new acquisition systems such as land streamers and evaluating alternate seismic sources together with optimal acquisition parameters using side-by-side comparisons.

The feasibility of using land streamer systems for converted-wave acquisition was tested in a survey site near Priddis, Alberta. In August 2006, the first land streamer test was acquired to study the capabilities of this acquisition technique for imaging the upper 50 m of the subsurface. During March 2008, a second test was conducted in the same location but with the objective of doing a side-by-side comparison of a planted 3-C geophone line and a land streamer line.

The first land streamer test demonstrated how useful this system is for acquiring near-surface data with significant reductions in time and labour. Even with the limited configuration available, having only 20 receivers and short offsets, it proved capable of recording seismic reflections of the first 50 m of the weathering layer.

The second land streamer test allowed a direct comparison between 3-C data acquired with a planted-geophone line and a land streamer system. The various seismic events on the raw shot gathers were used as a comparison tool, to see if both systems could record them with similar characteristics. This analysis was complemented by generating average Fourier amplitude spectra of these same events.

The raw shot gathers, the spectra, and the processed unmigrated stacked sections all showed that the vertical component data have similar events and characteristics for

both systems; however, this was not the case for the radial channel. F-x spectral analysis of the planted geophone and land streamer stacked sections revealed that, for the P-wave, the signal levels are similar below 90 Hz, but with higher noise levels for the land streamer sections.

At the same location as the land streamer tests, different types of seismic data were acquired: 2D and 3D shallow surface seismic, and VSP data, with the objective of characterizing the geological and hydrological nature of the Priddis site. The 3D seismic volume was a key tool in correlating the different sets of data and well logs for this site; however, its quality was compromised as a consequence of the acquisition footprint created by the sparse source and receiver line spacing. To improve the image quality and continuity of the shallow events of this volume, we tested F-K-K post-stack footprint removal techniques. Of the various F-K-K filtering options, a post-stack trace interpolator on top of the K-notch filter produced the best results, improving the continuity of some shallow reflectors at 50 and 80 ms. However, acquisition footprint techniques in migrated data are not as effective as when applied to unmigrated data, which is one of the reasons why in our case it was not possible to remove all the aliased energy without harming the signal.

A seismic line was shot at the Spring Coulee site in Southern Alberta to compare three different seismic sources. The first part of the experiment was composed of two 54-shot seismic datasets. These datasets were created to be identical in all respects except that one used a dynamite source, while the other used two 48,000-lb vibroseis. After identical processing, the final stacked sections of the dynamite and vibroseis datasets are very similar in character and temporal resolution. Examination of the P-wave raw shot

records shows that, in terms of frequency content and signal strength, the explosive data appears superior to the vibroseis; however, the quality of the dynamite records is variable. F-x spectral analyses of the raw data and stacked sections reveal that both datasets showed similar characteristics for areas corresponding to noise, data and first breaks for the raw shot gathers. The same is true regarding power and coherence from 10 to 40 Hz for the P-wave stacked section, and from 10 to 25 Hz for the converted-wave stacked section. From our results, we could conclude that in terms of data quality any of the sources could be used; however, these criteria should be judged with respect to the total cost of the project and the most appropriate source for the project budget.

The second part of the experiment included 54-shot seismic datasets of all three sources. The dynamite and heavy vibroseis are once again included, but this time they are compared with an 18,000-lb vibroseis, which is a commonly used source for environmental and engineering applications. Comparisons of raw shot gathers, spectral analyses and stacked sections showed that in the vertical channel, the mini vibroseis data were confined to the first 1.5 s of data, showing the same strong reflectors as the dynamite and heavy vibroseis data. However, the mini vibroseis data showed a higher content of random noise, weaker reflections, and lower resolution in comparison with the other two sources. For the radial channel, the mini vibroseis data is of much lower quality, with no energy below 1 s and discontinuous reflectors. From these results, we concluded that the mini vibroseis is a good source for P-wave energy but not very effective for converted-wave generation.

6.2 Future work

Although our land streamer results demonstrated the versatility of this system and its potential for replacing conventional methods of seismic data acquisition, there are more equipment configurations and acquisition parameters that could be tested. Our experiments showed that conventional and land streamer methods are comparable in terms of data quality, but we did not quantify potential time and labour savings that could be achieved. To test land streamers advantages in terms of time and number, we would need a longer streamer that could acquire longer offsets at a much faster rate, without repeating the source line. To target shallow and deeper targets, we could try a variable receiver spacing within the streamer. Employing different seismic sources and receivers under different near-surface conditions could be a good test to see the effects in the receiver coupling. This last test could help us to validate some of the results presented in Chapter 2.

A unique footprint removal technique was tested in the post-stack migrated volume from Priddis. Applying more advanced techniques to improve the imaging of this volume could help identify sand channel systems, and characterize the Paskapoo formation. Re-processing the pre-stack data might help to reduce the footprint effect; also, the application of footprint removal techniques to pre-stack data might produce more noticeable changes and improvements than those presented in Chapter 3.

Our source comparison showed only slight differences between the heavy vibroseis and dynamite datasets. For our analyses, we assumed that the correct and most standard source and acquisition parameters were chosen for this test; however, vibrator sweep, dynamite charge size, and hole depth testing could improve the performance of

the individual sources and show more noticeable changes when comparing different types of sources.

For future comparisons, increasing the number of acquired shots would allow a higher fold and improve the performance of the signal enhancement processing techniques.

The statics solutions for the P- and converted-wave were good enough for the scope of our objectives; however, refining these solutions might increase or reduce the differences between the datasets.

Post-stack unmigrated data were used for some of our analyses; including pre-stack time migration in the processing sequence could yield better P-wave and converted-wave sections.

REFERENCES

- Anno, P. D., 1987, Two critical aspects of shear-wave analysis: statics solutions and reflection correlations: in Danbom, S. H. and Domenico, S. N. (editors), shear-wave exploration, Society of Exploration Geophysicists Geophysical Development Series, Vol. 1, 48-61.
- Bagaini, C., 2006, Overview of simultaneous Vibroseis acquisition methods: 76th Ann. Meeting, Society Exploration Geophysicists, Expanded Abstracts, 70-73.
- Bally, A. W., Gordy, P. L., and Stewart, G. A., 1966, Structure, seismic data, and orogenic evolution of southern Canadian Rocky Mountains: Bull. Can. Petrol. Geol., 14, 3, 337-381.
- Berkhout, A.J., 1984, Seismic resolution: a quantitative analysis of resolving power of acoustical echo techniques, Geophysical Press Limited.
- Blundun, G.J., 1956, The refraction seismograph in the Alberta Foothills: Geophysics, 11, 3, 828-838.
- Bremner, D.L., Tite, G., Thompson, P., and Brooks, J., 2002, Enhanced signal-to-noise ratio and bandwidth through explosive design: 72nd Ann. Meeting, Society Exploration Geophysicists, Expanded Abstracts, 64-66.
- Brocher, T.M., and Hart, P.E., 1991, Comparison of vibroseis and explosive source methods for deep crustal seismic reflection profiling in the basin and range province: J. Geophys. Res., 96, 18 197-18 213.
- Bühnermann, J., and Holliger, K., 1998, Comparison of high-frequency seismic sources at the Grimsel test site, central Alps, Switzerland: Geophysics, 63, 1363-1370.
- Calvert, A.S., Novak, J.M., Maher, J., and Burch, D.N., 2005, A tale of two surveys: experiences processing two similar but different land 3D-3C MEMS surveys: 75th Ann. Meeting, Society Exploration Geophysicists, Expanded Abstracts, 975-978
- Cieslewicz, D., and Lawton, D.C., 1998, The Blackfoot III buried geophone experiment: The CREWES Research Report, 10.
- Cox, M., 1999, Static corrections for seismic reflection surveys, Society of Exploration Geophysicists Geophysical References Series, 9.
- Damotte, B., and Bois, C., 1990, Near-vertical vibroseis versus large offset dynamite seismic reflection profiling; example of the ECORS northern France profile, in Leven, J. H., Finlayson, D. M., Wright, C., Dooley, J. C., and Kennett, B. L. N., Seismic probing of the continents and their margins: Tectonophysics, 173, No. 1-4, 95-106.

- Davis, T.L. and Lawton, D.C., 1985, Field testing of explosive surface sources in the Canadian thrust belt: *Geophysics*, 50, 56-62.
- Finlayson, D.M., Wake-Dyster, K.D., Leven, J.H., Johnstone, D.W., Murray, C.G., Harrington, H.J., Korsch, R.J., and Wellman, P., 1990, Seismic imaging of major tectonic features in the crust of Phanerozoic eastern Australia: *Tectonophysics*, 173, 211–230.
- Fox, F.G., 1959. Structure and accumulation of hydrocarbons in southern Foothills, Alberta, Canada: *Bull. Am. Assoc. Petrol. Geol.*, 43, 5, 992-1025.
- Gaiser, J.E., 1995, 3-D prestack f-k coherent noise suppression: 65th Ann. Meeting, Society Exploration Geophysicists, Expanded Abstracts, SP1.6, 1354-1357.
- Grasby, S., 2006. Paskapoo Formation – Alberta’s most heavily used aquifer: *The Fossil Water Report*, 1, No. 4, 1-3.
- Hamarbitan, N.S., and Margrave, G.F., 2001, Spectral analysis of a ghost: *Geophysics*, 66, 1267-1273.
- Hildebrand, S.T., 1982, Two representations of the fan filter: *Geophysics*, 47, 957-959.
- Inazaki, T., 2006, High-resolution S-wave reflection survey in urban areas using a woven belt type land streamer: *Near Surface 2006 Expanded Abstracts*, Paper A016.
- Ivanov J., Miller, R.D., Lacombe, P., Johnson, C.D. and Lane Jr., J.R., 2006, Delineating a shallow fault zone and dipping bedrock strata using multichannel analysis of surface waves with a land streamer: *Geophysics*, 71, A39-A42.
- Jahn, F., Cook, M., and Graham, M., 2003, *Hydrocarbon Exploration and Production*, First Edition: Elsevier Science B.V., 17-20.
- Karastathis, V.C., Louis, I.F., Karantonis, G.A., and Apostolopoulos, G.V., 1995, Comparison tests of shallow seismic reflection sources: 57th EAGE Conference & Exhibition, Expanded Abstracts, Paper P035, 2 p.
- Keating, L.F., 1966. Exploration in the Canadian Rockies and Foothills: *Can. J. Earth Sci.*, 3, 5, 713-723.
- Kruppenbach, J.A., and Bedenbender, J.W., 1975, Towed land cable: U. S. Patent 3 923 121. 1976, Towed land cable: U. S. Patent 3 954 154.
- Lawton, D.C., and Harrison, M.P., 1992. A two-component reflection seismic survey, Springbank, Alberta. *Canadian Journal of Exploration Geophysics*, 28, p. 30-43.

- Lawton, D.C., Stewart, R.R., and Bertram, M.B., 2008, 3D seismic surveys for shallow targets: 2008 CSPG CSEG CWLS Convention abstract, 283-286.
- Lawton, D.C., Stewart, R.R., and Bertram, M.B., 2008, 3D seismic surveys for mapping shallow targets: 2008 SAGEEP annual conference abstract, 8 p.
- Link, T. A., 1949, Interpretations of Foothills structures, Alberta, Canada: Am. Assoc. Petroleum Geologists Bull., 33, 9, 1475-1501.
- Lorenzo J.M., Saanumi, A., Westbrook, C., Egnew, S., Bentley, S. and Vera, E.E., 2006, Extensive testing of sled-mounted geophone arrays for near-surface (0-4m) layers in floodplain sedimentary facies: Atchafalaya Basin, Indian Bayou, Louisiana : 76th Ann. Meeting, Society Exploration Geophysicists, Expanded Abstracts, 1496-1499.
- Margrave, G.F., 1999, Seismic signal band estimation using f-x spectra: Geophysics, 64, 251-260.
- Marsden, D., 1993, Static Corrections-a Review, Part I: The Leading Edge, 12, 1, 43-49.
- Marsden, D., 1993, Static Corrections-a Review, Part II: The Leading Edge, 2, 2, 115-120.
- Marsden, D., 1993, Static Corrections-a Review, Part III: The Leading Edge, 12, 3, 210-216.
- Miller, R.D., Pullan, S.E., Waldner, J.S., and Haeni, F.P., 1986, Field comparison of shallow seismic sources: Geophysics, 51, 2067-2092.
- Miller, R.D., Pullan, S.E., Steeples, D.W. and Hunter, J.A., 1992, Field comparison of shallow seismic sources near Chino, California: Geophysics, 57, 693-709.
- Miller, R.D., Pullan, S.E., Steeples, D.W. and Hunter, J.A., 1994, Field comparison of shallow P-wave seismic sources near Houston, Texas: Geophysics, 59, 1713-1728.
- Miong, S., 2008, Borehole Geophysical Methods for Near Surface Characterization: MSc. Thesis, University of Calgary.
- Miong, S., Stewart, R.R., and Wong, J., 2008, Characterizing the near surface with VSP and well logs: 2008 CSPG CSEG CWLS Convention abstract, 346-350.
- Norris, D.K., 1993. Geology and structure cross-sections, Beaver Mines (West Half), Alberta British Columbia; Geological Survey of Canada, Map 183A, scale 1:50,000.

- Ostridge, L.A., and Stewart, R.R., 2008, Spring Coulee, Alberta: Geology, production and potential hydrocarbon bearing zones: 2008 CSPG CSEG CWLS Convention abstract, 432-435.
- Parker, J.C., Pelton, J.R., and Dougherty, M.E., 1993, A versatile shotgun source for engineering and groundwater seismic surveys: *Geophysics*, 58, 1511-1516.
- Pfiffner, O.A., Frei, W., and Valasek, P., 1988, Deep seismic reflection profiling in the Swiss Alps: Explosion seismology results for line NFP 20-EAST: *Geol.* 16, 987-990.
- Pugin, A.J.M., Larson, T.H., Sargent, S.L., McBride, J.H., and Bexfield, C.E., 2004, Near-surface mapping using SH-wave and P-wave land-streamer data acquisition in Illinois, U. S.: *The Leading Edge*, 23, 677-682.
- Pulland, S.E., and MacAuley, H.A., 1987, An in-hole shotgun source for engineering seismic surveys: *Geophysics*, 52, 985-996.
- Quigley, J., and Thompson, P., 2004, A comparison of seismic explosives-a case history: 74th Ann. Meeting, Society Exploration Geophysicists, Expanded Abstracts, 4 p.
- Richards, T.C., 1959. Broadside refraction shooting: *Geophysics*, 24, 4, 725-748.
- Scheffers, B.C., Otte, W.M.A., Meekes, S.A.C. and Arts, R.J., 1997, Special aspects of acquisition of 2D HRS data using dynamite and Vibroseis sources: 59th EAGE Conference & Exhibition, Expanded Abstracts, Paper P045, 2 p.
- Schrodt, J.K., 1987, Techniques for improving vibroseis data: *Geophysics*, 52, 469-482.
- Seeman, B., and Horowicz, L., 1983, Vertical seismic profiling: Separation of upgoing and downgoing acoustic waves in a stratified medium: *Geophysics*, 48, 555-568.
- Shaw, E.W., 1963. Canadian Rockies-orientation in time and space. In, Childs, O.E. (ed.), *Backbone of the Americas*. Am. Assoc. Petrol. Geol., Mem. 2, 231-242.
- Sheriff, R.E., 2002, *Encyclopedic Dictionary of Applied Geophysics*, Fourth Edition: Society of Exploration Geophysicists.
- Speece M.A., Betterly, S.J., Levy, R.H., Harwood, D.M. and Pekar, S.F., 2007, An over-sea-ice seismic reflection survey in Antarctica using a GI air gun and a snowstreamer : 77th Ann. Meeting, Society Exploration Geophysicists, Expanded Abstracts, 1-5.
- Staples, R.K., Hobbs, R.W., and White, R.S., 1999, A comparison between airguns and explosives as wide-angle seismic sources: *Geophysical Prospecting*, 47, 313-339.

- Steer, D.N., Brown, L.D., Knapp, J.H., and Baird, D.J., 1996, Comparison of explosive and vibroseis source energy penetration during COCORP deep seismic reflection profiling in the Williston Basin: *Geophysics*, 61, 211-221.
- Stewart, R.R., Gaiser, J.E., Brown, R.J., and Lawton, D.C., 2002, Converted-wave seismic exploration: Methods: *Geophysics*, 67, 1348-1363.
- Suarez, G.M. and Stewart R.R., 2007, Acquisition and analysis of 3C land streamer data: The CREWES Research Report, 19.
- Suarez, G.M., Miong, S., Wong, J., Stewart, R.R., Alcuia, A.D., Lu, H., and Al Dulaijan, K., 2008, Well-logging and near surface seismic methods for aquifer detection, EAGE Near Surface 2008 Expanded Abstracts, Paper A028, 4 p.
- Telford, W.M., Geldart, L.P., and Sheriff, R.E., 1990, *Applied Geophysics*, Second Edition: Cambridge University Press.
- Thomsen, L.A., 2001, Seismic anisotropy: *Geophysics*, 66, 40–41.
- Thomsen, L.A., 1999, Converted-wave reflection seismology over inhomogeneous, anisotropic media: *Geophysics*, 64, 678–690.
- Tilander, N.G., and Lattimore, R.K., 1994, Comparison of vibroseis and dynamite acquisition techniques from an area of rough surface topography and outcropping high velocity carbonates: 64th Ann. Meeting, Society Exploration Geophysicists, Expanded Abstracts, 1637-1638.
- van Baaren, P., 2001, Quantitative source testing — a comparison between a 60,000 lb vibrator and an 80,000 lb vibrator: 15th ASEG Geophysical Conference and Exhibition.
- van der Veen, M. and Green, A.G., 1998, Land-streamer for shallow seismic data acquisition: Evaluation of gimbal mounted geophones: *Geophysics*, 63, 1408–1423.
- van der Veen, M., Spitzer, R., Green, A.G. and Wild, P., 1999, Design characteristics of a seismic land streamer for shallow data acquisition, 61st EAGE Conference & Exhibition, Expanded Abstracts.
- van der Veen, M., Spitzer, R., Green, A. G., and Wild, P., 2001, Design and application of a towed land-streamer system for cost-effective 2-D and pseudo-3-D shallow seismic data acquisition: *Geophysics*, 66, 482–500.
- Wei, Z., 2007, Pushing the vibrator envelope — How high can we go?: 69th EAGE Conference & Exhibition, Expanded Abstracts, Paper P184, 5 p.

- Widess, M.B., 1982, Quantifying resolving power of seismic systems: *Geophysics*, 47, 1160–1173.
- Winkel, J.F., 1989, Shotholes revisited; a discussion on a parameter design for deep objectives: 59th Ann. Meeting, Society Exploration Geophysicists, Expanded Abstracts, 667-669.
- Winterstein, D. F., 1990, Velocity anisotropy terminology for geophysicists: *Geophysics*, 55, 1070-1088.
- Wong, J., Miong, S., Gallant, E.V., Bland, H.C., Bentley, L.R., and Stewart, R.R., 2007, VSP and well logs from the U of C test well: The CREWES Research Report, 19.
- Wong, J., Miong, S., Bentley, L.R., and Stewart, R.R., 2008, VSP and well logs from a shallow test well, 2008 SAGEEP annual conference abstract, 14 p.
- Yilmaz, Ö., 1987, *Seismic Data Processing. Investigations in Geophysics: 2*, Soc. Expl. Geophys.
- Yilmaz, Ö. *Seismic Data Analysis: Processing, Inversion, and Interpretation of Seismic Data*. Tulsa: Society of Exploration Geophysicists, 2001.
- Zhiwen, D., Xuefeng, Z., Shitian, C., Shifan, Z., Bangliu, Z., Xiaosong, J., Yabin, G., Yong, H. and Yudong, N., 2004, Converted wave seismic exploration & static correction: 74th Ann. Meeting, Society Exploration Geophysicists, Expanded Abstracts.

Appendix A : ANALYSIS OF THE WEST CASTLE SEISMIC SURVEYS

A.1 Introduction

The West Castle River area of southwestern Alberta (Figure A.1) was host to a group of seismic surveys conducted in the early fall of 2006 by the University of Calgary, the CREWES Project, and Kinetex Inc. These seismic surveys included a 10 km multicomponent seismic line and a simultaneously recorded ARAM line with vertical element geophones (Figure A.2). In addition, high-resolution 3C seismic surveys employing a hammer seismic source were acquired. A set of shallow, borehole seismic surveys with a downhole 3-C geophone and hydrophone cable were also undertaken (Stewart et al., 2006).

The area, in the front range of the Rocky Mountains, is highly structural and prospective for hydrocarbons (Figure A.3). Gas exploration in this area was abandoned in the 1970's when a few wells were drilled unsuccessfully. Since then; relatively little has been reported concerning the subsurface. Our intent was to conduct an integrated study that will provide useful information of this area. In addition to new knowledge about the area, this information will be useful for future geophysical efforts in optimizing the acquisition parameters for better seismic images.

Included in this study are the results of the near-surface characterization using the high resolution 3-C seismic surveys (Part I) and the processing of the 10 km vertical component seismic line recorded with the ARAM system (Part II). The final parameters used in the processing of this dataset will be used as a future reference for subsequent data, which justifies the extensive testing that has been undertaken to find the best parameters that will compensate for the acquisition and for the subsurface effects.

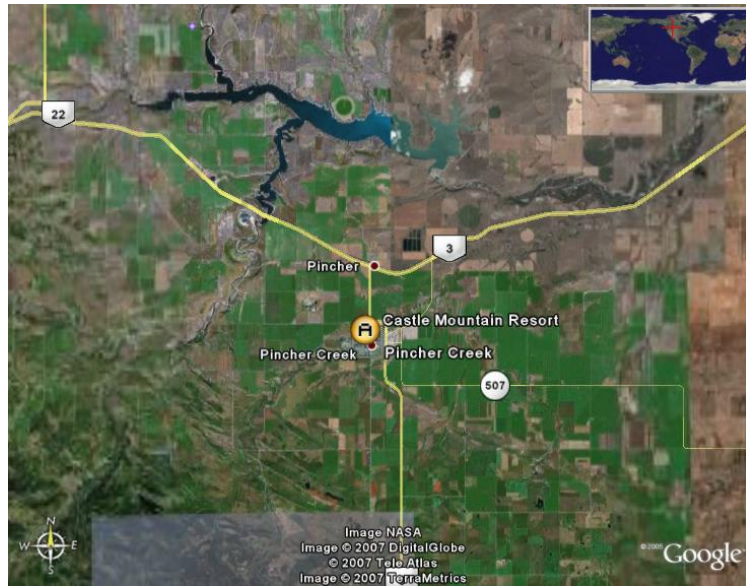


Figure A.1. Map showing the location of the Castle Mountain Resort area, which is close to the area where the seismic surveys were done.

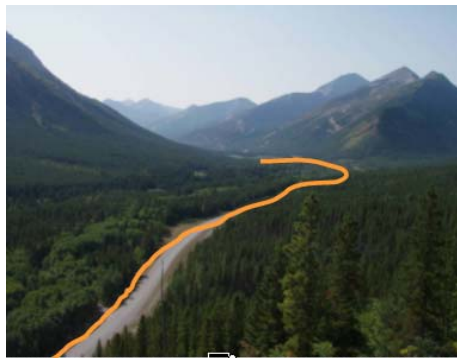


Figure A.2. Photograph, looking south, of the West Castle River area of southern Alberta with the seismic line (shot in August-September 2006) annotated (from Stewart et al., 2006).

A.1.1 Location of the Area of Study

The West Castle River valley is located in a mountainous district of south-western Alberta, south of the Crowsnest Pass, immediately east of the Continental Divide. The area is bounded on the west by the British Columbia-Alberta border around townships 4-5, range 3-4, west of 5th meridian. The study area is located 2 kilometres north of the Castle Mountain ski resort on road 93 (Figure A.1).

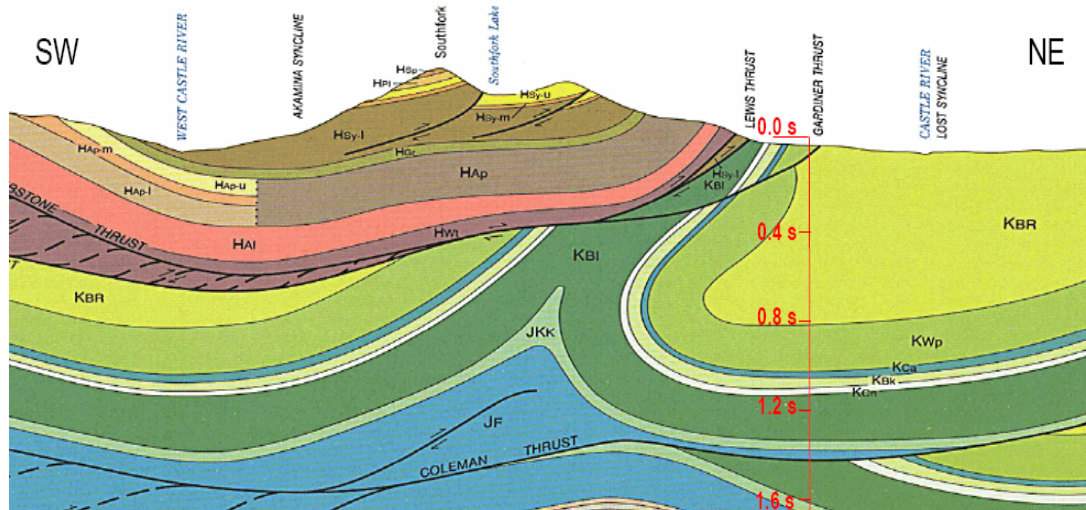


Figure A.3. Geologic cross-section from the south-west to north-east across the Lewis and Gardner Thrusts in the West Castle area (from Norris, 1993).

A.1.2 Previous geophysical investigations of the study area

During the 1940s, the early geophysical surveys (gravity and seismic) were undertaken in western Canada, leading to the discovery of the Jumping Pound, Sarcee and Pincher Creek gas fields (Link, 1949; Bally et. al., 1966). During the 1950s, extensive regional seismic surveys were undertaken, culminating in discovery of the Waterton, Wildcat Hills and West Jumping Pound fields.

Fox (1959), Shaw (1963), Keating (1966) and others, published regional sections that were based on seismic information and contributed greatly to a better understanding of regional structure and problems related to mountain building. However, there is still room for additional geophysical documentation relating to the geology of the Rockies and Foothills of Alberta and southeastern British Columbia.

Most of the geophysical exploration in this area has been accomplished by Shell Canada Limited. Some of this seismic information is presented by Bally et al. (1966) and detailed interpretations are presented by Richards (1959) and Blundum (1956). Kerber (1991) used information from three wildcat wells along North Kootenay Pass (Shell

North Kootenay Pass D-58-H/G-82-07 and Shell North Kootenay Pass 4-23-3-5W5) and to the east of it (Shell Waterton Home 7-3-6-3W5), as well as a migrated seismic section that extends west of the Alberta-British Columbia border at North Kootenay Pass to east of the Coleman fault.

Several other wells exist in the area as a result of hydrocarbon exploration, but the closest ones to the West Castle River area are Shell Waterton Home 7-3-6-3W5 and Shell West Castle 5-7-4-3W5.

A recent survey acquired in this area was undertaken during the fall of 2006 by the University of Calgary, CREWES, and Kinetex Inc. These data included two 10 km 2D seismic lines, a high-resolution 3C seismic surveys and a set of shallow, borehole seismic surveys with a downhole 3C geophone and hydrophone cable (Stewart et al., 2006).

A.1.3 Structure and stratigraphy of the survey area

The southern region of the survey area is situated on the hanging wall of the Lewis Thrust, within the middle Proterozoic sediments of the Helikian Purcell Supergroup. Grey and green argillites of the Lower Siyeh and Grinnell formations outcrop on the valley floor, which are traversed by the West Castle River (Figure A.3). The West Castle River crosses the Lewis Thrust, which is underlain by Jurassic and Cretaceous sediments of the Fernie, Kootenai, Crowsnest, Blackstone, Cardium, Wapiabi and Belly River formations (Stewart et al., 2006).

A.2 Part I: Near surface characterization using the high-resolution 3-C seismic survey

More and more attention has been paid to the applications of converted-wave exploration in assessing oil and gas reservoirs. Due to complexities in acquisition, statics, data processing and interpretation, the technology has taken some time to mature.

Complementing P-wave exploration, the information extracted from converted shear waves can enhance the reliability and precise of lithologic and reservoir prediction. Although multicomponent seismic exploration has been undertaken in many countries for over 10 years, converted-wave data are still challenged to meet the demand of lithologic and reservoir predictions due to the difficulties with the acquisition, processing and interpretation (Zhiwen et al., 2004).

Expectations for S-wave reflection quality are usually high because combined P- and S-wave section interpretations are often applied to subtle exploration problems. Anomalously large S-wave statics represent a challenge because they severely degrade reflection continuity on the stacked section if not given special care. The anomalous reflection delay times result from the sensitivity of S-wave velocity to near-surface and rock-matrix properties, whereas P-wave are primarily sensitive to more laterally constant properties due to saturating fluids in the near-surface rocks. Obtaining a good S-wave statics solution is, then, a key processing step to good S-wave reflection quality (Anno, 1987).

A significant challenge facing converted-wave exploration is the near-surface static corrections required for the P-S wave, which are more complicated than for the P-wave. Since fluids generally have less impact on P-S waves than simple P-waves, and P-S waves have lower near-surface velocities and a thicker low-velocity layer, the near-

surface static correction for P-S wave is often much higher than for P-wave and changes dramatically (Zhiwen et al., 2004).

The West Castle River area of southern Alberta was host to a group of seismic surveys conducted in the early fall of 2006 including a high-resolution 3-C seismic survey. This dataset is used to provide useful information of the very shallow strata, especially a near surface model that could be use as a refraction static model in the processing of multicomponent surface seismic data of the area. This is an important point to consider in Alberta, where the weathering statics problems are very severe due to the irregular thickness of glacial sediments.

The correction of this effect will improve the resolution and continuity of the reflections, especially for the shear-wave data. This first part of the study involved the generation of near surface models from the P-wave component and from the radial component data through the analysis of the first arrivals, using the ProMAX processing software, as well as GLI3D to generate the near surface models. Also to properly identify the first shear arrival in the radial component, polarization analyses were done.

A.2.4 Acquisition parameters of the high-resolution 3-C survey

The high-resolution multicomponent survey employed a hammer source and multicomponent geophones. The source consisted of a 12 lb. sledgehammer with handle trigger. The receivers were 10 Hz 3-C “nail”-type geophones that were being recorded at a 1 ms sampling rate by a Geometrics Geode recording system.

The acquisition was undertaken in four different areas along highway 93, by two different groups. The spread was divided in two fix spread of 100 m each, with receiver intervals of 2.5 m. Several shots for the same source point were done to enhance the

signal-to-noise ratio. In total around 12 shots were recorded for every one of the areas with 40 traces each.

For areas 1 and 4, traces of length 500 ms were recorded, while for areas 2 and 3 only 150 ms of data were recorded. However, because the availability of equipment was limited for area 2 we will not analyze it.

Examples of some of the shots showing the three components for areas 1, 3 and 4 can be seen in Figures A.4, A.5 and A.6. The data in these figures was trace-equalized and scale using a 500 ms sliding window for areas 1 and 4, and a 50 ms window for area 3. The scaling and equalization was applied on the shots to help on the first arrival picking process. From these figures, we can see how the vertical data contains the best data, as expected; however, through the analysis of the data we notice that the source was not a pure P-wave source. Some of the reasons might be the radiation patterns of a vertical impact on a half-space, or maybe the seismic source used did not hit exactly with a 90-degree angle to the horizontal.

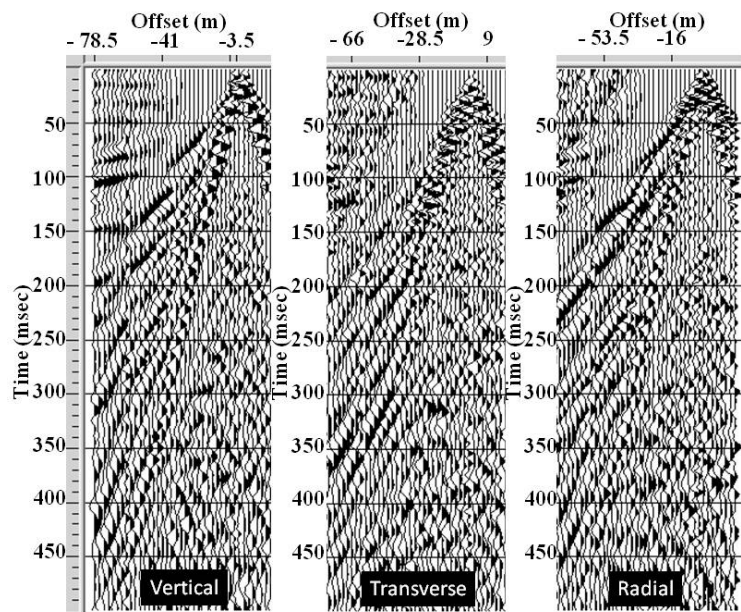


Figure A.4. Three-component shot gather for Area 1: vertical component (left), transverse component (middle) and radial component (right).

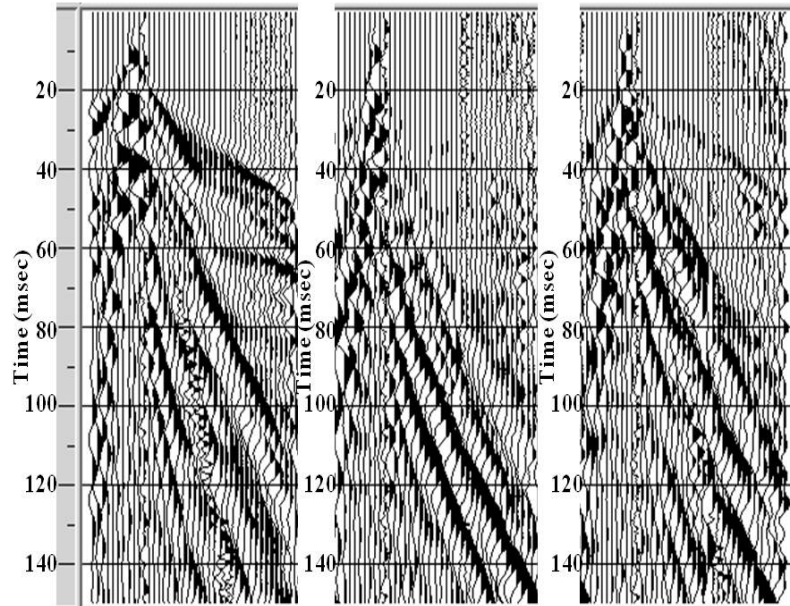


Figure A.5. Three-component shot gather for Area 3: vertical component (left), transverse component (middle) and radial component (right).

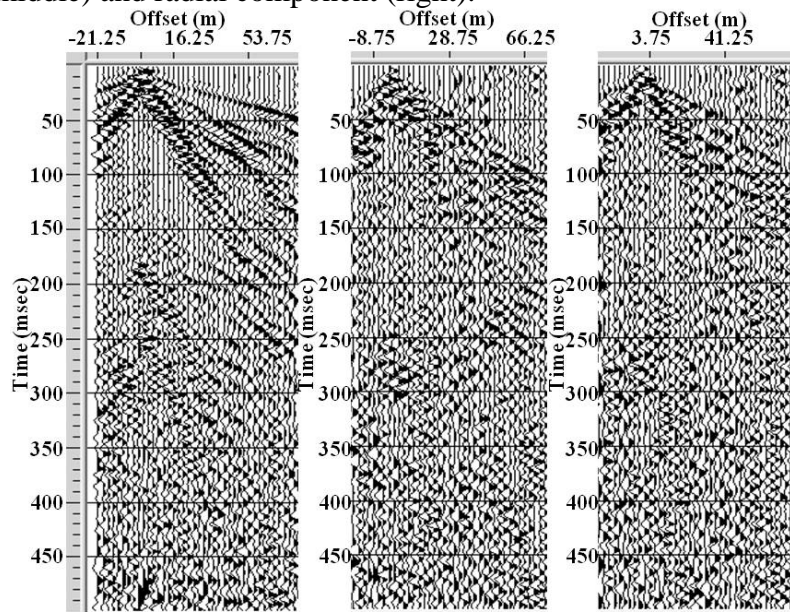


Figure A.6. Three-component shot gather for Area 4: vertical component (left), transverse component (middle) and radial component (right).

A.2.5 Near-surface velocity structure

Refraction analysis of the twelve records for each area was undertaken to calculate and compare the near surface P- and S-wave velocity, and depth profiles. In Figure A.5 we can see an example of a vertical component shot gather where the first

arrivals are observed across all traces, whereas the radial component does not show the refracted arrivals as clearly as in the vertical component.

The 100 m offset range for these surveys was a limitation, which is one of the reasons why we used the hand pick method to determine the first arrivals.

As we mention earlier, the refracted shear arrivals for the radial component could not be easily identified. To corroborate our observations three quality control techniques were used to validate the shear wave arrivals picked by hand. The first method was comparing the data for the three components, the second method was applying a linear moveout correction to the radial channel shot gather using the measured velocity for the vertical component first arrivals, and the third method was using hodograms to determine the polarization of the event that we thought represented shear-wave refractions.

With the first technique, we were trying to compare the three components to identify unique events for the radial component, which are then compared with the ones in the transverse component. The idea is that there are some kind of surface waves that should only be seen in the radial channel, which in this case should be the love waves or refracted transverse arrivals. Another characteristic is that the event identified as a shear-wave refraction would show several layers with lower velocities than the P-wave refractions.

For the second technique, three different linear moveout corrections of the radial channel shot gathers were done, each corresponding to the three different studied areas. Velocities of 1810 m/s, 2700 m/s and 2420 m/s were applied as the input velocity for the Linear Moveout module of ProMAX.

The third technique was generating hodograms. A hodogram is a graphical display of particle trajectory, often projected into a plane as a crossplot over a chosen time window of two orthogonal components of seismic data (Winterstein, 1990); it is one of the polarization methods that allow a visual estimation of the polarization. To create the hodograms was use the hodogram analysis module of the seismic processing package ProMAX.

In Figure A.7, we can see some of the hodograms created for the eighth receiver of the tenth shot of area 1. We can notice how the energy in the horizontal versus vertical component plot has a larger component in the horizontal axis than in the vertical; this same observation can be done in the inline- versus cross-line component graph where the energy has a larger component in the radial than in the transverse axis, showing some ellipticity as well. The same comments can be applied to the examples hodograms for area 3 and 4 (Figure A.7). The extra plot in Figure A.7 is to illustrate how a hodogram appears in areas where groundroll is present.

The next step in obtaining the near-surface model is to use the traveltimes observed from the P-wave refractions and shear refractions. As it was previously explained the method used in our study is an inversion method called Generalized Linear Inversion Method or GLI, which was implemented using the Hampson and Russell Software called GLI3D.

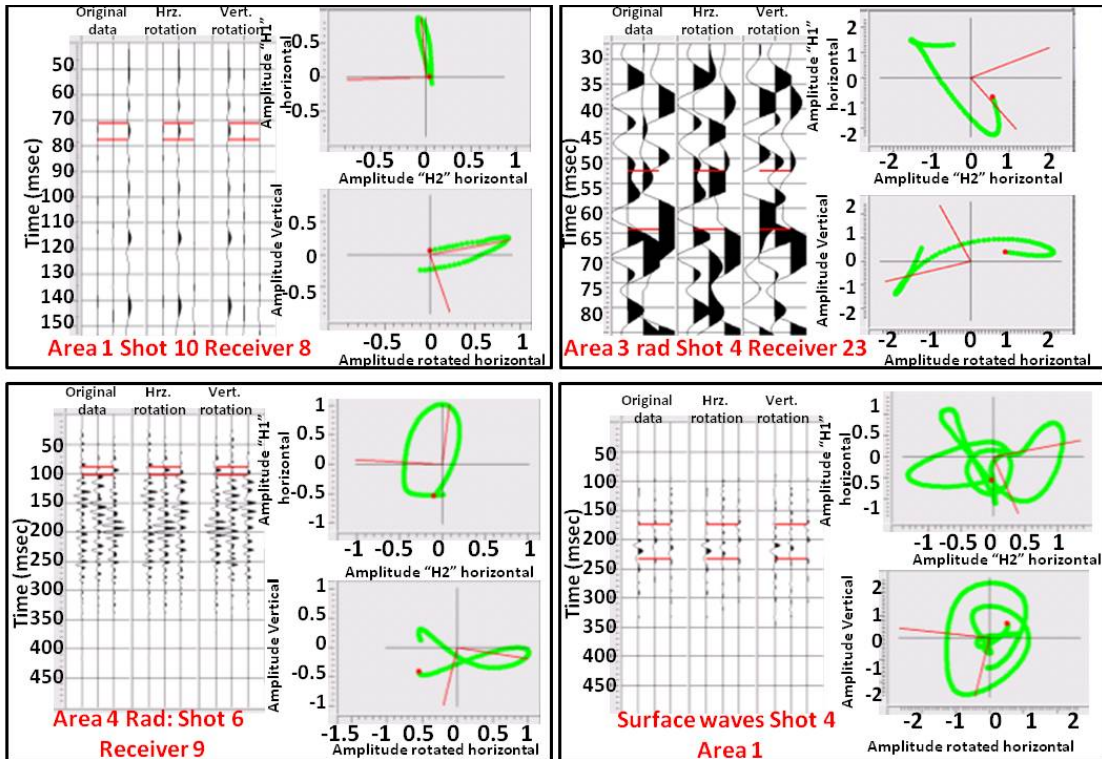


Figure A.7. Example of hodograms for some receivers of areas 1, 3 and 4.

The resulting near-surface models for areas 1, 3 and 4 are presented in Tables A.1, A.2 and A.3. In these tables the velocities and layer thicknesses for P-wave and S-wave data are presented. A determination of the S velocity in the surface layer was not obtainable from the radial component records; some of the possible reasons could be the contamination of the near-offset data by P-wave energy, or the wrong identification of the shear refracted arrivals.

The data from Tables A.1 to A.3 shows clearly that the velocities for P-waves and S-waves are very different, having V_p/V_s ratios between 2.8 (area 3), 3 (area 4) and 3.5 (area 1). We cannot make any assumption of the water table location until we will have information to compare with, as for example VSP data processed from the area; however, it is believed that the first shallow layer in this area has a thickness of around 7 m, which is being reflected by our results. The velocities values between 1800 and 2700 m/s could

indicate the location of the water table, considering the fact that its velocity should be around 1700 m/s for this area.

The differences in the near-surface P-wave and S-wave velocity structure have a significant impact on weathering static corrections. Some magnitudes of static corrections were calculated using as replacement velocity a value of 1800 m/s, which might not be the correct value for this area, but at least will give an idea of the necessary static corrections. These corrections were between 10 and 15 ms for the P-wave and between 20 and 50 ms for the S-waves.

Layer	P		S		V_p/V_s
	Velocity (m/s)	Thickness (m)	Velocity (m/s)	Thickness (m)	
1	640 ± 20	8	Not determined	5	-
2	1820 ± 30	-	520 ± 20	-	≈ 3.5

Table A.1. Resulting near surface model for Area 1.

Layer	P		S		V_p/V_s
	Velocity (m/s)	Thickness (m)	Velocity (m/s)	Thickness (m)	
1	1600 ± 20	6	Not determined	4.8	-
2	2700 ± 30	-	980 ± 20	-	≈ 2.8

Table A.2. Resulting near surface model for Area 3.

Layer	P		S		V_p/V_s
	Velocity (m/s)	Thickness (m)	Velocity (m/s)	Thickness (m)	
1	2420 ± 20	6	800 ± 10	3.8	≈ 3

Table A.3. Resulting near surface model for Area 4.

A.2.6 Discussion and Limitations

A main challenge in multicomponent seismic processing is accurate estimation of static values, velocities and thickness of the near surface layers.

Picking the shear refractions represented a real challenge, and even though alternative techniques were employed to help in its identification, there is still a high level of uncertainty. Another limitation was the short range of offset recorded, and the source variability due to the use of the hammer and different persons every time.

The issues surrounding first break analysis served to give us a first insight of the near surface structure of the West Castle River Area. Our final results were valuable for the refraction static solution of the 10 km seismic line, as they improved the continuity of some of the reflectors in this highly structural zone.

A.3 Part II. 2D seismic data processing and modelling of the vertical component data

A 10 km vertical component seismic line was acquired in southern Alberta with the purpose of imaging a geologically complex area underneath overthrust layers. The near-surface high velocity rocks, variable topography and lateral velocity changes each caused problems for seismic data acquisition and processing as they gave rise to seismic signal attenuation, noise contamination and distortions of arrival times.

Acquisition parameters and seismic data processing description

This vertical vibrator crooked line was acquired with a split-spread configuration (+/- 2000 m), source interval of 10 m and group-receiver interval of 5 m. The split-spread receiver configuration had 272 channels at a 5 m station interval. The nearest offset was 5 m and farthest 3110 m. The data were noisy and suffered from statics problems caused in part by the high velocity, absorbent rocks at the surface, the considerable changes in elevation (from 1100 m to 1400 m), and the rough topography. Figure A.8 and A.9 show shot gathers for the south, middle and north of the line, as well as the raw data stack section. We can see how the quality of the shots in the middle and north of the line

degrades, with a higher signal-to-noise ratio in the south. High amplitude, low-velocity surface wave noise dominates the near offsets, while back-scattered surface waves degrade reflections. The data was processed as well as possible to attenuate the noise, enhance coherency, resolve the statics problems and determine velocity models for stack and migration.

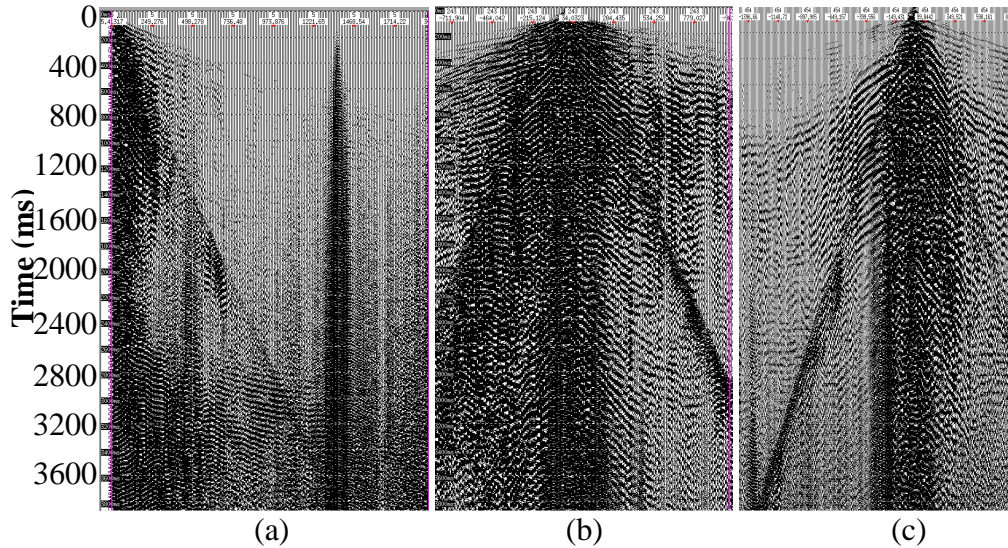


Figure A.8. Raw shots after geometry: (a) South of the line, (b) middle of the line shots, and (c) north of the source line.

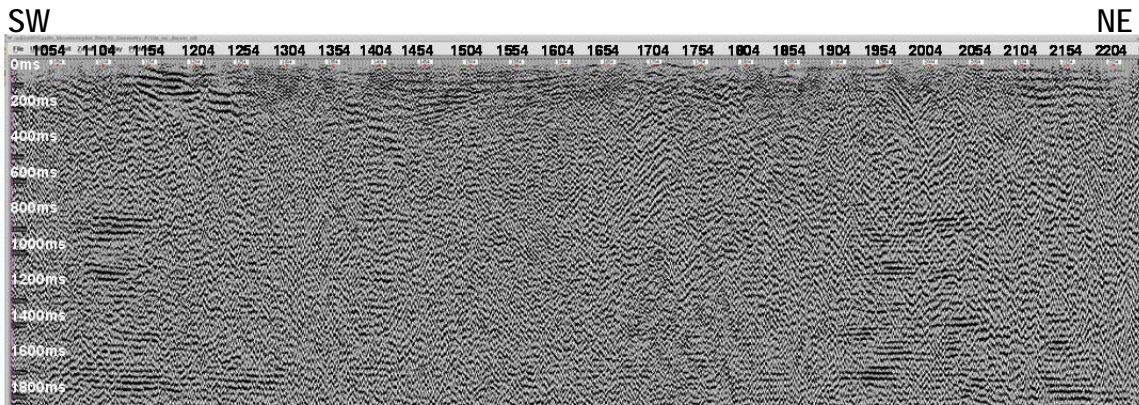


Figure A.9. Brute stacked section.

Extensive testing was done to derive a refraction static solution; the methods tested included a delay time method (MISER), Tomography and the Extended Generalized Reciprocal Method (EGRM). The EGRM method showed the best solution

even though this surface-consistent technique is best suited for linear first breaks and regular acquisition geometries, which is not the case for crooked line geometries (Cox, 1999; Yilmaz, 2001; and Marsden, 1993). Despite the theoretical limitations of this method, the refraction statics solution removed the static inconsistencies observed and helped to enhance some reflections. We also applied residual statics later in the processing flow allowing a maximum shift of 32 ms. To address the problem of noise three passes of signal enhancement techniques were applied at different stages of the processing. The first pass targeted surface wave noise, coherent and random, as well as some linear noise such as airblast. The noise attenuation techniques were applied in the shot domain and included an air wave removal technique, f-x filters, generation of noise models that are removed using match filters, and spatial median filters applied in the frequency domain for limited and small frequency bands. This first pass of signal enhancement was followed by a surface-consistent deconvolution testing, which produced the best results using an operator length of 160 ms and a single window (Figure A.10).

Velocity analysis on these data was not an easy task even after filtering, because there did not seem to be many coherent events and some of them were masked by the remnants of the surface wave and airblast. In total, 6 velocity analyses were done for this data, after first pass of noise attenuation, after refraction statics, after residual statics and deconvolution, after first pass of pre-stack time migration and after final migration to pick final stacking velocities.

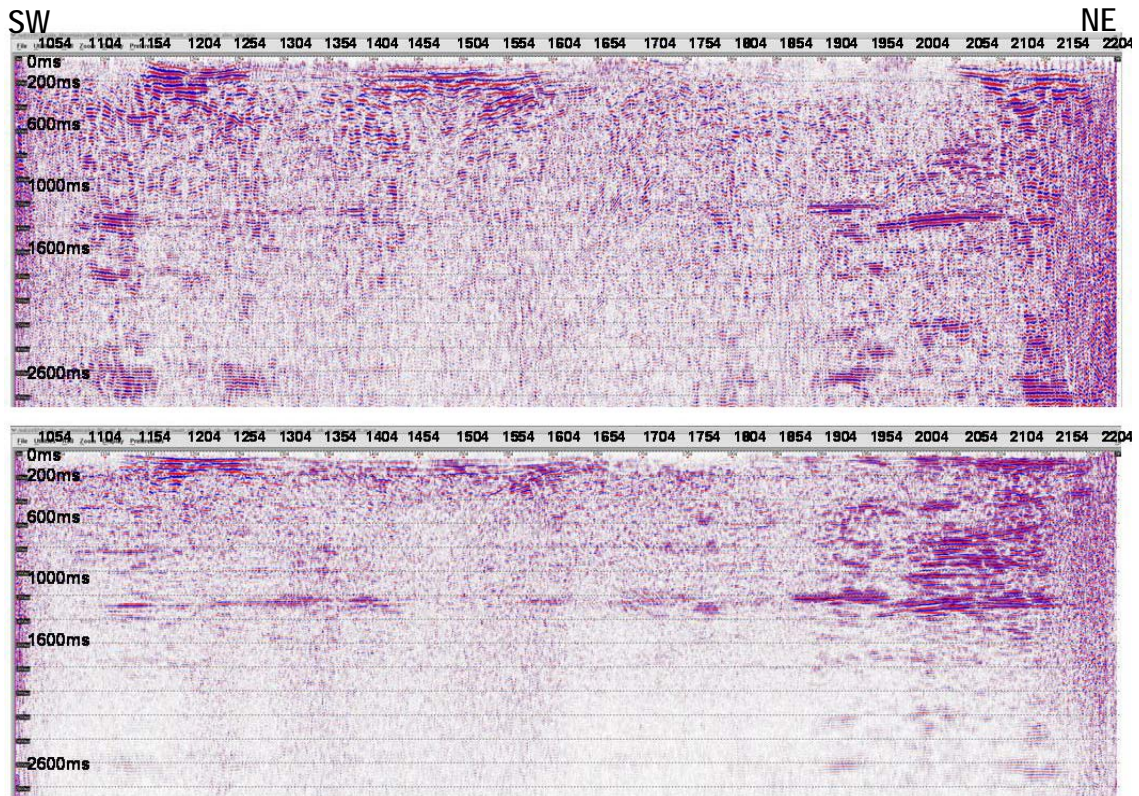


Figure A.10. Stacked section before and after deconvolution : Stack section with 1st pass of noise rejection (top), stack section with 1st pass of noise rejection + surface consistent deconvolution (bottom).

After deconvolution a second pass of signal enhancement was applied in the shot and CMP domain, where the domain used depend on how random was the noise and how effective was the noise rejection algorithm for some specific domains. Up to this point only an exponential gain amplitude compensation method has been applied to the data, looking unbalanced as a consequence of the poor performance of the exponential gain due to the low signal-to-noise ratio. All the stacked sections generated since the raw data until the deconvolution stacked section have had a pre-stacking automatic gain control of 500 ms window as an alternative to the unbalance amplitude and the high level of noise. To try to balance the amplitudes a Surface-Consistent Amplitude Compensation method

(SCAC) was applied to the data, compensating for the amplitude variations that are caused by acquisition effects and not by the subsurface geology. In the presence of some high amplitude spikes, SCAC adds some extra noise to the data, so a noise rejection technique to eliminate these new spikes of the data is necessary. The third pass of signal enhancement was applied after SCAC in the CMP domain, once again it was used a spatial median filter in the frequency domain to attenuate the high amplitude spikes.

Despite the three passes of noise rejection there is still some remaining random noise in the data; in cases such as this one a 3D approach is very effective at attenuating random noise. One of these approaches for 2D data is the 3D random noise attenuation that uses a 3D grid where the main direction is offset and the secondary direction is CMP numbers.

The last step to be completed is the migration. The first migration test for this dataset was a post-stack migration using a finite difference and Kirchhoff algorithm. Both migrated sections suffer from migration artifacts because of the low signal-to-noise ratio, but show surprising differences in reflector locations and character, even though the migrations were based upon the same velocity model. Because of the difficulty of interpreting these different post-stack time migrated sections with any confidence, an iterative pre-stack time migration analysis was done using a 3D approach for a 2D dataset. Two passes of the pre-stack migration were done followed by a velocity analysis. We found that, for some areas along the line, the velocities that flattened the CMP gathers were unreasonably high, and in some others we were unable to pick velocities at all. In the absence of picks, we interpolated from the areas of better quality data. The final migrated section and its comparison with the proposed preliminary interpretation

over the processed image from Hall et al. (2007) are shown in Figures A.11 and A.12. However, because of the lack of information about the velocities in the area, we cannot have a great deal of confidence that the interval velocities represent the true velocity structure of the subsurface because of the limited amount of good data and consequent lack of good focusing picks. There was no well data available to provide constraints on the velocity model.

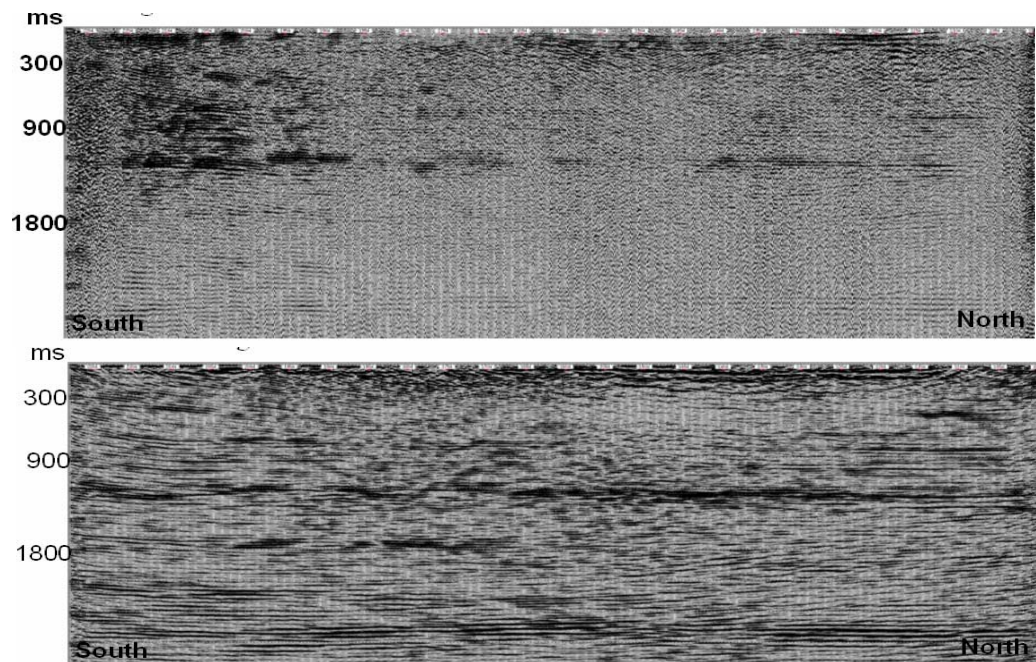


Figure A.11. Stacked section before (top) and after (bottom) pre-stack migration.

sediments V_p/V_s is from 2 up to 8. According to our results, the water table location could be at 8 m with velocities between 1800 to 2700 m/s.

Conclusions for Part II:

The 2D seismic data set processed for the West Castle area constituted a challenge in terms of amplitude compensation, noise rejection and migration. The low signal-to-noise ratio caused by the strong air wave and surface waves made difficult the observation of the seismic reflectors for this area. The quality of the data was variable along the line, especially in the areas close to the West Castle River. Strong reflectors were observed in the south of the line and they allowed the interpretation of some of the small faults and thrusts of the area. The small spacing between receivers and sources was not an advantage for a geologically complex area as this one; instead a more powerful vibroseis source is suggested as well as a bigger spacing between receivers. Explosive sources might be a good idea for this area, helping to eliminate some of the vibroseis source generated noise.